Materials Today Electronics 11 (2025) 100138

Contents lists available at ScienceDirect

Materials Today Electronics

journal homepage: www.elsevier.com/locate/mtelec

Roadmap on metal-halide perovskite semiconductors and devices

Ao Liu [a,*], Jun Xi [b,*], Hanlin Cen [b], Jinfei Dai [b], Yi Yang [c], Cheng Liu [c,*], Shuai Guo [d], Xiaofang Li [e], Xiaotian Guo [f], Feng Yang [e,*], Meng Li [d], Haoxuan Liu [g,h], Fei Zhang [g,h,*], Huagui Lai [i], Fan Fu [i,*], Shuaifeng Hu [j,*], Junke Wang [j], Seongrok Seo [j], Henry J. Snaith [j], Jinghui Li [k,l], Jiajun Luo [k,*], Hongjin Li [m], Yun Gao [m], Xingliang Dai [m,n,*], Jia Zhang [o], Feng Gao [o,*], Zhengxun Lai [p], You Meng [p,q,r,*], Johnny C. Ho [q,r,s,*], Wen Li [t], Yuntao Wu [t,*], Liping Du [a], Sai Bai [a], Huihui Zhu [u,v,*], Xianhang Lin [v], Can Deng [v], Liyi Yang [v], Liu Tang [v], Ahmad Imtiaz [v], Hanxiang Zhi [v], Xi Lu [v], Heng Li [v], Xiangyu Sun [v,*], Yicheng Zhao [v,*], Jian Xu [w,*], Xiaojian She [x,*], Jafar Iqbal Khan [y,*], Guanglong Ding [z,aa], Su-Ting Han [ab], Ye Zhou [z,ac,*], Ruifu Zhou [ad], Jang-Sik Lee [ad,*], Geonwoong Park [ae], Youjin Reo [ae,*], Yong-Young Noh [ae,*]

[a] Institute of Fundamental and Frontier Sciences, State Key Laboratory of Electronic Thin Films and Integrated Devices, Key Laboratory of Quantum Physics and Photonic Quantum Information of the Ministry of Education, University of Electronic Science and Technology of China, Chengdu 611731, China
[b] Key Laboratory for Physical Electronics and Devices of the Ministry of Education & Shaanxi Key Lab of Information Photonic Technique, School of Electronic Science and Engineering, Xi'an Jiaotong University, No.28, Xianning West Road, Xi'an, 710049, China
[c] Department of Chemistry, Northwestern University, 2145 Sheridan Rd, Evanston, Illinois 60208, United States
[d] Key Lab for Special Functional Materials of Ministry of Education, National & Local Joint Engineering Research Center for High-efficiency Display and Lighting Technology, School of Nanoscience and Materials Engineering, and Collaborative Innovation Center of Nano Functional Materials and Applications, Henan University, Kaifeng 475004, China
[e] College of Physics, Henan Key Laboratory of Advanced Semiconductor & Functional Device Integration, Henan Normal University, Xinxiang 453007, China
[f] School of Physics and electronic engineering, Xinxiang University, Xinxiang 453007, China
[g] School of Chemical Engineering and Technology, Tianjin University, Tianjin, 300072, China
[h] Collaborative Innovation Center of Chemical Science and Engineering (Tianjin), Tianjin, 300072, China
[i] Laboratory for Thin Films and Photovoltaics, Empa-Swiss Federal Laboratories for Materials Science and Technology, Duebendorf 8600, Switzerland
[j] Clarendon Laboratory, Department of Physics, University of Oxford, Oxford OX1 3PU, United Kingdom
[k] Wuhan National Laboratory for Optoelectronics and School of Optical and Electronic Information, Huazhong University of Science and Technology, Wuhan 430074, Hubei, China
[l] School of Physics and Optoelectronic Engineering, Hangzhou Institute for Advanced Study, University of Chinese Academy of Sciences, Hangzhou 310024, China
[m] School of Materials Science and Engineering, State Key Laboratory of Silicon and Advanced Semiconductor Materials, Zhejiang University, Hangzhou, China
[n] Wenzhou Key Laboratory of Novel Optoelectronic and Nano Materials and Engineering Research Centre of Zhejiang Province, Institute of Wenzhou, Zhejiang University, Wenzhou, China
[o] Department of physics, chemistry and biology (IFM), Linköping University, Linköping, 58183, Sweden
[p] Changsha Semiconductor Technology and Application Innovation Research Institute, College of Semiconductors (College of Integrated Circuits), Hunan University, Changsha 410082, China
[q] Department of Materials Science and Engineering, City University of Hong Kong, Kowloon 999077, Hong Kong SAR, China
[r] State Key Laboratory of Terahertz and Millimeter Waves, City University of Hong Kong, Kowloon 999077, Hong Kong SAR, China
[s] Institute for Materials Chemistry and Engineering, Kyushu University, Fukuoka 816-8580, Japan
[t] Shanghai Institute of Ceramics, Chinese Academy of Science, 201899, China
[u] School of Physics, University of Electronic Science and Technology of China, Chengdu 611731, China
[v] State Key Laboratory of Electronic Thin Films and Integrated Devices, School of Integrated Circuit Science and Engineering, University of Electronic Science and Technology of China, Chengdu 610054, China
[w] Advanced Research Institute of Multidisciplinary Sciences, Beijing Institute of Technology, Beijing, China

* Corresponding authors.
E-mail addresses: ao.liu@uestc.edu.cn (A. Liu), jun.xi@xjtu.edu.cn (J. Xi), cheng.liu@northwestern.edu (C. Liu), yangfeng@htu.edu.cn (F. Yang), fei_zhang@tju.edu.cn (F. Zhang), fan.fu@empa.ch (F. Fu), shuaifeng.hu@physics.ox.ac.uk (S. Hu), luojiajun@mail.hust.edu.cn (J. Luo), shanfeng@zju.edu.cn (X. Dai), feng.gao@liu.se (F. Gao), youmeng2@cityu.edu.hk (Y. Meng), johnnyho@cityu.edu.hk (J.C. Ho), ytwu@mail.sic.ac.cn (Y. Wu), hhzhu@uestc.edu.cn (H. Zhu), 3120205557@bit.edu.cn (X. Sun), zhaoyicheng@uestc.edu.cn (Y. Zhao), jianxu.xu@bit.edu.cn (J. Xu), xjshe@zju.edu.cn (X. She), j.khan2@hull.ac.uk (J.I. Khan), yezhou@szu.edu.cn (Y. Zhou), jangsik@postech.ac.kr (J.-S. Lee), yjreo97@postech.ac.kr (Y. Reo), yynoh@postech.ac.kr (Y.-Y. Noh).

https://doi.org/10.1016/j.mtelec.2025.100138
Received 19 October 2024; Received in revised form 16 January 2025; Accepted 24 January 2025
Available online 27 January 2025

[x] State Key Laboratory of Extreme Photonics and Instrumentation, College of Optical Science and Engineering, Zhejiang University, Hangzhou, 310000, China
[y] Department of Physics, School of Natural Sciences, University of Hull, Cottingham Road HU6 7RX, Hull, UK
[z] State Key Laboratory of Radio Frequency Heterogeneous Integration, Shenzhen University, Shenzhen 518060, China
[aa] College of Electronics and Information Engineering, Shenzhen University, Shenzhen 518060, China
[ab] Department of Applied Biology and Chemical Technology, The Hong Kong Polytechnic University, Hung Hom, Hong Kong SAR, China
[ac] Institute for Advanced Study, Shenzhen University, Shenzhen, China
[ad] Department of Materials Science and Engineering, Pohang University of Science and Technology (POSTECH), Pohang, Gyeongbuk, 37673, Republic of Korea
[ae] Department of Chemical Engineering, Pohang University of Science and Technology (POSTECH), Pohang, Gyeongbuk 37673, Republic of Korea

ARTICLE INFO

Keywords:
Halide perovskite
Optoelectronic devices
Photophysics

ABSTRACT

Metal-halide perovskites are emerging as promising semiconductors for next-generation (opto)electronics. Due to their excellent optoelectronic and physical properties, as well as their processing capabilities, the past decades have seen significant progress and success in various device applications, such as solar cells, photodetectors, light-emitting diodes, and transistors. Despite their performance now rivaling or surpassing that of silicon counterparts, halide-perovskite semiconductors still face challenges for commercialization, particularly in terms of toxicity, stability, reliability, reproducibility, and lifetime. In this Roadmap, we present comprehensive discussions and perspectives from leading experts in the perovskite research community, covering various perovskite (opto)electronics, fundamental material properties and fabrication methods, photophysical characterizations, computing science, device physics, and the current challenges in each field. We hope this article provides a valuable resource for researchers and fosters the development of halide perovskites from basic to applied science.

Introduction

Ao Liu*
Institute of Fundamental and Frontier Sciences, University of Electronic Science and Technology of China, Chengdu 611731, China
E-mail address: ao.liu@uestc.edu.cn

The past decade has witnessed significant progress in metal-halide perovskites across various applications, from initial energy harvesting and light emission/detection to recent advances in electronics [1–7]. Their broad modulation of physical dimensionality and chemical composition, and consequently optoelectronic properties, makes halide perovskites versatile for various applications. This emerging semiconductor family possesses remarkable optoelectronic properties, including large absorption coefficient in the order of 10^5 cm^{-1}, [8]. composition-tunable band gap, mild charge-carrier mobilities up to hundreds of cm^2 V^{-1} s^{-1}, [9]. long carrier lifetime up to 1 μs and diffusion lengths of ~1 μm, high emission efficiency, small exciton binding energy, and small Urbach energy as small as 12.6 meV. [8,10,11]. Meanwhile, halide-perovskite materials can be easily fabricated from solution or vapor, enabling integration into industrial manufacturing and facilitating low-cost mass production [12]. As a result, significant strides have been made in developing high-performance solar cells, light-emitting diodes (LEDs), detectors, and electronic devices such as memory and transistors. Concurrently, there has been an increase in fundamental studies aimed at understanding the underlying physical, chemical, and electronic properties of halide perovskites, which will drive future advances in device performance.

In this Roadmap, we summarize key aspects to provide an overview of the current status of perovskite semiconductor research and highlight promising directions for future research. We firstly introduce fundamental properties and unique characteristics of this class of materials. In later Sections, we discuss key strategies for improving the efficiency and stability of halide perovskite solar cells, focusing on interface passivation, tandem construction, self-assembled monolayer hole transport layers, and low-dimensional perovskite layers. At this stage, lead (Pb) halide perovskites represent the most promising candidates for next-generation photovoltaic technologies. Considering its toxicity, we also discuss the safety of Pb for commercial applications. The following sections delve into the other intriguing optoelectronic topics of perovskite LEDs, laser diodes, and photodetectors for broadband and circularly polarized light. The demonstration and discussion of a high-throughput solution deposition approach is expected to further enhance the efficient and reproducible batch fabrication of diverse perovskite optoelectronics.

The success of halide-perovskite semiconductors in high-performance optoelectronics has reignited great interest among theoreticians and physical scientists in exploring and highlighting the underlying optical and physical mechanisms and functionalities. The following sections will specifically introduce the theoretical studies on defect engineering, charge transport property, and the photophysics, respectively. Besides their giant progress in various optoelectronic devices, we are excited to see halide perovskites extend their applications in diverse electronic devices, such as the neuromorphic electronics for applications in brain-inspired computing and artificial sensorimotor nerves, and memory and filed-effect transistors.

I. Fundamental properties of metal hybrid perovskites

Jun Xi*, Hanlin Cen, Jinfei Dai
Key Laboratory for Physical Electronics and Devices of the Ministry of Education & Shaanxi Key Lab of Information Photonic Technique, School of Electronic Science and Engineering, Xi'an Jiaotong University, No.28, Xianning West Road, Xi'an, 710049, China
E-mail address: jun.xi@xjtu.edu.cn

1. Status of the field

In general, metal hybrid perovskites (MHPs) adopt the corner sharing octahedra, following a similar manner of $CaTiO_3$ ($Pm\bar{3}m$ space group), to crystallize in a three-dimensional (3D) network [11]. The typical formula is ABX_3 (Fig. 1a), for which A refers to methylammonium (MA^+), formamidinium (FA^+) and cesium (Cs^+) cation, B denotes Pb^{2+}, Sn^{2+}, and Ge^{2+} divalent cation, and X includes the halogen anion. According to Goldschmidt's tolerance factor (t), [13]

$$t = (r_A + r_X) / \sqrt{2}\,(r_B + r_X)$$

where r_A, r_B and r_X represents the radii of corresponded ion, supposed t falls in a range of (0.81~1.11), the structure is allowed to be stabilized. Accordingly, to promise the target optoelectronic properties and reinforce stabilities, the MHP composition can be designed more flexible by rationally choosing hybrid A, B and X ions.

In addition to 3D structure, two-dimensional (2D) architype has been widely investigated owing to its peculiar anisotropic exciton and improved formation energy [14]. Accordingly, for 2D perovskites, the carrier mobility along the inorganic plane can be at least one order of magnitude higher than that out of the plane, which will be beneficial for on-chip integrated electronic energy supply. In principle, 2D lattice can

viewed as the bulky organic cations (spacers) intercalating into inorganic octahedra sheets (one to several layers) by van der Waals interactions (Fig. 1a) [15]. Considering the strain release ability of local spacer on octahedra, *t* used in defining 3D lattices is not adapted to 2D ones any more, making oversized A cations (such as guanidium (GA)) enter the cavity possible [16]. Notably, when bulky cations cannot support the 2D arrangement, the octahedra fashions becomes single chains or clusters, leaving 1D or 0D prototypes (non-perovskite metal halides). By virtue of leveraging novel spacers as well as A cations, a plenty of unprecedented 2D structures can be expected for versatile applications [17,18]

MHPs are known as direct gap semiconductors, that the valence band maximum (VBM) and conduction band minimum (CBM) lie at the same position in *k*-space. Taking $MAPbI_3$ as an example (Fig. 1b), CBM is dictated by Pb 6p orbital while VBM is composed of hybrid orbitals by I 5p and Pb 6s in an approximate ratio of 3:1 [10]. Following this electronic theory, most studies have proved that the bandgap of MHPs can be tuned in a ultrabroad range by introducing variegated $[BX_6]^{4-}$ stoichiometry, thus greatly favoring the tandem photovoltaics and colorful diodes. Regarding 2D structures, due to their natural quantum-well regime, the bandgap is more like a hybrid from spacer barrier and $[BX_6]^{4-}$ well, where VBM resembles 3D fashion but CBM involves more

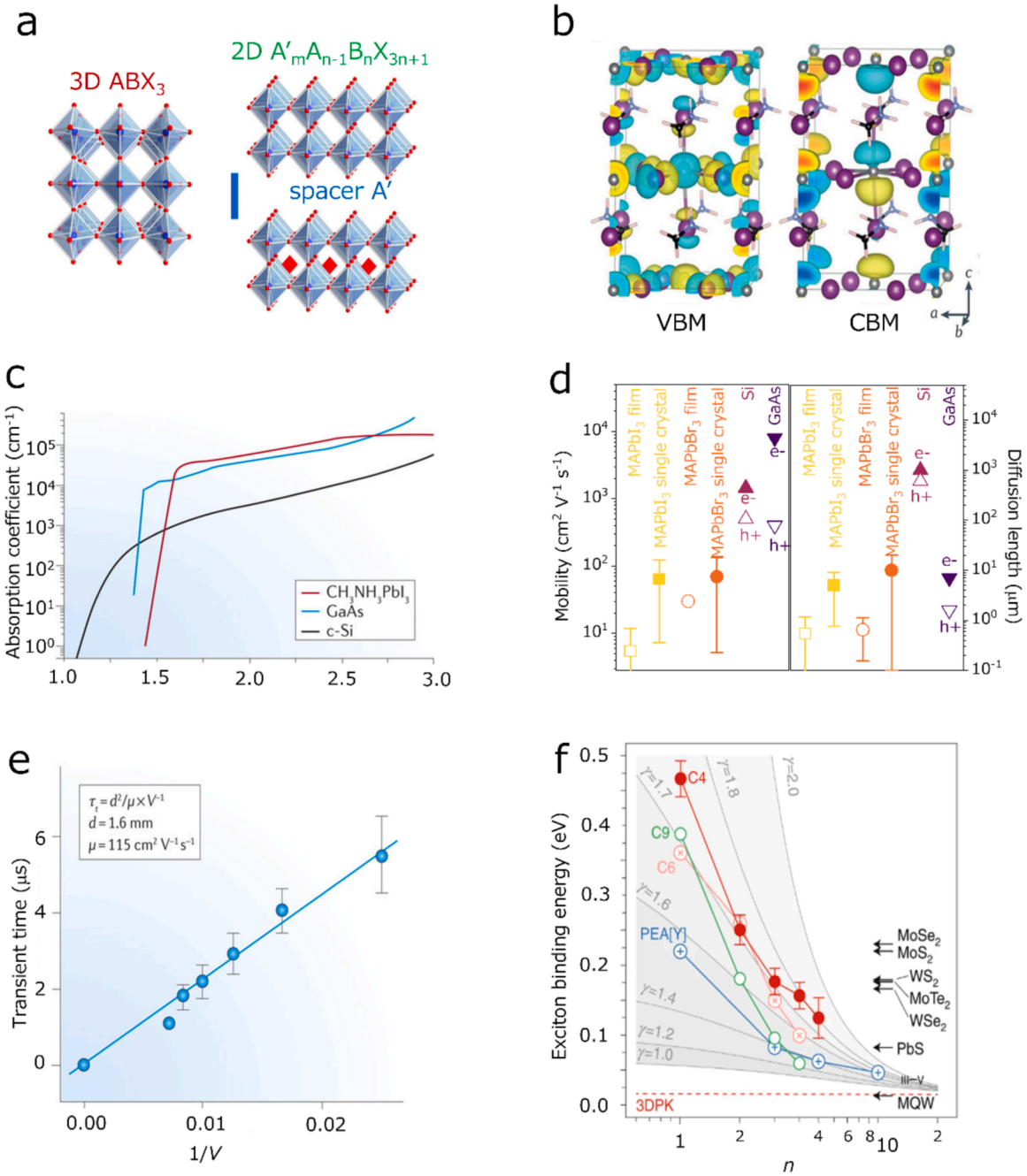

Fig. 1. a, Schematic diagram and basic formula of halide perovskite structure from two-dimensional to three-dimensional, [26]. **b,** The wave functions of $MAPbI_3$ at the gamma point in VBM and CBM demonstrate the distribution of electrons and holes in the material. VBM is mainly composed of the p orbitals of iodine (I), while CBM is mainly composed of the p orbitals of lead (Pb), [11]. **c,** Absorption coefficient, [11]. **d,** mobility and diffusion length of charge-carrier in different semiconductors, **e,** Transient time measurement results including charge-carrier diffusion length (*D*) and mobility (μ) of $MAPbBr_3$ single crystal, [11]. **f,** Comparison of exciton binding energy (E_b) and exciton effective mass (m^*) of III-V compound quantum wells, two-dimensional graphene materials, two-dimensional halide perovskites, and three-dimensional halide perovskites [11,24]

complexity with strong spin-orbit coupling [19]. As such, reduced dimensions open more possibilities to modulate bandgap with manageable exciton states.

Unlike the defect sensitive natures of traditional semiconductors, MHPs are gifted with highly defect tolerance, that the mostly observed vacancies work as more like shallow defect states [20]. Hence, MHPs present efficient charge-carrier diffusion capacity and high photoluminesce quantum yield. Here we summarize several key physical parameters of MHPs compared with some traditional semiconductors (Figs. 1c and 1d). Although the effective mass (m^*) revealed in MHPs is close to that in Si and GaAs, the charge-carrier mobility (μ) cannot compete, lagging behind several magnitudes [21]. Nonetheless, the charge-carrier diffusion length (D) is considerable (Fig. 1e). Such low correlation between μ and D interrogates what dominates the charge-carrier mechanism [11]. In light of the Boltzmann equation ($\mu = (e/m^*)^*\tau$, τ is thermal scattering lifetime), scattering issues should matter the mobility with the lower effective mass [11]. Due to the shallow defect states, phonon interactions with charge-carriers have been deduced as the possible interpretation for the mediated mobility [22]. Meanwhile, large polarons, which are induced by the dynamic lattice decorated with charge-carriers, can fully address the superb diffusion length due to charge screening effect [23]. Last, one should be aware of the exciton binding energy (E_b) when discussing charge-carriers in particular MHPs (Fig. 1f): as dimensions decreased from 3D to 2D and even to 0D, E_b can increase from tens to hundreds millielectronvolt (meV), making free carriers to bound excitons, which can be applicable for desired optoelectronics [24,25]

2. Current and future challenges

Different from the strong covalent bond in their chalcogenide analogues, the ionic bonding natures of $[BX_6]^{4-}$ units in MHPs pose highly risk of degradation especially exposed to humidity or even high-energy stimuli [27]. Previous works reveal that the halide vacancies as the active sites can significantly trap the water and oxygen molecules in ambient, and their long-lives states can trap excitons to induce I_2-associated photochemical degradation upon light soaking (Fig. 2a) [28]. In this scenario, it is of high significance to improve the structure stability of MHPs used in particular devices.

Afterwards, most optimization usually adopt hybrid compositions especially the mixed halides used in wide-bandgap MHPs. Such design is found extremely sensitive to long-term light soaking or electrical driving, that the binary I/Br or Br/Cl moieties separate easily each other [29]. In parallel, the weakly bonded B-X is able to initialize ion (halide) migration along the vacancies-channel under stimuli, leading to defective hysteresis and lattice collapse (Fig. 2b) [30]. Hence, the challenges on the hybrid halide MHPs lie in confining the homogeneous domains and regulating ionic activities.

Regarding the lower dimensional MHPs, a wealthy of issues remains on the crystallographic and atomic levels given the vast variety of compositions. Despite the difficulty in setting scaling laws here, the community should pay more attention to the synthesis reproducibility when using particular spacer/ligand molecules (Fig. 2c) [31]. This is due to the uncertain miscibility of the preset compositions in a hybrid polar-nonpolar solvent system for single crystal growth. In addition, the identification of anisotropy properties strongly depends on the layer thickness, which asks for more reliable thin-sample fabrication especially for the strongly interacted Dion-Jacobson phase [15].

As discussed above, MHPs can be tailored as narrow- or wide-bandgap, which is formed by Pb-Sn alloyed or I-Br binary compositions. In Pb-Sn alloyed system, due to the easy tendency of Sn (II) being oxidized, the lattices are forced to break down, degrading into I_2, SnO_2, and excess PbI_2 [32]. In Br-I mixed one, halide separation as mentioned is the key problem to limit access to commercialization of tandem device. Definitely, when connecting narrow- with wide- bandgap MHPs in heterojunction regime, the local molecular interfaces have to be designed carefully to greatly resist ion shuttle effects between these two different MHPs [33].

During the past progress, irrespective of lattice compositions, MHPs are more prepared in polycrystalline film states. Even though the

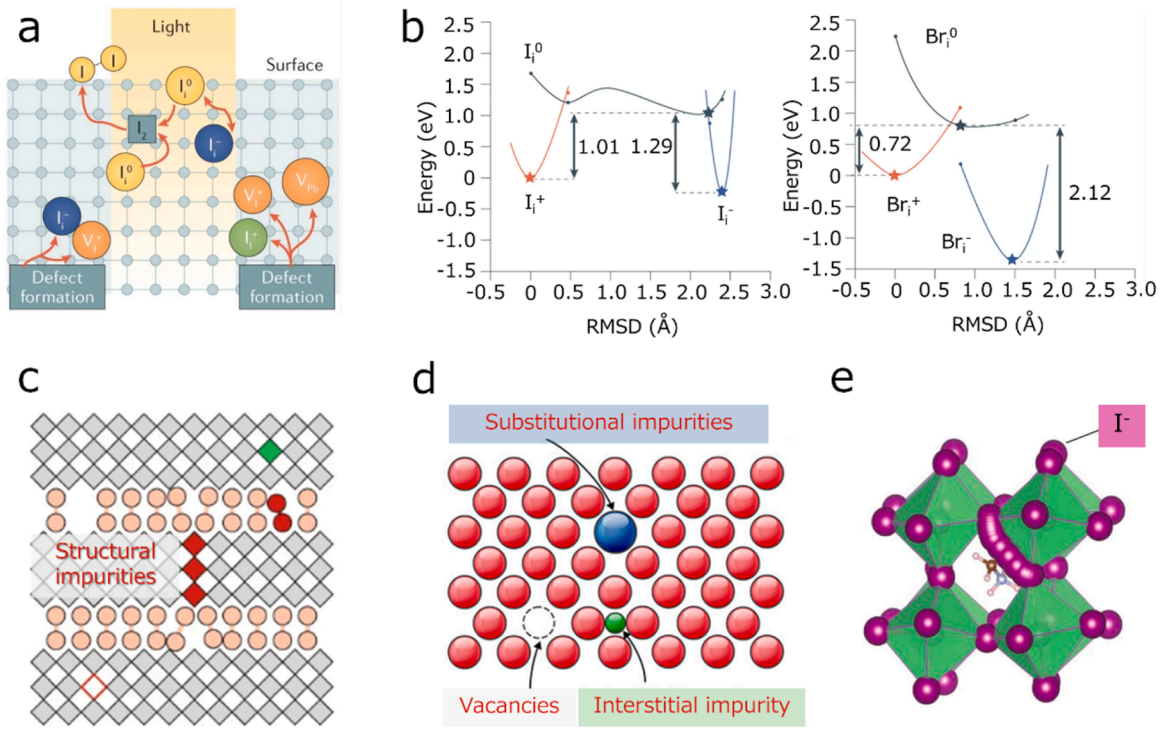

Fig. 2. a, Illustration of the migration path of I^- ions in $MAPbI_3$ crystal [30]. **b,** The relative energy diagram of the gap between bromine and iodine ions which indicates that the negative bromine ion gap is more difficult to oxidize than its iodine homologues [30]. **c,** Schematic diagram of phase purity and crystal orientation structure [24]. **d,** Schematic diagram of possible doping sites in 3D perovskite, especially doping sites within grain boundaries [34]. e. Schematic diagram of ion (I^-) migration channels in $MAPbI_3$ [36].

theoretical superior charge-carrier behaviors, as the nucleation and coarsening processes evolves, exotic impurities can be introduced into the perfect periodic dot matrix (Fig. 2d), breaking the centrosymmetric structures. Hence, deeper trap states likely produce to scatter charges, and Rashba and Dresselhaus effects will be generated [34]. In this case, charge-carrier behaviors have to be treated critically, that the detailed events (mobility, diffusion length etc.) need to be well decoupled under standard conditions.

Last, we revisit the ionic-electronic hybrid natures of MHPs. Inevitably, ion migration always accompanies with the charge-carrier motions even using the lower dimensional MHPs in operando devices (Fig. 2e) [35]. In other words, dynamic competition between ions and charges cannot easily detangled for their respective kinetics. This leaves a complex impact: On one hand, mobile ions that induced internal field screening will result in performance degradation for optoelectronic devices; On the other hand, well controlled ion conductivity will shine light on non-volatile memristivity characteristics for developing artificial neural networks. Following the potential, to draw a clearer picture on ionic-electronic mechanism in MHPs remains a great challenge.

3. Advances to meet challenges

Since MHPs have different degrees of structural vulnerability to ambient air, radiation exposure, and electric fields, the community should always pay attention to the decomposition mechanism behind each factor from a thermodynamic perspective. In most well-performing optoelectronic devices, 3D MHPs are the main active compounds, and their low native formation energy is a key factor limiting their stability [37]. Based on this knowledge, owing to the enhanced formation energy in lower dimensional (2D/1D/0D) structures, incorporating these moieties into 3D frame forming bulk heterojunction, or assembling these staffs upon 3D interfaces forming planar heterojunction, have been proposed to resolve the stability issue (Fig. 3a) [38]. Such strategies can be further generalized to MHPs with various bandgaps, especially Pb-Sn alloyed series.

Nevertheless, spacer/ligand molecules presented in different MHP systems and devices cannot invariably reach a consensus on the formed local microstructure and produced physical effects. For the purpose of building a spacer/ligand database on structure-property relationship, it is imperative to elaborate associated principle by determining key thermodynamics factors, and interpret the quantitative effects related to stability, including vacancy densities and halide separation rates. Correspondingly, machine learning can be a powerful tool to accelerate the development of this scope [39]

Except for the dimensionality reduction manner, high quality single crystals can greatly suppress the bulk trap states in MHPs, resulting in improved stability and charge-carrier mobility (Fig. 3b) [40]. Another way to surpass the dilemma is to replace the natural ionic bond with strengthened covalent bond, such as metal chalcogenide (Fig. 3b). However, this should be carefully treated due to the critical formation energies of general Pb-S/Se bonds and the potential 2D or 1D lattice formation instead of expected 3D archetype.

We would like to underline that aforementioned engineering strategies have been further validated to decrease the trap densities, suppress the phonon interaction, cultivate the built-in field, which turn to improve charge-carrier motion in both lattice structures and electronic devices. For potential ion issues, reverse electric pulses on the operating device and high scan speeds of *J-V* measurements can be used to diagnose factors affecting ion migration at built-in potentials (Fig. 3c) [36, 41]. Accordingly, targeted engineering (e.g., bulk passivation, dimensionality tuning, etc.) can be adopted to minimize ion effects to achieve steady-state output in practical scenarios.

4. Concluding remarks

MHPs are believed as the perfect semiconductors to outperform in cutting-edge electronic applications. Their relaxed crystallographic lattices do not ask for strictly following tolerance factor theory, leaving large space to tune the electronic levels and charge-carrier behaviors. Their ionic bonds and soft lattices, however, raise most concerns on phase instability and phonon-mediated charge-carrier mobility. With years of dedication in both science and engineering, finely designing the

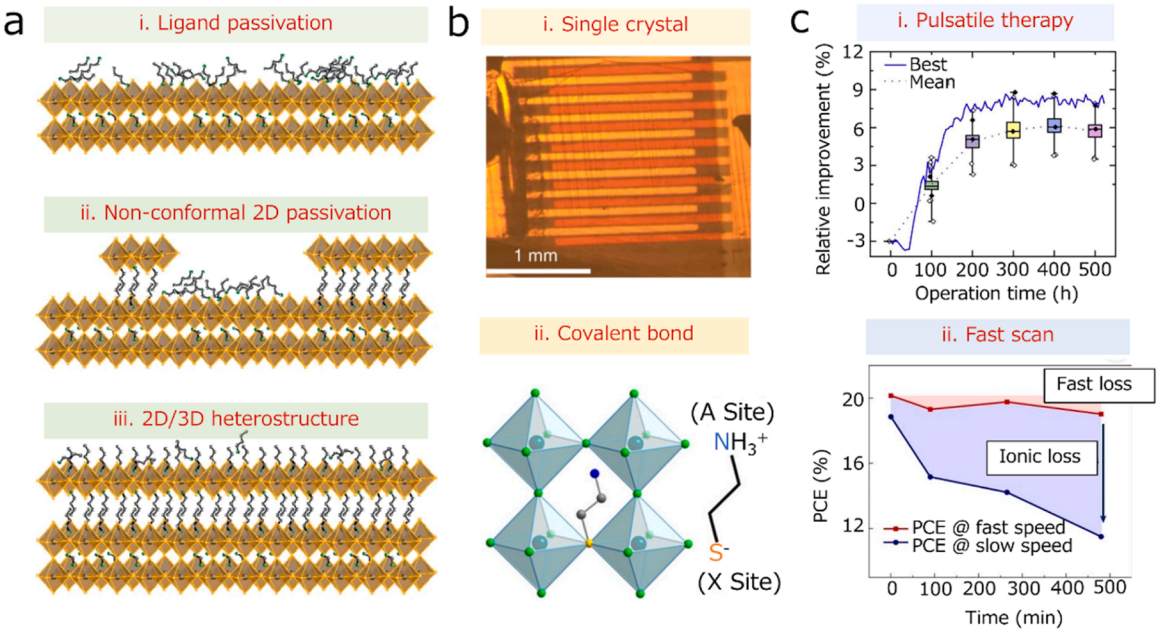

Fig. 3. a, Three interaction case of ligand molecular with MHPs surface: (I) The ligands reacting with the perovskite work as covers on the surface of the 3D perovskite surface, (II) Partial ligands reacting with perovskite form a non-conformal 2D perovskite layer, (III) Ligands sufficiently reacting with perovskite lead to a conformal 2D perovskite layer formed upon 3D layer [38]. **b,** (I) Photos of integrated single crystal devices for perovskite solar cells, (II) Structural schematic diagram of (A) (MA) PbX_3: A new lead halide perovskite structure formed by combining CYS molecules act as zwitterions, with the amino end (NH^{3+}) serving as the cation A site and the sulfur end (CH_2S^-) serving as the anion X site [41,42]. **c,** (I) A schematic diagram of the impact of Pulsatile therapy (PT) on the long-term stability of perovskite solar cells and its comparison with maximum power point tracking (MPPT), (II) Schematic diagram of the variation of steady-state and ion freezing efficiency with aging time measured at different scanning speeds [36].

mixed lattices or even dimensional heterostructures in thin-films as well as single-crystals states has advanced the relevant photophysics and facilitated the device performance. In near future, their device commercialization still calls for comprehensive insights of structure-property interplay and exceptional techniques of device architecture.

II. Interface passivation for high-efficiency and stable perovskite solar cells

Yi Yang, Cheng Liu*

Department of Chemistry, Northwestern University, 2145 Sheridan Rd, Evanston, Illinois 60208, United States

E-mail address: cheng.liu@northwestern.edu

1. Status of the field

Perovskite solar cells (PSCs), composed of multiple functional layers, contain numerous interfaces that are critical to their performance. The efficient operation of PSCs relies on the effective separation of charge carriers within the perovskite active layers and the subsequent transport of these carrier across interfaces [43]. However, during fabrication or under operating conditions, unintended perovskite defects and minority carriers at these interfaces often lead to significant non-radiative recombination, which undermines device performance [44]. The impact of recombination losses becomes even more pronounced in tandem devices due to the increased number of interfaces [45].

Defects in perovskite materials can be classified into point defects and higher-dimensional defects [46–48]. Point defects include vacancies (missing ions at lattice sites), interstitials (extra ions at non-lattice sites), and anti-site occupations (ions at incorrect lattice sites) [49–51]. Higher-dimensional defects encompass one-dimensional (1D) dislocations (irregularities within the crystal lattice), two-dimensional (2D) grain boundaries (interfaces between different crystalline grains), and three-dimensional (3D) precipitates (clusters of impurities or secondary phases within the crystal) [52].

Minority carriers, which are less abundant charge carriers, generally arise due to thermal excitation, doping, or external stimuli such as light or radiation [53]. At PSC interfaces, these minority carriers (electrons at the p-type interface and holes at the n-type interface) serve as recombination centers, thereby increasing contact resistance for majority carriers [44,54]. Reducing surface defects and minimizing minority carrier recombination are therefore crucial for enhancing the performance of PSCs.

Interface passivation has emerged as the most effective strategy for mitigating carrier recombination at interfaces and can be categorized based on the passivation mechanism. Chemical passivation involves treating the perovskite surface with functional molecules—such as ammonium halide salts [55–58], Lewis acids/bases [59–62], and cationic metal ions [51]—that react with defect sites, forming covalent or ionic bonds with perovskites and deactivating the electronic or chemical reactivities of these defects [63]. Physical passivation, on the other hand, improves material properties by altering the physical structure or relieving internal stresses through methods such as strain relaxation, thermal annealing treatment, or surface polishing [64,65]. Additionally, field-effect passivation reduces recombination rates by creating an electric field at the interface to repel minority carriers, achieved either through materials with built-in electric fields or applying external electric fields [66,67].

2. Current and future challenges

Despite significant advancements in passivation strategies that have improved the efficiency and stability of PSCs, several challenges persist, including the complexity of interface recombination, the stability of passivation layers, and the difficulty of passivating buried interfaces.

The surfaces of perovskite films often exhibit various defects, leading to complex recombination processes at PSC interfaces [44,68]. For instance, volatile organic halides may escape during solvent evaporation and high-temperature annealing, leaving behind halide vacancies at the X-sites (occupied by anions in the perovskite structure) and cation vacancies at the A-sites (occupied by cations in the perovskite structure) on perovskite surfaces [47]. Additionally, the presence of minority carriers at the interface increases the recombination rates, exacerbating energy loss. The interaction among different defect types, charge carriers, and materials within the solar cell, especially in tandem structures, further complicates the identification and mitigation of all recombination sources.

Moreover, while bulk perovskite stability has been well-studied, the stability of passivation layers has received comparatively less attention [69]. The cations in common passivation materials, such as ammonium halide salts or their low-dimensional perovskites, tend to migrate into the 3D perovskite bulk under thermal stress, degrading device performance [70]. Additionally, the decomposition of passivation materials during operation is a concern. For example, ammonium-based passivation ligands can deprotonate into amines and react with formamidinium on perovskite surface, which may create new recombination pathways and degrade the long-term stability of the device [71,72]. Addressing the stability of passivation layers is therefore critical for ensuring sustained performance improvements in PSCs.

Buried interfaces present further challenges, as they can harbor defects that are difficult to diagnose and access for direct passivation. Moreover, most interfacial modulation materials tend to dissolve in perovskite precursor solvents and may be washed away during coating process. Beyond addressing defects at buried interfaces—similar to those on the top surface caused by the abrupt interruption of the perovskite lattice—the properties of these interfaces significantly influence perovskite nucleation, film growth, defect formation, and overall stability [73]. For example, the development of organic hole transport materials at buried interfaces has rapidly advanced inverted (p-i-n) PSCs, but hydrophobic nature of these materials increases the likelihood of void formation and reduces interface contact between the perovskite and hole transport layers [74]. Additionally, exposure of buried interfaces to sunlight raises concerns about ultraviolet (UV) stability, as the degradation of contact materials or their photocatalytic effects on perovskite under UV light can lead to interface degradation during operation [75,76].

3. Advances to meet these challenges

Overcoming these challenges requires a thorough understanding of the defect landscape in perovskite films, the development of more robust and durable passivation materials, and innovative strategies to manage buried interfaces (**Table** S1).

Several approaches have been proposed to address the complex recombination processes at PSC interfaces. For instance, Liu et al. identified intricate recombination mechanisms at the perovskite/electron transport layer interface and proposed a bimolecular passivation strategy, employing two types of functional molecules for comprehensive surface passivation (Fig. 4a) [44]. Sulfur-modified methylthio molecules were used to passivate surface defects and suppress recombination through strong coordination and hydrogen bonding, while diammonium molecules repelled minority carriers and reduced contact-induced interface recombination through field-effect passivation. Based on this bimolecular passivation, Chen et al. incorporated 4-chlorobenzenesulfonate as a dual-site binding ligand to minimize the energy mismatch with the fullerene electron-transfer layer (Fig. 4b) [77]. These studies demonstrate that a multimolecule passivation approach, with diverse functionalities, is a promising direction for developing next-generation passivation strategies to achieve improved performance and stability in PSCs. The concept of creating multifunctional passivation ligands capable of simultaneously passivating multiple defect types is also worth exploring, although integrating all these benefits into a single molecule remains challenging.

To enhance the stability of passivation layers, tuning molecular structures has emerged as a key strategy. Addressing cation migration, Liu et al. tuned the ligand structures of aromatic phthalimide moieties and developed a set of perovskitoids of varying dimensionality to serve as passivation materials (Fig. 4c) [78]. Among these perovskitoids, a 2D perovskitoid $(A6BfP)_8Pb_7I_{22}$—where A6BfP stands for N-aminohexyl-benz [f]-phthalimide—provided the most efficient passivation.

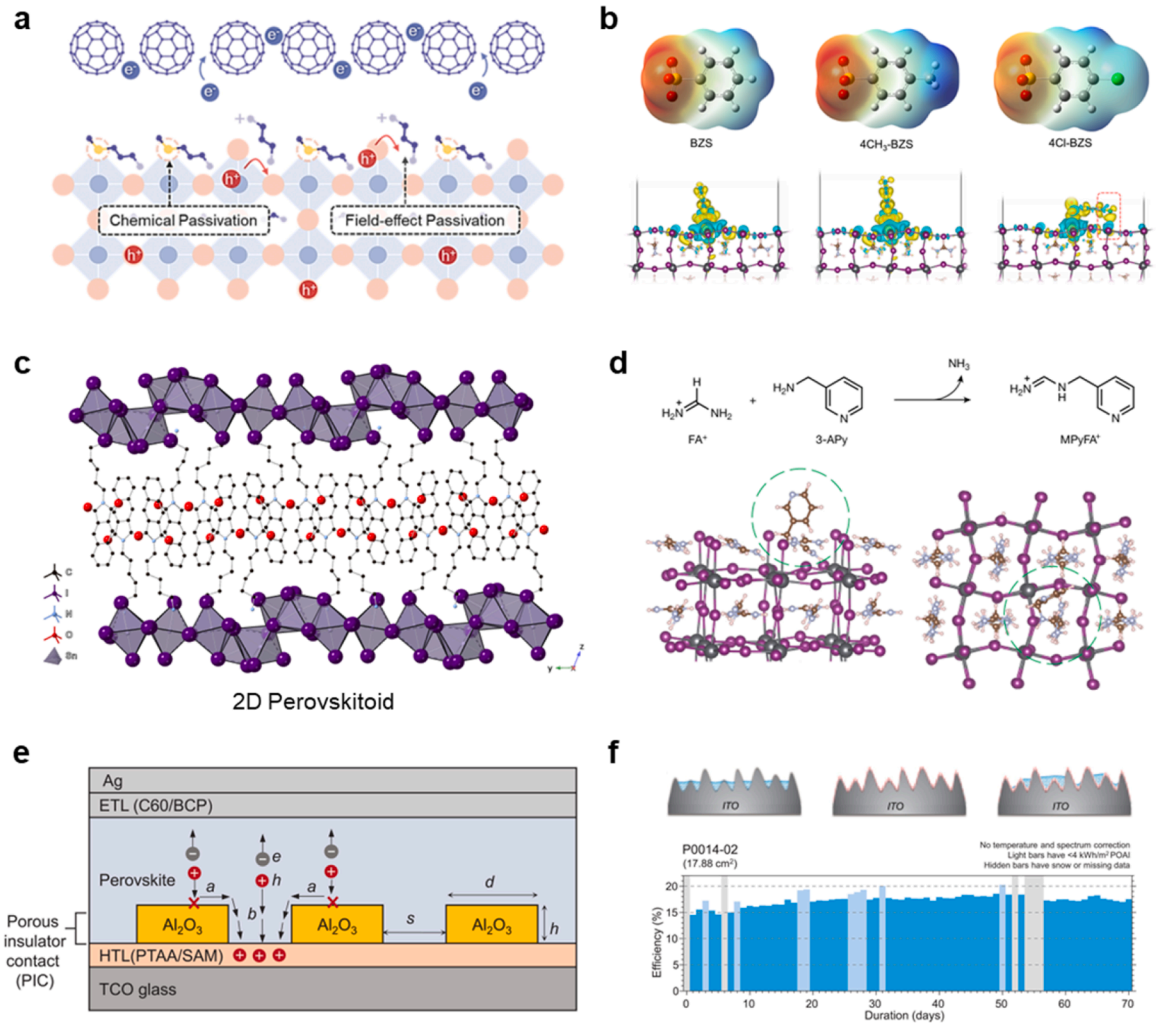

Fig. 4. **a,** Schematic of the perovskite surface without passivation and with both chemical and field-effect passivation [44]. **b**, Structure and electrostatic potential of BZS, 4CH3-BZS, and 4Cl-BZS ligands and atomic structures of ligand adsorbed in a preferred orientation on the perovskite surface [77]. **c,** Crystal structure of 2D perovskitoid $(A6BfP)_8Sn_7I_{22}$. Carbon, nitrogen, oxygen, tin, and iodine are shown in black, blue, red, lavender, and purple, respectively. Hydrogens are omitted for visual clarity [78]. **d,** Condensation reaction scheme of FA^+ and 3-APy and DFT modelling of the atomic structures of the perovskite with charged V_I and 3-APy modification. The brown, blue, pink, black and purple spheres denote C, N, H, Pb and I atoms, respectively [72]. **e,** Schematic description of the "porous insulator contact" device structure with Al_2O_3 passivation at the perovskite/SAMs interface [73]. **f,** Illustrations for the different HTMs on the ITO substrate and the outdoor stability of the minimodules based on the hybrid hole transport materials [75].

The superior performance of $(A6BfP)_8Pb_7I_{22}$ over other perovskitoids is due to its higher dimensionality, increased corner-sharing octahedral connections, and improved charge transport from out-of-plane orientations atop perovskite films. The robust organic-inorganic networks, enabled by combined corner-, edge-, and face-sharing, effectively suppressed cation migration within the perovskitoid/perovskite heterostructures. Furthermore, Liu et al. designed the structural isomers of phenylenediammonium and designed *ortho*-(phenylene)di(ethylammonium) iodide (*o*-$PDEAI_2$) as non-2D passivation ligands, which do not react with PbI_2 or 3D perovskite to form 2D perovskites, thereby suppressing cation migration at the interface [63]. Park et al. systematically investigated various ligand molecular structures and found that fluorinated anilinium, such as 3,4,5-trifluoroanilinium, offer interfacial passivation while simultaneously minimizing reactivity with perovskites and spacer cation penetration [79]. In addition to molecular structure tuning, Luo et al. introduced a cross-linked polymer layer between the 2D and 3D perovskite layers, inhibiting the diffusion of cations from the 2D perovskite passivation layers into the 3D perovskite active layers [80].

Beyond cation migration, the deprotonation instability of commonly used ammonium ligands presents a critical yet insufficiently addressed challenge. Recently, Yang et al. introduced a library of amidinium ligands that leverage the resonance-stabilized N–H bonds to resist deprotonation, thereby enhancing the thermal stability of passivation layers on perovskite surfaces [81]. These ligands not only retain their dual role in field-effect and chemical passivation but also achieve a more than 10-fold reduction in the deprotonation equilibrium constant, markedly improving the operational stability of devices under elevated temperature conditions. Additionally, Wang et al. and Jiang et al. proposed a pre-reaction strategy involving amines and formamidinium to synthesize iminium-based passivation materials. These materials, characterized by high acid dissociation constant values, exhibit enhanced resistance to deprotonation, thereby improving the passivation efficiency and thermal stability of perovskite films (Fig. 4d) [71,72]. The innovative structures of these passivation agents simultaneously enhance efficiency and long-term stability, providing a promising foundation for future passivation design strategies.

Despite the challenges in passivating buried interfaces, efforts are being made to reduce defects and improve the wettability and stability of interfaces beneath perovskite layers. Low-dimensional perovskites

have been constructed at the buried interface to passivate defects and improve energy alignments, though the formation process requires precise control [82]. Emerging hole transport materials, such as self-assembled monolayers (SAMs), have been explored to enhance the buried interface passivation in inverted PSCs [83]. These materials form strong chemical or coordinating bonds with transparent conducting oxide substrates and the perovskite surface, providing effective passivation and improving overall device performance. However, compared to metal oxide charge transport materials, widely used SAMs such as [2-(9H-carbazol-9-yl)ethyl]phosphonic acid and (4-(3,6-dimethyl-9H-carbazol-9-yl)butyl)phosphonic acid often suffer from poor wettability. This can lead to insufficient contact with perovskite films at the buried interface, especially in large-area film deposition. Depositing additional inorganic nanoparticle layers, such as NiO_x and Al_2O_3, can improve the wettability of the perovskite precursor and enhance the overall quality of the perovskite films (Fig. 4e) [73,84]. Additionally, inserting a blocking layer at the buried interface can prevent contact between the perovskite and photocatalytically active charge transport layers, thereby improving UV stability [85]. Enhancing the chemical bonding between the perovskite, charge transport layers, and transparent conducting oxides also contributes to improving the UV stability of buried interfaces (Fig. 4f) [75].

4. Concluding remarks

Interface passivation strategies—whether chemical, physical, or field-effect—have shown significant promise in mitigating recombination losses due to surface defects and interface minority carriers, which are critical for enhancing the efficiency and stability of PSCs. However, several challenges persist, including the management of complex recombination processes at different interfaces, ensuring the long-term stability of passivation layers, and effectively passivating buried interfaces. Future directions for perovskite passivation could focus on multi-molecule passivation strategies, the design of more stable passivating materials, and the development of robust heterostructures. These advancements, coupled with innovative material designs and comprehensive defect management, will be essential for driving the widespread adoption of PSCs in next-generation optoelectronics.

III. Self-assembled monolayer as the hole-selective materials for the inverted perovskite solar cell

Shuai Guo[1], Xiaofang Li[2], Xiaotian Guo[3], Feng Yang[2]*, Meng Li[1]

[1]Key Lab for Special Functional Materials of Ministry of Education, National & Local Joint Engineering Research Center for High-efficiency Display and Lighting Technology, School of Nanoscience and Materials Engineering, and Collaborative Innovation Center of Nano Functional Materials and Applications, Henan University, Kaifeng 475004, P. R. China

[2]College of Physics, Henan Key Laboratory of Advanced Semiconductor & Functional Device Integration, Henan Normal University, Xinxiang 453007, P. R. China.

[3]School of Physics and electronic engineering, Xinxiang University, Xinxiang 453007, P. R. China.

E-mail address: yangfeng@htu.edu.cn

Abstract

Self-assembled monolayers (SAMs) have obviously emerged as a promising candidate to become the hole-selective materials for the perovskite solar cells, especially in the p-i-n structure. The efficiency and stability of the device can be improved by using SAMs as the hole-selective materials. Here, we provide an introduction to the fundamental properties of SAMs, list the applications of these commonly used molecules in devices, summary the effect of the functional groups on the performance of the solar cells, provide insights into the current challenges faced, and hope that this review will provide researchers with new ideas and thoughts.

1. Status of the field

Perovskite solar cells (PSCs) are rapidly becoming a popular research topic in the new generation photovoltaic technology due to their excellent performance [1,86–88]. Single-junction metal halide perovskite solar cells have achieved an efficiency of 26.7 %, which are very close to that of conventional silicon-based solar cells [89]. Stability and reproducibility are key issues for its commercialization [90–93]. The hole-selective layer, as a pivotal structure of perovskite solar cells (Fig. 5a), has a significant impact on the final performance of the device [94,95]. Since self-assembled monolayers (SAMs) was first selected as the hole transport material for inverted perovskite solar cells in 2018[83,] [96], there have been several reported studies on it. Recent reviews on the application of self-assembled monolayers (SAMs) in perovskite solar cells (PSCs) emphasize their potential in enhancing both device performance and stability. Suo et al. summarized the dual roles of SAM molecules in PSCs, where they function both as charge transport materials and as interfacial modulators [97]. Yu et al. discussed current research on the stability of buried interfaces in SAM-based PSCs and proposed strategies to achieve excellent interface stability [98]. Wu et al. highlighted the significant advantages of SAMs in terms of scalable fabrication and cost-effectiveness, while also addressing the major bottlenecks hindering their commercialization and offering possible solutions [99]. This review is based on the molecular structure and properties of self-assembled monolayers (SAMs), focusing on recent advancements in improving the efficiency and stability of perovskite solar cells (PSCs). It also provides a brief overview of the current state of SAMs in the field of PSCs. We believe that this review will inspire researchers and contribute to the further application of SAMs in PSCs.

Compared to conventional polymers or inorganic materials, SAMs offer a simpler fabrication process for large-area production owing to the lower synthesis cost [100,101]. The introduction of SAMs has also led to obvious advancement in efficiency and stability of inverted perovskite solar cells [69,72,102]. Compared to poly [bis(4-phenyl)(2,4,6-trimethylphenyl)amine]. (PTAA), the previously widely used hole transport material, perovskite precursor solutions on SAMs exhibit a smaller contact angle. This is because SAMs can be optimized to form surface chemistry that enhances the perovskite affinity, significantly improving the wettability of the precursor solution, as well as the morphology and crystallinity of the perovskite film [103,104]. In addition, SAMs can tune the work functions of the transparent electrodes for matching with perovskite, which enhances hole extraction capacity [105]. Generally, SAMs are often spin-coated onto the substrate for small-area devices, while dip-coating is used for large-area devices. Thermal vapor deposition is a recently proposed method that has further facilitated the large-scale production of perovskite [106]. Utilizing the interaction between the anchoring groups and the metal oxide substrates, mixing the SAM into the perovskite solution and depositing them together is also a novel approach [107,108].

2. Functional head groups of SAMs

SAMs have a molecular structure comprising of three parts: an anchoring group, a linking group, and a terminal group (Fig. 5b) [109,110]. The anchoring group generates a strong physical or chemical force with the substrate surface, ensuring that the molecular layer remains tightly fixed to the substrate and preventing displacement during use. The most common and widely used anchoring groups include phosphonic acid (-$PO(OH)_2$), carboxylic acid (-COOH), and silanes (-SiR_2OH), which are able to interact with hydroxyl groups (-OH) on the surface of the substrate and coordinate with metal atoms [111,112]. The anchoring process can modify the work function of the substrate surface and affect the interfacial dipole moment, electron transport, binding energy of the electrode surface, and contact resistance [113]. The linking group connects the anchoring and terminal groups, supporting the entire molecular layer. Alkyl chain and aromatic group are two typical linking units with different charge transfer rates [114,115]. The charge transfer ability of intermediate chains is affected by their length and rigidity. Longer intermediate chains can form more regular and continuous charge transfer channels, improving the charge transfer efficiency [113]. Rigid intermediate chains can maintain the stability of the molecular structure and reduce the scattering effect of charge transfer. Linking groups can have an effect on the lateral interactions

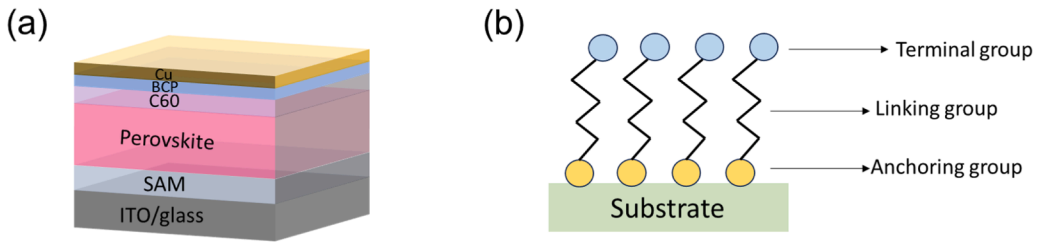

Fig. 5. (a) the typical structure of SAM-based inverted perovskite solar cell, (b) the arrangement of SAM molecules on the substrate.

between molecules and ultimately on the orientation of self-assembled molecules [114]. The terminal group interacts directly with the perovskite layer and is able to influence the morphology and structure of the overlayer. The choice of appropriate functional groups allows energy level matching between the perovskite layer and the self-assembled molecular layer, which optimizes the charge carrier transport process, increases the open circuit voltage and short circuit current, and improves the overall efficiency of the device [116–118]. In inverted perovskite solar cells (IPSCs), both carbazole-based and triarylamine-based self-assembled monolayers (SAMs) are widely used due to their excellent charge transport properties and ability to enhance device stability. Carbazole-based SAMs, which typically utilize phosphonic acid as the anchoring group and a carbazole derivative as the terminal group, are known for their chemical stability, favorable energy

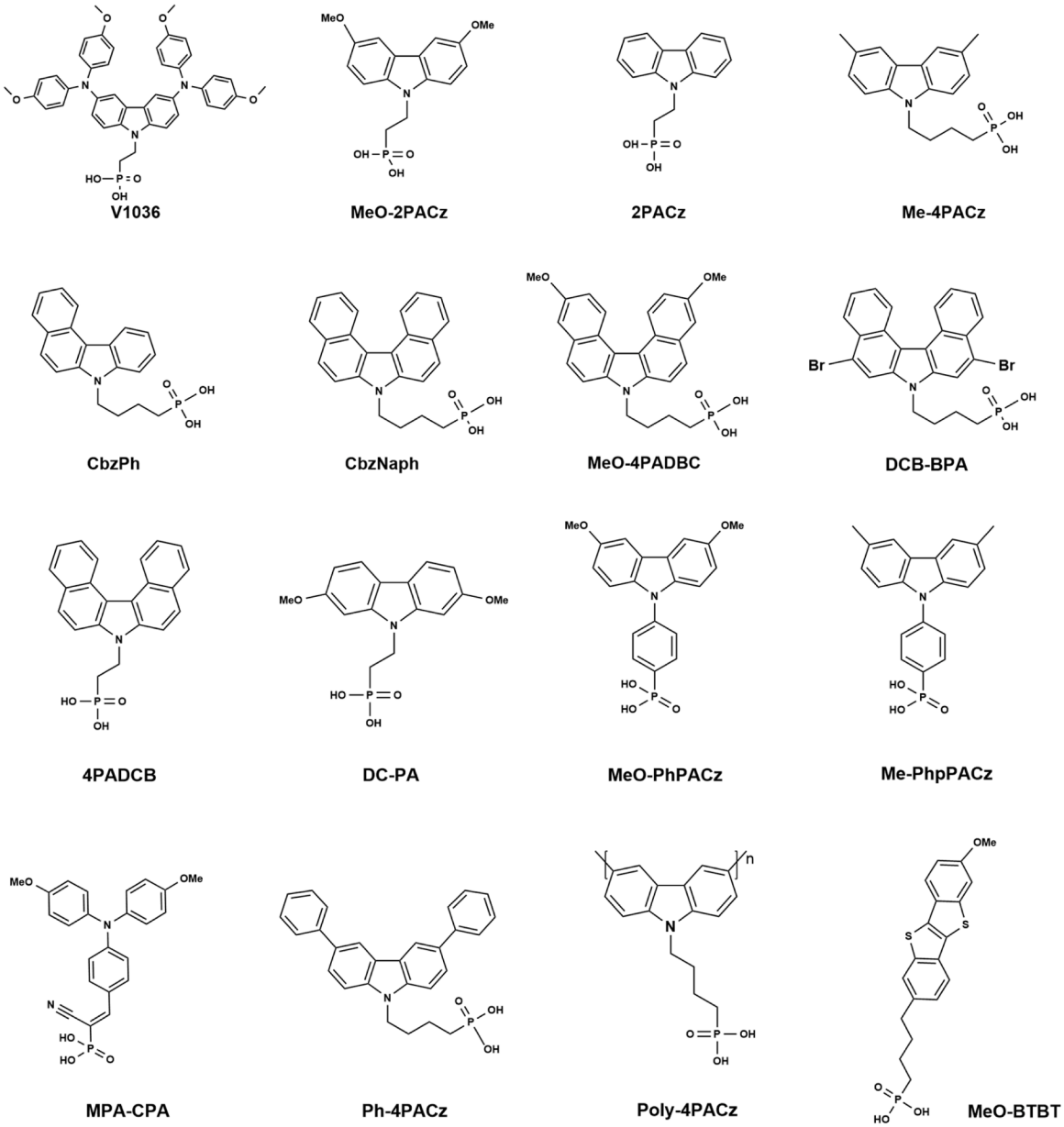

Fig. 6. Some typical molecular structures of SAMs used as hole transport materials.

level alignment with perovskites, and high hole mobility. These materials play a critical role in improving hole extraction and minimizing interfacial recombination, thereby significantly enhancing the stability and performance of IPSCs. In contrast, triarylamine-based SAMs are distinguished by their extended conjugated systems and superior hole extraction capabilities. These SAMs improve hole mobility and help reduce charge recombination at the interfaces, further boosting device efficiency and long-term stability. Both types of SAMs are crucial for optimizing interfacial properties, charge transport, and the operational lifespan of inverted PSCs. The choice of SAM depends on the specific performance requirements and stability needs of the device. Additionally, specific groups have the ability to resist environmental interference, safeguarding the perovskite layer from external factors such as oxygen, moisture, and ultraviolet rays [119]. This enhances the stability of the perovskite layer and prolongs the operating life of device. The photovoltaic parameters of SAM-based IPSCs and recent commonly used SAM molecules are summarized in **Table** S2 and Fig. 6.

3. Efficiency improvement by SAMs

SAMs play a significant role in improving the efficiency of perovskite solar cells. Through reasonable molecular design, including the introduction of specific functional groups or the change of molecular structure, the SAM molecular dipole moment can be adjusted to match the energy level of perovskite [120]. SAMs are a dense and organized layer via molecule interaction with the substrate surface such as chemical bonding or electrostatic which can extract the charges well, suppress non-radiative recombination, reduce parasitic absorption loss and adjust the work function [121,122]. As known, the quality and grain size of the perovskite crystals have a significant impact on the final performance of the device, and grain of larger sizes are desired [123]. Smaller perovskite grains may not absorb sunlight adequately, resulting in lower light energy utilization. Additionally, smaller grains increase the number of grain boundaries, leading to compound losses of carriers at the boundaries [124]. In addition, smaller grains make the device more vulnerable to environmental factors, reducing the long-term stability of the device. Higher quality of the SAMs layer can distinctly increase the crystallinity and orientation of the perovskite, improving the crystal grains size [125]. Zeng et al. chose MeO-2PACz as the hole-selective material and compared it with poly [bis(4-phenyl)(2,4,6-trimethylphenyl)amine]. (PTAA), and found that the contact angle of the SAM-based substrate was smaller(Fig. 7a and b) [103]. It implies that there has a better wettability of perovskite precursor solution on SAM layer. Furthermore, compared to PTAA, the contact between the SAM layer and the perovskite layer was much tighter (shown in Fig. 7c and d). This phenomenon also had a positive effect on the photovoltaic performance of the SAM-based perovskite solar cells.

Qu et al. developed a novel SAM, [4-(3,6-dimethyl-9Hcarbazol-9-yl) phenyl]PA (Me-PhpPACz), which replaces the flexible alkyl linker in widely used Me-4PACz with robust phenylene linker (Fig. 8a) [97]. This modification results in a more densely ordered arrangement of SAM molecules on the substrate and therefore improves charge extraction. This structural change enhances the aspect ratio and dipole moment of the molecules and forms a better energy alignment with perovskite layer (Fig. 8b). The power conversion efficiency (PCE) of the PSC based Me-PhpPACz achieved 26.17 % compared with 24.14 % for Me-4PACz. This improved means can also be used in other carbazole-based SAMs.

4. Stability improvement by SAMs

Stability is an important indicator for the photovoltaic device [126–128]. A high-quality photovoltaic device not only exhibits high efficiency and low cost but also ensures long-term operational stability [92,129,130]. The introduction of SAMs is considered to be an excellent strategy for the stability improvement of PSCs. The effects of SAMs include the following: 1) Form a good interfacial bond with the perovskite materials and improve interfacial adhesion. 2) Protect the perovskite materials from attack by water, oxygen, etc. 3) Suppress the ion migration between perovskite and electrode. People are ongoing commitment to developing innovative SAMs for improving the stability of the perovskite solar cells. Al-Ashouri et al. found that the Voc of the PTAA-based cells decreased significantly under light soaking, while the Voc of the SAM-based cells remained stable except for a small initial decrease. This may be due to the fact that under open-circuit voltage illumination, iodine diffusion into the PTAA interface affects the structure of the PTAA, whereas SAM, due to its lightweight and chemically stable nature, is less affected by ionic accumulation and less susceptible to structural effects [131]. Aktas et al. synthesized two type of self-assembled monolayers with carbazole as the host structure, 4-(3,6-bis(2,4-dimethoxyphenyl)-9H-carbazol-9-yl) benzoic acid (EADR03) and 4-(3,6-bis(2,4-dimethoxyphenyl)-9H-carbazol-9-yl)- [1,1-biphenyl]-4-carboxylic acid (EADR04), which were used for the hole transport materials of the inverted perovskite solar cells (Fig. 9a) [132]. Around 24 hours after performing the maximum power point (MPP) measurement, the control PTAA device dropped below 85 % of its initial efficiency, and the device using SAMs showed significant stability. The EADR04 device recovered its initial efficiency after 150h and eventually maintained 95 % of the initial efficiency. SAMs devices have advantages over PTAA devices in terms of stability, which can be attributed to their greater stability under ultraviolet light. This is because UV light induces the polymer PTAA to break down, while having little effect on SAMs (Fig. 9b, c and d).

Liu et al. developed a SAM based [1]. benzothieno- [3,2-b]. [1]. benzothiophene (BTBT) (Fig. 9e) [133]. Compared with the traditional MeO-2PACz, the device using MeO-BTBT has higher efficiency and filling factor, and the SEM image of the buried interface before and after

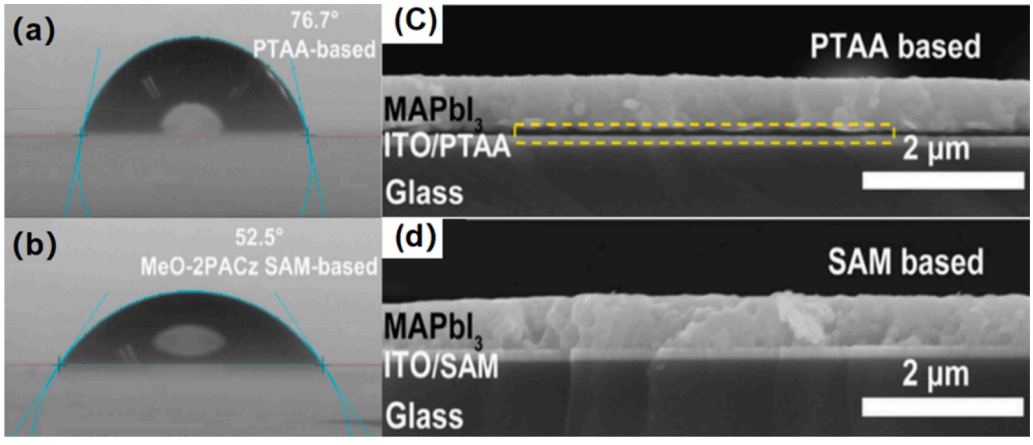

Fig. 7. The contact angles of a PTAA-based and b SAM-based. Cross-section SEM images of perovskite films blade-coated on c PTAA-based substrate, and d SAM-based substrate [103].

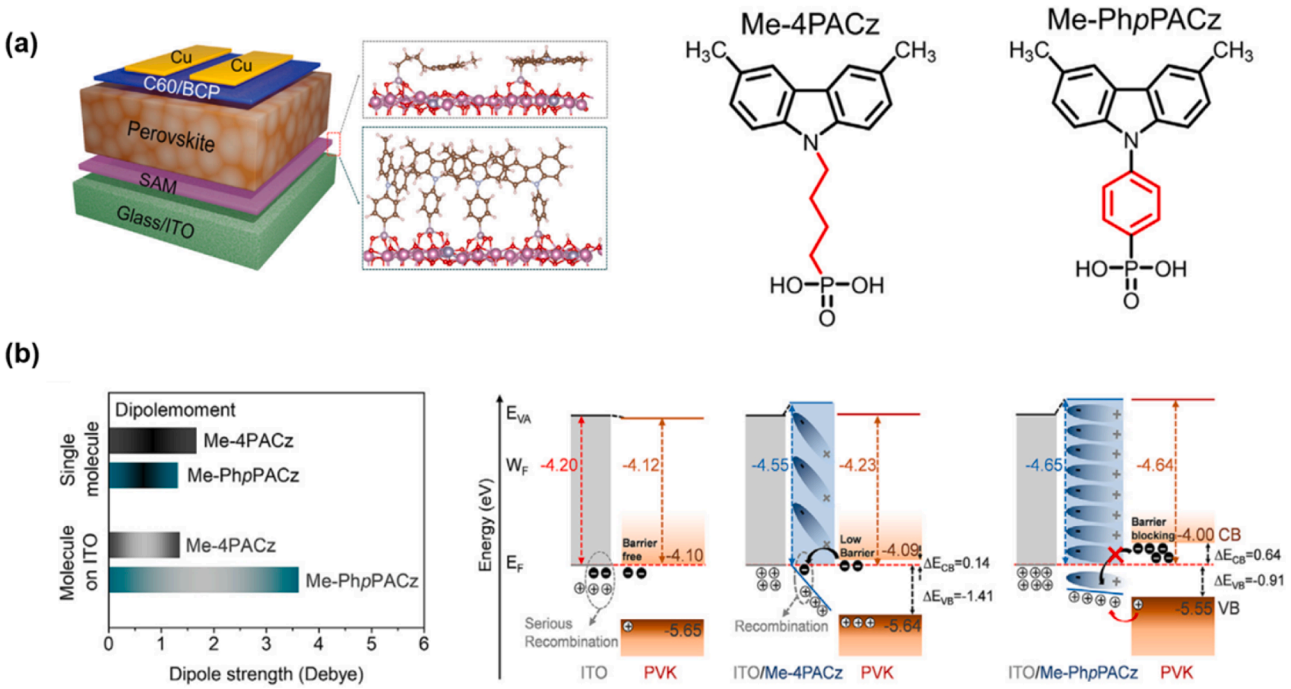

Fig. 8. a. Molecular structures of Me-4PACz and Me-PhpPACz and their stacking simulations in the device. b. Molecular dipole moment variation and energy alignment of Me-4PACz and Me-PhpPACz [97].

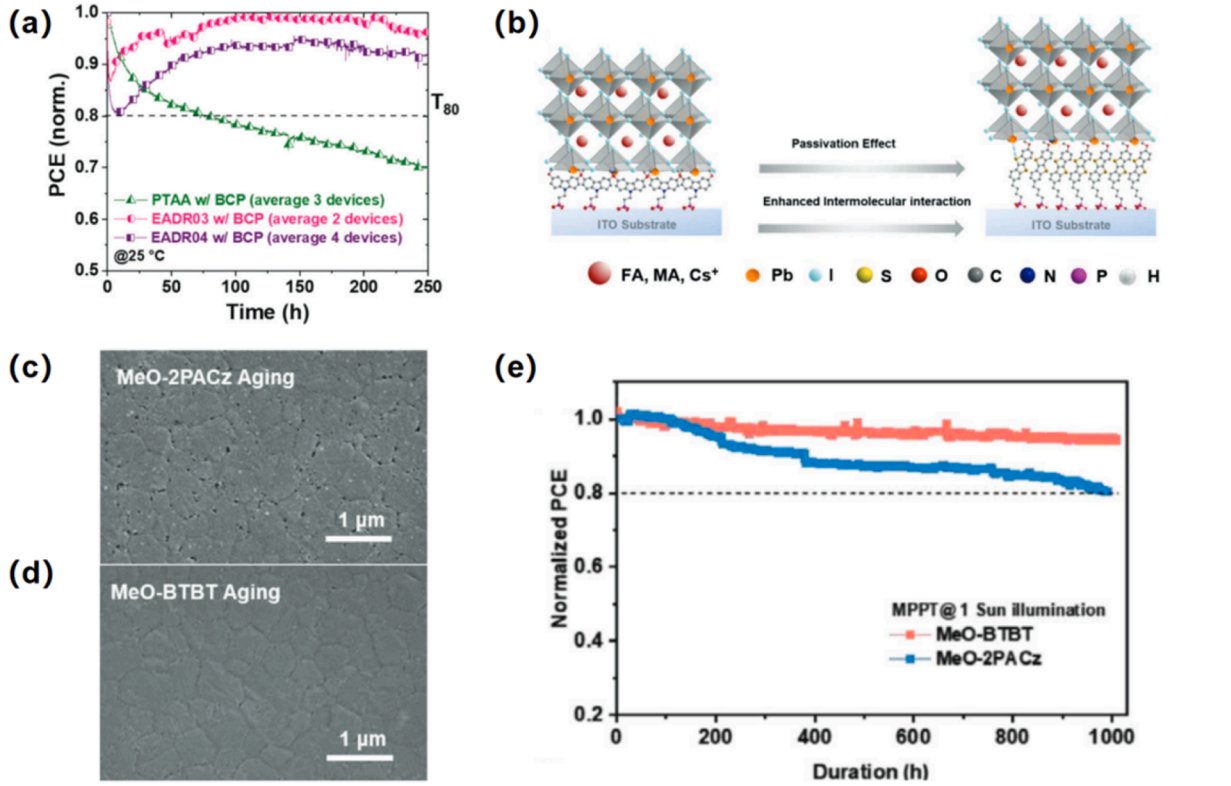

Fig. 9. (a) Long-term continuous maximum power point tracking of EADR03, EADR04 and PTAA based devices with BCP at 25 degrees Celsius [132]. (b) the interfacial interactions diagram between ITO/SAM/perovskite. (c,d) SEM images of aged perovskite films peeled off from c MeO-2PACz and d MeO-BTBT modified substrates. (e) MPP tracking of PSCs under 1 sun continuous illumination [133].

aging is almost unchanged. The perovskite crystals deposited on MeO-2PACz are partially decomposed, and there were voids near the grain boundaries accompanied by lead iodide particles. Devices using MeO-BTBT achieved an efficiency of 24.53 % and maintained better photothermal stability. This is due to the fact that MeO-BTBT molecules have larger dipole moments, better energy level arrangement. At the same time, larger radius sulfur atoms can strengthen the intermolecular interaction, and can coordinate with lead ions to passivate defects.

Self-assembled monolayer molecules are usually dissolved in a solvent (e.g. IPA) to function. However, due to their amphiphilic nature, SAM molecules tend to form micelles, which is detrimental to SAM coverage on the substrate. Liu et al. used N,N-dimethylformate (DMF) as a co-solvent to add to the solvent of SAM, and found that it was effective in reducing the critical micellar concentration of SAM molecules (Fig. 10a) [134]. CbzNaph devices treated with co-solvents were able to achieve a PCE of 24.98 % and a fill factor of 85.6 %. It was able to maintain 82 % of the initial efficiency under MPPT conditions for 700 h and 89 % of the initial efficiency after continuous heating at 654°C for 400 h, both of which were significantly higher than those of the control group, demonstrating excellent operational and thermal stability (Fig. 10b).

Moreover, the traditional method for covering SAMs on substrates is solution deposition, but the wettability of certain materials is not ideal. Farag et al. first used vacuum deposition to cover carbazole-based SAMs (e.g. 2PACz, MeO-2PACz and Me-4PACz) on substrates and found no significant difference from devices prepared by solution deposition [106]. The vacuum deposition method resulted in a more uniform coverage of the SAMs and a significant improvement in the wettability of Me-4PACz, which was not well covered by solution deposition, and the fabrication yield was close to 100 %. This suggests that the vacuum evaporation method is an excellent means of covering SAMs and also provides insight for faster commercialization of perovskite solar cells.

5. Concluding remarks

In recent years, the efficiency of inverted perovskite solar cells has significantly increased, largely due to the development and optimization of SAMs. SAMs have attracted considerable attention from researchers because of their low cost, solution processability, flexibility for structural modification, and reduced parasitic absorption. While the beneficial role of SAMs in improving perovskite solar cells has been widely recognized, challenges remain in their successful application. In this context, we will explore the future development prospects of SAMs and propose feasible strategies to address the current challenges they face.

The development of SAMs with novel molecular structures is crucial for the commercial application of PSCs. As previously stated, the SAM molecule is comprised of three distinct structural components: an anchoring group, a linking group, and a terminal group. The novel SAMs are developed by making adjustments to the group sums between the three partial groups. Currently, phosphonic and carboxylic acids are often used as anchoring groups, however, strong acidity may lead to substrate corrosion. It would be beneficial to investigate the potential of utilizing weak acids in lieu of strong acids as anchoring groups in the future.

Stability is critical to the application of photovoltaic products in the marketplace. Although SAM-based PSCs exhibit excellent PCE, maintaining long-term operational stability remains a challenge, as light and heat can damage the structure of the SAM molecules. Therefore, researchers should focus their efforts on developing SAMs with enhanced stability under light and heat conditions.

The linking group in SAMs typically consists of alkyl chains or aromatic moieties. However, strong interactions between aromatic moieties may deteriorate the wettability of the SAM, which could negatively affect device performance. Additionally, the length and orientation of alkyl chains can influence the crystallization of the perovskite layer, so researchers should explore the use of suitable linking groups for optimal SAM performance. The introduction of appropriate functional groups can interact with the perovskite layer and impact carrier transport and interfacial stabilization. Therefore, terminal groups should be selected according to the specific application purpose.

In addition to their use in perovskite solar cells, SAMs show great potential in other fields. For example, SAMs are increasingly being studied for applications in organic photovoltaics (OPVs), organic light-emitting diodes (OLEDs), organic sensors, catalysis, molecular electronics, and high-performance batteries. In these fields, SAMs can optimize interfacial properties, enhance device stability, and improve

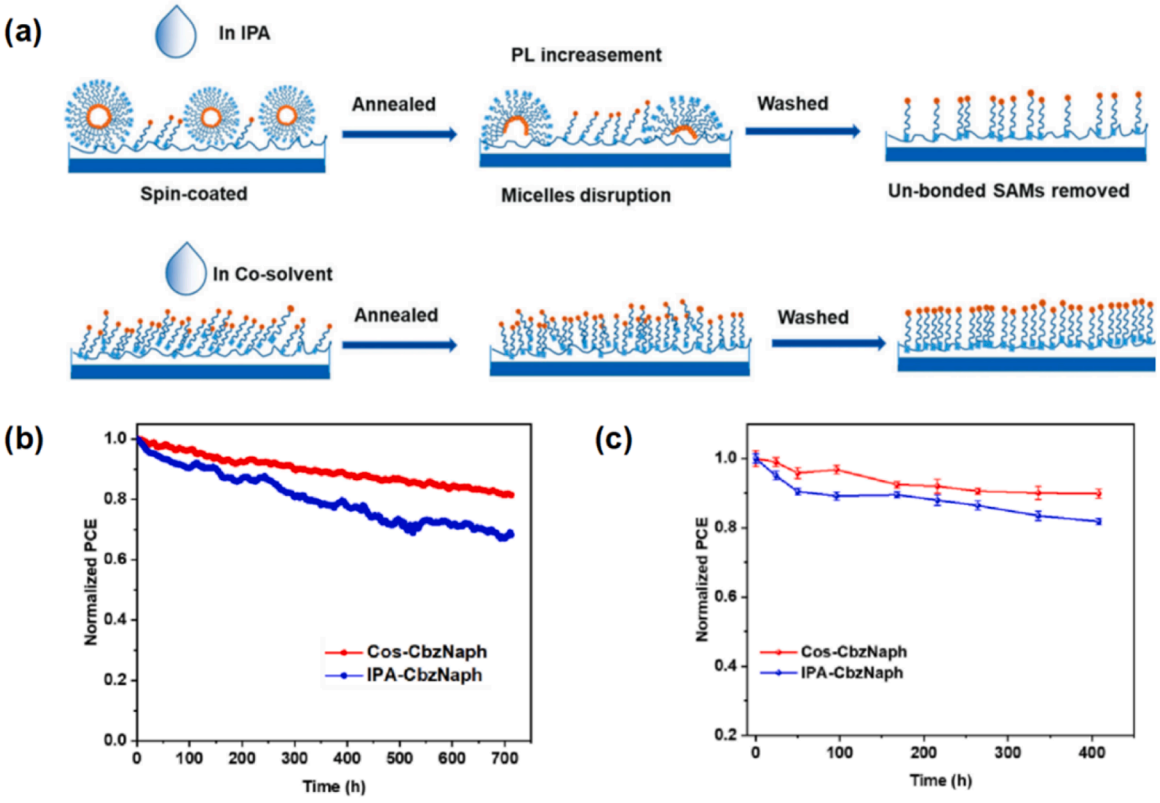

Fig. 10. a. Schematic diagram of the modulation process of SAMs by IPA and co-solvent. Steady power output at MMP tracking under one sun illumination in nitrogen atmosphere at b 45 °C and c 65 °C [134].

energy efficiency. As technology continues to advance, SAMs are also expected to play a significant role in large-scale manufacturing and cost-effective applications.

Moreover, the issue of SAM coverage uniformity in devices with different active areas remains a significant challenge in practical applications, especially as the active area increases. Due to the ultrathin nature of SAMs, current characterization methods are limited, and it is difficult for researchers to obtain accurate information about the distribution of SAMs on the substrate surface. This calls for the development of improved characterization techniques to obtain more precise data.

CRediT authorship contribution statement

Shuai Guo: Data curation, Investigation, Writing-original draft. XiaoFang Li: Data curation. Xiaotian Guo: Data curation. Meng Li: Writing-review, Funding acquisition, and editing. Feng Yang: Data curation, Resources, Writing-review and editing.

Data availability

Data will be made available on request.

Declaration of competing interest

The authors declare that they have no known competing financial interests or personal relationships that could have appeared to influence the work reported in this paper.

Acknowledgments

The work was financially supported by the China Postdoctoral Science Foundation (No. 2022M721026), the Joint Fund of Provincial Science and Technology Research and Development Plan of Henan Province (No. 232301420004), Natural Science Foundation for Young Scientists of Henan Province (242300421069), National Natural Science Foundation of China (No. 22103022) and Henan Postdoctoral Sustentation (20213036).

IV. All-perovskite tandem solar cells

Huagui Lai, Fan Fu*

Laboratory for Thin Films and Photovoltaics, Empa-Swiss Federal Laboratories for Materials Science and Technology, Duebendorf 8600, Switzerland

E-mail address: fan.fu@empa.ch

1. Status of the field

Metal halide perovskite-based tandem solar cells (TSCs) have emerged as a promising technology to exceed the efficiency limitations of traditional single-junction solar cells. The efficiency of single-junction solar cells is constrained by the Shockley-Queisser (S-Q) limit, approximately 33 %, primarily due to non-absorbed photons and thermalization losses [135]. Tandem architectures can mitigate these losses by combining absorber materials with complementary bandgaps, each optimized to absorb different portions of the solar spectrum. This configuration offers the potential to enhance overall efficiency beyond 40 % with two bandgap (E_g)-matched absorber materials, and potentially even higher with the inclusion of more absorbers [136]. The broadly tunable bandgap of halide perovskites is particularly advantageous, allowing them to be engineered as top cells in tandem structures to paire with various existing bottom cells. These bottom cells can be made from crystalline silicon (c-S, 1.12 eV) [137], copper-indium-gallium-selenide (CIGS, ~1.10 eV) [138], cadmium selenium telluride (CdSeTe, ~1.39 eV) [139], organic semiconductors (~1.33eV) [140], or even perovskite itself (~1.2 eV) [141]. Among these tandem technologies, perovskite-perovskite (all-perovskite) monolithic TSCs stand out due to their unique advantages, including low cost, simple solution-based fabrication, and compatibility with flexible substrates. As illustrated in Fig. 11a, a broad range of the solar spectrum can be efficiently covered by an ideal all-perovskite tandem design that combines a wide bandgap (WBG) perovskite top cell (~1.8 eV) with a narrow bandgap (NBG) perovskite bottom cell (~1.2 eV). In this architecture, the top cell absorbs most of the visible light, while the remaining near-infrared light is captured by the bottom cell. A recombination layer is required for efficient operation, where electrons and holes from the WBG and NBG sub-cells are recombined [142].

Recent years have seen substantial progress in the development of all-perovskite TSCs, with a notable increase in power conversion efficiency (PCE). As shown in Fig. 11b, the PCE of conventional two-junction all-perovskite monolithic TSCs on both rigid and flexible substrates has rapidly increased, with the highest certified PCE recently exceeding 30 % on rigid substrates [143]. For flexible tandem devices, which offer a high power-to-weight ratio, PCEs of around 24 % have been achieved using substrates like polyethylene naphthalate (PEN) and

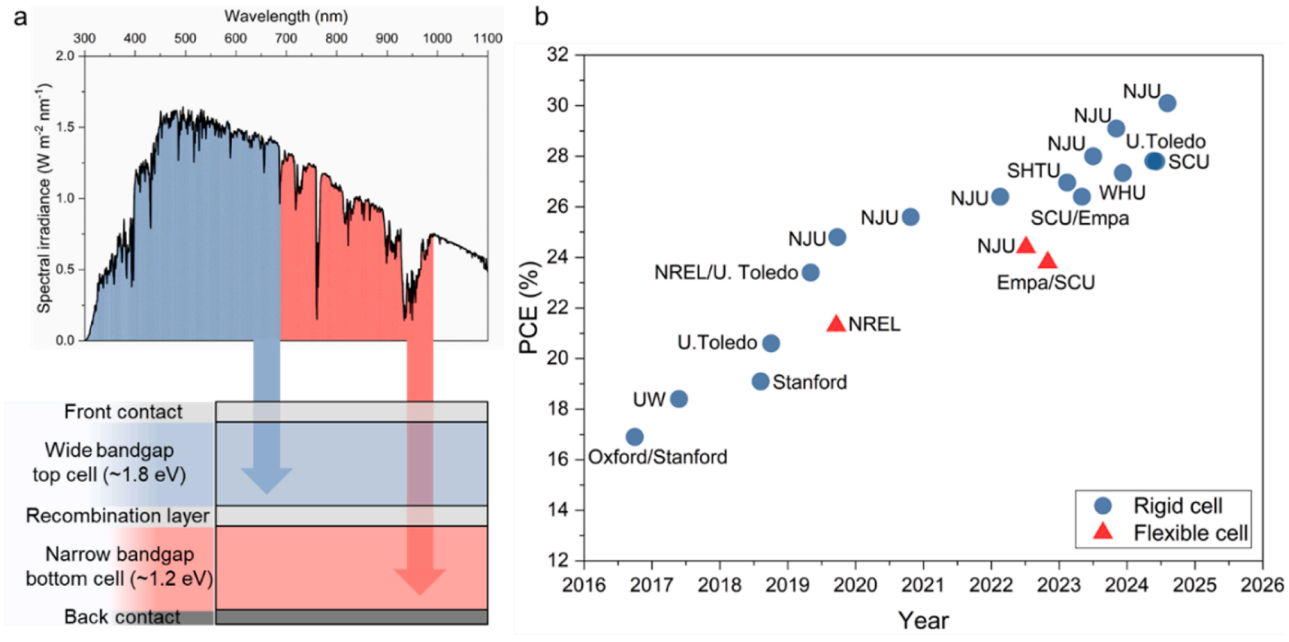

Fig.11. (a) Reference solar spectrum on earth (AM 1.5G) up to 1100 nm. The blue area depicts the photons that have energy above the wide bandgap perovskite (1.8 eV), and the red area depicts the photons that are not absorbed by the wide bandgap perovskite but are absorbed by the narrow bandgap perovskite (1.2 eV), below is the schematics show a two-junction all-perovskite monolithic TSCs. (b) Efficiency evolution of conventional all-perovskite monolithic TSCs (two-junction). Details are summarized in Table S3.

polyethylene terephthalate (PET) [144,145].

2. Current and future challenges

Performance Losses: Achieving high PCE is a critical objective in the development of photovoltaic technologies. In all-perovskite TSCs, the WBG and NBG sub-cells are facing different challenges. WBG sub-cell, is suffering from large open-circuit voltage (V_{OC}) deficit (E_g/q-V_{OC}), which is mainly due to defects in the bulk and surface of the WBG perovskites, and their suboptimal band alignment with charge selective layers (CSLs) [146]. As shown in Fig. 12a, perovskite solar cells (PSCs) with an E_g around 1.5-1.6 eV are approaching 95 % of their theoretical S-Q limit for V_{OC}, while WBG devices (~1.8 eV) rarely exceed 90 % of this limit. The low open-circuit voltage (V_{OC}) is thus limiting the overall V_{OC} of the TSCs.

For the NBG sub-cell, typically composed of lead-tin (Pb-Sn) perovskites with an E_g around 1.2 eV, challenges arise in achieving thick absorber (>1 μm) with high quality [147]. Pb-Sn perovskites generally exhibit shorter carrier diffusion lengths and lower absorption coefficients compared to their Pb-only counterparts. This limitation hampers their ability to capture near-infrared light effectively [148]. As shown in Fig. 12b, few devices (~1.2 eV) achieve short-circuit current density (J_{SC}) values close to 90 % of the S-Q limit. This is in stark contrast to devices with higher bandgaps (>1.5 eV), which more consistently reach near-limit J_{SC} values. Realizing uniform, thick, and high-quality Pb-Sn perovskite is thus, crucial for reducing the J_{SC} losses in TSCs

When combining WBG and NBG sub-cells in a monolithic tandem configuration, the recombination layer poses another significant challenge. As depicted in Fig. 12c, current recombination layers are not yet optimized, suffering from substantial optical and electrical losses. An ideal recombination layer would efficiently facilitate carrier recombination, minimize light absorption and reflection, and provide mechanical robustness to protect underlying layers during fabrication [149]. Additionally, the overall current output from a monolithic TSC is constrained by the sub-cell with the lowest current. Therefore, optimizing the optical coupling between the sub-cells and other functional layers, such as the front contact, is crucial for achieving optimal current matching and maximizing the device's output.

Stability challenges: The stability of all-perovskite tandems is determined by the combined stability profiles of the WBG sub-cell, recombination layer, and NBG rear sub-cell. WBG sub-cells, typically incorporating around 40 % bromine (Br) to achieve an E_g near 1.8 eV, are prone to phase segregation under prolonged light exposure [128,168]. Fig. 12d shows that photoluminescence (PL) measurements reveal an increasing emission from iodine-rich regions over time, indicating the formation of iodide-rich phases [128]. This poses a significant threat to the long-term operation of both the WBG sub-cell and the entire tandem device. NBG sub-cells based on Pb-Sn perovskites also face severe stability challenges. Divalent tin (Sn^{2+}) is highly sensitive to oxidation, converting to Sn^{4+} when exposed to oxygen, which rapidly degrades the absorber quality [167,169]. As illustrated in Fig. 12e, without an antioxidant, Pb-Sn perovskite solutions oxidize noticeably, evidenced by a color change [167]. This oxidation leads to the formation of Sn vacancies, degrading the film quality and device performance. Furthermore, other layers within the tandem structure, such as PEDOT:PSS (a hole selective layer) and ultrathin metals (e.g. Ag, Au) used in recombination layers, are susceptible to degradation from environmental factors like humidity, oxygen, light, or thermal stress, and ion migration [170]. Ensuring the long-term stability of all-perovskite TSCs thus remains a major challenge, despite their promising efficiency potential.

Upscaling challenges: Despite significant progress in enhancing the PCE of all-perovskite TSCs, scaling this technology from laboratory-scale to industrially relevant levels remains challenging. As summarized in Fig. 13, some efforts have been made towards scaling up all-perovskite TSCs into tandem solar modules (TSMs) [171–174]. Despite these

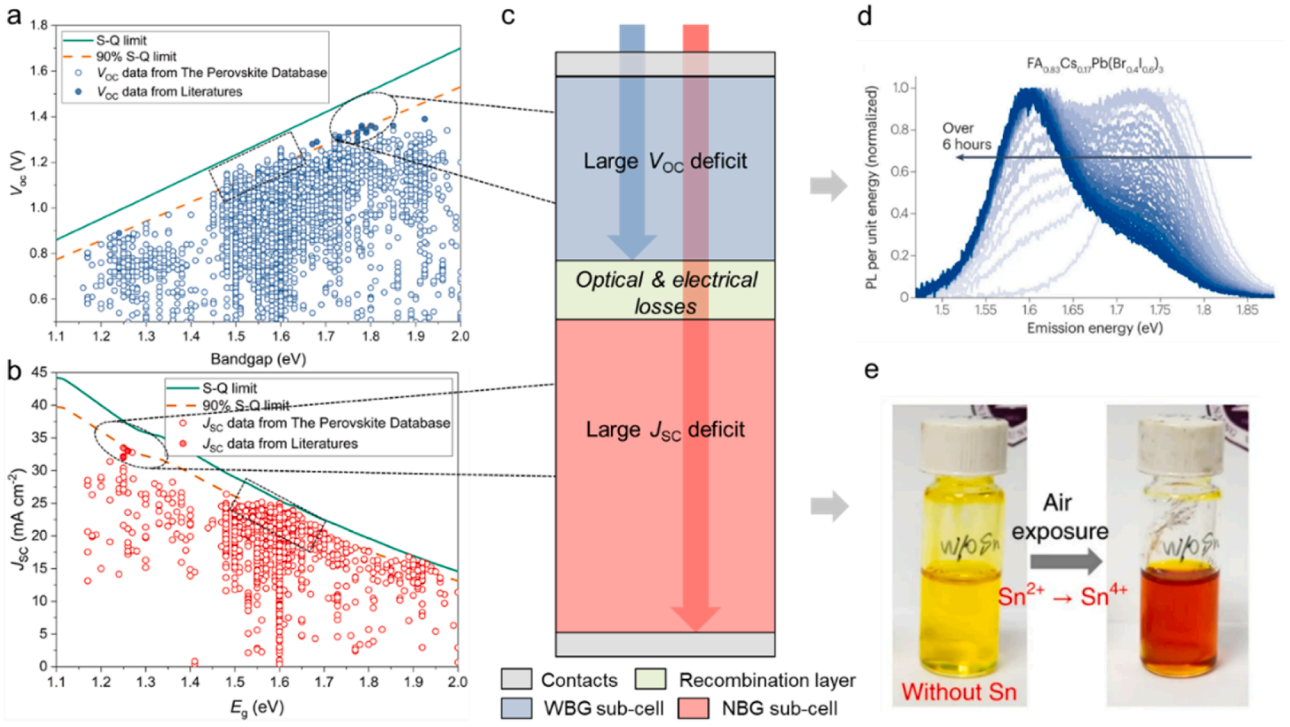

Fig. 12. (a) Open-circuit voltage (V_{OC}) of single-junction perovskite solar cells (PSCs) as a function of bandgap; the V_{OC} from the S–Q limit, and 90 % of the S–Q limit are shown. Data based on The Perovskite Database till 20240704 and other literatures [45,141,150–161]. (b) Short-circuit current-density (J_{SC}) of single-junction PSCs as a function of bandgap; the J_{SC} from the S–Q limit, and 90 % of the S–Q limit are shown. Data based on The Perovskite Database till 20240704 and other literatures [150,162–166]. (c) Simplified schematics show a two-junction all-perovskite monolithic TSCs with possible performance losses from different regions. (d) Photoluminescence (PL) measurements of a WBG perovskite film (40 % Br) show the increase of emission from iodine-rich regions as a function of illumination time [128]. (e) Photographs showing the ease of oxidation of Sn^{2+} to Sn^{4+} in ambient air [167].

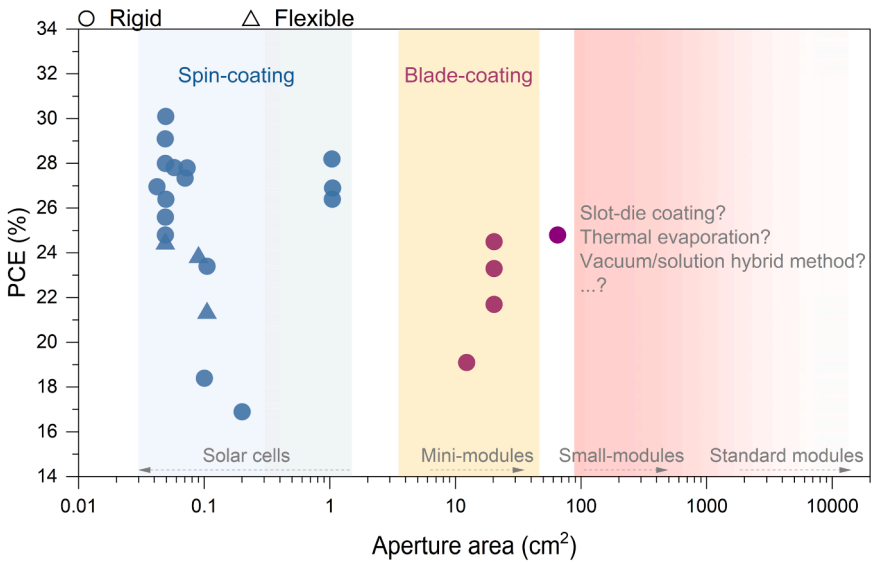

Fig. 13. PCE as a function of the aperture for monolithic all-perovskite TSCs and modules with an indication of deposition techniques for the absorbers. Details are summarized in **Table** S3.

achievements in efficiency metrics, it is important to acknowledge that the development of TSMs is still in its early stages. It can been seen that spin-coating is still the predominant method for depositing small-scale all-perovskite TSCs in the lab. For larger-scale fabrication, solution-based blade-coating methods have demonstrated scalability to areas up to 20.25 cm^2 [173]. A very recent report has announced a certified PCE of 24.8 % for all-perovskite TSMs on an aperture area of 65 cm^2, of which the fabrication methods have not yet been disclosed [175]. Despite these advancements, the reported modules remain at the mini-module scale, and the development of larger-area TSMs continues to present significant challenges. To scale up to standard module sizes, it is essential to overcome issues related to achieving uniformity, reproducibility, and compatibility with high-throughput production processes. This will likely involve exploring industrial-scale deposition methods such as slot-die coating, thermal evaporation, vacuum/solution hybrid method, etc [176,177]. Moreover, the development of lightweight flexible all-perovskite TSMs, a promising direction for future commercialization, remains underexplored. Key challenges include achieving conformal coating, ensuring compatibility between multiple processing steps for flexible substrates, laser scribing for module fabrication, and developing reliable, flexible encapsulation methods. Addressing these issues is essential for advancing the technology towards practical, large-scale applications.

3. Advances to meet challenges

The best certified PCE for all-perovskite TSCs has now reached 30.1 %, with key performance metrics including a V_{OC} of 2.2 V, a J_{SC} of 16.72 mA cm^{-2}, and a fill factor (FF) of 81.8 %. As the field progresses, an exciting but challenging milestone is to push the PCE beyond 35 %, which is surpassing the theoretical limit for single-junction cells. Achieving a PCE >35 % will require a V_{OC} of approximately 2.3 V, a J_{SC} of around 18 mA cm^{-2}, and a FF of about 85 %. To realize it, all the J-V characteristics must be meticulously optimized through multifaceted approaches. These efforts must also be balanced with the need to enhance the stability of the devices, which remains a critical concern. In this context, recent advances that address various challenges in achieving high-performance and stable all-perovskite TSCs have been widely discussed below.

Performance enhancements: For the WBG sub-cell, the primary sources of performance losses stem from issues within the perovskite absorber's bulk and the interfaces between the perovskite and contact layers, leading to a significant V_{OC} deficit. In 2022, a notable breakthrough was achieved with the realization of a low V_{OC} deficit of ~0.42 V for a 1.75 eV WBG PSC, accomplished by reducing defect density through a finely controlled crystallization process during blade-coating [156]. Interface engineering is playing a crucial role in modifying band alignments between the perovskite and CSLs, which is essential for reducing non-radiative recombination [45,141,151,153,154,159,164]. For example, He et al. designed a self-assembled monolayer (SAM), specifically (4- [7H-dibenzo(c,g)carbazol-7-yl]butyl)phosphonic acid (4PADCB) (Fig. 14a), to improve the interface quality between perovskite and indium tin oxide (ITO) (Fig. 14b), achieving a V_{OC} deficit of ~0.46 V in a 1 cm^2 WBG PSC [141]. Another progress was made by Cui et al., who sequentially deposited two different SAMs to enhance the buried interface quality, resulting in a record low V_{OC} deficit of 0.42 V in a 1.78 eV PSC [151]. Additionally, the engineering of the interface between the perovskite and electron selective layer, such as C_{60}, is also important. Chen et al. demonstrated the effectiveness of introducing diammonium molecules to regulate perovskite surface potential. Their work showed that using 1,3-propane diammonium (Fig. 14c), as opposed to butylammonium iodide, helped maintain the photoluminescence quantum yield (PLQY) after C_{60} deposition (Fig. 14d), enabling 1.79 eV PSCs with a certified V_{OC} of 1.33 V, corresponding to a low V_{OC} deficit of ~0.46 V [45].

In the NBG sub-cell, preventing oxidation has been a key area of focus. Optimizing anti-oxidation strategies in the perovskite solution have been widely explored to suppress the oxidation of Sn^{2+} and enhance the quality of the perovskites [162,167,178–181]. Research has also extensively investigated the oxidation pathway of Sn^{2+} in conventional solvent systems, such as dimethyl sulfoxide, highlighting the need to explore alternative solvents to further improve device performance [182–185]. In addition, many efforts has also been devoted to modify the interfaces between Pb-Sn perovskites and CSLs [163,186–190]. Recently, Lin et al. developed an innovative approach by creating an immiscible 3D/3D bilayer perovskite heterojunction at the interface between the Pb–Sn perovskite and the electron selective layer. This structure suppresses interfacial non-radiative recombination and enhances charge extraction (Fig. 14e) [163]. As a results, a PCE of 23.8 % with a 1.2-μm-thick absorber was achieved, underscoring the critical role of interfacial engineering in improving the performance of NBG PSCs.

In a tandem configuration, replacing the conventionally used metal or transparent conductive oxide (TCO) has been a main focus for reducing both the optical and electrical losses [140,141,166,191–193]. Recently, Wu et al. have replaced PEDOT:PSS with solution-processed

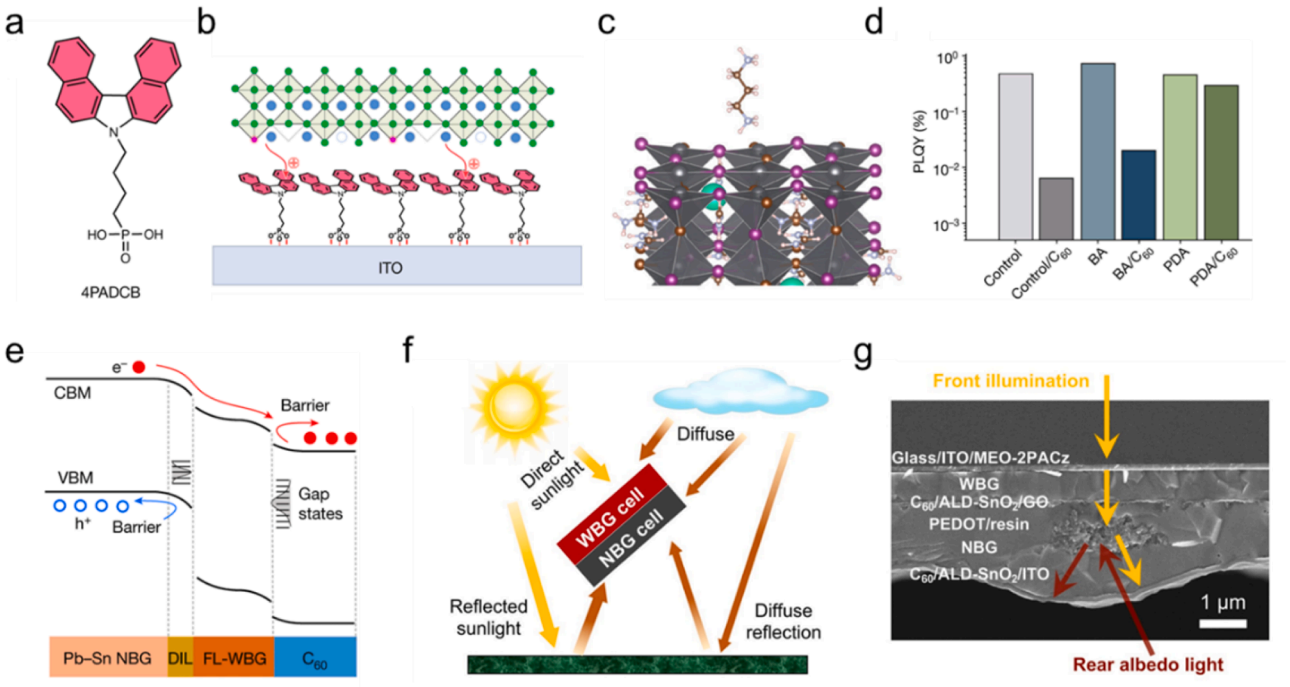

Fig. 14. (a) Molecular structure of 4PADCB [141]. (b) Schematic of the interconnection between ITO, 4PADCB and perovskite [141]. (c) Schematic crystal structure of perovskite surface treated with a PDA ligand [45]. (d) Photoluminescence quantum yield (PLQY) data from control, BA- and PDA-treated films, with and without C60, on an ITO/hole selective layer substrate [45]. (e) Energy diagram for the Pb–Sn PSC with 3D/3D bilayer perovskite heterojunction. The heterojunction enables holes to be driven away (blue lines) and accelerates the drift of electrons (red lines) into the C_{60} transport layer, thereby reducing the non-radiative recombination at the defective surface layer. The black and blue lines denote the non-radiative recombination pathways and the directions of carrier drift, respectively [163]. (f) Sketch of light absorption in a bifacial all-perovskite tandem device with additional albedo light [194]. (g) Scanning electron microscope (SEM) image of a bifacial all-perovskite tandem device [194].

ITO nanocrystals (NCs) to reduce the parasitic absorption in all-perovskite TSCs, which largely reduced the current losses [191]. Similarly, Li et al. use ITO NCs to enhance the anchoring of carbazolyl-based self-assembled monolayers in NBG PSCs, which delivers a high J_{SC} of 33.5 mA cm^{-2} and contributes to a J_{SC} of 16.7 mA cm^{-2} when applied into all-perovskite TSCs [166].

Bifacial and multi-junction TSCs: Recent developments in bifacial all-perovskite TSCs present a promising avenue for enhancing PCE [194,195]. As shown in Fig. 14f, a bifacial tandem is realized by replacing the rear metal electrodes of monofacial tandem with TCO electrodes, which therefore show a high-power output potential due to the rear illumination gain (see the scanning electron microscope image of a bifacial tandem in Fig. 14g. In addition, the optimal bandgap of the WBG perovskite can thus be reduced due to the changed current matching condition, which is beneficial for improving the stability [194]. In a recent report, Li et al. have reported a bifacial all-perovskite TSCs tandems with a high output power density of 28.51 mW cm^{-2} under a realistic rear illumination (30 mW cm^{-2}), showing the great potential of the bifacial tandem [195].

Furthermore, research on multi-junction TSCs, especially the triple-junction configurations, is gaining traction [196–202]. The perovskite triple-junction TSCs, not only offer the potential for higher PCE but also improved stability by avoiding unstable perovskites with an E_g of ~1.8 eV [197]. In 2023, Wang et al. achieved the first certified PCE of 23.3 % for all-perovskite triple-junction TSCs with a perovskite E_g of ~1.22 eV, 1.6 eV, and 2.0 eV [201]. Despite a current lag behind two-junction TSCs, this work emphasizes the promise of all-perovskite triple--junction TSCs.

Towards better stability: Although challenging, research has made remarkable progress in improving the stability of all-perovskite TSCs. Fig. 15a summarizes the reported maximum power output (MPP) tracking results for all-perovskite tandem devices. It can be seen that currently, all the operational lifetimes of the devices generally remain below 1000 hours. One approach to enhancing stability has been the replacement or removal of the problematic PEDOT:PSS layer for NBG sub-cell, extending tandem device lifetimes to ~1000 hours [203,204]. Noticeably, Li et al. have developed fully inorganic $CsPbI_{3-x}Br_x$ with an E_g of 1.77 eV, which offers superior light and thermal stability compared to commonly used organic-inorganic mixed WBG perovsites [205]. They reached a PCE of 25.6 % for tandem cells, which maintained 96 % of their initial performance after 1000 hours, as shown in Fig. 15b. Another significant development involves the application of substrate configuration in tandem device, reported by Wang et al [206]. In a substrate configuration, the bottom NBG sub-cell is deposited first, followed by the deposition of a top WBG sub-cell. This design effectively protects the more oxidizable NBG sub-cell by burying it, resulting in an encapsulated device that retains 100 % of its initial efficiency after 600 hours of operation (Fig. 15c), indicating the advantageous of this architecture in terms of stability. Additionally, the substrate configuration also expands the range of compatible flexible substrates, enhancing the commercial potential of all-perovskite TSCs.

4. Concluding remarks

All-perovskite tandem solar cells (TSCs) have demonstrated exceptional promise over the past few years, positioning themselves as a highly attractive candidate for the next generation of photovoltaic technology. The unique capability of all-perovskite TSCs to be processed on various flexible substrates offers an exceptionally high power-to-weight ratio, providing significant advantages over traditional silicon photovoltaics in specific applications such as building-integrated photovoltaics (BIPV), the Internet of Things (IoT), wearable electronics, and space applications. However, to fully realize this potential, the next decade must see continued efforts to overcome critical challenges. These include achieving higher efficiencies, enhancing long-term stability, and scaling up to larger module sizes. Addressing these challenges will be

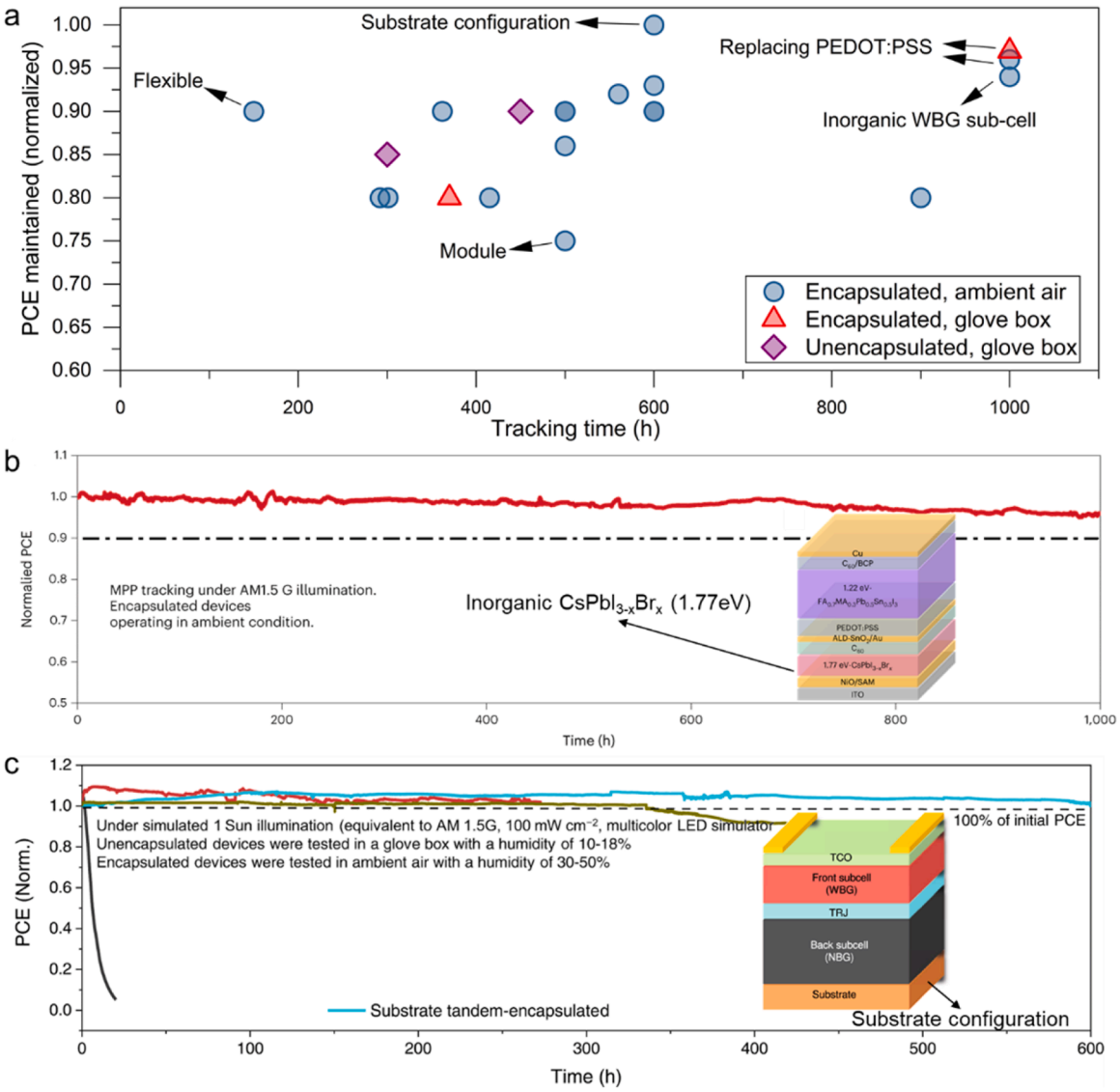

Fig. 15. (a) Reported operational stability data for all-perovskite tandem devices under different tracking conditions. Details are summarized in Table S4. (b) Continuous maximum power output (MPP) tracking of an encapsulated tandem cell over 1,000 hours under simulated 1-sun illumination (equivalent to AM1.5 G, 100 mW cm^{-2}, multi-color LED simulator) in ambient air. Device architecture inserted [205]. (c) Operating stability of unencapsulated superstrate- and substrate-configured tandems, and encapsulated superstrate- and substrate-configured tandems. The encapsulated device retained 100 % of its initial efficiency after 600 hours of operation. All tests were carried out under 1-sun illumination (100 mW cm^{-2}) and MPP tracking. Device architecture for substrate configuration inserted [206].

pivotal in advancing all-perovskite TSCs from the research phase to widespread commercial adoption, unlocking their full potential in a range of innovative and demanding applications.

Conflicts of interest

There are no conflicts to declare.

Acknowledgments

This work has received funding from the European Union's Horizon Europe research and innovation programme under grant agreement No 101075605 (SuPerTandem). This work has also been financially supported by Swiss National Science Foundation (grant no. 200021_213073) and Swiss Federal Office of Energy (SFOE, grant no. SI/502549-01). Huagui Lai thanks the China Scholarship Council (CSC) funding from the Ministry of Education of P. R. China.

V. On the stability of perovskite-containing multijunction photovoltaics

Shuaifeng Hu*, Junke Wang, Seongrok Seo, and Henry J. Snaith

Clarendon Laboratory, Department of Physics, University of Oxford, Oxford OX1 3PU, United Kingdom.

E-mail address: shuaifeng.hu@physics.ox.ac.uk

Abstract

The efficiency of perovskite-containing tandem photovoltaic (PV) devices has increased rapidly over the past decade, thanks to the intensive efforts from the academia and industrial communities. However, solid advancements in their stability are limited, particularly for "all-perovskite" multi-junction solar cells. In this chapter, we summarize the efficiency and stability results of the most studied perovskite-containing multijunction PVs, specifically "perovskite-on-silicon" and "all-perovskite" tandems. We provide an overview of the field's performance developments and investigations into various ageing protocols, highlighting the importance of studying the stability of multijunction PVs under combined light and temperature conditions. We propose potential approaches to detect the origins of instability in multijunction devices and explore possible degradation channels and mitigation strategies for each subcell. With further developments, we anticipate a deeper understanding of the material and device degradation mechanism, ultimately aiding in advancing the stability of

perovskite-containing multijunction PVs.

1. Status of the field

Multijunction photovoltaics (PVs) [207–211]. hold the potential to achieve power conversion efficiencies (PCEs) of over 50 %, with three or more photovoltaic junctions [212], showing exceptional capability in reducing the carbon footprint per unit energy generated [213–216]. Within the monolithic two-terminal perovskite-on-silicon device configuration, PCEs of over 34.6 [217], a value that surpassed the radiative limit of single-junction solar cells, at approximately 33.7 % [218], and between 28.6 % [217]. and 30.1 % [219] have been reported for devices in small areas (~1 cm^2) and M6 size wafer-level devices, respectively. Leveraging this tandem technology, encouragingly, the 60-cell residential-size modules have also achieved an efficiency of 26.9 % [220], surpassing the current best silicon modules (approximately 25 %) with a similar designated module area. In parallel, monolithic two-terminal perovskite-perovskite tandems have also reached efficiencies of up to 30.1, 28.2, and 24.5 % [221] for the small area, 1-cm^2, and 20.25-cm^2 (minimodule) devices, respectively [222]. Monolithic two-terminal perovskite-containing tandem cells with a junction number of over two show great potential [223–226], presenting a leading PCE of up to 28.7 % (certified 27.28 %) with the perovskite-perovskite-perovskite triple-junction devices [227,228]. Besides the greatly reduced embodied energy, more encouragingly, the triple-junction (or even higher junction) cells should be very likely to lead the efficiency race soon through further mitigated carrier thermalisation in theory [212] and experimentally reduced optical and recombination losses [213]. Given the superior efficiencies achieved, the device stability is critical to minimise the levelized cost of electricity and secure the practically operating perovskite-containing tandem PVs with a reasonable payback time [229,230].

Although the maximum power point tracking (MPPT) test under elevated temperature (over 65°C) is becoming more often used for single-junction devices, the stability evaluation of tandems is largely dominated by the "normal" in-lab MPPT test, i.e., ageing the devices under the simulated AM1.5G irradiation at or near room temperature. For example, the reported best-in-class perovskite-on-silicon and perovskite-perovskite tandem cells show encouraging 80 and 93 % efficiency retainment after 347 [231] and 600 [232] hours of operation, respectively, from the normal in-lab MPPT test. Although it is a convenient protocol to primarily measure the in-lab device stability, the MPPT test will not be able to provide sufficiently informative results for the stability evaluation of devices being operated under practical outdoor conditions [233], where the portion of ultraviolet light differs [234] and the temperature varies [235] upon geographical locations and time of the day. This, therefore, leads to the MPPT stability results being less informative, and most of the time, normal in-lab MPPT results would overestimate the stability of practical devices. In particular, we found that the in-lab MPPT test conducted at room temperature under simulated AM1.5G irradiance (also specified as International Summit on Organic Photovoltaic Stability (ISOS)-L-1 protocol [236]) suggests a T80 lifetime (the time at which the performance of the solar cell has reached 80 % of its original value) of over 150 times longer than that of the lifetime acquired under 85°C near 1-sun light intensity at open-circuit voltage (V_{OC}) ageing conditions (ISOS-L-2 [236]) for the same type of all-perovskite multijunction cells [227]. This suggests that photo-catalysed thermal degradation plays a crucial role in the stability of multijunction devices, a factor that the normal in-lab MPPT test cannot assess. This motivates us to call attention to studying the degradation of multijunction devices and integrated materials under these combined ageing conditions. Historically, the knowledge gained, and the database built should ultimately be invaluable in facilitating the development of commercially viable perovskite-containing tandem PVs.

2. Current status and future challenges

We statistically summarised the efficiency and stability results for the perovskite-on-silicon and all-perovskite tandem PVs reported in the past decade. From the results (Fig. 16), we learn that both types of tandems have focused on the double-junction cells, while the development of the triple-junction devices is very limited with only 14 publications in total, and no report on the devices with more than three junctions, e.g., quadruple-junction devices. As for the number of device terminals [237], the development intensity on two-terminal devices historically overcomes the four- and three-terminal devices and no three-terminal cells have been reported for the all-perovskite tandems. By combining a semi-transparent wide bandgap (~2 eV) perovskite

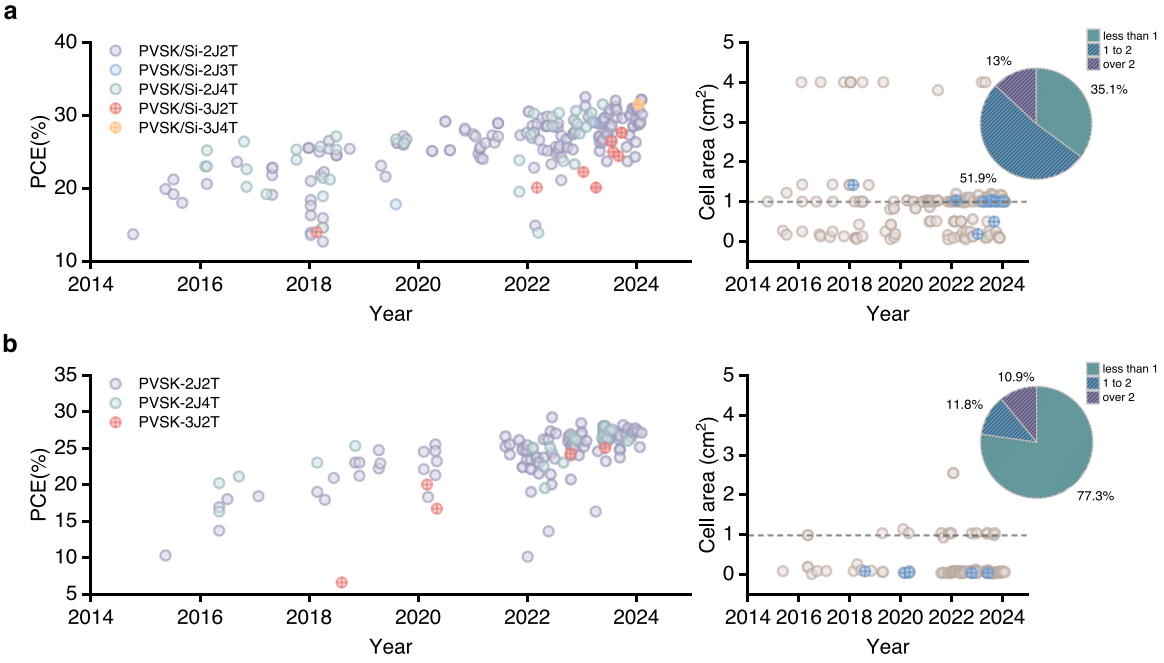

Fig. 16. Evolution for efficiency reported from the literature of **a,** perovskite-on-silicon and **b,** all-perovskite multijunction cells with the device area (data for the cell area over 5 cm^2 and modules are not presented, for clarity) plotted on the right side; inset pie charts displaying the percentage of device types on the active area. PVSK: perovskite, T: terminal, J: junction. Data updated by the 21st of July, 2024.

single-junction top cell and middle bandgap (~1.52 eV) perovskite-silicon monolithic tandem bottom solar cells, for example, the latest four-terminal triple-junction perovskite-perovskite-silicon cells report a combined PCE of up to 31.5 % [238]. Although this is higher than the highest reported monolithic perovskite-perovskite-Si triple junction cell at 27.62 % [226], by the author's admission, the four-terminal tandem was measured by filtering the rear cell with a similar cell of the same structure, to the electronically tested top cell, rather than making a true four-terminal tandem cell measurement. Compared to monolithic two-terminal tandems, mechanically stacked four-terminal cells, however, experience significant optical losses due to additional illumination transmission between the cells and air (if no refractive-index-matching film is included) and parasitic absorption by the electrode [239]. Four-terminal devices incur higher costs and are less scalable, e.g., to terawatt-scale PVs, primarily because they require more transparent conductive glass and electrical connections, often containing the earth-scarce element indium and precious metals [240]. Positively, a four-terminal structure offers a distinct advantage in pairing new PV materials with an existing mature PV technology as its insensitive nature on current mismatch resulting from spectrum variation [241] and the facile wiring process. In perovskite-on-silicon tandem, for instance, utilizing the four-terminal structure is more feasible for fabricating a tandem cell that achieves superior efficiency and stability concurrently compared to its two-terminal counterparts. The paired efficient perovskite top-cell can be that near 1.60 eV with a well-studied composition — e.g., MA-free and neat iodide/low bromide perovskites — that exhibits no light-induced halide segregation and demonstrates high stability even under accelerated testing conditions [242].

For the all-perovskite tandems, we see the high-efficiency potential of bifacial cells [243,244]. For example, the 1.65 eV (neat lead (Pb) perovskites)/1.25 eV (narrow bandgap mixed tin–lead (Sn–Pb) perovskites [245,246]) device generates an equivalent efficiency of up to 29.3 % under illumination with 30 % of albedo light [247]. Besides the improved performance, this strategy should also provide the tandem cells with better stability due to the reduced bromine content at the X-site of the wide bandgap neat Pb perovskites, compared to the mono-facial devices utilizing the 1.8 eV perovskite front absorber, which can exhibit detrimental light-induced halide segregation [248]. According to the detailed balance limit [218], the PCE of the multijunction cells should be increased with the junction number thanks to the progressively reduced thermalization losses. Given the successful development of low parasitic absorption interconnecting layer materials, bifacial triple-junction PVs should achieve PCE values much higher than the currently leading double-junction devices. We also recognize the high energy yield potential of bifacial four-terminal multijunction devices. When the front and rear terminals are electrically connected in separate circuits in a module, all the increased current density in the rear cell from the albedo effect can be converted into useful energy, without upsetting the current matching requirement. Considering the difficult-to-control Sn-containing perovskites [211,249], the silicon-involving triple-junction tandems unexceptionally employ the near 1.50 eV bandgap neat Pb perovskite as the middle subabsorber [209,225,226,238,250–254], because this is the lowest bandgap that can be accessed with the neat Pb perovskite composition. Therefore, all the reported perovskite-perovskite-silicon triple-junction cells show a large current density mismatch with the perovskite-perovskite subjunction limiting. For example, the best-in-class cells show the current density values of 12.22, 11.29, and 15.63 mA cm^{-2} by integrating the external quantum efficiency spectra of the 1.93 eV-perovskite, 1.55 eV-perovskite, and 1.12 eV-silicon subcells, respectively, with the AM1.5G sunlight spectrum [226]. The monolithic silicon-based multijunction cells thus present large limitations on the maximum achievable PCE values regarding their theoretical limit, when Sn-containing perovskites are excluded. Accordingly, enriching the bandgap continuity with the existing Sn-containing perovskite materials via compositional engineering ($APb_xSn_{(1-x)}I_yBr_{(3-y)}$ (A = A site cation)) or developing new alternative PV materials is critical for producing efficient silicon-containing multijunction cells as the junction number increases to three or more.

With the addition of narrow bandgap Sn-containing perovskite materials [245,246,255–257], in contrast, monolithic multijunction cells should achieve higher PCE values due to reduced current mismatch and enhanced device V_{OC}. Based on the theoretical photovoltage limit, for example, the 1.97 eV/1.61 eV/1.25 eV all-perovskite triple-junction cells could achieve the maximum summed V_{OC} of 3.954 V (1.655 + 1.318 + 0.981 V), much larger than that of 3.730 V (1.655 + 1.215 + 0.860 V) for the 1.97 eV/1.50 eV/1.12 eV triple-junction perovskite-perovskite-silicon cells [258]. However, depositing the Sn-containing perovskite films requires additional care regarding the rapid film crystallization and the facile oxidation of Sn(II) to Sn(IV), these also undermine their device stability [211]. Despite the challenges, the current indispensable role of Sn-containing perovskite materials warrants further investigation.

By collecting the active area of the cells, we also find that the perovskite-on-silicon device field is becoming increasingly standardized to an active area of approximately 1 cm^2. In contrast, high-performance all-perovskite tandem cells rely heavily on utilizing small areas, typically with an active area smaller than 0.1 cm^2, due to their considerably improved device fill factor (FF) compared to larger area cells. This suggests that maintaining spatial homogeneity and quality of perovskite films, as well as the resistance of devices, becomes challenging as the area increases. However, the scientific insights gained from devices with increased area will likely accelerate device optimization and drive their ultimate development towards practical implementation at a greater level. We therefore encourage further investigation of multijunction devices with larger areas, such as 1 cm^2, as their silicon-based counterparts, which also deserve greater recognition.

Looking into the stability results (Fig. 17), we notice that the stability evaluation on the perovskite-on-silicon tandems shows more diversity compared to all-perovskite tandem cells, where no documented results on the bias, outdoor, and light-cycling stability. The trend clearly shows that, in general, the ratio of cases with stability evaluation to the total number of counted cases has been increasing each year, thanks to the globally increased stability research input. Specifically, the room temperature MPPT test has dominated stability protocols since 2017 and 2018 for perovskite-on-silicon and all-perovskite tandems, respectively. This also results in a larger number of cases that conducted single light stability evaluation with respect to that of the single thermal stability study. Unexpectedly, only 8 cases (7 for perovskite-on-silicon and 1 for all-perovskite tandems) examined the stability of the multijunction devices under the combined light and thermal stressors (ISOS-L-2). This very limited cases of stability evaluation also can be seen for the bias (2 for perovskite-on-silicon tandem) and thermal cycling (2 for perovskite-on-silicon and 1 for all-perovskite tandems) tests. However, stressing the devices under the factors of, e.g., light, heat, bias, humidity, etc., in their single and combined form is necessary to evaluate their stability, which could also provide invaluable information to facilitate the development of more feasible and viable perovskite multijunction PVs [259]. Considering the complex practical surroundings, we emphasise the importance of studying the stability of perovskite devices under harsh conditions, e.g., ISOS-V-3, ISOS-L-2 (open-circuit), ISOS-T-3, as well as outdoor/field circumstances.

3. Advances to meet challenges and concluding remarks

To study the stability of multijunction cells, we propose using multiple LED lights to selectively illuminate the integrated subcells according to their bandgaps [260]. This approach will enable us to evaluate the lifespan of each subcell individually and aid in developing strategies to improve the stability of their multijunction cells. Taking the triple-junction all-perovskite cells as an example, the current most efficient devices include the wide bandgap (~2 eV) perovskite as the front sub-absorber. The wide bandgap perovskite is generally composed of

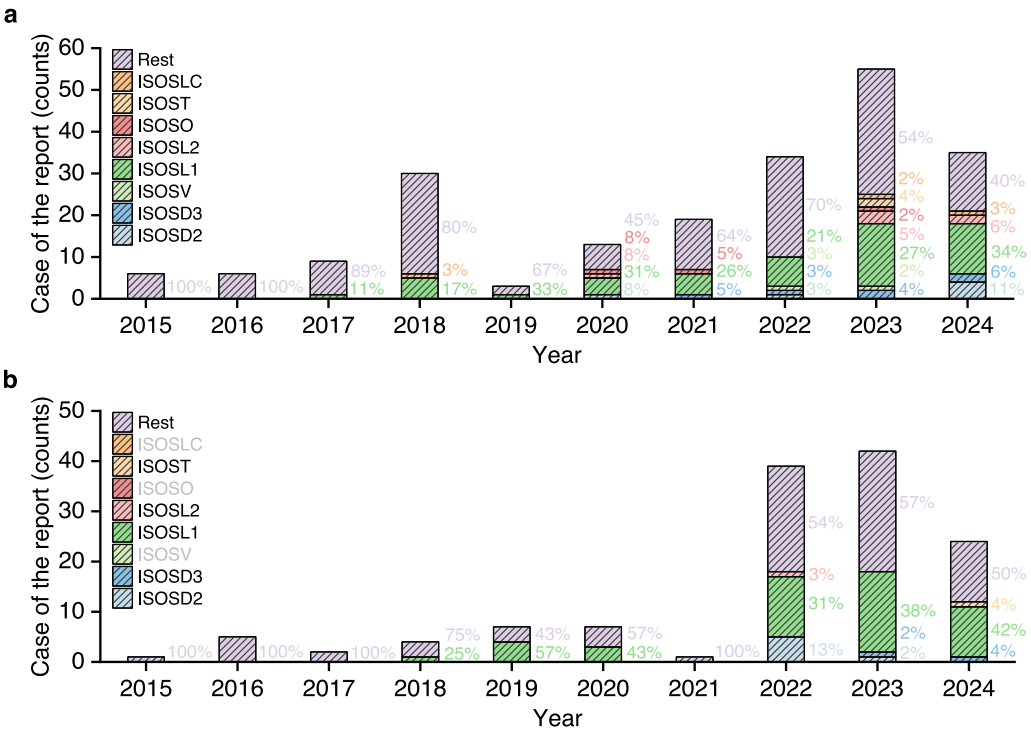

Fig. 17. Stability results extracted from the reported literature and classified with the applied examination protocols [236], i.e., thermal stability (no less than 65°C, ISOS-D-2), damp-heat (85°C and 85 relative humidity, ISOS-D-3), bias stability (ISOS-V), long-term MPPT or light stability (ISOS-L-1), light and thermal (no less than 65°C, ISOS-L-2) stability, outdoor (ISOS-O), thermal cycling (ISOS-T), and light-cycling (ISOS-LC). The ISOS-D-1, steady-state, and no stability evaluation reports are grouped and subjected to the case of "Rest". The ratios of each tested ageing protocol are provided based on the data reported by year. Data updated by the 21st of July, 2024.

about 60 % Br^- at the X-site of the three-dimensional ABX_3 perovskite structure [223], suggesting a necessity for improving the photostability of the materials as the well-known halide segregation is prone to occur. For the middle bandgap (~1.60 eV) sub-absorbers, the largely reduced X-site halide heterogeneity suggests the absence of halide segregation and improved phase stability. For example, the corresponding PV devices show T80 lifetimes of hundreds and thousands of hours, even when aged under harsh conditions [242]. Research on the stability of perovskite materials with different bandgaps has progressed independently with single-junction device architectures, with a dominant focus on bandgaps below 1.65 eV. However, the study on the stability of perovskites with a bandgap of approximately 1.8 eV or higher is relatively limited [261,262], with those near 2 eV posing the most significant challenges [223,224]. For the rear mixed Sn–Pb absorber, the facile oxidation of Sn(II) to Sn(IV) and the acidic water-dispersed PEDOT:PSS (poly(3,4-ethylenedioxythiophene) polystyrene sulfonate, hole transport material) introduced material losses should account for most of the instability of their devices, as more specifically reviewed together with the mitigation approaches provided in our previous publications [211, 249,263].

The number of interfaces is about 5 times the junction number in a typical solar cell device, where the triple- and quadruple-junction cells yield interface numbers of about 15 and 20, respectively. In multijunction PVs, new interfaces are created along with the insertion of interconnecting layers (ICLs), which generally involve the transparent conducting oxide (TCO) or ultrathin metal as a charge recombination layer (CRL). For instance, in perovskite-on-silicon tandem PVs, the CRL constructed with doped polycrystalline-silicon (poly-Si) – poly-Si(n^+)/poly-Si(p^+) – tunnelling junction shows a considerable positive effect on improving the resultant device stability, thanks to the stronger adsorption of the hole selective self-assembled monolayer onto poly-Si(p^+) than onto the conventional indium zinc oxide (IZO) [235,264,265]. In addition, LONGi and their collaborators reported that the CeO_2-doped In_2O_3 (ICO) not only reduced total electrical power loss by 0.1 %, but also played a decisive role in enhancing the stability of their single-junction silicon devices [266–268]. This also suggests the high potential of innovative TCO layers, stacked on silicon contacts to assist in collecting carriers to electrodes, in improving the performance and stability of the silicon-containing tandem PVs. As for all-perovskite multijunction PVs, Au or TCO are typically used as the CRL [211]. However, conclusive evidence on how material selection impacts device stability is limited, although some negative effects have been observed in single-junction cells using metal electrodes [269]. In our opinion, the sputter-coated TCO films, given that no active species are contained, should have a superior ability to prevent material cross-diffusion due to their high compactness compared to nanometre-thick metal nanoclusters [211].

This further emphasizes the importance of addressing potential degradations at interfaces with a high density of active sites, which can lead to detrimental reactions and material diffusion. From the device optimization perspective, tuning the bandgap and the thickness of each sub-absorber to reduce the device current mismatch is critical, as the resulting electrical field as an internal factor applied to the limiting subcell (the one, most of the time will be the perovskite subcell(s) in the silicon-containing tandems, does not generate enough charges to recombine with those from the non-limiting cell) will cause severe ion migration that raises material losses and shortens device lifespan [229]. This should be one of the most pressing issues that monolithic perovskite-perovskite-silicon triple-junction tandems are currently facing, as discussed above. In addition, the light and heat applied externally will be sources of energy that could accelerate the deleterious side reactions and the destructive material losses, leading to the deterioration of device performance. Aside from ensuring the stability of the perovskite bulk material, there is an urgent need for robust interface engineering and effective encapsulation or lamination techniques to enhance the stability of all types of these intricate perovskite-containing

multijunction PV devices.

Acknowledgements

We acknowledge the Engineering and Physical Sciences Research Council (EPSRC), UK, under grant numbers EP/S004947/1, EP/X038777/1, EP/X037169/1, EP/T028513/1, UK Research and Innovation (UKRI) under the UK government's Horizon Europe funding Guarantee under grant number 10054976 (The NEXUS project has received funding from the European Union's Horizon Europe research and innovation program under grant agreement No. 101075330, Views and opinions expressed are however those of the author(s) only and do not necessarily reflect those of the European Union or RIA. Neither the European Union nor the granting authority can be held responsible for them), and the Marie Skłodowska Curie Actions Postdoc Fellow (UKRI Guarantee, EP/Y029216/1) for funding.

Author contribution

The manuscript was written through the contribution of all authors.

Conflicts of interest

H.J.S. is the co-founder and CSO of Oxford PV Ltd.

VI. Minimizing lead toxicity for perovskite solar cells

Haoxuan Liu[1,2] and Fei Zhang[1,2*]

[1]School of Chemical Engineering and Technology, Tianjin University, Tianjin, 300072, China.

[2]Collaborative Innovation Center of Chemical Science and Engineering (Tianjin), Tianjin, 300072, China.

E-mail address: fei_zhang@tju.edu.cn

1. Status of the field

Perovskite solar cells (PSCs) have undergone a rapid evolution over the past decade, with their power conversion efficiency (PCE) soaring from 3.8 % to above 26 % [77,270–272]. However, the use of lead (Pb) in these high-efficiency solar cells, while essential for their performance, poses a significant threat to the ecosystem and human health. With the field of perovskite photovoltaic witnessing exponential growth in high-tech enterprises and scientific research teams, the need to address this pressing issue has become more urgent than ever.

However, Pb is a key component of current high-efficiency PSCs thanks to its unique atomic orbital properties [273]. As PSCs are exposed to various environmental conditions, including acidic rains, heavy snow, and hail, they pose a significant risk to the ecosystem by releasing Pb from damaged and discarded devices due to their solubility in water. Lead substantially threatens humans and wildlife, undermining efforts to achieve environmentally friendly and sustainable objectives. Consequently, lead safety is a critical issue in its practical application, and the solar cell community has devised techniques, such as using lead-free elements [274,275], recycling [276,277], and chemisorption [278], to address the lead toxicity problem (Fig. 18).

2. Current and future challenges

The potential risks of lead toxicity are extensively documented. Ingestion or inhalation of lead can lead to severe health issues, primarily because lead has a strong affinity for thiols, numerous enzymes, proteins, and cell phosphate groups of cell membranes. The urgency of addressing this issue is evident, as it has profound implications for human health and the environment.

A life-cycle assessment (LCA) has concluded that PSCs are environmentally sustainable compared to alternative technologies, such as commercial Si solar cells. However, the potential leaking of Pb from PSCs remains a significant concern. The panels' exposure to increasingly severe weather conditions, as warned by the World Meteorological Organization (WMO), could lead to the disintegration and dispersion of lead due to rainfall. This could result in lead leakage into aquatic environments, contaminating the atmosphere and food chain thousands of times more than the stringent regulations allow. Given these potential toxic effects, the urgency of finding an effective strategy to control lead leakage in PSCs cannot be overstated. It is a significant challenge for researchers today but must be met for our health and the environment.

Various categories of lead-free perovskites have been reported to mitigate toxicity, such as Sn^{2+}, Ge^{2+}, and Bi^{3+} [279]. By adding FPEABr,

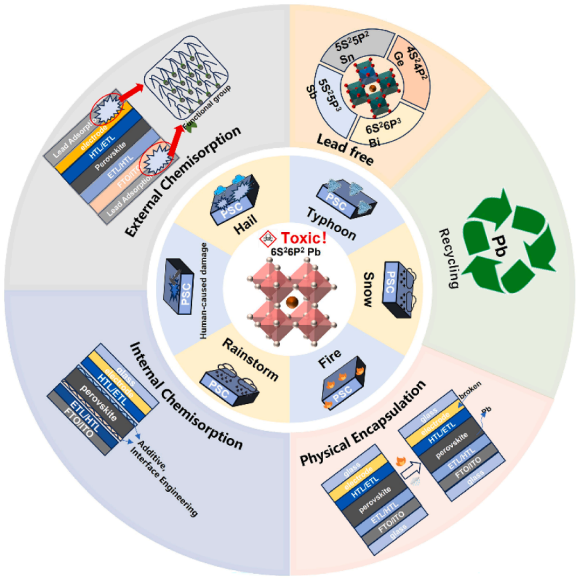

Fig. 18. Strategies to minimize lead toxicity for PSCs.

Zhao et al. successfully created 2D/3D heterojunction on 3D $FASnI_3$, leading to the highest device performance of 14.81 % (14.03 % certified) and stability [280]. Other lead-free materials, such as $CsBi_3I_{10}$ [281]. and $Ag_xBi_yI_{x+3y}$ (x = 1-3, y = 1-2) [282]. still exhibited a low PCE of around ~5 %. Despite significant progress in lead-free PSCs, the stability and efficiency challenges hinder their further development.

Recycling lead from PSCs can also reduce lead contamination; however, the PCE of PSCs made from recycled PbI_2 could not always match that made from new PbI_2. Physical encapsulations were first proposed to address the challenges of Pb leakage. However, the physical encapsulations can only slow the lead leakage. Chemisorption is a highly effective method for preventing the leaching of Pb by using Pb absorbents within or outside of device structures, in addition to physical encapsulation.

3. Advances to address these challenges

3.1 Methods for preventing Pb leakage

Physical encapsulation generally uses polymer and inorganic materials [283]. on the outer surface of PSCs, which could improve their stability. However, physical encapsulation can only slow lead leakage and cannot prevent the leakage. In addition, the additional glass substrate will also increase the cost.

Chemisorption strategies are more effective measures to prevent lead leakage. Lead-absorbing materials are primarily derived from some containing functional groups such as -C=O, $-S^{-}$, $-SO_3^{-}$, and $-PO_4^{-}$, which offer effective binding sites for interaction with mobile Pb^{2+} and capture it. They are generally divided into internal and external chemisorption according to the reported locations. Chen et al. introduced cation-exchange resins (CERs) containing sulfonic acid group structure to the metal electrodes of the PSCs module, significantly reducing lead leakage by approximately 90 % [284]. Later, the same group designed a mesoporous sulfonic acid as an insulating scaffold for PSCs to further reduce the amount of Pb leakage in acidic water [285], reducing the lead ion concentration from 16.0 ± 0.8 ppm to 4.51 ± 0.68 ppm. Although lead adsorption additives and interface modifiers with a certain thickness (~20-50 nm) have improved performance and reduced lead leakage, they cannot wholly prevent lead ions from leaking from the typical ~500-1000 nm perovskite film. And they are not necessarily compatible with different efficient perovskite compositions and device structures. Excessive additives can affect PSCs' performance, which can also increase costs.

In contrast, the external Pb-chemisorption strategy has a more significant potential advantage because of its adaptability to different

device structures. This not only effectively inhibits lead leakage but also improves PSCs's stability. We first reported two Pb sequestrating materials, P, P′-di (2-ethylhexyl) methanediphosphonic acid (DMDP) and N, N, N′, N′-ethyl enedia- minetetrakis (methylenephosphonic acid (EDTMP-PEO) on the glass and metal side, reducing the lead leakage of 96 % [286]. However, it required additional spin coating processes, which also increased the complexity of device fabrication and may limit its scalability. Then, we designed a tape-like film consisting of a standard EVA layer and a bladed-coated DMDP film, encapsulated on both sides of a device with the normal structure or the inverted structure, achieving an extraordinary lead sequestration efficiency (SQE) of over 99 % [287]. To reduce the cost and make the film fast-degraded, we developed the sulfosuccinic acid-modified polyvinyl alcohol (SMP) coating that prevented lead leakage and enhanced device stability without compromising device performance, effectively preventing lead leakage by over 99 % [288].

3.2 Recycling lead from PSCs

Another essential way to reduce lead contamination is to recycle lead from waste PSCs. In 2016, lead was recovered from PSCs by the electrochemical method for the first time, and the lead recycling rate was up to 99.8 % [289]. Since then, more and more lead recycling strategies have been developed. Chen et al. used dimethylformamide (DMF)and CER to dissolve the perovskite layer and recycle PbI_2 [276]. The PCE of PSCs made from recycled lead differed greatly from the original device. Park et al. first used DMF to remove metal electrodes, HTM, and dissolved perovskite. Then, the hollow composite material of iron-modified hydroxyapatite (HAP/Fe) with a negative surface charge was used. Then, the KI solution was added to obtain the recycled PbI_2 with a recycling rate of 99.97 % [290]. However, due to the complex composition of PSC modules, recycling them is usually very difficult. Although there are some feasible and effective methods, they are still limited to the laboratory. To achieve large-scale recycling in the future, researchers need to further optimize and improve the recycling method of lead in terms of cost and process. The lead-acid battery industry has developed many mature lead recycling technologies, from which we can get some ideas and inspiration to be applied to PSCs.

4. Concluding remarks

To sum up, to improve the lead safety of PSCs, the introduction of lead-absorbing materials is essential. Developing new materials with one or more lead-absorbing groups is a practical way to mitigate environmental lead diffusion. However, the current research on lead leakage is not deep enough, and there are still many areas to be improved in developing lead-absorbing materials. The performance and stability of PSCs should not be negatively affected by absorbent materials employed as additives or modifiers, as these materials directly impact charge transfer, perovskite crystallization, and non-radiative recombination at the bulk or interface. The adsorbent material needs high transmittance to allow sufficient light to reach the perovskite active layer while maintaining device performance. From the point of view of molecular engineering, advanced lead-absorbing materials should have a variety of functions, such as self-cleaning, anti-reflection, and defect passivation. In addition, other properties, such as resistance to environmental stimuli (UV exposure, high temperature, and humidity), impact resistance, and long-term reliability, are also essential considerations. Additionally, in flexible devices, the adsorptive film should exhibit good deformability to ensure consistent adsorption efficiency under various bending conditions while maintaining the device's optical performance. Finally, for large-area devices, the adsorptive film must demonstrate excellent long-term stability and durability, cost-effective, to ensure the sustained performance and stability of the device over extended operational periods. Regarding technology commercialization, lead-absorbing materials should be cost-effective and reusable, considering their large-scale processability and industrial utility.

To further improve lead safety, we must develop standard test protocols for lead leakage testing of PSCs, simplify data acquisition methods, and build mathematical models of lead leakage to simulate actual meteorological conditions in computers. For economic reasons, lead is not a high-value metal that can be recycled from waste PSCs. Still, because lead is so harmful to organisms and the environment, recycling lead from PSCs should also attract widespread attention from environmental considerations. Future research priorities include integrating various encapsulation methods and recycling strategies to reduce costs and lead leakage, improve efficiency, and develop testing standards. Most importantly, the government should also formulate relevant policies, which may be the key to further mitigating the environmental impact and public acceptance of PSCs.

Acknowledgments

This work was financially supported by the National Natural Science Foundation of China (52203237).

VII. Metal halide perovskites for lighting

Jinghui Li[1,2], Jiajun Luo[1]*

[1]Wuhan National Laboratory for Optoelectronics and School of Optical and Electronic Information, Huazhong University of Science and Technology, Wuhan 430074, Hubei, China.

[2]School of Physics and Optoelectronic Engineering, Hangzhou Institute for Advanced Study, University of Chinese Academy of Sciences, Hangzhou 310024, China

E-mail address: luojiajun@mail.hust.edu.cn

1. Status of the field

Lighting consumes nearly 20 % of the world's electrical energy annually. The primary consumption way is white-light illumination, which mimics natural sunlight. The most popular white light-emitting diodes (WLEDs) are made by combining GaN blue emission chips with a phosphor coating. However, this multi-color mixing method for producing white light suffers from energy loss from secondary excitation and color degradation over time [291]. Recently, efficient and bright white electroluminescence has been developed using single-component perovskite halides that eliminate these issues, which position it as an ideal white lighting sources [292,293].

Single-component perovskites (SCPs) that emit white light stand out as prime contenders for illumination applications, attributed to their broad emission spectra, high color rendering index (CRI), and outstanding luminescence efficiency. For instance, $Cs_2Na_{0.4}Ag_{0.6}InCl_6$: Bi and $(OCTAm)_2SnBr_4$ both boast a broad white emission spectrum, with respective full widths at half maximum of 158 nm and 136 nm, coupled with remarkable photoluminescence quantum yield (PLQY) values of 86 % and 100 % [292,294]. This broad white emission is a result of a strong electron-phonon coupling effect. Furthermore, the high PLQY values are attributed to the reduced electronic dimension, where the unit with a lower permittivity envelopes the unit with a higher permittivity, thereby enhancing the Coulombic interaction between electrons and holes, ultimately improving the efficiency of radiative recombination.

2. Current progress and future challenges

As shown in Fig. 19, we analyse the performance metrics between WLEDs utilizing either SCPs or a hybrid design integrating GaN chips with a phosphor coating. GaN-based WLEDs should be fabricated through a MOCVD method at temperatures over 700°C and depends on a phosphor coating with uniformly distributed micron-sized luminescent particles [295,296]. This reliance poses challenges for miniaturization and integration. In contrast, SCP-based WLEDs can be easily prepared using simpler methods like solution spin-coating or thermal evaporation, offering lower manufacturing costs than GaN-based WLEDs. Additionally, SCPs can be patterned into miniaturized arrays using photolithography or ultra-fine masks and integrated onto silicon-based driver circuits for specialized lighting applications [297]. Moreover, the white emission spectrum from GaN-based WLEDs often suffers from inconsistent decay rates between blue and yellow components over time, leading to color degradation and reduced lighting quality. Conversely, the white light spectrum of SCPs-based WLEDs originates from a single component material, resulting in superior color stability.

Despite the promising photoluminescence properties, the strong

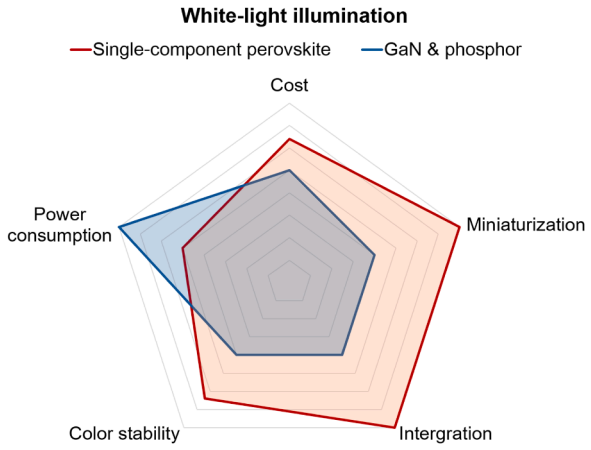

Fig. 19. A comparative analysis of the performance metrics between white light-emitting diodes (WLEDs) utilizing either single-component perovskite (SCP) or a hybrid design integrating GaN chips with a phosphor coating. The SCP-based WLEDs demonstrate noteworthy color stabilibity, lower manufacturing costs, and a capacity for miniaturization and integration. However, it is worth mentioning that these advantages are counterbalanced by their power consumption, which lags significantly behind GaN-based WLEDs.

electron-phonon interactions and low electronic dimensions within SCPs crystal lattice pose formidable hurdles for carrier injection in WLEDs [298]. The heavy effective mass of carriers in lead-free SCPs also results in poor carrier transport. Electron-hole injection remains challenging in SCPs, ultimately translating into a marked disparity in electroluminescence efficiency between SCP-based WLEDs and their GaN-counterparts [299].

As shown in Fig. 20a, enhancing the electroluminescence performance of SCPs-based WLEDs requires continuous optimization of each functional layer in the device structure. For instance, achieving higher luminescence efficiency and more efficient charge transport is crucial for SCPs-based white emissive layer. Electrons and holes in SCPs tend to be bound by lattice defects and subsequently annihilated non-radiatively. Common solutions include defect engineering and composition engineering. As illustrated in Fig. 20b, Song et al. from Jilin University effectively passivated defects generated during the growth of $CsPbCl_3$:Eu white emissive materials by introducing creatine phosphate (CP), increasing the PLQY of $CsPbCl_3$:Eu white emissive films from 35 % to 61 %. They also achieved different spectral compositions of white light emission by altering the Eu component ratio. At a Eu molar ratio of 3.5 %, they achieved a maximum external quantum efficiency of 5.4 % and a maximum brightness of 1678 nits for SCPs-based WLEDs (Fig. 20c) [300]. Moreover, electrons in SCPs white emissive materials are easily affected by lattice phonons, resulting in insufficient charge transport. Additive engineering and energy transfer engineering are commonly used to address this issue. Shi et al. from Zhengzhou University introduced an additive containing a carbazole group into $CsCu_2I_3$ material [301]. This additive not only passivated Cu_{Cs} and Cu_I antisite defects via interaction with uncoordinated Cu^+. Importantly, the electron donor made it easier for electrons to be oxidized, leaving holes in the orbitals to facilitate transport. This effectively improved the charge injection capability of $CsCu_2I_3$ white emissive layer, increasing the external quantum efficiency of SCP-based WLEDs by nearly 8.5 times. Chen et al. from Fujian Normal University used 2,6-DCzPPY and $Cs_2Na_{0.4}Ag_{0.6}In_{0.97}Bi_{0.03}Cl_6$ as host and guest materials, respectively, to construct a host-guest system for SCP-based WLEDs. The host material was used to replace charge transport and injection, ultimately achieving efficient charge injection and luminescence [302]. For the carrier injection layer, it is crucial to ensure the efficient and smooth transfer of charges into the SCPs white emissive layer. Therefore, carrier injection engineering and

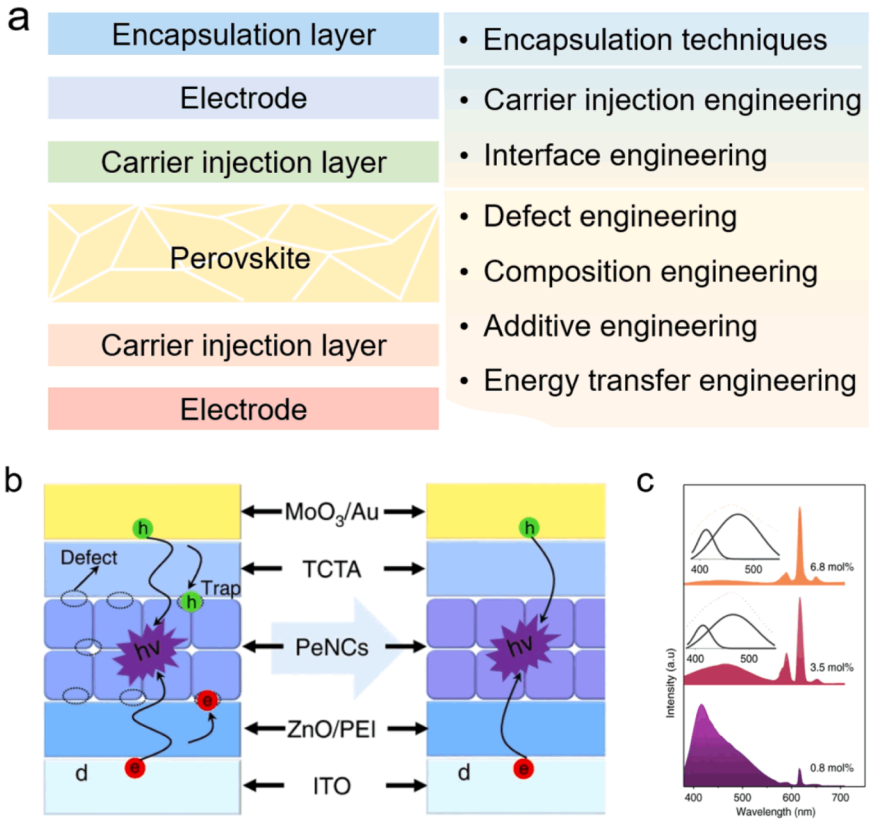

Fig. 20. **a**, The structure and optimization strategies for SCP-based WLEDs. **b**, The schematic diagram of defect engineering in lanthanide ions doped $CsPbCl_3$. **c**, EL spectra of WLEDs constructed by lanthanide ions doped $CsPbCl_3$ with different compositions.

interface engineering are essential to achieve balanced electron and hole injection within the device and efficient charge transfer at the interface with the SCPs white emissive layer. Lastly, since SCPs are relatively sensitive to moisture and oxygen in the air, leading to irreversible damage, advanced encapsulation techniques are necessary to ensure the stable operation of SCPs-based WLEDs.

Despite significant efforts to improve the performance of SCPs-based WLEDs, their performance remains well below the threshold for commercial applications due to their relatively short development period. For example, the CIE, CRI, EQEs, and luminance of the SCPs-based WLEDs mentioned above have been included in Table S5, which should be further improved to meet the requirements for commercial applications. However, it is evident that SCPs-based WLEDs, which achieve white emission covering the visible spectrum using a single component material, possess several inherent application advantages. For instance, the device structure is greatly simplified compared to traditional WLEDs, which require multiple materials emitting different colors to form a complex structure for white light emission [303]. The SCPs-based WLEDs significantly reduces the number of material layers and interfaces, thereby avoiding issues related to energy distribution and uneven performance degradation among different materials [304]. Additionally, the simplified device structure facilitates heterogeneous integration with silicon-based logic circuits, enabling intelligent on-chip light source applications.

3. Concluding remarks

It can be anticipated that the research field of SCPs-based WLEDs will receive increasing attention. For individual SCPs-based WLEDs, there are significant challenges to achieve the performance meeting commercial application requirements. Effective injection of charge carriers is a key issue that needs to be addressed in the future. In terms of integrated SCPs-based WLEDs applications, achieving heterogeneous integration on silicon-based logic circuits is needs to be conquered. More effort is needed to advance the development and practical application of SCPs-based WLEDs. For instance, the SCPs-based WLEDs is promising to realize full-color display by combining with color-filters.

VIII. Perovskite quantum dot LEDs

Hongjin Li[1], Yun Gao[1], and Xingliang Dai[1,2*]

[1]School of Materials Science and Engineering, State Key Laboratory of Silicon and Advanced Semiconductor Materials, Zhejiang University, Hangzhou, China

[2]Wenzhou Key Laboratory of Novel Optoelectronic and Nano Materials and Engineering Research Centre of Zhejiang Province, Institute of Wenzhou, Zhejiang University, Wenzhou, China

E-mail address: shanfeng@zju.edu.cn

1. Status of the field

Colloidal perovskite quantum dot light emitting diodes (Pe-QLEDs) represent a promising technology for next-generation displays and lighting due to their superior color purity, tunable emission wavelengths, and solution processability [305–309]. A typical LED comprises an emissive layer sandwiched between charge (electron/hole) injection layers. In this device architecture, electrons and holes are injected from the cathode and anode, transported through charge transport layers, and recombined within the quantum dot emissive layer to generate photons (Fig. 21a). The external quantum efficiency (EQE), defined as the ratio of the number of photons emitted from the device to the number of electrons injected into the device, is a critical metric for evaluating device performance. The equation for EQE is given by:

$$EQE = \eta_{int} \times \eta_{ext} = \eta_R \times \eta_I \times \eta_{ext} \quad (1)$$

where η_{int} represents the internal quantum efficiency, η_{ext} is the external coupling efficiency, η_R is the radiative recombination ratio in the emissive layer, and η_I denotes the efficiency of carrier injection balance. Thus, achieving optimal performance in Pe-QLEDs necessitates a delicate balance of carrier injection, high radiative recombination rates in

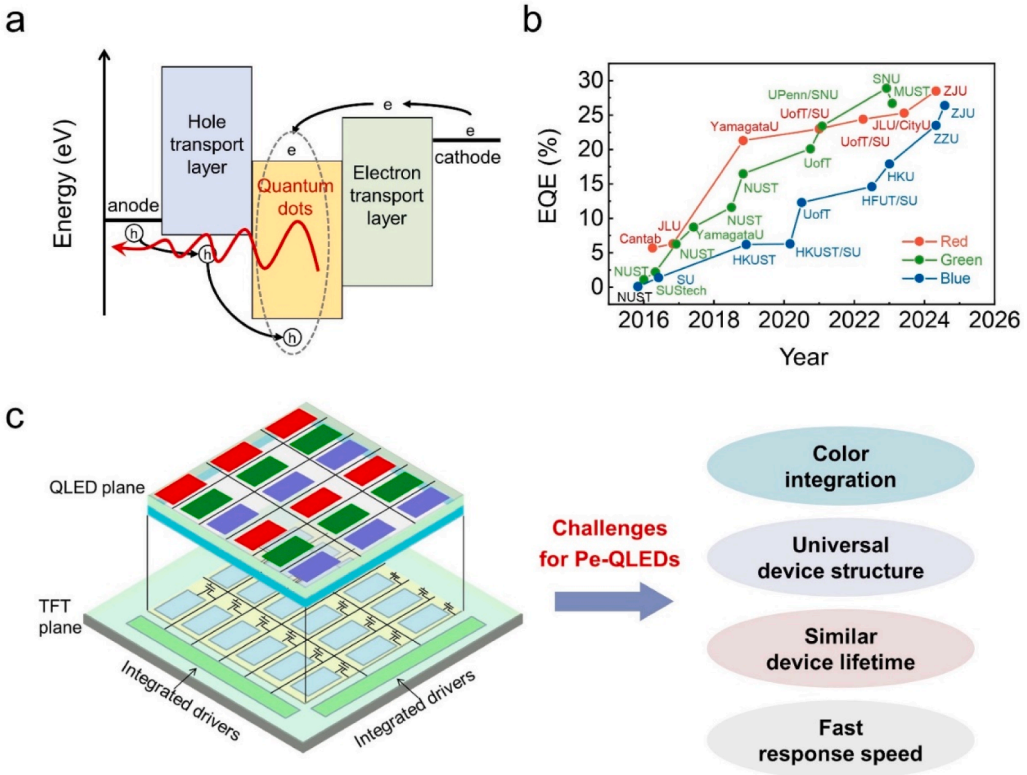

Fig. 21. a, Working principle of multi-layer Pe-QLEDs. **b,** Evolution curves of the peak EQEs in reported red [311,313–318], green [307,310,319–327], and blue [308,310,312,328–333]. Pe-QLEDs. **c,** Schematic illustration of the proposed structure of active matrix Pe-QLED displays and the challenges faced by Pe-QLEDs. Adapted with permission from Dai et al., Adv. Mater. 29, 1607022 (2017). Copyright 2017 John Wiley and Sons.

the emissive layer, and effective light outcoupling.

For perovskite quantum dots, the high surface-area-to-volume ratio and weak ligand bonds of the surface result in surface vacancies, often halide vacancies, and associated defects, which trap a portion of charge carriers, preventing them from emitting light. Therefore, surface features critically impact the performance of Pe-QLEDs, prompting extensive efforts to reconstruct quantum dot surfaces. Since their first demonstration in 2015 [310], Pe-QLEDs have made considerable progress, reaching EQEs of more than 28 % for green ($(FA_{0.7}MA_{0.1}GA_{0.2})_{0.87}Cs_{0.13}PbBr_3$)/red ($CsPbI_3$) [307,311], and more than 26 % for blue ($CsPb(Br/Cl)_3$) (Fig. 21b) [312], comparable to state-of-the-art organic and traditional Cd-based QLEDs.

Recently, significant efforts have been directed toward achieving active-matrix Pe-QLED displays through advanced processing techniques (Fig. 21c). Ye group integrated Pe-QLEDs with specifically designed thin-film transistor (TFT) circuits, demonstrating state-of-the-art solution-processed microsecond-response and efficient active-matrix perovskite displays with a resolution of 90 pixels per inch (ppi). The displays feature uniform emission across each pixel, allowing for independently controllable pixel output [311,334]. Additionally, Zhang *et al.* developed a nondestructive, ligand-assisted direct photolithography approach for quantum dots using rationally designed cross-linkers, achieving high-resolution (~4000 ppi) perovskite quantum dots patterns [335]. Prototype LED with these patterned layers demonstrated high performance for perovskite electroluminescent devices, with a maximum luminance of over 60,000 cd m^{-2} and a peak EQE of 16 %.

2. Current and future challenges

Despite the rapid advancement of Pe-QLED technology, several critical challenges remain to be addressed. Here, we primarily focus on two major issues crucial for their further development to commercialization: device stability and color integration.

Device stability. Operational stability remains a paramount challenge for Pe-QLEDs. State-of-the-art blue, green, and red Pe-QLEDs show a lifetime of 59 h (T_{50}, defined as the time for the brightness to decrease to 50 % of the initial value) [336], 31,808 h (T_{50}) [307], and 780 h (T_{90}, defined as the time for the brightness to decrease to 90 % of the initial value) [309] at 100 cd m^{-2}, which is far beyond commercial standards. The instability in device operation is mainly due to several factors: the intrinsic material instability of halide perovskites, the impact of charge injection/transport interlayers, and device instability caused by external factors such as applied bias, sustained stress, and thermal effects. Addressing these factors requires an integrated approach involving materials science, interface engineering, and optical design to enhance device stability.

Ion migration is considered a significant factor affecting the operational stability of the devices. Surface defects usually introduce ionic mobility channels, with vacancy and interstitial defects facilitating halide migration by acting as shuttles for halide hopping. Besides, ion migration is strongly field-dependent within the device. Under an electric field, ions tend to accumulate at the LED interfaces and defect sites within the emissive layer, degrading material interfaces, affecting charge injection and transport, and further compromising device stability [337,338].

Color integration. Patterning full-color photo-excited quantum dot films has been achieved through techniques such as photolithography [339], inkjet printing [340,341], nanoimprinting and transfer printing [342], and laser direct writing [343] (Fig. 22). However, most studies on Pe-QLEDs concentrate on prototype devices featuring only a single emission pixel. Integrating these patterned quantum dot films into full-color high-resolution Pe-QLED devices faces significant hurdles, as existing patterning approaches struggle to achieve patterned full-color quantum dot films with superior integrity, and excellent optoelectronic performance.

The ionic nature of perovskite quantum dots leads to rapid ion exchange upon contact with different perovskite materials, thereby altering their emission color purity. Additionally, the significant differences in the energy band structures of red, green, and blue (RGB) quantum dots complicate the design of a universal device structure, leading to energy level mismatches that adversely affect charge injection and transport. Furthermore, the varying lifetimes of different colored quantum dots, especially the relatively short lifetime of blue quantum

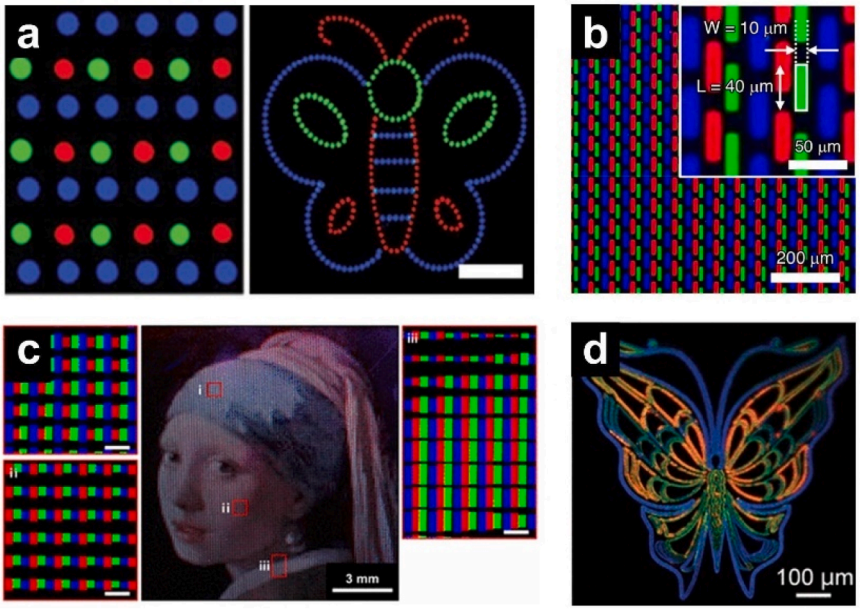

Fig. 22. **a,** Typical PL images of the electrohydrodynamic printed microscale line arrays of RGB under 365 nm UV excitation. Multicolor pattern of a butterfly using three-color perovskite. Scale bar: 200 μm [340]. **b,** Full-colored micro pixelated image of respective Perovskites from consecutive ligand-assisted direct photolithography processes [339]. **c,** PL images of transfer-printed Perovskite RGB pixelated patterns displaying the Girl with a Pearl Earring painting by J. Vermeer. Insets (i) to (iii) are magnified fluorescent images showing scaled RGB subpixels to express the full-color image. Scale bars, 100 μm [342]. **d,** Typical PL images of the multicolor patterns produced with $CsPb(Cl_{1-x-y}Br_xI_y)_3$ NCs in the Cl^--Br^--I^- codoped glass. The colorful patterns were produced by adjusting the parameters during writing [343].

dots, would cause color shifts during operation, leading to inconsistent color output. These issues all need to be addressed to achieve successful integration of RGB-based Pe-QLED.

3. Advances to address these challenges

Over the years, various approaches have been explored to improve device stability, and researchers have dedicated significant efforts to achieving active matrix full-color Pe-QLEDs displays.

Improving device stability. Given the above factors contributing to the instability of Pe-QLEDs, several advanced strategies are commonly employed to enhance their lifetimes. These strategies include passivating the surfaces and interfaces of the quantum dot emissive layer to mitigate defects and ion migration, doping transport layer materials to optimize the device architecture, and promoting balanced carrier injection to ensure efficient and stable device performance.

Surface modification through ligand engineering is prospective to reduce defects, and haloid acid is demonstrated to effectively drive nanosurface reconstruction of quantum dots [311]. The synergistic dual-ligand approach is considered to facilitate long-range-order quantum dot films by altering the size distribution and arrangement of quantum dots in films, enabling ultra-long operational stability for red Pe-QLED [309]. Besides, combined with in-situ treatment during deposition of quantum dot film, pseudo halogen anions, e.g., thiocyanate (SCN^-), tetrafluoroborate (BF_4^-), and hexafluorophosphate (PF_6^-) can further fill the halide vacancies due to their similar ionic radius to halide ions, compensating for inevitable ligand loss during solvent evaporation [334].

The energy barriers between multiple interfaces and carrier mobility of the transporting layer influence carrier injection in Pe-QLEDs. Charge transfers between quantum dots and contiguous electron/hole transporting layers may also induce luminescence quenching of quantum dot films. Mixing electron-transporting materials or employing multi-electron-transporting layers can effectively modulate electron injection. Additionally, inorganic transport materials offer a promising alternative for achieving rapid and balanced carrier injection.

Full color active-matrix Pe-QLEDs. The goal of commercialization is to realize high-resolution arrays of RGB pixels for highly efficient and quick response active matrix Pe-QLEDs. This necessitates the development of full-color display arrays with TFTs, enabling independent control of RGB pixels. Researchers have verified the feasibility of integrating Pe-QLEDs with TFT circuits using solution processes. To achieve patterned RGB perovskite quantum dot films, a direct photolithography process utilizing surface ligand photo-crosslinking could be a promising approach [335]. This method preserves the optical properties of the quantum dots and maintains efficient carrier transport performance. The crucial issue in such a process is to ensure the color purity of each RGB pixel by inhibiting halogen ion exchange. As the synthesis of quantum dots is separate from the patterning process, various surface modifications and functionalizations of quantum dots can be applied beforehand. Incorporating a thin barrier layer between patterned films of different colors, while maintaining the excellent electrical performance of the emitting layers, may also help suppress ion exchange.

4. Concluding remarks

While Pe-QLEDs show immense promise for future display applications, overcoming stability and color integration challenges is essential for their commercialization. Continued advancements in quantum dot surface passivation, transport layer doping, and innovative patterning techniques are vital. Developing strategies for inhibiting ion migration is pivotal in advancing active matrix Pe-QLED displays, with ongoing improvements aimed at achieving full-color display, enhancing resolution, uniformity, and operational lifetime. The future of Pe-QLED technology hinges on overcoming these challenges to achieve stable, high-performance devices suitable for commercial applications. Collaboration between material science, engineering, and device physics is essential to address these complex issues and realize the practical active-matrix Pe-QLED display technology.

Acknowledgments

This work was financially supported by the Fundamental Research Funds for the Central Universities (K20240042, X.L. Dai).

IX. Towards metal halide perovskite laser diodes

Jia Zhang[1] and Feng Gao[2]*

[1]The state key laboratory of photovoltaic science and technology, Shanghai frontiers science research base of intelligent optoelectronics and perception, Institute of optoelectronics, Fudan University, Shanghai 200438, China.

[2]Department of physics, chemistry and biology (IFM), Linköping University, Linköping, 58183, Sweden

E-mail address: feng.gao@liu.se

1. Status of the field

Laser diodes (LDs), or named the electrically pumped lasers, are a series of semiconductor devices similar to the light-emitting diodes (LEDs), where light is generated through electrical injection. Different from LEDs where the noncoherent light sources are generated through spontaneous emission, LDs utilize the stimulated emission to emit highly coherent laser light sources [344]. As a result, the high-quality light sources from LDs enable broader applications than LEDs, including fiber-optic communications [345,346], barcode readers [347], laser pointers [348], CD/DVD/Blu-ray disc reading/recording [349], laser printing [350], and laser scanning [351]. By integrating these LDs into thin-film matrix, more advanced applications such as face recognition and optical chips appear nowadays [352,353]. However, current thin film LDs are fabricated with several inorganic semiconductors, which requires high-temperature epitaxy [354]. It hinders the direct deposition of LDs on field effect transistors for high-density-pixel tuning. Thus, the fabrication cost increases exponentially with increased LD pixel density, which suppresses the further advancement of thin film LDs. It is urgent to develop new materials candidates that are low-temperature processable for the next-generation LDs.

With decades' efforts to explore the next-generation LDs, two categories of materials appear to be promising: organics [355]. and colloidal quantum dots (QDs) [356]. Both materials can be processed with the easy solution fabricating method, which successfully demonstrates excellent light emitting properties as well as superior optically pumped lasing actions. However, the real LDs based on these materials have not been realized yet. The possible limitations might be the serious Auger recombination that competes with the lasing actions and serious degradation at high current densities due to poor conductivity nature of the materials.

2. Metal halide perovskite as the candidate of next-generation laser diodes

There are three basic requirements for a successful operation of an LD: good gain medium, intense current injection, and feedback cavity. Interestingly, the metal halide perovskites seem to meet all these requirements according to their excellent optoelectronic properties and low-cost processing methods. Specifically, the high gain coefficient and ultra-low lasing thresholds are observed in metal halide perovskites [357,358], which ensures the perovskites as the good gain medium. The high carrier mobilities and crystalline nature allow for the effective operation of perovskite devices under high electrical injections [359–362]. The relatively soft nature and low-temperature processing provide great convenience for the fabricating perovskite cavities [363–365].

As shown in Fig. 23a, the first demonstration of the perovskite lasing action was dating back to 1998, through optical excitation on 2D perovskite $(C_6H_{13}NH_3)_2PI_4$ at low temperature (16 K) [366]. Since the low-temperature operation prohibits various detrimental pathways against lasing actions, this observation has not drawn much attention for more than 20 years. In 2014, Xing et al reported the room-temperature amplified spontaneous emission (ASE) phenomenon in different 3D perovskites pumped by femtosecond lasers for the first time (Fig. 23b) [367]. This observation, demonstrating the promise of perovskite-based lasers, triggered booming explorations of various optically pumped metal halide perovskite lasers [368]. These efforts, mainly using the

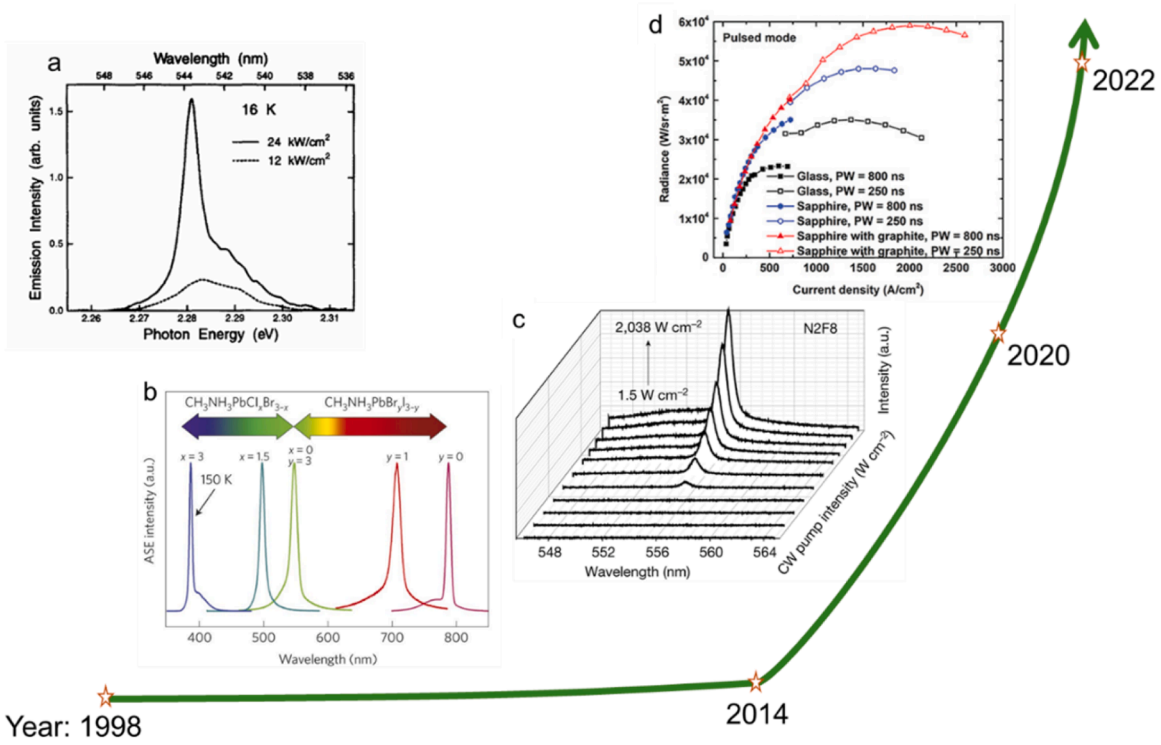

Fig. 23. Development of metal halide perovskite laser diodes: (a) first demonstration of 2D perovskite $(C_6H_{13}NH_3)_2PI_4$ lasing action at 16 K. The solid and dashed lines show the spectra under the excitation of 24 kW/cm^2 and 12 kW/cm^2, respectively [366]. (b) First demonstration of room-temperature wide wavelength tunability of ASE wavelengths from low-temperature solution-processed organic–inorganic halide perovskite films fabricated by mixing the precursor solutions [367]. (c) First demonstration of perovskite laser under CW excitation [369]. (d) Demonstration of perovskite devices showing intense current injection by the radiance–current density curves of perovskite LEDs on glass or sapphire substrates, with or without a graphite heat spreader and copper heat sink, all driven in pulsed mode [361].

femtosecond lasers as pump sources, prove that metal halide perovskites are excellent gain medium. Moreover, various feedback cavities have been demonstrated, which led to high-performance optically pumped lasers based on metal halide perovskites. Owing to the small ON time/OFF time ratio for the femtosecond lasers, the lasing death issue, another challenge towards LD operation has not been explored yet. In 2020, Qin et al addressed the lasing death issue through the triplet management strategy, resulting in the first optically pumped perovskite laser with continuous wave (CW) excitation at room temperature (Fig. 23c) [369]. This milestone highlights the potential for the perovskite gain medium as the LD application. Simultaneously, perovskite-based LEDs showed ultrahigh injection current densities, with the values exceeding 1 kA/cm^2 (Fig. 23d) [359,361]. These high values indicate that the intense current injection can be fulfilled in metal halide perovskites based electrical devices. Up till now, the three basic requirements for realizing LDs, good gain medium, intense current injection, and feedback cavity, have been fulfilled individually. The next step is to integrate these three conditions into one working device, to realize the goal of perovskite LDs.

3. Challenges and opportunities towards perovskite laser diodes

The integration of perovskite LDs is challenging from several aspects: 1. The loss mechanism against perovskite lasing action; 2. The efficiency roll-off in perovskite LEDs; 3. The compatibility of cavity structures with perovskite devices.

Loss mechanism against lasing action: Although various optical measurements have verified that the threshold carrier density of the perovskites can be very low, in some cases even as low as in the range of 10^{17} cm^{-3} [357]. the loss mechanism in the electrical case is seldom explored. Our previous work pointed out that the hot carriers induced Auger recombination is one of the loss mechanisms to the perovskite lasing action [370]. It increases the lasing threshold significantly, which might be the one of the main origins for the failure of perovskite LDs. For the real electrical injection case, similar loss mechanisms should be addressed. Here, more efforts are suggested in the research directions related to figuring out the loss mechanisms in the operating electrical devices rather than isolated perovskite thin films. For example, the possible effects of the intense electrical injection or strong electric field inside the device on the perovskite gain property remains unknown.

Efficiency roll-off in perovskite LEDs: the theoretical threshold current densities for the operation of perovskite LDs are in the range of kA/cm^2 or even below if the external quantum efficiency (EQE) of the device is considerably high [358]. However, most perovskite LEDs show high EQEs only in the range below 100 mA/cm^2, suggesting a big derivation towards LDs [371]. According to the free electron hole radiative recombination nature (similar to the one in inorganic LDs), the perovskite LEDs are supposed to work as efficiently as the inorganic LDs under intense electrical injection. However, serious EQE roll-off always appears in perovskite LEDs, hindering the development of perovskite LDs. Although intense electrical injection has been demonstrated in perovskite LEDs, the roll-off issue is seldom explored, or at least not fully addressed. Here, several possible factors might be the origin, such as the ion migration, imbalanced electron-hole injection and device degradation.

Compatibility of cavity structures with perovskite devices: Integration of the electrical device into a rationally designed cavity is the final step towards perovskite LDs, which requires extra efforts to ensure the maintenance of the perovskite gain property and intense electrical injection simultaneously. This strict requirement increases the risk additionally. There are two promising cavity structures for perovskite LDs: the distributed Bragg reflector (DBR) cavity [372] and the distributed feedback (DFB) cavity [373]. For the former one, two reflective mirrors are introduced to sandwich the gain medium, where the preferred laser output mode is tuned by the distance between these two mirrors. The integration of the DBR cavity into the perovskite LDs seems to be

independent from the perovskite electrical devices. However, such structural integration faces at least two challenges: 1. the high-quality DBR mirrors require ultra flat surfaces, which are not so compatible with the rough perovskite devices that are usually fabricated through combined solution processing for perovskite layers and thermal depositing for electrodes. 2. The DBR mirrors usually rely on long-time high temperature thermal deposition, which can easily damage the perovskite devices via penetration or thermal heating. For the latter one, the whole gain medium is embedded in a distributed reflector structure, where the one-dimensional grating structure is widely used. The fabrication of the DFB cavity structure is simpler than that of the DBR cavity. However, the electrical injection might be affected by the possible shunt current through the corners of the gratings owing to the unevenness.

4. Concluding remarks

The development of the next generation thin-film LDs with low temperature processing method and low cost is urgent to further advance the current technologies. Metal halide perovskites appear to be one of the promising candidates, which have shown excellent potential for good gain medium, intense injection and feedback cavities individually. The next step is to integrate these three factors into one successful LD. For a practical roadmap, it is suggested to first realize the electrically pumped amplified spontaneous emission (ASE) in the perovskite devices, i.e. the electrically pumped lasing action without cavity structure. The focus will be on unraveling the loss mechanism from the perspective of perovskite gain medium and addressing the EQE roll-off issue from the perspective of perovskite LEDs.

X. Perovskite photodetectors: from deep ultraviolet (DUV) to near infrared (NIR)

Zhengxun Lai[1], You Meng[1,2,3*], Johnny C. Ho[2,3,4*]

[1]Changsha Semiconductor Technology and Application Innovation Research Institute, College of Semiconductors (College of Integrated Circuits), Hunan University, Changsha 410082, China

[2]Department of Materials Science and Engineering, City University of Hong Kong, Kowloon 999077, Hong Kong SAR

[3]State Key Laboratory of Terahertz and Millimeter Waves, City University of Hong Kong, Kowloon 999077, Hong Kong SAR

[4]Institute for Materials Chemistry and Engineering, Kyushu University, Fukuoka 816-8580, Japan

E-mail address: youmeng2@cityu.edu.hk; johnnyho@cityu.edu.hk

1. Status of the field

The photodetector is one of the most promising device applications of halide perovskites, which plays a vital role in optical communication and imaging, covering the light wavelengths from DUV to NIR [374–377]. According to the device architectures, photodetectors can be categorized into three types, i.e., photodiodes, photoconductors, and phototransistors (Fig. 24). Like photovoltaic devices, photodiodes usually have a vertical configuration with p-n, p-i-n structures, or a Schottky junction, exhibiting low dark current, large detectivity, and fast response speed but low responsivity, and EQE. Photoconductors have the simplest metal-semiconductor-metal (MSM) structure with large responsivity and EQE but relatively slow response speed and small detectivity because of the photoconductive gain mechanism. Phototransistors usually have a three-terminal device structure analog to the field-effect transistors (FETs). Thus, the charge concentration in phototransistors can be tailored by the gate voltage, which can reduce the dark current or enhance the light current.

The DUV photodetectors, especially the solar blind DUV photodetectors, are technologically essential in civil and military applications encompassing missile warning systems, shipboard communication, medical imaging, etc [379,380]. For 3D halide perovskites ABX_3, they should not be ideal choices since their bandgaps are primarily located in the visible light range. However, 3D halide perovskites can perform well in DUV detection when a down-conversion layer is used [381]. In addition, ion doping was also used to improve the performance of 3D halide perovskites-based UV detectors. For example, Ce^{3+} can not only improve the UV absorption and stability of $CsPbCl_3$ but also reduce the perovskite's defects, which contributes to the low dark current and high detection rate of $CsPbCl_3$:Ce^{3+} based UV detector [382]. When it comes to low dimensional halide perovskites, i.e., 2D, 1D, and 0D halide perovskites, their bandgaps can be broadened and extended to the DUV region, which can be applied to the DUV detection directly [383–386].

Visible light photodetectors are predominantly utilized in daily life. Owing to the broad absorption of halide perovskites in the visible region, almost all kinds of halide perovskites, including 3D, 2D, 1D, and 0D, can be applied to visible light detectors. Because of the strong visible light absorption of the halide perovskites, the visible light detectors show much higher performance than the DUV and NIR ones. Since the visible light detectors have thriving development, multifunctional detectors have also been explored, including self-powered detection, polarized light detection, angle-sensing detection, etc [387–390].

NIR detectors have garnered extensive usage in health diagnosis, monitoring systems, space communications, etc [391–395]. However, as we know, the bandgaps of 0D, 1D, 2D, or even the Pb-based 3D halide perovskites can hardly reach the NIR region. To achieve NIR detectors in these halide perovskites, methods like constructing heterostructures and utilizing surface trap states have been proposed [396,397]. Besides, Sn-based 3D halide perovskites like $CsSnI_3$ and $MASnI_3$ can be used in NIR detection owing to their narrow bandgaps of around 1.4 eV. Nevertheless, the Sn^{2+} can easily be oxidized to Sn^{4+}, leading to dramatic instability of the halide perovskites, impeding its widespread application [169,398,399].

Unlike solar cells, the performance of the halide perovskite-based photodetectors can be characterized by a series of performance parameters; among them, responsivity, detectivity, and response times are paramount. The responsivity R can be defined as $R = I_p/\Phi S$, where I_p is the photocurrent, Φ is the light intensity, and S is the active area of the photodetector. The detectivity is analytically described as $D^* = RS^{1/2}/(2eI_d)^{1/2}$, where e is the electronic charge, and I_d is the dark current of the photodetector. The response speed can be acquired from photoresponse's rise and decay times. After the tremendous development in the past decade, the merits of the halide perovskite-based photodetectors have been improved to more than satisfactory values in numerous reports (Fig. 25) [385,396,400–413]. However, only high-performance parameters are far from enough to achieve commercial photodetectors.

2: Current and future challenges

Despite significant progress in halide perovskite-based photodetectors, challenges still crop up. Defects in the perovskites can enlarge the dark current of the detectors and accordingly cause a low detectivity, which should be kept to a minimum in most electronic devices. Besides, since perovskites will degrade rapidly when exposed to harsh conditions

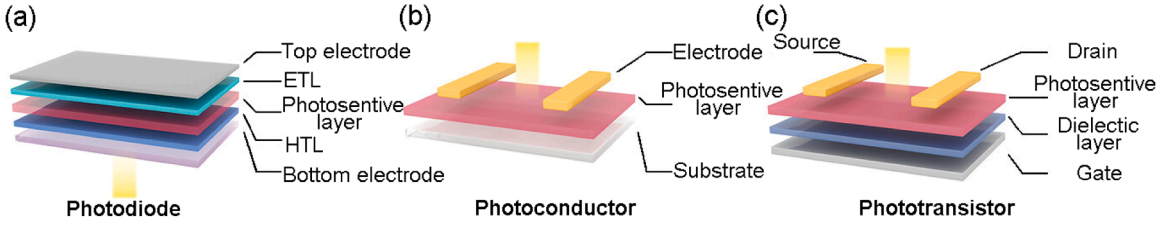

Fig. 24. Schematic illustrations of the device structures: **a,** photodiodes, **b,** photoconductors, and **c,** phototransistors [378]. Copyright 2023, Wiley-VCH GmbH.

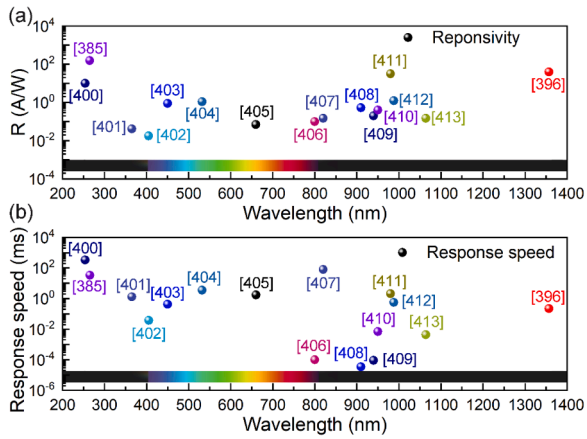

Fig. 25. Performance comparison of halide perovskite-based photodetectors from DUV to NIR.

(e.g., high photon energy, high temperature, and high humidity), achieving long-term stability of the detector is also challenging, which is one of the main barriers to its commercialization. For example, UV irradiation can cause ion migration and compositional degradation in perovskite films [414,415]. Moreover, although the Sn-based perovskites can be used to achieve NIR detectors, the poor stability of the Sn-based perovskites also greatly hinders their application [416,417].

Additionally, the perovskite-based flexible detectors and integrated perovskite detectors also need more attention, which can contribute to developing wearable devices and their imaging and neural network functions. Last but not least, although there are several performance parameters to evaluate the photodetectors, it is also not reliable to directly compare two detectors in different works by them. Unlike the PCE of solar cells, the traditional performance evaluation system of photodetectors can cause wide divergences when they are acquired by different measurement or calculation methods.

3: Advances to meet these challenges

Several effective methods have been proposed to reduce the defects in perovskite films, including antisolvent assistant spin-coating, solvent annealing, hot casting, etc [418–420]. To minimize defects in the samples, single crystals are the better choice for photodetectors than polycrystals. Different methods to synthesize halide perovskite single crystals have also been proposed [421–424]. Given that the crystal growth process varies, insights into them and the application of the single crystals to the photodetectors still need more effort.

Intensive efforts have been made to address the stability issue of halide perovskites. For instance, different methods have also been proposed to enhance the UV irradiation stability of the halide perovskites. For example, Fu et al. achieved a stable tolerance factor of 0.903 for $Cs_{0.7}DMA_{0.3}PbI_3$ (DMA = dimethylammonium cation) by partially replacing A site Cs^+ in $CsPbI_3$ nanocrystals with one kind of large cation of DMA, which improved the stability of the perovskites under the irradiation of UV light [425]. To stabilize the Sn-based halide perovskites, He et al. used one multi-functional additive 4-amino-2,3,5,6-tetrafluorobenzoic acid to passivate Sn-Pb perovskite NIR photodetector, acquiring a high-performance, stable device, derived from the reduced defects and enhanced hydrophobicity [426]. Zheng et al. introduced benzylamine boron trifluoride to the $FASnI_3$ precursor solution, inhibiting the oxidation of Sn^{2+} and improving the performance of the $FASnI_3$-based photodetector [427].

The application scope of the perovskite-based photodetectors has also been explored and expanded to demonstrate their versatility. Two aspects have been studied to achieve flexible photodetectors: one is reinforcing the halide perovskites' flexibility, and the other is designing appropriate device structures. For example, Lai et al. improved the flexibility of the quasi-2D halide perovskites by introducing diamine cation of ethylenediammonium to the films [428]. Sun et al. fabricated halide perovskite-based photodetector arrays with high flexibility by a novel PVD-spin-coating combined with a photolithographic process [429]. Some efforts have been made to generate different methods and ideas for the integrated perovskite photodetector and the corresponding multi-functional devices [430]. Wang et al. fabricated photodetector arrays based on quasi-2D $(BA)_2FAPb_2I_7$ perovskites through a bottom-up photolithography method achieving high-resolution imaging [431]. Huang et al. designed an n-perovskite/p-spiro-MeOTAD heterojunction diode, enabling photovoltaic, photodetection, and photosynaptic functions in a single device [432].

Some measuring protocols have also been proposed to characterize figures of merit of low-dimension materials-based photodetectors accurately. Huang et al. reported that the more accurate noise equivalent power and detectivity of the photodetectors can be acquired by separate measurements of the frequency and illumination intensity-related noise spectral density and responsivity [433]. Hu et al. pointed out that the detectivity of 2D materials-based photodetectors is consistently overestimated because of the improper calculation of noise and misestimation of device active area, where incident light power density and inconsistent bandwidth of measured responsivity and noise can also lead to the overestimation [434].

4: Concluding remarks

In conclusion, we briefly summarize the halide perovskite photodetectors within the detection range from DUV to NIR. Beyond solar cell study, the rapid development of perovskite-based photodetectors suggests their promise in high-sensitive photodetecting and high-resolution imaging applications. However, there are still chronic challenges: the stability issue, the unsatisfactory evaluation parameters of the performance, and the low-defects single crystal detectors, etc. All these challenges need our attention to realize practical applications of high-performance halide perovskite-based photodetectors.

XI. Low-dimensional halide perovskite scintillators

Wen Li, Yuntao Wu*

Shanghai Institute of Ceramics, Chinese Academy of Science, 201899, China

E-mail address: ytwu@mail.sic.ac.cn

1. Status of the area

Inorganic scintillators as indirect detection materials play an important role in the applications of medical imaging, non-destructive inspection, and homeland security. Classical inorganic scintillators for X-ray detection are CsI:Tl and Gd_2O_2S:Tb crystalline materials. In the recent years, metal halide perovskites have become promising scintillation materials for high-performance X-ray detection due to their advantages of efficient radioluminescence and ease of preparation [435–437]. According to the connection mode of metal halide polyhedral units at the molecular structure level, they can be categorized into three-dimensional (3D), two-dimensional (2D), one-dimensional (1D) and zero-dimensional (0D). 3D perovskite scintillators have well-known issues, such as thermal quenching at room temperature and severe self-absorption effect. For example, the light yield of $CH_3NH_3PbBr_3$ single crystal is 116,000±23,000 photons/MeV at 8 K, but it significantly drops to about 1,000 photons/MeV at room temperature [438]. In principle, by decreasing the structural dimension and increasing the interval spacing between the metal halide polyhedra as luminescent units, higher luminescence efficiency is expected due to stronger confinement effect. Up to now, many of high-performance low-dimensional lead-based, copper(I)-based, manganese(II)-based and other metal halide perovskites as X-ray scintillators are developed (Fig. 25).

Lead-based perovskites. Lead-based perovskites usually exhibit free-exciton emission characteristics. Compared with 3D lead-based perovskite scintillators, 2D lead-based perovskites due to the feature of quantum-well structure, exhibit stronger quantum confinement and higher exciton binding energy, which can enhance radioluminescence and thermal stability at room temperature. For example, $(PEA)_2PbBr_4$

has a light yield of 14,000 photons/MeV at room temperature, and achieves a high spatial resolution of > 11 lp/mm for X-ray imaging [439, 440]. The scintillation performance of 2D lead-based perovskites can be further optimized through codoping strategies (such as Li^+, Ba^{2+} and Sr^{2+}), self-wavelength shifting and dielectric engineering [441–445]. Among them, the light yield of Li-doped $(PEA)_2PbBr_4$ was improved by nearly 80 % along with the good α/γ discrimination capability [441]. Tang et al. applied $(PEA)_2PbBr_4$ scintillators with self-wavelength shifting to demonstrate imaging reconstruction in positron emission tomography (PET) [444]. There is limited research on the use of 1D lead-based perovskites for X-ray scintillators. 0D all-inorganic lead--based perovskites have a large bandgap and strong radioluminescence. As for the Cs_4PbBr_6 as the representative 0D halide, a large number of $CsPbBr_3$ phases inevitably appear during its preparation process [446, 447]. The $CsPbBr_3$ NCs@Cs_4PbBr_6 scintillation, prepared by adding $CsPbBr_3$ nanocrystals emitter into the solid-state Cs_4PbBr_6 host, has been proven the high resolution X-ray imaging performance [448,449].

Copper(I)-based perovskites. The luminescence of copper-based halides usually stems from self-trapped excitons, which possess advantages such as high photoluminescence quantum yield (PLQY), large Stokes shift, negligible self-absorption, and strong radioluminescence. The 0D all-inorganic copper-based scintillators represented by $Cs_3Cu_2I_5$ single crystal have attracted great attention in the field of radiation detection. $Cs_3Cu_2I_5$ single crystal exhibits a light yield of approximately 32,000 photons/MeV and a high energy resolution of 3.4 % at 662 keV [450]. It is proven that the scintillation efficiency of $Cs_3Cu_2I_5$ single crystals can be significantly enhanced by doping strategies, such as Tl^+, In^+ and Mn^{2+} [451–453]. In particular, Tl-doped $Cs_3Cu_2I_5$ single crystal has a steady-state scintillation efficiency of 150,000 photons/MeV under X-ray irradiation, and a light yield of 87,000 photons/MeV under ^{137}Cs gamma-ray irradiation [451]. The 1D halides have the similar exciton confinement effect with that of 0D halides. In addition, due to the preferential growth orientation, 1D halides are apt to grown into oriented crystalline film with needle-like structure. The nature feature of 1D halides can secure the high-resolution imaging capability. For instance, thanks to the negligible dangling bonds at grain boundaries and preferential growth orientation along <001> direction, 1D $Cs_5Cu_3Cl_6I_2$ scintillation film has a high light yield of 67,000 photons/MeV, a superior X-ray imaging spatial resolution of 27.1 lp/mm, and a negligible afterglow of 0.1 % at 10 ms [454]. In addition to all-inorganic copper-based halide scintillators, numerous organic-inorganic hybrid copper-based scintillators have also been discovered due to the diversity of organic ligands. For example, 0D $(MTPP)_2Cu_4I_6$ has a high steady-state scintillation yield of 63,700 photons/MeV and a high spatial resolution of 18.49 lp/mm [455]. The 2D $(CISDM)_4$ $[Cu_4I_8]\cdot 2H_2O$ has a light yield of 41,000 photons/MeV and an ultra-high spatial resolution of 108 lp/mm [456].

Manganese(II)-based perovskites. Mn^{2+} is an efficient luminescence center. The emission characteristics of manganese-based perovskites strongly depend on the coordination environment around Mn ions. Due to crystal field effects, tetrahedrally and octahedrally coordinated Mn^{2+} show green and red emission respectively, and have photoluminescence (PL) lifetimes ranging from microseconds to milliseconds. The luminescence intensity of manganese-based perovskites is related to the distance between the emission centers of Mn-Mn. A longer Mn-Mn distance can effectively weaken the electronic interactions and non-radiative energy transfer between adjacent tetrahedral or octahedral units of manganese halides, thereby enhancing the radioluminescence intensity. Manganese-based perovskites with large steric hindrance of organic cations are prone to form 0D structures. Due to large spacing between polyhedra by organic cations, they exhibit high radioluminescence. For example, 0D $(C_{38}H_{34}P_2)MnBr_4$, as the first hybrid manganese-based scintillators, has a high light yield of 80,000 photons/MeV and a low detection limit of 72.8 nGy/s [457]. As $[MnX_6]^{4-}$ octahedral has a shared angle, edge, or face chain structure, 1D hybrid manganese-based perovskites greatly shorten the Mn-Mn distance, interfere with the d-d transition rules and transition energy, and easily lead to weaker luminescence than 0D manganese-based perovskites. In addition, recently manganese-based hybrid perovskites mostly have crystal-glass-ceramic transition characteristics [458,459]. Transparent ceramic or glass scintillation screens can be prepared by melt-quenched or cold sintering processes, providing an alternative option of preparing low-cost, large-size X-ray imaging screens.

Others. Other low-dimensional metal perovskite scintillators, including Sn^{2+}, Zn^{2+}, Sb^{3+}, Ag^+, Eu^{2+} and Ce^{3+}, etc., have their own characteristics, such as emission wavelength, light yield, decay time, and stability, providing more choices for the application of X-ray perovskite scintillation materials. For example, among a series of 0D materials, Cs_4EuBr_6 and Cs_4EuI_6 single crystal show a high light yields of 78,000±4,000 photons/MeV and 53,000±3,000 photons/MeV, respectively [460]. Cs_2ZnCl_4 and Cs_3ZnCl_5 crystals have ultra-fast scintillation decay times of 1.66 ns and 0.82 ns respectively [461], and $(PPN)_2SbCl_5$ has excellent environmental stability [462]. In 1D perovskites, Rb_2AgBr_3 exhibits a short decay time of 5.31 ns, a light yield of 25,600 photons/MeV, and ultra-fast dynamic imaging [463]. $Cs_3CeCl_6\cdot 3H_2O$ single crystal with efficient ultraviolet emission, has a light yield of 31, 900 photons/MeV, and is a promising substitute for narrowband ultraviolet photodetectors [464]. In addition, higher quality single crystals or scintillation screens for X-ray imaging can be prepared by finely controlling crystal growth, composition ratio, and other methods, further improving their scintillation performance and spatial resolution in X-ray imaging field (Fig. 26).

2. Current and future challenges

An overlook issue of exciton-exciton interaction and exciton-defect interaction under ionizing radiation. In principle, the light yield is inversely proportional to the band gap. Low-dimensional halide perovskites typically have a bandgap of 2.5-3.5 eV, and theoretically can reach a light yield ranging from 120,000 to 200,000 photons/MeV. However, currently, their practical light yield values are far below the theoretical ones. For example, the $Cs_3Cu_2I_5$ has a theoretical light yield of 150,000-180,000 photons/MeV, but measured light yield is about 32,000 photons/MeV [450]. In fact, the light yield of halide perovskites is associated with the scintillation process. When scintillator absorbs high-energy X-ray photons, electrons in the inner layer of the atom will be excited from the valence band (VB) to the conduction band (CB). A large number of electrons and holes will be transported separately in CB and VB after relaxation. Subsequently, electron-hole pairs will emit light through radiative recombination at the luminescent center. The photons emitted by the scintillator are then detected and converted into electrical signals by photodetectors (e.g. silicon photomultiplier, photomultiplier tubes, or charge-coupled devices), and finally imaging can be achieved through electrical signal processing and conversion. Low-dimensional halide perovskites often exhibit exciton emission, such as self-trapped exciton emission and defect-bound exciton emission. Halide perovskites with low-dimensional structures at the molecular level have looser and softer lattices, exciton relaxation effect was enhanced, resulting in a large Stokes shifts and a weak self-absorption. At the same time, the energy transfer between luminescent polyhedra is weakened, exciton migration is suppressed, thereby reducing the probability of exciton quenching, intrinsic defect capture, and non-radiative recombination caused by exciton-exciton interaction and exciton-defect interaction, resulting in higher luminescence efficiency of metal halides

The method for preparing a large-sized high resolution X-ray imaging screen. In X-ray imaging, reducing material scattering and diffuse reflection can more accurately transmit X-ray information to the detector to improve imaging resolution. Moreover, many imaging applications require large-sized scintillation materials to ensure that a sufficiently large area is covered in a single imaging process without the need for image stitching, thereby improving imaging efficiency and reducing image artifacts generated by stitching. However, in the preparation process of high-quality scintillation films, ceramics, and single

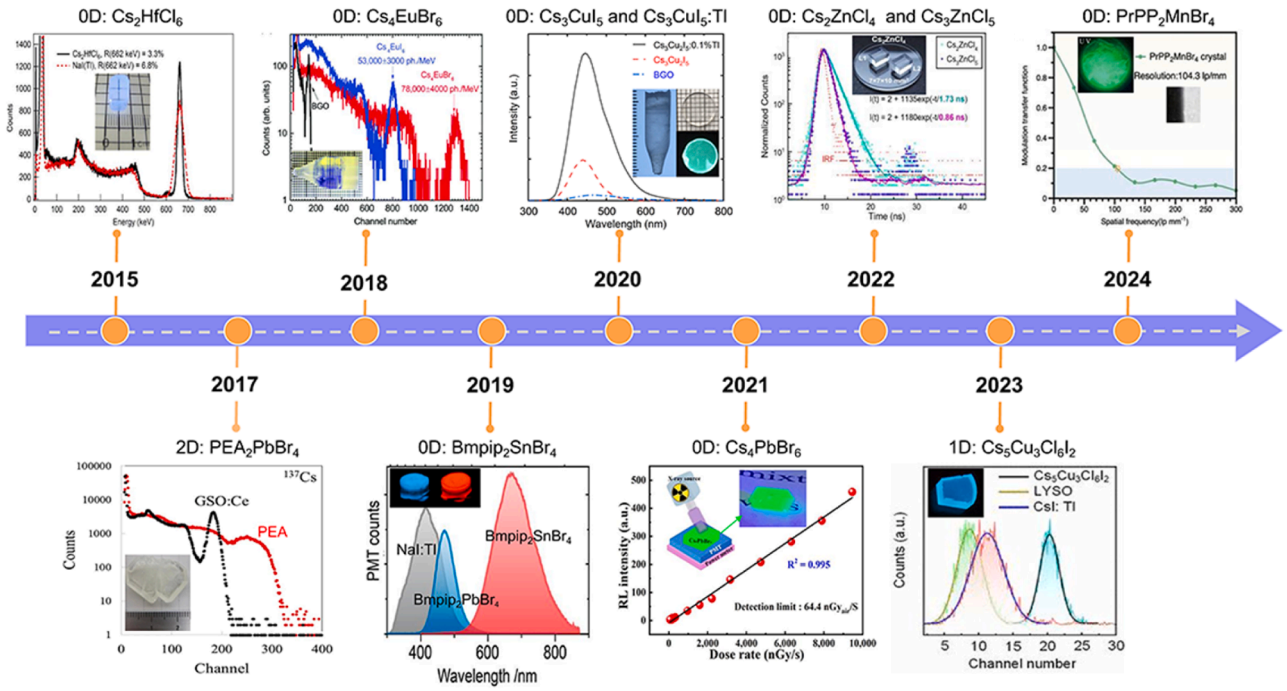

Fig. 26. Overview of recent R&D of low-dimensional metal perovskite scintillators [440,448,450,451,454,460,461,465–467].

crystals, it is difficult to simultaneously ensure that the materials meet high optical performance and large-area requirements [468,469]. At present, most materials used for X-ray imaging are composed of large-area thin films, ceramics, and glass. The gaps, defects, or grain boundaries present in these materials will inevitably lead to signal crosstalk and decrease detection efficiency. Single crystal scintillators with high optical transmittance can meet the requirements of low defect density, high scintillation performance and high-quality X-ray imaging. However, the growth of large-sized single crystals with high-quality requires more stringent conditions. Therefore, it is necessary to further improve and refine the preparation processes of thin film, ceramic, and single crystal scintillations to meet the requirements of large-area and high X-ray imaging resolution.

3. Advances to meet challenges

Strategies of enhancing scintillation yield of low-dimensional halide perovskites. In the past few years, some strategies have been proposed to improve the light yield of halide perovskites to meet the requirements of X-ray detection and imaging (Fig. 27).

(1) ***Manipulating exciton interaction.*** First, by reducing the structural dimension, the confinement effect of halide perovskites can be enhanced. Thus, higher luminescence efficiency is expected as the exciton binding energy is increased. For instance, under ^{137}Cs irradiation, 1D $CsCu_2I_3$ exhibits a light yield of 16,000±2,000 photons/MeV [470], while 0D $Cs_3Cu_2I_5$ shows a higher light yield of 29,000±580 photons/MeV as the dimension decreases [450]. Second, doping with appropriate ions can weaken the non-radiative recombination caused by interactions between excitons in low-dimensional halides, resulting in an increase of light yield. For example, by exciton-harvesting via Tl doping into $Cs_3Cu_2I_5$ lattice, the formation of Tl-bound excitons can efficiently suppress the exciton-exciton interactions, and then enhance the radiative recombination probability, achieving a superior light yield close to the theoretical value of 150,000 photons/MeV [451]. Third, through dielectric engineering, the difference in dielectric constant between the organic layer and the inorganic layer in 2D halide perovskites can used to enhance the Coulomb force between electron-hole pairs, avoiding exciton dissociation, increasing the radiative transition rate. For example, 2D BM_2PbBr_4 scintillator with high exciton binding energy designed and prepared by the dielectric engineering strategy, has a time resolution of 207 ± 2.2 ps, which is better than 250 ± 3.1 ps of LYSO which is the most widely used scintillator in PET [445].

(2) ***Constructing energy transfer channels.*** The intrinsic strain in 2D perovskite crystals has been proven to be a common phenomenon. It can be utilized as self-wavelength shift to reduce self-absorption effects without sacrificing radiation response speed [444]. Energy transfer can occur by introducing luminescent ions whose excited state energy levels match the emission spectra of the host halide perovskites, which can reduce the self-absorption of materials and improve the utilization rate of photons. For instance, adding manganese Mn(II) dopant to 2D DA_2PbBr_4 increases its PLQY from less than 8 % to 61 % [471], and 0D $Cs_3Cu_2I_5$:15 % Mn scintillator has increased light yield from 11, 900 photons/MeV to 67,000 photons/MeV compared to the undoped sample [472]. In addition, through embedded structure design, halide perovskite materials can be sandwiched between different functional metal halide materials. By optimizing the optical properties and energy level matching of each species of materials, self-absorption can be reduced. For example, the "emitter-in-matrix" structure has recently been proposed. Based on this structure, the $CsPbBr_3$@Cs_4PbBr_6 scintillation crystal is designed by taking advantage of the fact that the wide band gap Cs_4PbBr_6 is transparent to the green emission of $CsPbBr_3$ quantum dots to further decrease self-absorption [449].

Optimization of preparation processes for single crystal, thin film, and ceramic scintillators. In X-ray imaging, high spatial resolution requires the scintillation screen have a small pixel size and high resolution, which means that the scintillator/screen must be able to efficiently convert X-rays into visible light and effectively collect and transmit light signals within a small-sized pixel area.

(1) **Single crystal scintillators.** Single crystals with a highly ordered lattice structure and a low density of defect states can be prepared

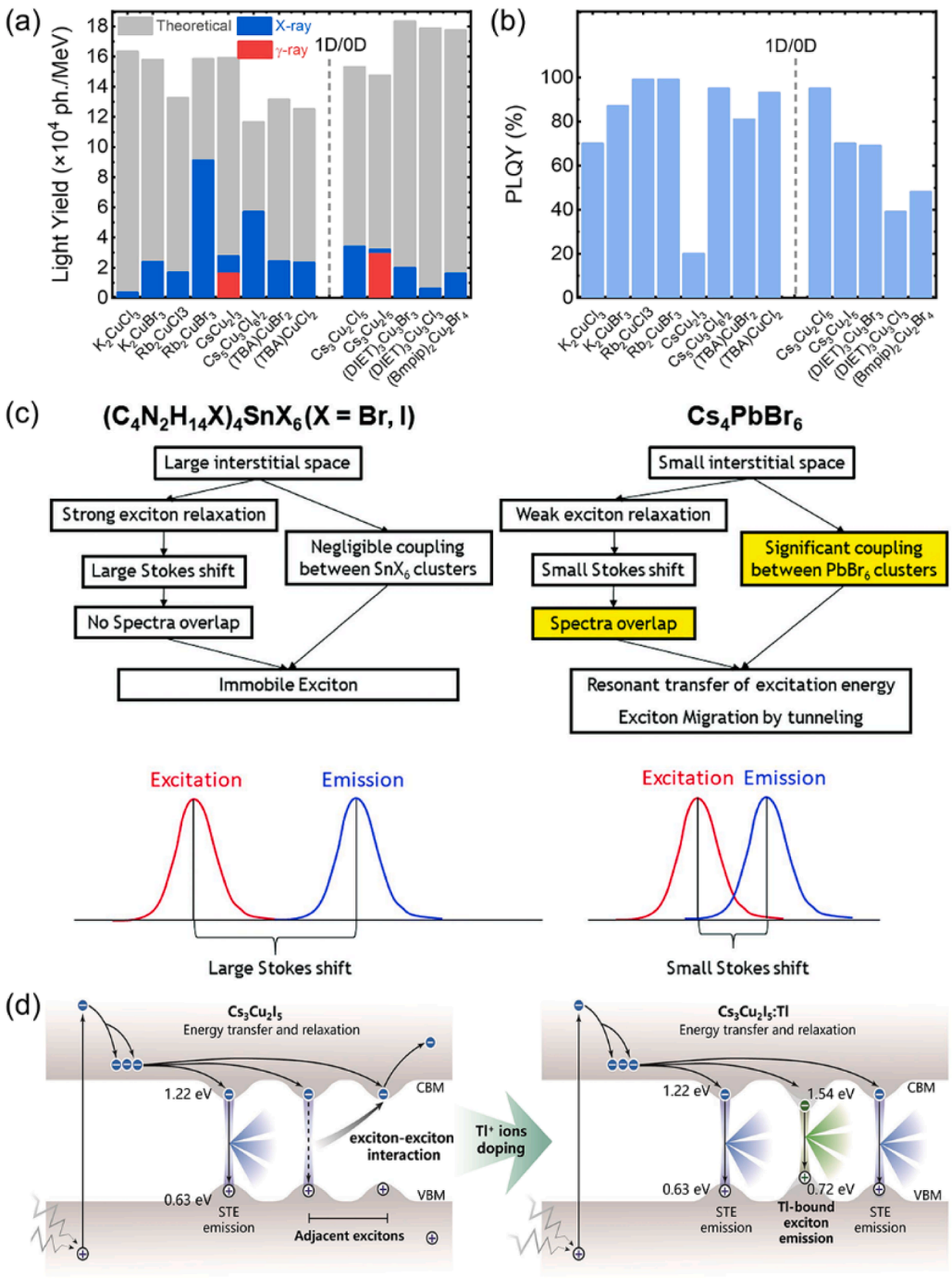

Fig. 27. (a) Light yields and (b) PLQYs of low-dimensional copper-based halide scintillators. (c) Illustration of the mechanisms that lead to the immobile excitons in $(C_4N_2H_{14}X)_4SnX_6$ (X = Br, I) and the mobile excitons in Cs_4PbBr_6. (d) Theoretical single-particle electronic energy levels and scintillation emission mechanisms in $Cs_3Cu_2I_5$ and $Cs_3Cu_2I_5$:Tl under ionizing radiation [473,474].

by solution method and melt method. For solution method, combining the spatially confined solution method with the traditional solution method [475] or adopting local heating solution evaporation method, low-dimensional halide perovskite single crystals with high transparency, adjustable thickness and large-area can be prepared (Fig. 28a). For example, 0D layered TEA_2MnI_4 single crystal with a size of 50 mm × 60 mm × 0.82 mm was grown by the local heating solvent evaporation method [476]. Different melt growth methods have been attempted for low-dimensional halides. Taking $Cs_3Cu_2I_5$ as an example, 1-inch diameter $Cs_3Cu_2I_5$ single crystals have been successfully prepared using the Bridgman method [477] and $Cs_3Cu_2I_5$:Tl crystals with sizes of Φ15 mm and Φ12 mm were successfully prepared using the Czochralski method and the Edge-Defined Film-Fed method [478].

(2) **Thin film scintillators.** The traditional physical blending method faces some problems such as powders agglomeration, uneven luminescence, severe light scattering, and poor transparency, greatly reducing the spatial resolution. In recent years, the columnar morphology advantage of 1D halide perovskite crystals has been utilized to design thin films with oriented structures. By using in-air sublimation method and nanoscale

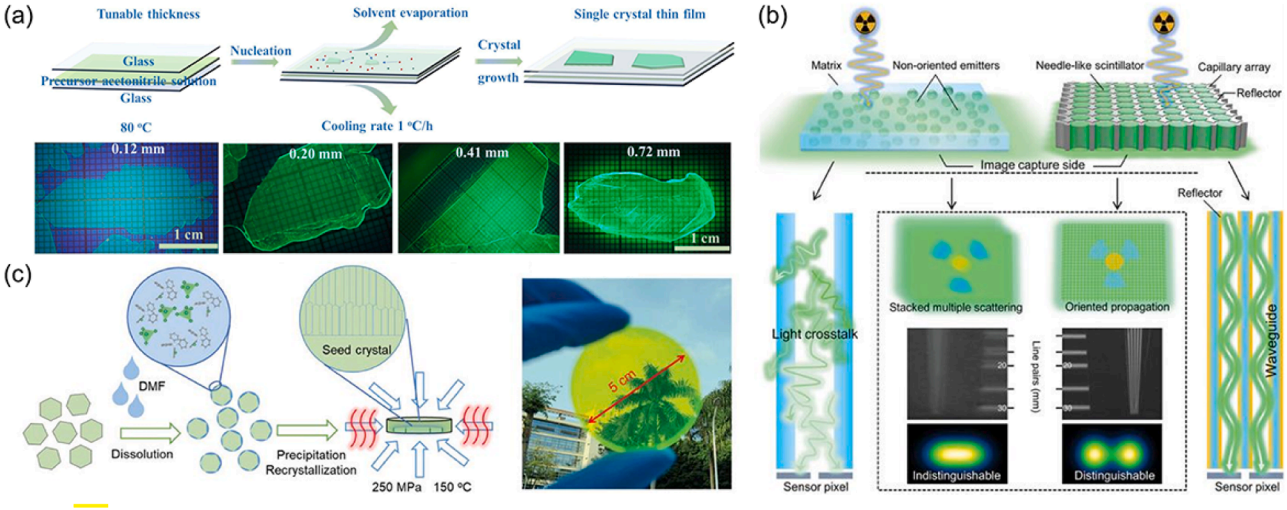

Fig. 28. (a) Scheme for growth of metal hybrid halide single crystal and the inch-size $(C_{25}H_{22}P)_2MnCl_4$ single crystal with a tunable thickness. (b) Light propagation mechanisms and results of conventional nonstructured scintillators and structured capillary needle-like array scintillators in X-ray imaging. (c) Fabrication process via the seed-crystal-induced cold sintering process and photograph of textured TPP_2MnBr_4 ceramic scintillator [475,480,481].

seed screening strategies, large-area $CsCu_2I_3$ [479] and $Cs_5Cu_3Cl_6I_2$ films with directional nano or micron rod structures have been successfully prepared. Among them, the $Cs_5Cu_3Cl_6I_2$ film realizes fast X-ray imaging with a resolution of 27 lp/mm and a frame rate of up to 33 fps [454]. In addition, scintillation thin films with pixelated arrays have been developed using waveguide structure engineering. By embedding high refractive index metal halides into low refractive index template matrice, the lateral diffusion of scintillation light in each pixel is limited, thereby improving the spatial resolution. Manganese halide needle-like array scintillator has been achieved a high spatial resolution of 60.8 lp/mm (Fig. 28b) [480]. When faced with diverse X-ray imaging requirements, large-area flexible scintillation screen have been prepared by combining nano particle sized perovskite scintillators with polymer matrices, it can not only reduce the optical crosstalk caused by Rayleigh scattering and improve imaging resolution, but also meet the imaging needs of non-planar objects.

(3) **Ceramic scintillators.** Traditional ceramics are non-transparent, which is not conducive to X-ray imaging applications. By using high-purity raw materials, selecting a material system with cubic symmetry structure, controlling sintering and other effective methods, it is possible to eliminate a large number of light scattering sources such as pores and anisotropic grain boundaries inside the ceramic, and achieve transparency of the ceramic. Recently, a seed crystal-induced cold sintering process was used to manufacture TPP_2MnBr_4 transparent ceramic scintillator with a diameter of 50 mm, high quality, directional light transmission and <001> orientation. It has a high light yield of about 78,000 ± 2,000 photons/MeV, an energy resolution of 17 %@662 keV, a low detection limit of 8.8 nGy/s, and a high spatial resolution of 15.7 lp/mm (Fig. 28c) [481]. In addition, various low-dimensional halide scintillators have shown the property of crystal-glass-ceramic phase transformation. Through further exploration of phase transformation engineering, it is expected to realize more large-area transparent ceramic scintillators with directional transmission based on halide perovskites.

4. Concluding remarks

In summary, low-dimensional halide perovskites have demonstrated great potential as X-ray scintillators. Abundance of low-dimensional lead-based, copper-based, and manganese-based halide perovskites with excellent scintillation performance have been successfully developed. However, due to the overlook of exciton-exciton interaction and exciton-defect interaction under ionizing radiation and the underdeveloped preparation methods for large-sized and high-resolution X-ray imaging screens, these issues limit the further performance improvement and the practical imaging applications. To address these challenges, the use of exciton modulation strategies and the construction of energy transfer channels have successfully enhanced the light yield of halide perovskites. Moreover, based on more advanced and sophisticated growth methods, high-quality and large-sized single crystal, thin film, and ceramic scintillators have been successfully utilized for high-resolution X-ray imaging applications

XII. Chiral perovskite circularly polarized light detection

Liping Du[1], Sai Bai[1], Huihui Zhu[2]*

[1]Institute of Fundamental and Frontier Sciences, University of Electronic Science and Technology of China, Chengdu 611731, China

[2]School of Physics, University of Electronic Science and Technology of China, Chengdu 611731, China

E-mail address: hhzhu@uestc.edu.cn

1. Status of the field

Circularly polarized light (CPL) with varying polarization state interacts with substances to reveal physical and chemical information, essential for applications in polarimetric imaging [482], LiDAR [483], secure communication [484], and magnetic recording [485]. Therefore, it is crucial to accurately detect the two different states of CPL, namely left-circularly polarized (L-CPL) and right-circularly polarized (R-CPL) light, and convert them into electrical signals. Due to the lack of intrinsic chirality in inorganic semiconductors such as Si or GaAs, conventional CPL-sensitive photodetectors typically require the use of a quarter-wave plate and/or linear polarizer, complicating miniaturization and integration. The use of polarization-sensitive materials could eliminate the need for bulky and rigid optical components, showing great promise for large-scale integration and flexible electronics.

In the early stages, chiral lanthanide complexes [486] and chiral organic molecules [487] were used for CPL detection. However, the relatively complex synthesis processes and high production costs of these materials, combined with the low carrier mobility of organic molecules resulting in low detection efficiency, have hindered their commercialization. Fortunately, the emerging chiral perovskites, which combine both handedness-sensitive optical absorption with efficient charge transport, are polarization-sensitive and can directly detect CPL, originating from their anisotropic crystal structure or morphology.

In chiral perovskites, the electronic structure consists of a two-level system with electrons in a doubly degenerate $J_e = ½$ state and holes in a $J_h = ½$ state (where J_e and J_h represent the angular momenta of electrons and holes, respectively) [488]. Upon illumination with CPL (σ^- for left-handed and σ^+ for right-handed), optical transitions occur with a change in the magnetic quantum number m_J of $\Delta m_J = +1$ for σ^- and $\Delta m_J = -1$ for σ^+, [489] which leads to a high degree of spin polarization. Thus, chiral perovskites with spin-orbit coupling exhibit selective responses to different spin-polarized states, enabling them to distinguish between the absorption of LCP and RCP, i.e., circular dichroism (CD). Therefore, chiral materials provide an opportunity to fabricate photodetectors for the direct detection of CPL.

Chiral perovskites can be formed by introducing chiral organic molecules [489] or by spontaneous resolution based on achiral building blocks [490], thereby achieving CPL sensitivity. Chiral perovskites with excellent CPL sensitivity have been applied in CPL detection, making exciting progress in this field. The timeline of developments in this area can be found in Fig. 29. The first chiral perovskite 1D (S-PEA)$PbBr_3$ crystals was reported in 2003, and the corresponding 2D (R-/S-MBA)$_2PbI_4$ single crystals in 2006 [491,492]. However, the chiroptical properties were not initially explored. It wasn't until 2017 that the chiroptical properties of chiral perovskites were investigated [493], and CPL detection based on chiral perovskites was first realized in 2019 [494]. Since then, CPL-sensitive detection using chiral perovskites has been widely reported [495–502].

Depending on the different device structures, CPL-sensitive photodetectors can be divided into photoconductor, photodiode and phototransistor, each serving a wide range of applications. A typical photoconductor structure includes a semiconductor layer contacted by two metal electrodes. Upon CPL illumination, electrical conductivity increases due to the generation of photo-induced carriers in the chiral perovskite active layer. In photodiode, excitons are generated in the chiral perovskite active layer under CPL illumination, and the excitons are separated into photogenerated carriers assisted by the built-in potential or an applied voltage. Furthermore, the internal E-field allows for the separation of photogenerated charges without external bias, giving rise to "self-powered" photodetectors. In phototransistors, chiral perovskites can either form the active channel or serve as CPL-sensitizer. The active layer generates different numbers of photogenerated carriers when irradiated with L-CPL or R-CPL. CPL detection phototransistors offer both the signal amplification and CPL detection capabilities.

For CPL photodetectors, there are several figures of merit used to evaluate the performance. Among them, the responsivity (R), specific detectivity (D^*) and anisotropy factor of responsivity (g_{res}) are important features. For some applications, spectral range and a high response speed are also required. (1) R quantifies the ability of a CPL detector to convert incident light into an electric current, which is given by $R = \frac{I_{light} - I_{dark}}{E_{light}}$, with E_{light} being the power of CPL. (2) D^* is calculated by $D^* = R\sqrt{A}/i_n$ (where R is responsivity, A is the effective area). (3) g_{res} is defined as $g_{res} = \frac{2(R_L - R_R)}{R_L + R_R}$ (where R_L and R_R represent the responsivities under illumination by LCP and RCP, respectively)

2. Current and future challenges

CPL photodetectors employing chiral perovskites are anticipated to achieve competitive performance in the realm of CPL detection. In 2019, photodetectors fabricated using (*R*-/*S*-α-PEA)PbI_3 achieved directed CPL detection (Figs. 30a-c), with a g_{res} value as high as 0.1 [495]. The responsivity can reach 797 mA W^{-1} (corresponding to a photoconductor gain of 253 %), which is nearly two orders of magnitude larger than the chiral molecule-based [487] and chiral plasmonic metamaterials-based [482] CPL photodetectors. The exceptional responsivity of (*R*-/*S*-α-PEA)PbI_3 is attributed to the efficient charge transfer within its inorganic framework. Moreover, an impressive detectivity of up to 7.1×10^{11} Jones has been achieved, approaching the CPL-insensitive detectivity of approximately 10^{12} Jones found in commercial Si photodiodes. Similarly, a hBN/(*R*-/*S*-MBA)$_2PbI_4$/MoS_2 heterojunction was used as a CPL photodetector, achieving a g_{res} value of 0.09 at a bias of 3 V and a responsivity of 0.45 A W^{-1} [494].

In 2020, the (*R*-MPEA)$_2MAPb_2I_7$ with n = 2 was used as the photoactive layer to fabricate flexible CPL photoconductor [497], achieving a high g_{res} value of up to 0.2 at 10 V bias voltage, a responsivity of 1.1 A W^{-1}, and a D* of 2.3×10^{11} Jones (Fig. 30d-f). This work modulates the crystallization dynamics of the films to facilitate carrier transport, maximizing the carrier collection efficiency in parallel-oriented chiral perovskite films with a homogeneous energy landscape. That same year, a direct detection of CPL signals in the helical 1D (*R*-/*S*-NEA)PbI_3-based photodiode was fabricated, achieving an R of 0.28 A W^{-1} and an extremely high polarization discrimination ratio R_L/R_R of 25.4 (corresponding to a g_{res} value as high as 1.85) [498], which largely surpasses that of the field-effect transistor–type chiral photodetector using chiral plasmonic metamaterials and organic materials ($R_L/R_R < 4$) [482,487]. However, the performance of these CPL detectors using chiral perovskites are still limited by the poor conductivity and limited photoresponsivity. Therefore, a direct CPL detector by utilizing a heterojunction between the chiral (MBA)$_2CuCl_4$ absorber layer and a semiconducting single-walled carbon nanotube (s-SWCNT) transport channel has been developed [500]. The chiral heterostructure shows high photoresponsivity of 452 A W^{-1}, a competitive g_{res} of up to 0.21, and low working voltage down to 0.01 V (Figs. 30g-i). A nanoscale heterostructure as an effective strategy indicates a new direction for using chiral perovskites in high-performance CPL detection, even in

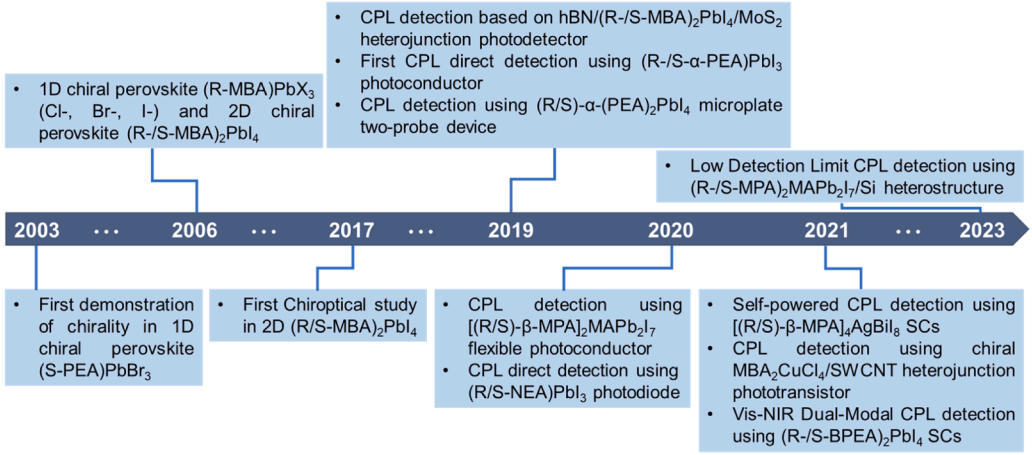

Fig. 29. The timeline of research on the chiroptoelectronic properties of chiral perovskites and their application in CPL detection.

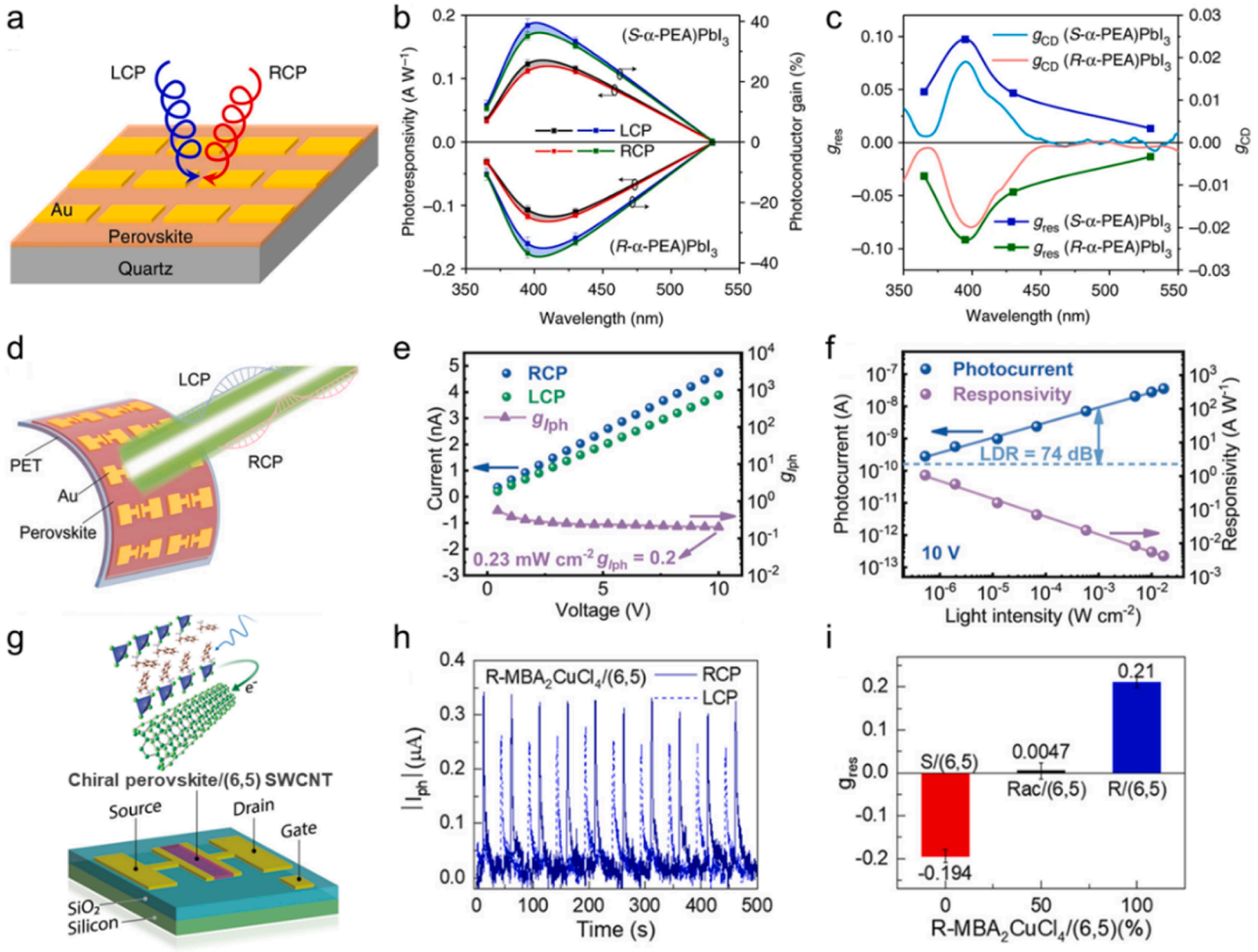

Fig. 30. **a,** Schematic illustration of a CPL photodetector based on the 1D chiral perovskite (*R*-/*S*-MBA)PbI_3 (MBA^+ = α-methylbenzylammonium) as the active layer. **b,** The responsivity and photoconductor gain under LCP and RCP at different wavelengths. **c,** The wavelength-dependent g_{res} and absorption dissymmetry factor (g_{CD}) spectra. **d,** Schematic illustration of the flexible CPL-sensitive photodetector based on the chiral reduced-dimension $[(R)\text{-}\beta\text{-MPA}]_2MAPb_2I_7$ film. **e,** I–V curves and the g_{Iph} of the flexible device under RCP-532 nm and LCP-532 nm illumination. **f,** The photocurrent and corresponding responsivity of the device. **g,** Schematic illustration of a CPL photodetector based on a heterojunction between 0D chiral (*R*-/*S*-MBA)$_2CuCl_4$/(6,5) SWCNT. **h,** The time-dependent photocurrent ($|I_{ph}|$) response for (*R*-MBA)$_2CuCl_4$/(6,5) SWCNT heterojunctions under 405-nm RCP and LCP laser illumination and a drain-source voltage (V_{DS}) of 2 V. **i,** Dependence of g_{res} factor on (*R*-/*S*-/rac-MBA)$_2CuCl_4$/(6,5) SWCNT under 405 nm RCP and LCP illumination. (a-c) adapted with permission from Wang., Nat. Commun. 10, 1927 (2019). Copyright 2019 Nature Publishing Group. (d–f) adapted with permission from Wang., Angew. Chem. Int. Ed. 59, 6442 (2020). Copyright 2020 Wiley-VCH. (g–i) adapted with permission from Hao *et al.*, ACS Nano 15, 7608 (2021). Copyright 2021 American Chemical Society.

highly insulating chiral metal halides. Simultaneously, this work demonstrates the feasibility of detecting CPL on a highly integrated photonic platform, facilitating the development of miniaturized and integrated devices for direct CPL detection. Recently, visible-near-infrared (vis--NIR) dual-modal CPL detection has been realized using chiral perovskite bulk crystals (*R*-/*S*-BPEA)$_2PbBr_4$ [501] with g_{Iph} values higher than 0.1 and I_{on}/I_{off} ratios higher than 10^3. Benefiting from the strong light-matter interaction of the layered structure, dual-modal Vis-NIR CPL-sensitive direct detection has been achieved.

3. Advances to meet challenges

At this stage, the performance of CPL photodetectors is still far from that required for practical applications. In-depth work is still needed to increase the g_{res} (ideally g_{res} should be 2) of chiral perovskite materials. Potentially effective strategies include fabricating 2D/3D mixed-phase [503] films where the 2D component determines chiral activity, while the 3D component contributes excellent charge transport properties. Enhancing film crystallinity (large organic cation size engineering, Lewis acid-base adduct coordination, compositional/additive engineering, and solvent engineering) aims to reduce defects and facilitates charge transfer [6,504–507]. Moreover, utilizing chiral induction [490] to create a chiral environment can promote the assembly of chiral structures. Currently, most efforts on chiral perovskites remain focused on bottom-up strategies through molecular design [492,508,509]. However, the experience gained from other chiral systems, such as small molecules, supramolecular assemblies, and aggregates, will help guide the design of chiral perovskites with higher g_{res} [510–512]. Top-down strategies for creating chiral perovskite metasurfaces are highly promising [513–516]. These methods combine the advantages of strong chirality with the remarkable optoelectronics properties of perovskites.

To improve the D* of a CPL photodetector, it is essential to reduce both dark current and noise. Dark current, closed linked to leakage current under reverse bias, can be minimized by using energetically well-aligned selective interface materials with a low density of interfacial defects [517]. The use of anti-solvents [518] or gas-quenching deposition [519] techniques, and defects passivation [520–522], has been shown to significantly improve film quality. At the same time, the response speed of CPL photodetectors needs to be improved by facilitating fast charge extraction.

Compared with their zero- to two-dimensional counterparts, 3D chiral perovskites are expected to exhibit smaller exciton-binding

energies and longer carrier-diffusion lengths, which are advantageous for chiroptoelectronic applications. However, the synthesis of 3D chiral perovskites remains in its early stages. Recent theoretical calculations have demonstrated that 3D chiral perovskites ($CHFClNH_3^+$ or $CHDFNH_3^+$) should be both thermodynamically and kinetically stable [523]. Moreover, nucleation-mediated growth has successfully been used to synthesize single-crystalline 3D $MAPbBr_3$ (MA, methylammonium) to serve in a CPL photodetector prototype [524].

The development of lead-free chiral perovskites is highly desirable to replace hazardous metals and enable safer devices. Lead is problematic due to its toxicity, which results from its ability to mimic other metals and disrupt biological functions [525]. Tin (Sn^{2+}) is considered the most promising alternative, given its similar ionic radius to lead and the spin polarization of up to 94 % in tin-based chiral perovskites [526]. Furthermore, other lead-free chiral perovskites based on bismuth [499] and copper [500] have also been reported for CPL detection.

4. Concluding remarks

Since the discovery of chiral perovskites in 2003 and their chiroptical activity in 2017, these materials have garnered significant interest for their potential in chiroptoelectronic and spintronic devices. The differential absorption of left- and right-handed light by chiral perovskites, combined with their semiconducting properties, enables control of light, making CPL photodetectors feasible. Moving forward, advancements in the physical mechanisms and structural modulation of chiroptical activity in chiral perovskites are expected to significantly enhance their application in CPL detection. Furthermore, the exploration of novel properties and new application areas by researchers will likely lead to pioneering developments in this field.

Acknowledgments

This work was financially supported by the National Natural Science Foundation of China (62474029) and National Key Research and Development Program of Ministry of Science and Technology (No. 2024YFB3614200).

XIII. Transforming liquids to electronics: High-throughput intelligent experiments for solution-processed semiconductors and devices

Xianhang Lin†, Can Deng†, Liyi Yang†, Liu Tang, Ahmad Imtiaz, Hanxiang Zhi, Xi Lu, Heng Li, Xiangyu Sun*, Yicheng Zhao*

State Key Laboratory of Electronic Thin Films and Integrated Devices, School of Integrated Circuit Science and Engineering, University of Electronic Science and Technology of China, Chengdu 610054, P. R. China

E-mail address: 3120205557@bit.edu.cn;zhaoyicheng@uestc.edu.cn

Xianhang Lin†, Can Deng†, Liyi Yang† contributed equally to this work

1. Bckground and challenge

The solution-processed semiconductors—such as metal-halide perovskites, conducting polymers, quantum dots, and MXenes—are extensively utilized in photovoltaics, displays, and detection technologies [527,528]. These materials offer the advantages of facile processing, meanwhile introducing a vast array of parameters. The parameters including solvent ratios and annealing protocols have a significant influence on the growth and assembly of functional layers, affecting the interaction from atomic interaction to mesoscopic crystal growth, and ultimately shaping the macroscopic device performance [529,530]. These comprehensive parameter space presents a formidable challenge for researchers to understand global optimization of solution-processed semiconductors and devices [531]. The conventional method of manual experimentation has small sample sizes that yield biased conclusions and lead to local optimization. The small data set does not allow us to utilize most material information. Given metal-halide perovskite semiconductors as example, the chemical formula ABX_3 of perovskite structure, where A is a monovalent cation (*e.g.*, K^+, Rb^+, Cs^+, MA^+, FA^+), B is a divalent metal ion (*e.g.*, Pb^{2+}, Sn^{2+}) or a combination of metal ions (*e.g.*, $Ag^+ + Bi^{3+}$), and X is a monovalent anion (*e.g.*, I^-, Br^-, Cl^-, F^-, SCN^-, OCN^-), as shown in Fig. 31a [532]. The typical constituent of metal-halide perovskites are ten core ions (*e.g.*, MA^+, FA^+, Rb^+, Cs^+, Pb^{2+}, Sn^{2+}, Br^-, I^-, SCN^-, OCN^-) along with over ten additive ions (e.g., PEA^+, NMA^+, HA^+, $PhPA^+$). The systematic study of alloying/mixing of the A, B, and X sites (Fig. 31b) and its effects is important for the full exploration of the potential of these materials. For example, incorporating four A-site ions, two B-site ions, and three X-site ions at 2 % step would require nearly 10^7 of different stoichiometric samples. Additionally, fabricating perovskite solar cells, especially advanced tandem cells, requires numerous processing steps. Each step involves optimization across various scales, from colloidal control at the molecular level to interfacial passivation at the mesoscale and functional layer design at the macroscale (Fig. 31c). This complex interaction of compositional and processing parameters illustrates the limitations of manual trial-and-error experimentation, which, restrained by a small data set, proves insufficient to address the complexities of these solution-processed material systems.

2. Advances to meet challenges

The three principal techniques, high-throughput computation, literature mining, and high-throughput experimentation for generating big data and building data factories are prominent among researchers [531,533]. Among them, high-throughput computation offers valuable understanding and deep perspectives [534], but its impact on optimizing solution-processed semiconductors is constrained, as the electronic structure of an ideal crystal is only one among many variables that influence device performance. Literature mining is effective in tracking research trends but hard in providing fresh physical insights, optimization strategies, or breakthroughs that push the boundaries of human knowledge [535]. Finally, the high-throughput experiments [536] conducted through multi-channel automated systems, are considered the most robust and powerful tool for generating high-quality, large--scale data. These experiments are expected to yield an unbiased, comprehensive understanding of material properties, facilitating exploration and optimization across extensive parameter spaces.

However, three key infrastructures must be established to unleash the power of high-throughput experiments for advancing electronic devices (Fig. 32). First, an automated high-throughput fabrication system is essential for efficiently producing samples of various compositions and processing conditions. This requires automatic multi-channel pipettes, spin coaters, and evaporators for streamlined device fabrication. Second, a high-throughput characterization system is required to meet the demand for large-sample analysis. For example, automatic UV-vis absorption, photoluminescence, and spectrum-dependent photocurrent measurements are crucial for assessing semiconductor properties and device performance. As rich information is normally hidden in the spectra and images yielded from high-throughput characterizations, therefore computer-aided data analysis with programs, such as Python codes, is necessary to automatically extract meaningful insights that would otherwise be beyond the reach of manual processing. Finally, artificial intelligence models must be developed to facilitate the interpretation, optimization, and generation of data about solution-processed semicondcutors [537,538]. For example, Variational Autoencoders (VAEs) can capture intrinsic features within semiconductor descriptors, while algorithms like XGBoost efficiently model relationships between experimental parameters. Gaussian Process Regression (GPR) with Bayesian optimization further enhances decision-making for subsequent experiments [539,540], paving the way for continuous improvement in material and device development.

3. Status of the area

To date, numerous research groups have embarked on automated experimental systems for solution-processed materials. Burger et al. pioneered the use of a mobile robot for autonomous photocatalyst screening, conducting 688 experiments in just eight days [541]. Similarly, Coley et al. created a platform capable of designing synthetic routes by generalizing chemical reactions from published data and executing refined recipes [542]. Zhao et al. developed a robotic platform

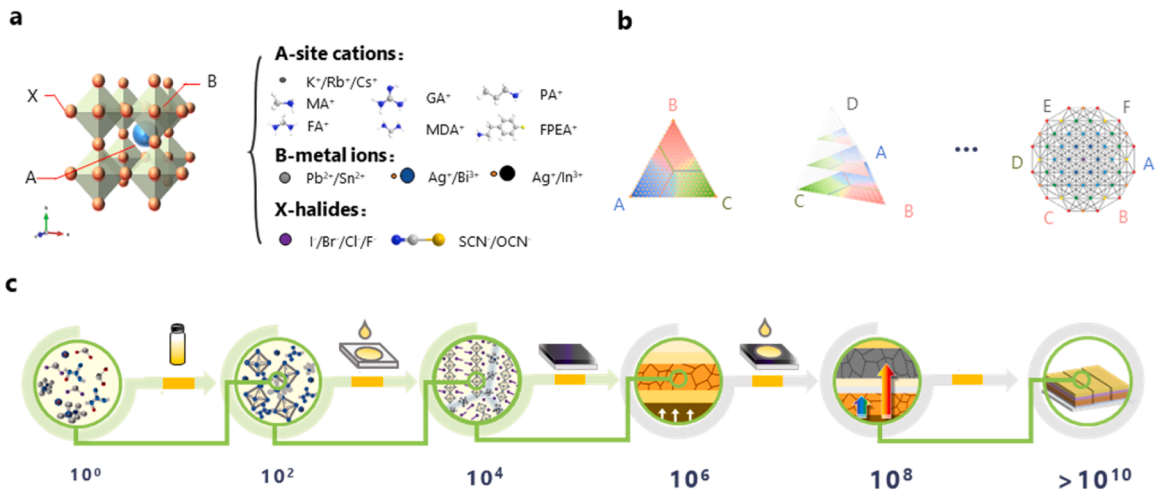

Fig. 31. Illustration of the complexities in metal-halide perovskites. (a) Crystal structure and typical ions of metal-halide perovskite materials. (b) Ternary phase diagrams represent the combinatorial complexity of alloying at the A, B, and X sites. (c) Schematic of the multidimensional aspects in fabricating perovskite solar cells, from precursor solutions, thin-film deposition, crystallization, and device fabrication. The possible combinations will be more than 10^{10}.

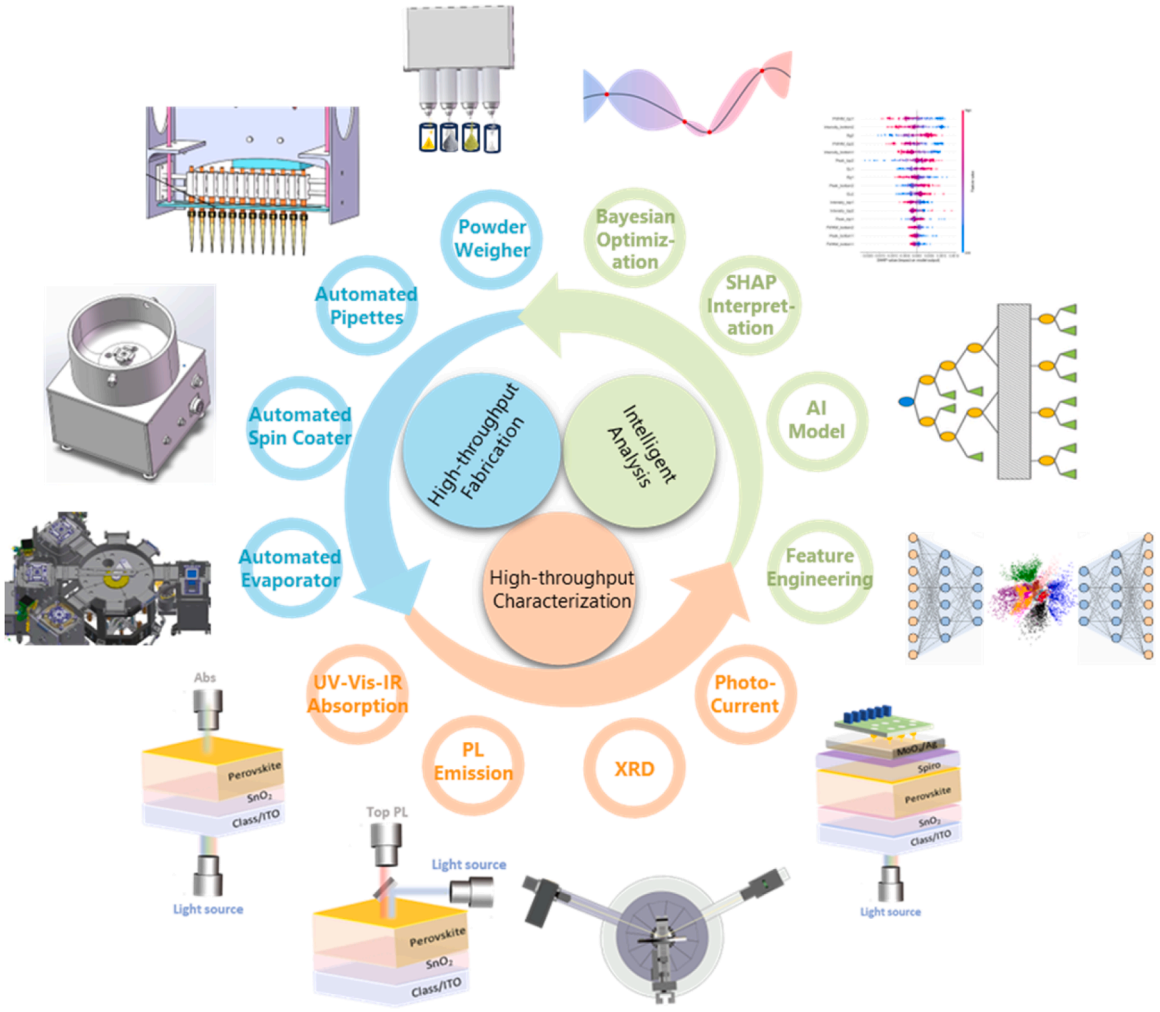

Fig. 32. Schematic of a high-throughput intelligent experimental platform for solution-processed semiconductor research. The system integrates automated fabrication (pipettes, weighers, spin coaters, evaporators), comprehensive characterization (UV-Vis, PL, XRD, photo-current), and intelligent analysis (AI models, Bayesian optimization [540], feature engineering). This closed-loop setup enables efficient data-driven optimization for rapid material discovery.

for controlled nanocrystal synthesis with specific morphologies, advancing research in inverse engineering [543]. However, these studies mainly focus on materials synthesis and thin-film fabrication, rather than end-to-end automated workflows extending from materials synthesis to device fabrication—essentially transforming liquids into electronics. Recently, Brabec et al. established an automated production line for organic solar cells, including solution preparation, film deposition, and electrode evaporation, although it is limited to producing around 100 devices per day due to constraints in evaporator capacity (private communication) [544]. These pioneering efforts are crucial for developing closed-loop autonomous experimental systems in materials research (Fig. 33a).

On the artificial intelligence front, significant progress is being made to harness big data for materials science [545]. Coley et al. developed an open-source software suite trained on reaction data from Reaxys and the U.S. Patent and Trademark Office, which generalizes reactions and demonstrates applications in flow chemistry for small molecules [542]. MacLeod et al. utilized a self-driving laboratory, Ada, to optimize palladium film production by defining the Pareto front for conductivity and processing temperature, discovering low-temperature processing conditions suitable for diverse plastic substrates [546]. Brabec et al. integrated high-throughput experimentation with Bayesian optimization to rapidly improve the photostability of quaternary OPV mixtures, screening 2000 combinations with minimal material use [544]. Sun et al. proposed a physics-constrained sequential learning framework using Bayesian optimization to identify stable perovskite compositions within the $Cs_xMA_yFA_{1-x-y}PbI_3$ system with only 1.8 % sampling, achieving a 17-fold increase in stability over $MAPbI_3$ (85°C, 85 % RH, 0.15 Sun) [547]. Recently, our group has developed a framework that combines high-throughput experimentation with interpretable machine learning [548], which reveals the relationship between cation selection and the stability of metal-halide perovskite films, and, for the first time, identifies a temperature-induced stability reversal effect. We have further developed a gradient high-throughput screening framework that

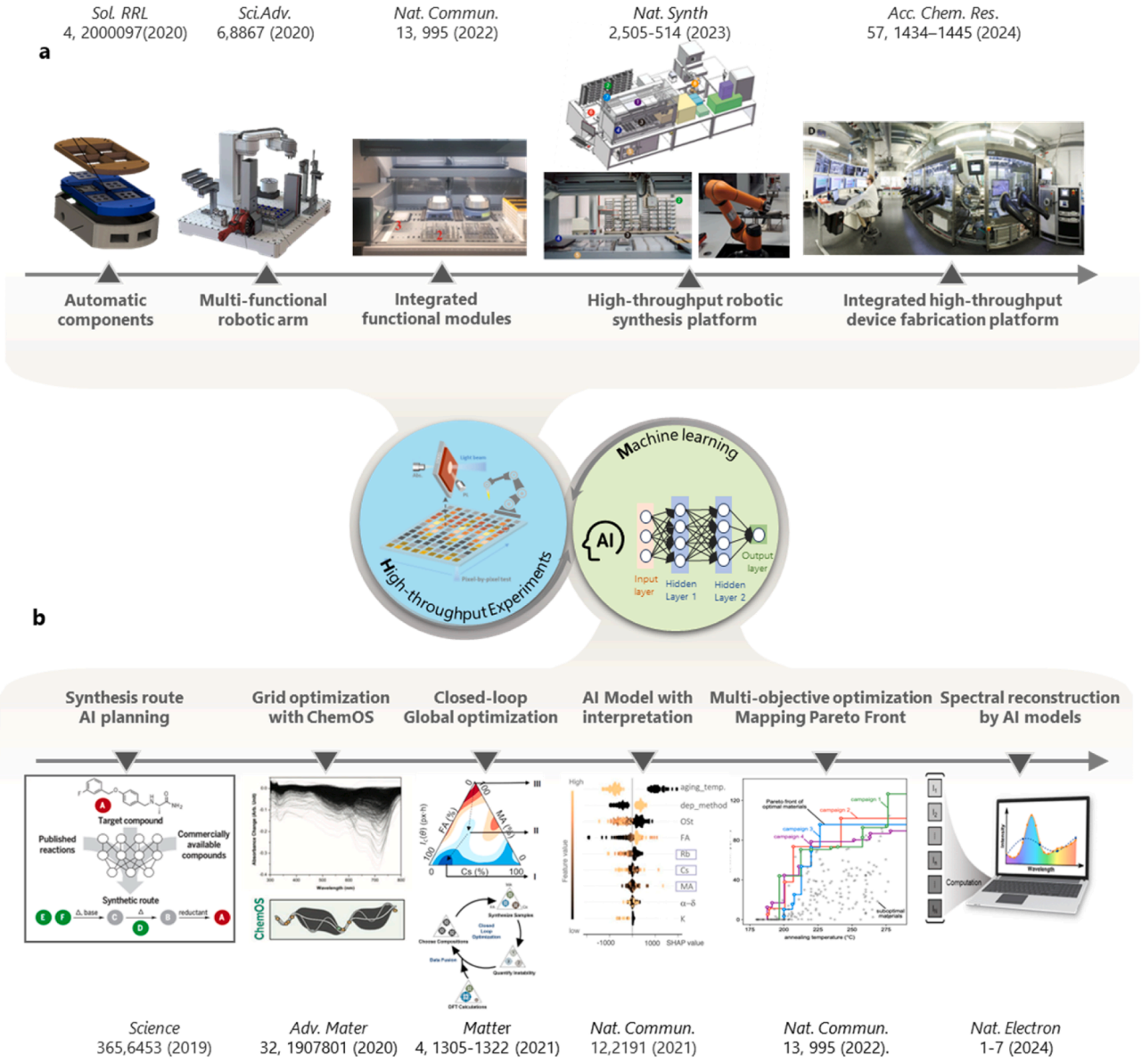

Fig. 33. Trends in high-throughput intelligent experimental platform integrated with AI-driven data analytics for solution-processed semiconductor research. (a) Automation setups, from robotic arms to full-chain device fabrication [543,546,549–551]. (b) AI progress in materials science, from synthesis planning and optimization to AI interpretation and spectral reconstruction, highlighting its role in accelerating material discovery and device optimization [542,544,546,547,552,553].

reflects practical operating conditions to optimize photo-thermal stability in perovskites. Recently, by training an artificial neural network on photocurrent response data, we have realized a reconstructive spectrometer that leverages amplitude and relaxation-time information to achieve high resolution (Fig. 33b).

4. Introduction to high-throughput plus machine learning platform

Our group has recently developed a high-throughput plus machine learning platform (HM-Platform), focused on solution-processed thin film and devices, such as metal-halide perovskite photovoltaics, as depicted in Fig. 34. This platform integrates four essential modules—Design of Experiments (DoE), High-Throughput Fabrication (HTF), High-Throughput Characterization (HTC), and Machine Learning (ML) [554–557]—to establish an iterative optimization loop. The workflow proceeds as follows: Initial DoE with orthogonal sampling → HTF → HTC → Intelligent spectral analysis and ML modeling → DoE with Bayesian optimization.

The DoE module works in three stages. First, it uses orthogonal sampling to initiate experiments and collect data. Next, it converts experimental parameters into machine-readable instructions, enabling the automatic experiments by the HTF module. Following the first round of experiments, GPR-based Bayesian optimization is used to guide the next round of sampling.

The HTF module features at least nine key components, all working together to optimize the fabrication process. The workflow begins with solution preparation based on DoE specifications. An 8-channel pipetting system extracts, mixes, and transfers solutions from stock bottles to a vibration table via a multifunctional gripper. This gripper then loads indium tin oxide (ITO) glass substrates from an 8-channel carrier onto an angle-fixed spin coater, ensuring precise control over solution dispensing and film coating. After spin-coating, the films undergo thermal annealing on a touchpad heating plate, where optical images are captured for quality assessment. Then, the devices are transferred to a 36-channel carrier for electrode deposition. A specialized robotic arm transports the substrates into thermal evaporators to complete electrode deposition. Once this process is finalized, the robotic arm places the devices in a designated area for further characterization. In the HM-Platform, the fabrication setups are all integrated into a N_2-filled glovebox.

The HTC module comprises photoluminescence and UV-vis-IR absorption spectroscopy units, a photoelectric testing module, and an automated robotic arm. These components enable systematic optical and photoelectric characterizations, measuring photoluminescence and UV-visible absorption spectra and performing customized photoelectric tests with channel-switching capabilities. Robotic arms streamline the workflow, allowing each 8-channel carrier cycle to complete within ten minutes and achieving a daily throughput of approximately 1,000 devices. All characterization data are seamlessly integrated into the HM-Platform database, enabling ML analysis. The characterization setups are also integrated into a N_2-filled glovebox.

The ML module provides spectral analysis, modeling, and interpretation to inform subsequent DoE samplings. It initially processes fluorescence and absorption spectra, XRD patterns, and photoelectric responses, creating a comprehensive database that integrates experimental parameters with device performance metrics. This data, combined with ML modeling, facilitates real-time adjustments and optimizations, enabling a fully iterative, data-driven approach to enhancing perovskite device performance.

5. Reproducibility of high-throughput experiments

The reliability of big data hinges on the reproducibility of high-throughput experiments. The high-throughput fabrication module integrates a spin-coater with a built-in atmosphere purification system that guarantees high reproducibility of films (see Acknowledgement). To validate this, we employed an antisolvent-free method to fabricate $FA_{0.83}Cs_{0.17}PbI_3$ films under identical processing conditions. These films were subsequently used to fabricate solar cells with an ITO/SnO_2/Perovskite/Spiro/MoOx/Ag architecture.

The automatic fabrication and characterization protocol initially involves the deposition of SnO_2 and perovskite through spin coating, followed by absorption (Abs) and photoluminescence (PL) characterization, deposition of the Spiro layer through spin coating, deposition of electrode layer through evaporation and current-voltage (I-V) measurement. Here, the Abs, PL, and I-V results reflect reproducibility from different perspectives: Abs mainly reflects the bulk property of the film,

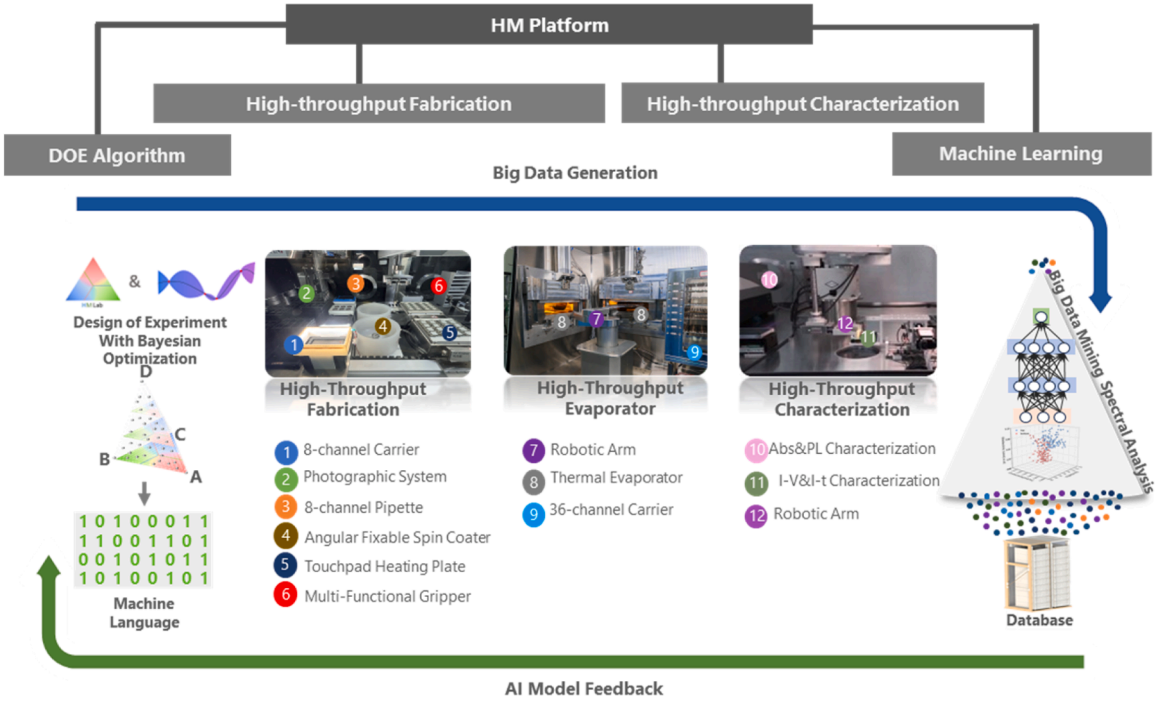

Fig. 34. High-Throughput + Machine Learning Platform. The platform is comprised of four modules: Design of Experiments (DoE) algorithm, High-Throughput Fabrication (HTF), High-Throughput Characterization (HTC), and Machine Learning (ML).

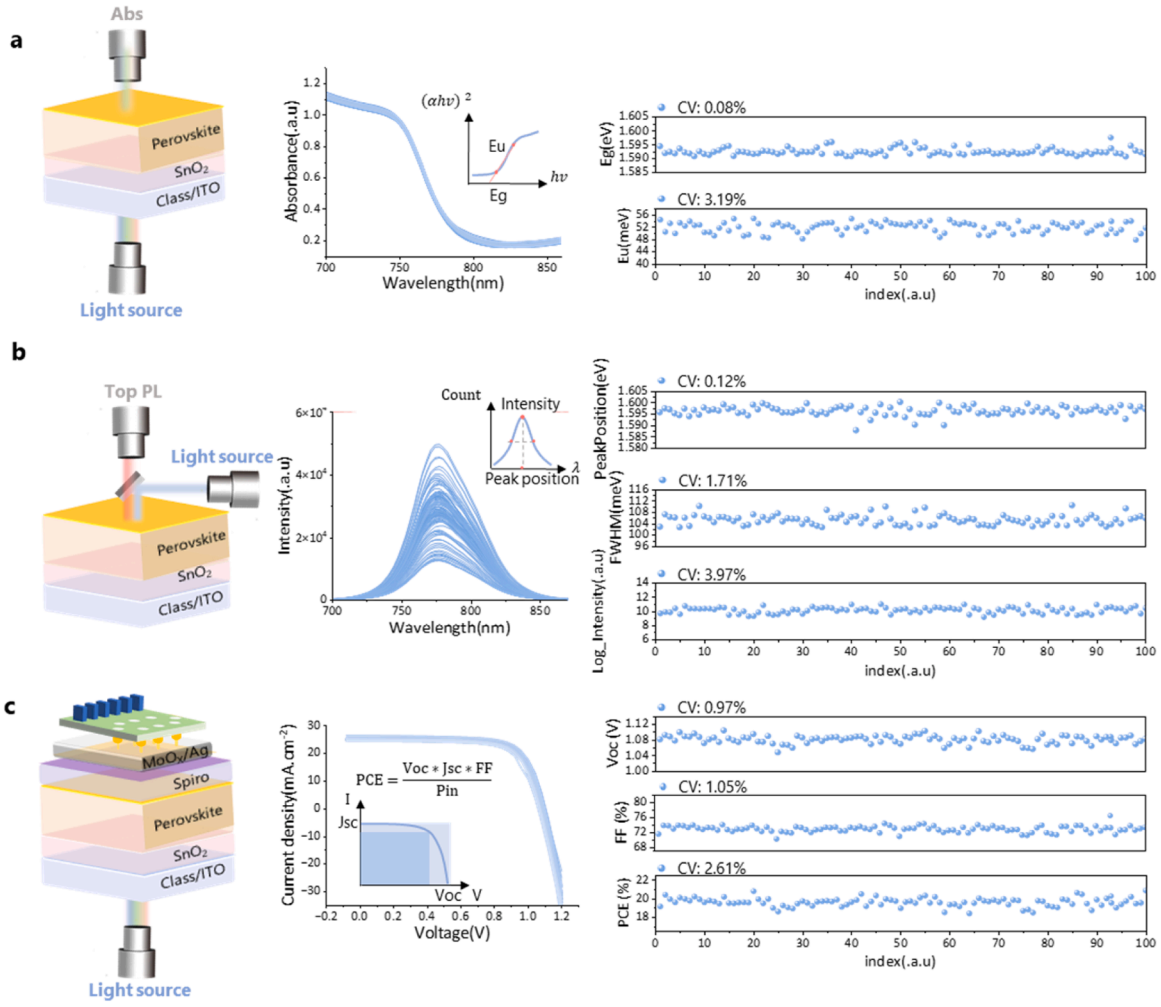

Fig. 35. Reproducibility of perovskite films and devices from HM-Platform. (a) Schematic of high-throughput absorption spectrum characterization, corresponding absorption spectra and CV results of automated extracted urbach-energy and bandgap. (b) Schematic of high-throughput PL spectrum characterization at upper interfaces, corresponding PL spectra and CV results of automated extracted PL intensity, peak position, and FWHM. (c) Schematic of High-Throughput IV Test, corresponding IV curve and CV results of automated extracted V_{OC}, J_{SC}, FF and PCE.

PL mainly reflects the surface property of the film, and I-V reflects the device performance.

In Fig. 35a, the absorption spectral data from 100 identically processed perovskite films are presented. We developed Python codes to automatically translate wavelength into energy coordinate, and extract the absorption bandgap (Eg) and Urbach energy (Eu) through fitting. The results show a low coefficient of variation (CV) for Eg at 0.08 %, whereas a higher CV of 3.19 % for Eu. This result suggests that Eu is a more sensitive indicator of impurities and defects within the thin film than Eg.

The surface properties of the film are further evaluated using photoluminescence (PL) spectra. Fig. 35b shows the PL data from the top film surface, where Python codes with Gaussian Mixture Model (GMM) are developed to analyze peak number, peak intensity, peak position, and full width at half maximum (FWHM) [558]. The peak position shows a CV of 0.12 %, indicating relative insensitivity to environmental effects, although slightly higher than that of absorption, likely due to greater susceptibility to surface defect states. In contrast, the FWHM's CV of 1.71 % highlights that it more effectively reflects impurities and inhomogeneity within the thin film than the peak position, thereby serving as a reliable measure for PL reproducibility. The intensity displays the highest CV of 3.97 %, which is mainly attributed to the surface roughness that affects the light absorption and emission.

In Fig. 35c, the I-V curves of the devices based on the 100 identically processed perovskite films also shows an evident variation. We also developed Python codes to extract the PV parameters, such as the open-circuit voltage (V_{OC}), fill factor (FF), and power conversion efficiency (PCE). The results reveal that, compared to the individual V_{OC} (0.97 %) and FF (1.05 %), the PCE displays a higher CV of 2.61 %, primarily attributable to the combined effect of multiple variable parameters on the PCE value. Furthermore, we find that CV of V_{OC} is much higher than CV of E_g and PL peak position. We attribute it to two factors: firstly, the introduction of additional variables during the deposition of functional layers such as Spiro-MeOTAD, and secondly, the smaller spot size during the PL and Abs characterizations compared to the I-V characterizations, which leads to a reduction in uniformity due to the increased area.

In summary, we demonstrate a high reproducibility of the HM-platform, showing a notable improvement over conventional manual methods, which typically yield a CV of around 4.5 % for PCE values [559]. This reproducibility can be credited to the platform's precise control of processing parameters, such as solution-dropping speed and height. The platform not only ensures consistency in key optical and electronic parameters but also offers insights into the variability across different characterization techniques. Going forward, reproducibility on the HM-platform may be further improved by minimizing the escape of volatile solvents and reducing fabrication time variability.

6. Outlook

In the future, HM-platform is expected to advance in throughput,

functionality, intelligence, and cloud integration [560]. Increased throughput involves a larger number of experimental channels and intelligent scheduling for complex experimental workflows. The platform will integrate further functionalities, such as powder handling, advanced dry/wet preparation techniques, and an extended range of physicochemical property characterizations, including thermal conductivity, mechanical constants, dielectric constants *etc.*. Robust intelligence facilitates autonomous decision-making within the platform, enabling manipulation of synthesis pathways and iterative self-optimization of solution-processed semiconductors and devices. Cloud integration focus on developing and optimizing large AI models that support comprehensive data analysis and predictive modeling. The cloud integration makes high-throughput experimental method to be a scalable approach that could leverage the entire efforts of the high-throughput experiments around the world, including a collection of perovskite datasets from identical compositions while processed under different conditions. In AI-assisted materials science research, the process typically begins with specialized AI models that are subsequently integrated into a unified framework. This approach culminates in a comprehensive model built upon a large-scale predictive foundation [561]. Cloud-based analysis algorithms provide users with seamless access to advanced technologies, thereby accelerating research and innovation in materials science and facilitating the discovery of novel materials. Ultimately, the convergence of increased throughput, expanded functionality, advanced intelligence, and improved accessibility will drive significant breakthroughs across diverse fields that rely on material innovation.

Acknowledgement

Y.Z. acknowledges funding from the National Natural Science Foundation of China (Grant No. 52372177). X.S. acknowledges supported by the China Postdoctoral Science Foundation under Grant Number GZB20240102. Y.Z. acknowledges the technical support from Sichuan Aientropy Technology Co., Ltd. that provides the key components including gripper, spin coater, and the atmosphere purification system for constructing the high-throughput experimental platform and the algorithms of DoE and spectral analysis.

XIV. Theoretical studies on defect engineering of halide perovskites

Jian Xu*

Advanced Research Institute of Multidisciplinary Sciences, Beijing Institute of Technology, Beijing, P. R. China

Email address: jianxu.xu@bit.edu.cn

1. Status of the area

Defect engineering stands as a crucial frontier in the study of halide perovskite materials, particularly for their application in optoelectronics. First-principles calculations play a pivotal role in understanding the defect properties of metal halide perovskite materials. Yin *et al* [48]. performed density functional theory (DFT) calculations with semilocal exchange-correlation functionals on lead halide perovskites, revealing that dominant defects, characterized by their low formation energies, create only shallow levels, whereas defects with deep levels exhibit high formation energies. Utilizing a more accurate approach, such as hybrid DFT functionals combined with spin-orbital coupling (HSE+SOC), independent researchers [562–564]. have reached a consensus that the iodine interstitial (I_i), a predominant defect in lead halide perovskites, generates deep levels within the bandgap, acting as non-radiative recombination centers. Expanding on this, Xu *et al* [565]. delved into the defect chemistry of mixed Pb-Sn perovskites, identifying a defect-tolerant region (30-70 % Sn content) with notably longer carrier lifetimes for 50 % Sn mixed perovskite compared to other compositions.

While these advancements have deepened our understanding of defect properties, this filed remains in its nascent stage. Numerous challenges for modeling defects in complex halide perovskites remain. The following section will discuss some of the challenges (Fig. 36), focusing on inequivalent defect sites in complex alloys, charged defect calculations at surfaces, and dynamic defect behaviors in large-scale

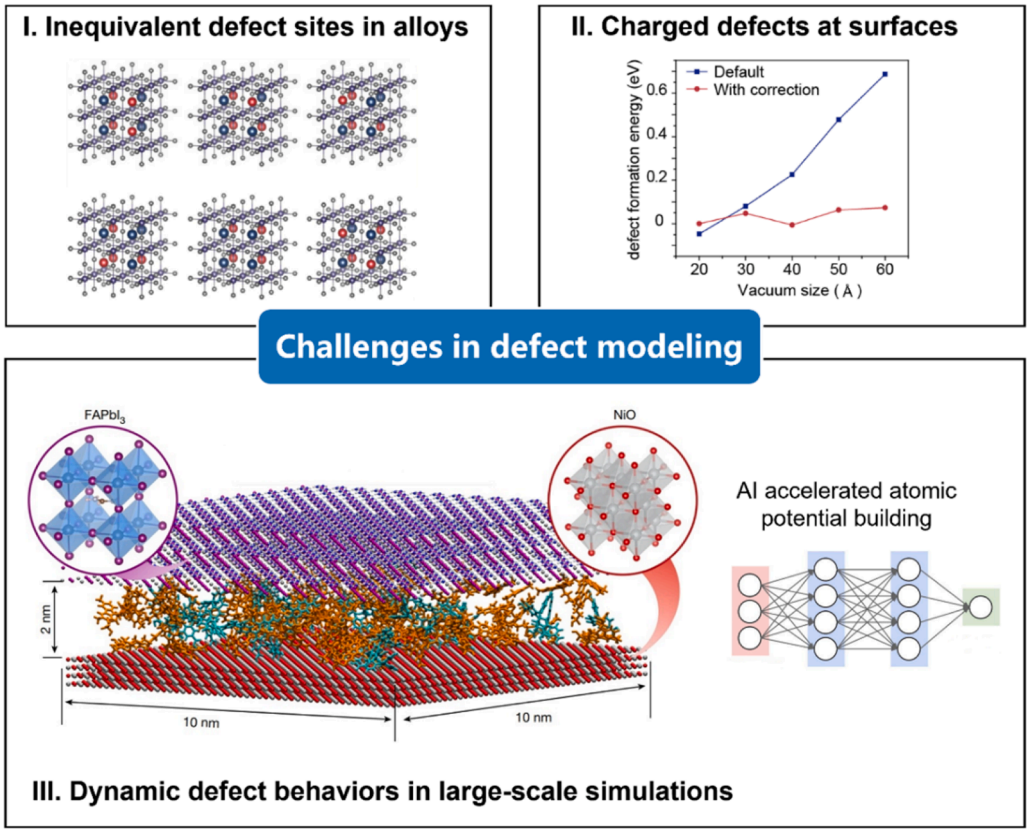

Fig. 36. Schematic diagram of the challenges about modeling defects in complex halide perovskites [308,576,580].

simulations.

2. Challenges and advances

(1) Inequivalent defect sites in complex alloys

The existence of inequivalent defect sites is a central challenge for the defect modeling in halide perovskites, especially in complex alloys like wide-bandgap $(FA_xMA_yCs_{1-x-y})Pb(I_aBr_bCl_{1-a-b})_3$, which are widely used in tandem solar cells. For example, in cubic $CsPbI_3$, there is only one inequivalent site for iodine vacancy, while in $Cs_{0.9}FA_{0.1}Pb(I_{0.6}Br_{0.4})_3$ alloys, multiple inequivalent defect sites emerge for iodine vacancies. For the same defect species, the defect formation energy may vary considerably across these inequivalent sites. One can define an effective formation energy of defect α in charge state q (ΔH_{eff} (α, q, T)) as a statistical average over all possible inequivalent defect sites (s) at a given temperature (T). This is expressed as $\exp[-\Delta H_{eff}(\alpha, q, T)/k_BT] = N^{-1}\sum_s \exp[-\Delta H_f(\alpha, q, T, s)/k_BT]$, where ΔH_f (α, q, T, s) is the defect formation energy of defect α at a specific site, and N is the total number of possible sites [566].

Halide perovskite alloys are modeled as a statistical ensemble of independent configurations, with the total independent configurations calculated using the site-occupancy disorder (SOD) code [567]. For example, in modeling the stable black-phase (γ-phase) $CsPb(I_{1-x}Br_x)_3$, a periodic supercell of pure $CsPbI_3$ containing 4 formula units is constructed, and I anions are substituted by Br anions at varying concentrations x=0, 1/12, 2/12, 3/12, 4/12, 5/12, 6/12, 7/12, 8/12, 9/12, 10/12, 11/12 and 1. Without considering the symmetry of the γ-phase (*pbnm*, space group 62), $CsPbI_3$ could have 4096 possible configurations (2^{12}). However, by considering the symmetry, the total number of possible configurations reduced to 592, with inequivalent configurations numbering 1, 2, 14, 30, 77, 104, 136, 104, 77, 30, 14, 2, 1 for alloys with x= 0, 1/12, 2/12, ..., up to 1, respectively.

To generate all possible low-energy defect configurations used for defect formation energy calculations, Defect and Dopant ab-initio Simulation Package (DASP), [568]. ShakeNBreak [569] and other packages are developed. Since some defect structures may reside in local minima of the potential energy surface, it is suggested to generate multiple configurations through local distortions followed by structural relaxation to identify lower-energy structures.

While the formalism for defect calculations is well-established, the computational expense of high-accuracy first-principles calculations, such as HSE+SOC and GW, presents a considerable challenge. Integrating machine learning techniques with DFT inputs offers a promising approach to handle the increased structural and compositional complexities.

(2) Charged defect calculations at surfaces

Compared to bulk defects, surface and interfacial defects in perovskites present at higher densities, leading to performance degradation of optoelectronic devices [570,571]. Improving the performance of halide perovskite devices necessitates a comprehensive investigation into surface defect chemistry and physics; this understanding can then be levered for the rational design of defect-passivating ligands.

In the bulk (*i.e.*, 3D systems), charged defect calculations traditionally employed the jellium approach [572]. In such systems, as the supercell size used in calculations increases, the formation energies of charged defects converge to a fixed value. However, in 2D systems, such as surface or interface slabs, these energies diverge almost linearly with vacuum size [573], which is physically illogical and highlights the limitations of conventional approaches.

To enable more accurate predictions of defect formation energies in slab models, reliable correction schemes for charged defects should be implemented [572]. Zhang *et al* [573] introduced a supercell extrapolation method based on the jellium model (named SEJM). Deng *et al* [574] proposed an alternative method by replacing the compensating jellium charge with the real host-band-edge charge, which is called transfer to real state model (TRSM). More recently, da Silva et al [575] developed a self-consistent potential correction (SCPC) method for charged defect calculations in slabs. Utilizing the SCPC method, Xu *et al* [576] mapped out the defect chemistry landscape of perovskite surfaces, revealing that surface defects exhibit properties distinct from those of bulk defects. For example, donor-like defects, such as iodine vacancy, are found to be deeper at the MAI-terminated perovskite surface than those in the bulk, while acceptor-like defects such as Sn/Pb vacancy and iodine interstitial tend to be deeper at the PbI_2-terminated surface compared to both the bulk and MAI-terminated surface. Therefore, tailored surface defect treatments could be employed depending on the specific dominant terminating surface.

(3) Dynamic defect behaviors in large-scale simulations

First-principles calculations based on DFT are typically constrained to simulation boxes containing fewer than 1000 atoms. To explore the dynamic behaviors of defects under operational and atmospheric stressors, simulations on a much larger scale — encompassing millions of atoms and picosecond time — are essential. Advanced packages such as DeePMD [577] and GPUMD [578] have been developed to enable these large-scale simulations. These tools employed deep learning scheme to fit neural network potentials based on a given set of structure, energy and force data derived from DFT calculations.

Although artificial intelligence (AI)-assisted approaches have already made some progress in materials science and chemistry, challenges remain in balancing efficiency, accuracy, scalability and transferability in machine learning models. One of the primary challenge lies in the sampling of training data when dealing with the trade-off between efficiency and capability to generalize. The training set should be complete, compact and sufficiently expressive to capture the underlying physics accurately. In active learning schemes [579], the model participates in the training set selection and prioritizes samples that will most effectively improve the performance of the current model.

3. Concluding remarks

Defect modeling in metal halide perovskites is a highly promising field, with the potential to significantly influence the design and property engineering of perovskites for optoelectronic applications. The ongoing advancements in first-principles computational methods, coupled with the increasing power of supercomputers, are accelerating the ability to precisely control defects in these materials. There is also a pressing need for the development of machine learning methods that excel in efficiency, accuracy, scalability, transferability, and generalizability (EASTG).

Current machine learning-based interatomic potentials often face limitations due to the constraints of their training sets, which hinder their generalizability. The prospect of creating a robust, universally applicable interatomic potential for halide perovskites—potentially named the Perovskite Large Atomic Model (PLAM)—is particularly exciting. Such a model would be capable of handling the complexities of the entire periodic table within a single framework, opening up new avenues for innovation and discovery in the field.

Acknowledgement:

This work was supported by the BIT Teli Young Fellow program.

XV. Charge transport of halide perovskites

Xiaojian She*

State Key Laboratory of Extreme Photonics and Instrumentation, College of Optical Science and Engineering, Zhejiang University, Hangzhou, 310000, China.

E-mail address: xjshe@zju.edu.cn

Abstract

Charge transport in metal halide perovskites is the base for optoelectronic processes of perovskite devices. Its key figure of merit, carrier mobility, is demanded with a high value for better device performance. This section aims to provide an overview of current understanding on charge transport in metal halide perovskites, with four parts: the role of high carrier mobility in optoelectronic applications, experimentally probed charge transport mobilities in halide perovskites, physics of mechanisms limiting charge transport, and strategies of improving carrier mobility.

1. The role of high carrier mobility for optoelectronic

applications

In photo-vatic cells (PVs), high mobility can lead to reduced recombination rate in almost all the recombination kinetics because it helps fast splitting of electrons and holes in heterojunction interfaces and can accelerate the collection by electrodes. In light emitting diodes (LEDs), high mobility reduces the time carriers spend in non-radiative recombination centers or in regions where they might be trapped, so that more carriers can recombine radiatively to improve the LED's efficiency. Meanwhile, high carrier mobility can spread the current uniformly throughout the LED's active area, contributing to consistent light emission. In photodetectors (PDs), high mobility contributes to rapid transport of photogenerated carriers to the electrodes, leading to faster response times and shorter detection delays, and meanwhile can enhances the quantum efficiency of the photodetector because it reduces carrier recombination. In field-effect transistors (FETs), high mobility allows for high channel current density and fast switching speed. Overall, in order to pursue better performance of perovskite optoelectronic applications, it is prerequisite for us to understand charge transport in halide perovskites to seek insights of improving carrier mobility.

2. Experimentally probed mobilities in halide perovskites.

In the recent decade, extensive efforts through experimental and theoretical methods have been made to probe the values of carrier mobilities in different halide perovskites. The reported experimental techniques include Hall Effect measurement, space charge limited current measurement, terahertz conductivity measurement, time-of-flight measurement, transient microwave conductivity measurement and photoluminescence quenching measurement. By these methods, the mobilities probed for a range of halide perovskites range from 0.9 ~ 71 cm^2/Vs for polycrystalline films and 35 ~ 200 cm^2/Vs for single crystals [421,581–609], as shown in Fig. 37. However, it is still hard to tell which perovskite composition gives higher mobility from the reported mobility data, because these values are obtained by different measurements and different sample preparations which include variations and uncertainties raised from differences in sample fabrications and measurement details. Overall, the reported mobility measurement results show that mobilities of halide perovskite thin films are comparable to that of metal-oxide semiconductor thin films. The low mobility obtained in thin films with respect to that of single crystal ones is due to the defects in grain boundaries in the perovskite films. In particular, ionic defects act as charge traps and scattering centers both of which can significantly reduce carrier mobility, and their migration can lead to the change of local electrical fields which consequently affects carrier transport.

Nevertheless, the reported mobilities of halide perovskite single-crystals are lower than their primary theoretical predictions. The mobility of single crystal holds the limit of highest mobility can be achieved in halide perovskite thin film samples which are widely used for optoelectronic applications. Despite extensive efforts are need to optimize thin film quality to improve their carrier mobility approaching to that of single crystals, another important thing needs more efforts is to investigate what are the limitations for charge transport mobility within the perovskite lattice. In the below, we review the current knowledge obtained about the mechanisms limiting charge transport at lattice scale.

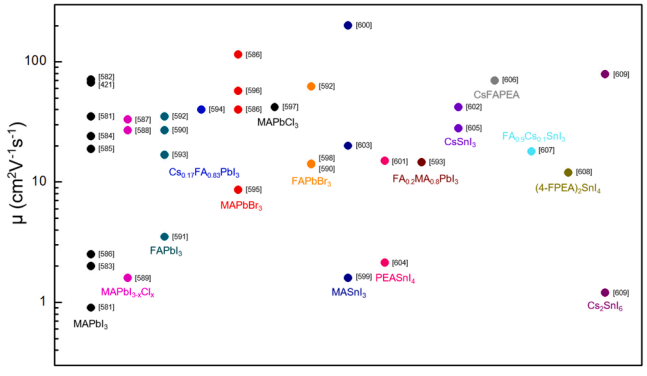

Fig. 37. Static sum of mobility values probed by experiments for different halide perovskite compositions.

3. Physics of mechanisms limiting charge transport

Charge transport in halide perovskites has been widely observed in the band-like transport regime, with its mobility increasing over deceasing temperature, as $\mu = T-r$, with $r \sim 1.3$-1.6 [581,610–612]. It suggests that the reduced mobility at room temperature is consequent from thermally activated mechanisms. In scattering limited charge transport model, carrier mobility is expressed as $\mu = e\tau\, m^*$ (where e is elementary charge, τ and m^* are the momentum relaxation time and the carrier effective mass) [9]. The prototype halide perovskite, $MAPbI_3$, is the most common one used to study carrier transport physics. The effective electron and hole mass in $MAPbI_3$ are found around 0.1 to 0.2 m_e (m_e is the free electron mass) by theoretical calculations on band curvature [613–617]. and experiment methods of magneto-absorption measurements [618–620], respectively. Based on this, Prof. Herz suggests that the mobilities around 100 cm^2/Vs observed in halide perovskites are associated with small momentum relaxation time about ten femtoseconds that indicates charge transport in halide perovskites is highly likely inhibited by electron-phonon coupling [45].

In ionic solids, electron-phonon coupling is categized into two types, one is potential deformation which refers to vibration of electronic structure during lattice vibration, the other one is polar interaction (Fröhlich interaction) which is induced by temporary electric field created between different ionic atoms during lattice vibration [9]. The mobility temperature relationship found in experimental observation [581,610–612]. agrees with the acoustic-phonon potential deformation (APD) model whose mobility temperature relationship follows $\mu = T^{-1.5}$ [621–623]. Nevertheless, some first-principle calculations argue that potential deformation by acoustic-phonon is weak in MAPbI3 crystal, and calculation taking APD model shows mobility is up to several hundred cm^2/Vs at room temperature that is much higher than experimental observations [624,625]. Thereby, it is not yet safely concluded that APD model plays as the dominating electron-phonon coupling mechanism in halide perovskites. By contrast, other first-principle calculations considering LO photon Fröhlich interaction show carrier mobility approaching 100 cm^2/Vs at room temperature and its mobility temperature relationship is close to the experimentally observed mobility temperature dependence at high temperature regime [626,627], suggesting that LO photon Fröhlich interaction is more likely to be one dominating electron phonon coupling mechanism for charge transport in halide perovskites at high temperatures. Apart from halide perovskites, Fröhlich interaction has also been widely observed in other polar semiconductors including GaAs, due to polar nature of their lattices. LO photon Fröhlich interaction is known of dependence on the frequency limit of dielectric function and the frequency of LO phonon, and values of the two parameters in halide perovskites (ABX_3) with higher ionicity of B-X bond are found benefit to stronger LO photon Fröhlich interaction [9].

In addition, polaron is the second factor that needs to be taken into account as a charge transport limiting mechanism in halide perovskites [22,628–630]. When a mobile carrier is presented in the perovskite lattice, it can polarize the surroundings ions so that potential well is created for the mobile carrier and thus the charge transport is slowed. As illustrated in Fig. 38, mobile carrier polarizes the lattice by distorting the BX3- sub-lattice [629]. and reorienting organic cation dipoles [628]. (such as MA+ which refers to methylammonium cation, FA+ which refers to formamidinium cation). Miyata et al calculated the polaron radii (rp) of MAPbX3 is around 4 nm that is one order of magnitude larger than their lattice constants [47], suggesting that charge transport in halide perovskites is of large polaron nature whose transport is not thermally activated compared with small polarons observed in organic

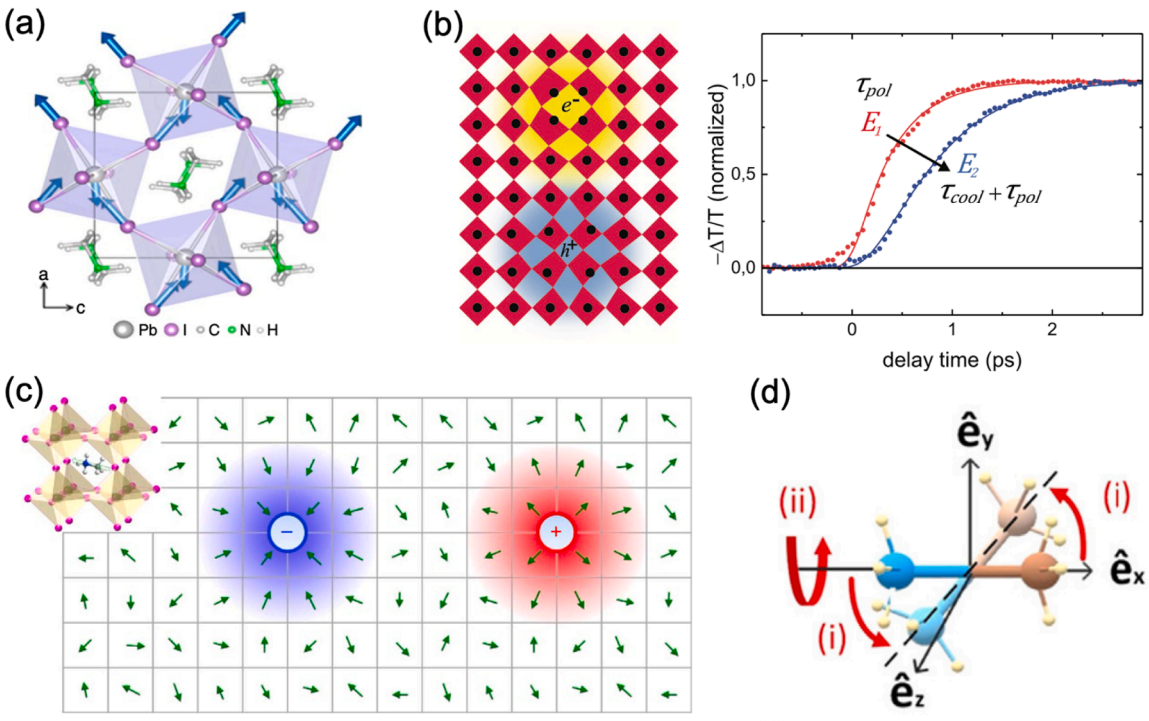

Fig. 38. **(a)** Schematic illustration of LO vibration of $MAPbI_3$, the blue arrows denote the displacements of the Pb and I atoms. **(b)** The polaron formation by the polarization of PbX_3^- sub-lattice. **(c)**, The polaron formation by dipoles from reoriented organic cations. **(d)** The MA^+ dipole ration. Images are from references [629, 22,23,634].

semiconductors.

At last, the orientation of organic cation is the third factor affecting charge transport [631]. The primary consideration is that the electronic structure of halide perovskites can be affected by the orientation of organic cations because of the polar nature of organic cations. Motta et al discovered if MA+ orients along a (011)-like direction in MAPbI3, the PbI6 octahedral cage will distort and the bandgap can become indirect [632]. Satya et al studied the influence of organic cation orientation on charge transport in $MAPbI_3$ transistor, found that the random orientation of MA+ can lead to pronounced electronic disorder and low mobility at room temperature [633]. Gelvez-Rueda et al studied the timescale of electronic disorders formation by MA+ rotational motion in $MAPbI_3$, their calculation shows that 90-degree MA+ motion at room temperature takes places within 3 ps which is about the timescale for charge transport between two sites in $MAPbI_3$, such that the MA+ rotational motion leaded electronic disorder can effectively affect the charge transport [634]. In addition, they found that the employment of nonpolar cation, Cs^+, can reduce the dynamic disorder effectively.

4. Summary and strategies to improve mobility

As discussed above, high charge transport mobility in halide perovskites is important for pursuing high performance perovskite optoelectronic applications. Charge transport in halide perovskites is associated with a number of limiting factors, the overcome of which is essential for obtaining high mobility. For resolving the defect problem in thin film sample preparations, methods such as additives engineering, solution processing engineering, post vacuum thermal annealing can be applied to optimize film crystallization and morphology. In addition, methods such as surface cleaning and passivation techniques to remove ionic defects resident in gain boundaries and passivate surface charge traps have also been developed, showing effectiveness in improving charge transport mobility. For minimizing affects from intrinsic charge transport limiting mechanisms, one effective route worthy more research efforts is to apply composition tuning where different elements can be tried in the ABX_3 to reduce the above electron-phonon coupling from Pb-X sub-lattice vibration, polaron interaction from Pb-X sub-lattice distortion and dynamic disorder by organic cation rotations.

XVI. Perovskite photophysics

Jafar Iqbal Khan*

Department of Physics, School of Natural Sciences, University of Hull, Cottingham Road HU6 7RX, Hull, UK

E-mail address: j.khan2@hull.ac.uk

1. Status of the field

The photohysics of perovskites is predominantly evaluated through time resolved spectroscopies and transient electro-optical characterization techniques [635–638]. Herein, the discussion is mainly constrained to time resolved spectroscopy as a diagnostic tool to elucidate the photophysics of perovskites as mostly the associated processes are taking place on femtosecond (fs) to nanosecond (ns) time scale [639–642]. In pristine metal halide perovskites, the free carrier generation occurs upon interaction with light (Fig. 39). These photogenerated charge carriers undergo a range of recombination mechanisms at distinct times on fs to microsecond (μs) range [643,644]. After generation the carriers diffuse to the surface (few ns), yet in parallel they also facilitate both non-radiative and radiative recombination [638,645]. The diffusion of the carriers to the surface depends on the surface velocity parameter whereas the radiative recombination is simply direct electron-hole recombination followed by emission of a photon. In contrast, several pathways co-exist for the non-radiative recombination (typically on ns), such as surface recombination, trapped carrier, Shockley-Read-Hall (SRH) recombination mechanisms and grain boundary recombination [646]. The trapped carriers are further decomposed into two sublets, namely shallow traps and deep level traps undergoing non-radiative recombination and are distinguishable as they facilitate recombination on a faster and a slower time scale, respectively [647]. Furthermore, a higher order recombination, Auger recombination, classed as non-radiative recombination emerges at higher photo excitation densities (10^{19} cm^{-3}). Additionally, a mechanism termed hot carrier generation and the subsequent relaxation of these co-exists and is probed through transient absorption (TA) spectroscopy as it occurs typically in fs time range [648]. In photovoltaics the focus is on the charge transfer

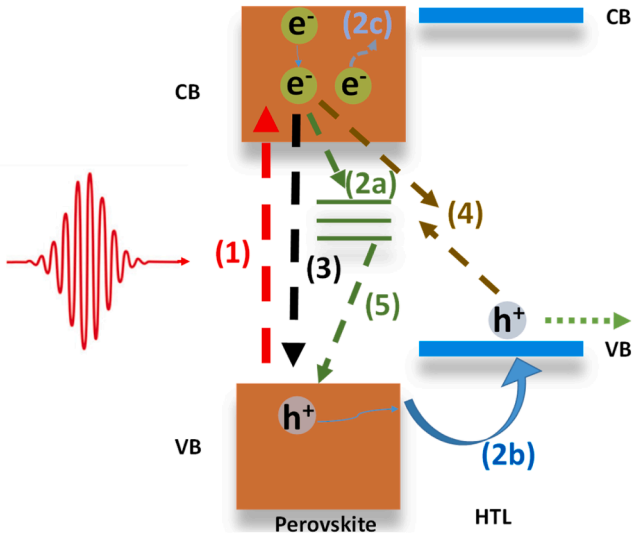

Fig. 39. Schematics of the important photophysical process in perovskite absorber layer adjacent to the hole transport layer (HTL) upon illumination of pulsed laser light. Pathway (1) describes the photoexcitation of the carries from valence band (VB) to conduction band (CB), additionally, hot carrier generation and the thermalization pathway of these is also sketched. Subsequently, carriers are trapped (2a), diffusion mediated hole transfer occurs (2b), generation of Auger electrons and their recombination takes place. Afterwards all sort of recombination; band to band recombination (3), interface recombination (4), trapped carrier recombination (5) occurs.

from the photoactive absorber layer to the adjacent charge transport layers (CTLs), i.e. hole and electron transport layers as depicted in Fig. 39 [649–652]. Typically, the transferred charges travel through these charge collection networks and reach the electrodes. The charge transfer mechanism is an additional photophysical process, yet also the interface formation between the photoactive layer and the adjacent charge transport layer promotes non-radiative interface recombination which competes with the former. A third process known as energy transfer under certain conditions can take place and is typically on the (ultra)fast time scale.

Considering all the above, the physical processes in perovskites tracked through ultrafast spectroscopy and transient photovoltage techniques yield a degree of complexity related to deconvolution of the respective components due to internal competition [646,653]. This leaves the community with the critical challenge of interpretation of the acquired charge carrier dynamics and subsequently fitting them using appropriate physical models describing the accurate physics. Utilizing different techniques yield access to distinct processes as they are conducted at specific set of parameters like excitation power, repetition rates and sample configurations such as half-stacks or complete-stacks of the optoelectronic device. This implies that another challenge is present associated to estimation of the charge transfer rate or quantification the recombination rates from the parametrized lifetimes.

2. Current and future challenges

The main challenges are consistency concerning sample preparation protocols, optical experiments, and modelling the obtained charge carrier dynamics. All the above-mentioned processes are taking place on time ranges of few fs to μs, with hot carrier generation and the subsequent thermalization being an ultrafast process, this response is detectable through high resolution TA spectroscopy. Vast processes are competing thus their spectral responses are largely overlapping in the detected signals. To that end, differentiation across these processes becomes complex, and further interpretation of the component associated charge carrier dynamics is reduced to being not trivial. Consequently, fitting the charge carrier dynamics using consistent physical models is often complex and is based on several assumptions not accounting for vast processes involved. In addition, depending on the applied technique the extracted charge carrier dynamics carry different information, yet the comparison across remains often inaccurate. For instance, in the TA experiments the ground state bleach signal is also convoluted of the photoluminescence and trap assisted recombination responses. Therefore, tracking the charge carrier dynamics in the apparent spectral range is not reflecting the evolution of a single component through the estimated recovery time of the bleach but a convoluted contribution. In contrast, using TRPL technique the insightful information related to the radiative recombination is gauged through the photoluminescence response of the material, which also exhibits indirectly the evolvement of the non-radiative recombination. Encouraging efforts have been made in proposing consistent models and fitting the charge carrier dynamics acquired from TRPL measurements [654].

Another crucial element is the sample preparation which differs from various protocols and yields distinct charge carrier dynamics. This implies that the extracted parameters such as the carrier lifetimes are inconsistent in literature. Hence, it is necessary to provide the respective sample preparation protocols precisely for the purpose of comparing the lifetimes. Subsequently, it is a prerequisite that the experiments are performed carefully as pulse duration, laser repetition rate, and laser fluences all have considerable impact on both the charge carrier dynamics and the estimated carrier lifetimes. In addition, the environment and applied experimental conditions are equally critical for the derived parameters. For instance, TRPL measurements performed using different techniques are highly sensitive to the aforementioned parameters and yield distinct charge carrier lifetimes. In fact, the extracted parametrized values are identified as associated to different processes, such as surface recombination or deep level trapped carrier lifetimes [647]. Additional critical parameter is the generated charge carrier density, which is distinct across different experiments due to the difference in excitation densities. This adds to the complexity associated to fitting the charge carrier dynamics obtained from TA and TRPL using the same physical model determining the charge transfer and recombination rates.

3. Advances to meet challenges

In order to understand the photophysics of perovskites, modelling the charge carrier dynamics using consistent physical models accounting for diffusion, radiative recombination, and nonradiative recombination of charge carriers is a necessity. To that end the latter channel becomes further complicated as SRH, Auger recombination, surface recombination and recombination at grain boundaries must be incorporated since all are non-radiative contributions. Single lifetimes extracted from non-physical models are inaccurate and do not reflect the physics at any point. In addition, with interest in determining the charge transfer rates using adjacent charge transport layers, interface recombination and charge extraction must be incorporated in the physical models. The modelling is simplified by considering the non-radiative contribution as one, so that only four quantities are incorporated.

Identifying the various processes require an experimental approach in combining time resolved spectroscopic techniques (TA and TRPL) and device characterization tools such as transient photovoltage to examine the charge carrier dynamics. Sample preparation protocol is another inconsistent element as the apparent layer properties vary from one sample to another. The experiments ought to be carried out applying similar laser fluences and environmental conditions. Additionally, it is pivotal that the same sample is implemented performing complementary measurements and preferentially the same illuminated region of the sample must be used. Also safeguarding that the collected data is representative it is advisable to translate the sample during the measurements in x and y-directions by using a stage upon laser irradiation. Comparing the data using half-stacks in the spectroscopic measurements and complete devices using characterization tools differ significantly, however the fluence regime yields critical information on the respective physical processes.

The simplified picture is using the neat perovskite as the fundamental processes must be rationalized prior to any complex structure

such as using the CTLs. There is a demand of carrying out fluence dependent spectroscopy at low fluence regime (nJ/cm^2) and ideally similar samples should be used across complementary techniques [655]. Here, the identified experimental barrier is that TRPL uses lower fluences compared to TA, this implies that determining the charge recombination and extraction rates are not comparable across. However, both the charge recombination and extraction can be evaluated against the photo generated excited state carrier density in apparent measurements.

Furthermore, combining transient absorption spectroscopy and transient reflection spectroscopy will provide viable information in differentiating the bulk recombination and surface recombination [656]. Here the latter technique enables accessibility to surface recombination in neat perovskites. Other approaches such as using teraherz pump-probe spectroscopy been employed with great deal of success and serves as a promising candidate for complementary measurements [657,658].

4. Concluding remarks

Evaluating and tracking the photophysical processes are critical for further advancement of the opto-electronic device's efficiency. Hence, it is of paramount importance to understand these processes and develop the experimental protocols to conduct accurate set of measurements and carefully perform the data analysis. Identifying the above-mentioned processes using complementary spectroscopic and electro-optical techniques are routes for further advancement with the necessity of developing consistent models to fit the charge carrier dynamics. With this we hope that the physical processes can be unraveled using the photoactive absorber layer, which can be gradually extended to half-stacks and complete device stacks to examine the additional processes of charge transport layers and electrodes.

XVII. Halide perovskite for neuromorphic computing

Guanglong Ding,[1,2] Su-Ting Han,[3] Ye Zhou[1,4*]

[1]State Key Laboratory of Radio Frequency Heterogeneous Integration, Shenzhen University, Shenzhen 518060, PR China

[2]College of Electronics and Information Engineering, Shenzhen University, Shenzhen 518060, PR China

[3]Department of Applied Biology and Chemical Technology, The Hong Kong Polytechnic University, Hung Hom, Hong Kong SAR, P. R. China.

[4]Institute for Advanced Study, Shenzhen University, Shenzhen, China.

E-mail address: yezhou@szu.edu.cn

1. Status of the field

The brain-inspired neuromorphic computing system demonstrates the interconnection between artificial neurons through artificial synapses, thereby establishing artificial neural networks (ANNs) to emulate the functions of biological neural networks. Diverging from conventional von Neumann computing architectures, neuromorphic computing systems enable in-memory computing, event-driven processing, and parallel computation for task execution. Therefore, constructing a hardware-level brain inspired-neuromorphic computing system has been widely regarded as an efficiency approach to enhance computational power and reduce power consumption for solving the contradiction between the generation of massive amounts of data and the low energy efficiency in processing capacity exhibited by von Neumann computing systems. Taking advantage of intrinsic physical phenomena of functional materials for exploring neuromorphic devices and modulating device resistances is a key idea.

Halide perovskites are the solution-processable semiconducting materials with the cubic crystal structure and general formula ABX_3 (A: monovalent cation, B: divalent metal cation, X: halide anion), which combines the advantages of both inorganic and organic materials in terms of electrical performance and flexibility. Halide perovskites can exhibit dynamic processes of both electronic charges and ions in response to various external stimuli (e.g., electric, pressure, magnetic, and illumination), supporting diverse resistive switching mechanisms such as halide ion migration-induced conductive filaments (CFs), electrochemical metallization (ECM), spin-dependent charge transport, and photosensitivity, which contribute to the precise modulation to the conductance state of memristors and synaptic transistors [659]. Furthermore, their high responsiveness to external stimuli, particularly photosensitivity, endows halide perovskites with excellent multifunctionality, making them one of the most promising options for developing neuromorphic devices within the "More than Moore" strategy.

2. Current and future challenges

Despite being a prominent area of research in the field of brain-inspired chips, practical applications for halide perovskite-based neuromorphic devices and computing systems are still distant. To achieve industrial practical application, some challenges need to be addressed in current scientific research and future mass production (Fig. 40).

2.1. Stability and reproducibility

The primary challenge in the field of halide perovskites is achieving stability. Most types of halide perovskites, particularly organic and inorganic hybrid perovskites, are highly sensitive to environmental factors such as oxygen, humidity, temperature, and light [660]. This sensitivity is largely influenced by parameters like crystallinity degree, grain size, and defect density [661,662]. The resulting instability can lead to low performance reproducibility and poor long-term reliability. Furthermore, the solution film formation process magnifies the influence of human factors and make it difficult to obtain repeatable film, further aggravating the device reproducibility.

2.2. Downscaling and integration

The development of practical brain-inspired chips not only require careful material innovation/selection and device design/optimization, but also necessitates the integration of various functional elements, such as artificial neurons/synapses and peripheral circuits, for realizing the efficient execution of the computing tasks with low power consumption. However, the integration of different halide perovskite based neuromorphic elements is still a challenge. Currently, most perovskite-based neuromorphic devices are limited to dot array or simple cross-bar structures. Moreover, the nano/micro lithography and patterning limitations of halide perovskite films have hinder the device downscaling required in integration processes.

2.3. Toxicity and implantability

The multifunctionality and solution-processable film formation property enhance the potential applications of halide perovskite-based neuromorphic devices in areas such as smart wearables, intelligent prosthetics, and brain-computer interfaces. However, the limited longevity in complex physiological environments, facile ion migration in liquid conditions, and toxicity of Pb to biological cells restrict the utilization of halide perovskites in these fields, particularly in certain implantable areas. Moreover, achieving a balance between electrical performance and biodegradability is interesting and challenging for developing non-toxic halide perovskite-based transient electronics [663].

3. Advances to address these challenges

To improve the film stability and device reproducibility, interface manipulation, surface passivation, protective coating, compositional engineering, ionic liquid, doping, and self-assembled monolayers have been introduced for optimizing the film composition, improving the film quality (reducing defects and increasing crystallinity degree), and protecting the film from external environment [660–662]. The recently reported liquid medium annealing method enables precise control over the crystal growth process, resulting in the fabrication of perovskite films of exceptional quality that exhibit remarkable stability under high humidity (80 %) and temperature (85 °C) conditions [664]. In comparison to solution film formation methods, the vacuum film deposition strategy offers a significant advantage by mitigating the potential negative influence of human factors, thereby facilitating high reproducibility [665,666].

The challenges associated with downsizing and patterning can be

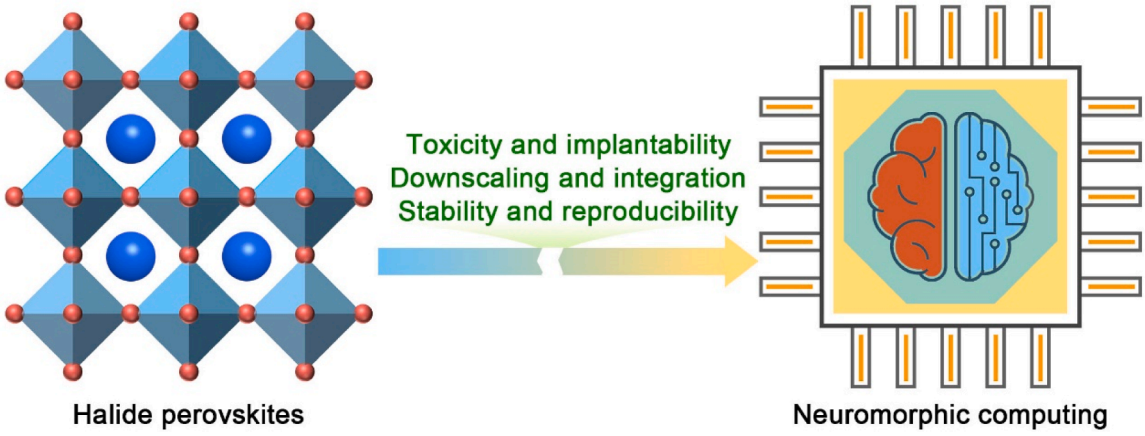

Fig. 40. Schematic diagram of the challenges about halide perovskites for neuromorphic computing.

partially mitigated through the implementation of a microplate seeding strategy, enabling the realization of perovskite crystal growth at a small size (10 μm) in specific spatial locations, while maintaining periodic arrangement over a large area (4-inch wafer) [667]. By integrating the film formation method with nanoengineered porous alumina membrane, the highly uniform and dense three-dimensional (3D) halide perovskite nanowires can be achieved. These nanowires exhibit excellent potential as resistive switching layers for developing memristor arrays with small cell size (lateral dimension: 14 nm), fast switching speed (approximately 100 ps), low performance variability, and high device density for data storage, neuromorphic computing, and visual identity [668–671]. Furthermore, the 3D vertical stack strategy can be also employed to facilitate the integration of perovskite neuromorphic devices [672].

The direct approach to reduce the device toxicity involves the exploration of high-performance lead-free perovskite materials [673, 674]. The replacement of Pb elements with alternative elements (such as Sn, Bi/Sb, and Cu/Ag) enables the development of lead-free perovskites, offering a promising avenue for interfacing biological cells/tissues with neuromorphic devices. Additionally, achieving implantability necessitates the integration of lead-free perovskites with other biocompatible device components (e.g., substrates and electrodes). Simultaneously, ensuring and balancing stability and reliability across all constituents of neuromorphic devices is crucial, particularly in transient electronics.

4. Concluding remarks

Achieving practical manufacturing of brain-like chips based on perovskite neuromorphic computing requires a sustained and extensive effort in material innovation, device design, and application exploration. To accomplish this objective, interdisciplinary collaboration among neuroscientists, material scientists, device engineers, and computer scientists is essential to address challenges related to stability, integration, and implantability while constructing hardware-based ANNs for achieving low power consumption and high efficiency computing.

Acknowledgements

We acknowledge grants from the National Natural Science Foundation of China (Grant No. 62304137), Guangdong Basic and Applied Basic Research Foundation (Grant No. 2023A1515012479), the Science and Technology Innovation Commission of Shenzhen (Grant No. JCYJ20220818100206013), RSC Researcher Collaborations Grant (Grant No. C23-2422436283), State Key Laboratory of Radio Frequency Heterogeneous Integration (Independent Scientific Research Program No. 2024010).

XVIII. Halide perovskite memory

Ruifu Zhou, Jang-Sik Lee*

Department of Materials Science and Engineering, Pohang University of Science and Technology (POSTECH), Pohang, Gyeongbuk, 37673, Republic of Korea

E-mail: jangsik@postech.ac.kr

1. Status of the field

The swift progression of technologies, including the Internet of Things (IoT) and artificial intelligence, has precipitated an increasing demand for next-generation memory devices. Emerging non-volatile memory technologies must deliver substantial storage capacity and high-speed performance. Notably, resistive switching memory (RSM) is known for its simple architecture, high speed operation, low power consumption, and prolonged data retention capabilities [7].

Metal halide perovskites have garnered significant attention as potential active layers in RSM devices, attributable to their cost-effective fabrication processes, tunable band gap properties, high resistive switching on/off ratios, and inherent mechanical flexibility [675,676]. Additionally, the hysteresis observed in the current-voltage characteristics of halide perovskites, resulting from the movement of defects and ions, can be strategically utilized in the development of RSM devices. Moreover, the ease of fabricating halide perovskite on flexible substrates is crucial for advanced flexible electronic devices [677].

The RSM device based on halide perovskite features a perovskite layer sandwiched between two metal electrodes (Fig. 41a). The resistive switching mechanisms can be generally categorized into filamentary-type and interface-type. In filamentary-type switching, the transition between resistance states is governed by the formation and rupture of conductive filaments, typically driven by metal ion migration or halide vacancies. Interface-type switching is controlled by changes in the Schottky barrier at the electrode-perovskite interface, which adjust the resistance of RSM devices and facilitate memory functionality [678]. The first report on the RSM device utilizing halide perovskite was published in 2015, which used $CH_3NH_3PbI_{3-x}Cl_x$ as the active layer, via spin-coating deposition [679]. Since then, various halide perovskites have been employed as active layers in memory devices, demonstrating outstanding performance characteristics.

2. Current and future challenges

Despite recent studies demonstrating the remarkable performance of halide perovskite-based RSM devices, a significant gap remains between their current research advancements and the prospects for formal commercialization. The implementation of halide perovskite-based RSM devices in practical applications necessitates enhancements in various properties, particularly the on/off ratio, endurance and retention time.

Halide perovskites facilitate low energy switching owing to their reduced defect formation and ion migration energy. However, they encounter significant challenges related to unstable conductive filament formation, which results in diminished endurance and elevated power consumption. Retention time is a critical performance metric for memory devices; however, retention times for halide perovskite-based RSM devices are generally limited. This limitation is primarily attributed to

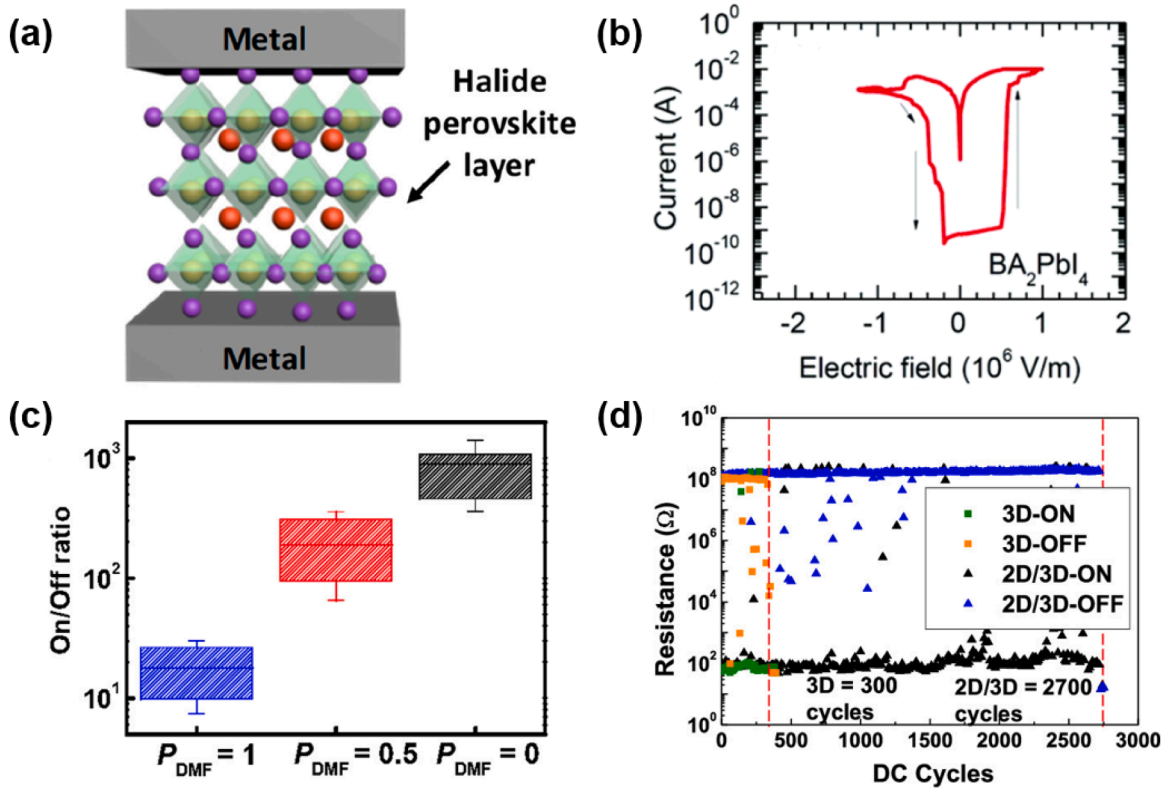

Fig. 41. (a) Schematic of the RSM structure with halide perovskites. Reproduced with permission from [ref. 656]. Copyright 2022, American Chemical Society. (b) I−V curve of the RSM utilizing the 2D BA_2PbI_4. Reproduced with permission from [ref. 661]. Copyright 2017, The Royal Society of Chemistry. (c) Variations in the on/off ratio across different V_{DMF}/V_{DMSO}. Reproduced with permission from [ref. 664]. Copyright 2022, American Chemical Society. (d) Endurance performance of the 2D/3D halide perovskite heterojunction. Reproduced with permission from [ref. 665]. Copyright 2020, American Chemical Society.

low ion migration barriers and a heightened sensitivity to environmental factors, both of which contribute to accelerated ion transport and structural degradation. Moreover, the issue of degradation resulting from moisture in the ambient air requires resolution [680,681].

3. Advances to meet challenges

Low-dimensional halide perovskite, particularly two-dimensional (2D) Ruddlesden−Popper phase, offers a promising solution for improving memory device performance. For example, Seo et al. demonstrated that two-dimensional (2D) BA_2PbI_4 exhibited superior resistive switching performance, including a higher on/off ratio, compared to three-dimensional (3D) $MAPbI_3$, as illustrated in Fig. 41b [682]. The dimensionality of the metal halide perovskites was modulated by adjusting the stoichiometric molar ratio between butylammonium (BA) cations and methylammonium (MA) cations within the perovskite layers. This enhanced performance can be attributed to the increased Schottky barrier heights and elevated thermal activation energy.

Stability is another critical attribute for memory devices as we mentioned above. The stability of 2D Ruddlesden−Popper phase halide perovskite is affected by the van der Waals gap, whereas Dion−Jacobson phase halide perovskite demonstrates augmented stability due to the direct bonding between contiguous inorganic perovskite layers. Lee et al. demonstrated that Dion−Jacobson phase metal halide perovskites exhibit superior cycling endurance compared to Ruddlesden−Popper phase halide perovskite, maintaining stable resistive switching performance even after 10 days in an ambient environment [683]. Furthermore, the adjustment of the proportion of dimethylformamide (DMF) and dimethyl sulfoxide (DMSO) effectively regulates the grain sizes of Dion−Jacobson phase halide perovskite, thereby facilitating changes in the on/off ratio within RSM devices, as shown in Fig. 41c. Furthermore, the integration of a 2D/3D heterojunction has been demonstrated to markedly enhance the endurance and stability of the device, as illustrated in Fig. 41d [684].

Furthermore, artificial synapses, which serve as the cornerstone of neuromorphic computing, have been the subject of extensive research in recent years. Halide perovskite-based RSM devices have attracted considerable interest as potential candidates for artificial synapses, owing to their high on/off ratios for resistive switching, cost-effectiveness, superior optical and charge transport properties, and mechanical flexibility. These devices enable the emulation of a variety of neural behaviors, providing a foundational framework for neuromorphic computing. Furthermore, they exhibit exceptionally low energy consumption, with the energy required for a single neural event estimated at approximately 0.7 fJ, which is comparable to the power consumption of biological synapses [685,686].

4. Concluding remarks

RSM device represents a viable alternative to traditional memory devices. Recent investigations have highlighted halide perovskite materials as promising candidates for RSM applications, capitalizing on their hysteresis characteristics and superior properties conducive to resistive switching behaviors. While current research indicates that the performance of halide perovskite-based RSM devices, particularly in terms of endurance and stability, does not yet meet commercial standards. However, it is important to acknowledge that this area of research is still in its early developmental phase. Through continued investigation of the material and device architectures, there exists considerable potential for substantial enhancements in performance in the foreseeable future.

XIX. Halide perovskites for high-performance field-effect transistors

Geonwoong Park, Youjin Reo*, Yong-Young Noh*

Department of Chemical Engineering, Pohang University of Science and Technology (POSTECH), Pohang, Gyeongbuk 37673, Republic of Korea

E-mail address: yjreo97@postech.ac.kr; yynoh@postech.ac.kr

1. Status of the field

The scope of perovskite electronics extends to transistors, specifically field-effect transistors (FETs). FETs are fundamental building blocks of modern electronics that amplify or switch electrical signals through voltage control and can serve as test platforms for electrical properties of the semiconducting materials [687]. Halide perovskites are excellent candidates for the channel layer of FETs, as their dispersive valence band maximum and small effective mass promote efficient charge transport [9,10].

FETs require horizontal carrier transport between the source and drain electrodes when given gate bias voltage. To quantitatively assess the electrical performance of FETs, these figures of merit should be taken into consideration: field-effect mobility (μ), on/off current ratio (I_{on}/I_{off}), threshold voltage (V_T), and the subthreshold swing (SS). μ refers to how quickly charge carriers can be transported through the channel layer when the electric field is applied. The mobility can be described by $\mu = \frac{q\tau}{m^*}$ where q is the elementary charge of an electron, m^* is effective mass estimated from first-principles calculations of band curvature, and τ is transport time affected by intrinsic phonon scattering and extrinsic effects such as grain boundaries and disorder [688]. I_{on}/I_{off} measures the switching efficiency from ON-state to OFF-state. V_T is the minimum gate-to-source voltage difference needed to begin significant conduction from the source to drain electrode. Lastly, SS quantifies the change in gate voltage needed to increase the drain current by one order of magnitude in the subthreshold region (below V_T), which are governed by the current-voltage relationship $I_D = \mu C_{ox}\frac{W}{L}(V_{GS} - V_T)^2$ in saturation region.

Transistors can be n-type, p-type or ambipolar, depending on their major carrier type. Appropriate combinations of n-type and p-type FETs are required to fabricate complementary circuits with reduced power consumption [689,690]. Research on p-type halide perovskite FETs is heavily focused on tin-based perovskites. The low formation energy of positively charged tin vacancies and their small hole effective mass bring tin-based perovskites as promising p-type semiconductor. The record-high performance of p-type tin-based halide perovskite FETs is based on the combination of triple A-site cations, cesium, formamidinium and phenethylammonium (CsFAPEA), achieving $\mu \sim 70$ $cm^2\ V^{-1}\ s^{-1}$, I_{on}/I_{off} of 10^8, V_T of 20.4 V, and SS of 0.5 V dec^{-1} [606]. Ambipolar behavior is often observed in lead-based perovskites due to the deeper Pb 6*s* state, causing lanthanide shrinkage, stronger spin-orbit coupling effect and consequently smaller electron effective mass [691,692]. Suitable electron doping and defect passivation can induce stronger n-type properties of lead-based perovskites, driving the current record parameters to $\mu \sim 33$ $cm^2\ V^{-1}\ s^{-1}$, I_{on}/I_{off} of 10^8, V_T of 1.84 V and SS of 0.24 V dec^{-1} [693]. Notably, the first all-perovskite complementary circuit was designed with p-type phenethylammonium tin iodide ($(PEA)_2SnI_4$) and n-type cesium tin(IV) iodide (Cs_2SnI_6), demonstrating a peak gain of 38 [694].

2. Current and future challenges

To achieve high-performance halide perovskite FETs, the perovskite community faces three fundamental challenges: fabrication of high-quality thin-film, efficient charge transport with good stability, and technical challenges in scalability and acute patterning of complex circuits. The quality of the thin-film ensures efficiency of charge transport associated with their intrinsic defects. Due to the heavy focus on solution-process as the fabrication method of halide perovskite FETs, issues regarding chemical properties and interactions of precursor materials and solvent should be considered. In tin-based perovskites, the strong Lewis acidity of Sn^{2+} drives the rapid crystallization of perovskite thin-film, causing poor uniformity with physical defects [695].

In addition, tin-based perovskites typically have high hole density due to intrinsically low formation energy of tin vacancies and facile Sn^{2+} oxidation, inducing self p-doping and resembling characteristics of a conductor [696]. To counteract this issue, large organic A-site cations were incorporated to control hole density, and protect $[SnI_6]^{4-}$ octahedra layer against oxidation by forming two-dimensional (2D) or quasi-2D halide perovskites [697–699]. However, these organic spacers demonstrate insulating properties with anisotropic charge transport, disrupting their transport efficiency. In contrast, three-dimensional (3D) halide perovskites support isotropic transport, which is more suitable for FET application. Therefore, recent studies reveal research interest focused on higher dimension tin-based perovskite FETs and achieving high-quality thin-film for high FET mobility.

High-performance FETs must be discussed together with high stability, including environmental and operational stability. Due to the facile Sn^{2+} oxidation, tin-based perovskite FETs face challenges in practical applications. Therefore, effective measures should be taken to hinder or reverse the oxidation process [700]. Compared to tin-based perovskites, lead-based counterparts demonstrate higher stability against oxidation due to deeper states of Pb 6*s*. However, the most critical issue arises from halide defects, causing ion migration to impede field-effect operation. Ion migration is one of the leading factors of hysteresis behavior, and poses limitations to possible measurement methods, narrowing the choices to low-temperature measurements and pulse-mode measurements at short intervals [701,702].

Furthermore, the development of high-performance p-type tin-based perovskite FETs and n-type lead-based perovskites directs our attention to their application in large-scale devices and their integration into complementary circuits. One of the essential step in fabrication of high-performance FETs based on high dimensional perovskites is anti-solvent dripping during thin-film crystallization [703]. While this step is crucial for initiating formation of nucleation sites, it is difficult to achieve high uniformity of anti-solvent effect on large-scale substrates. In addition, to precisely design an integrated circuit, fine resolution patterning of perovskite channel layer is required. The patterning of solution-processed perovskite thin-film faces fundamental challenges due to the fragility of perovskite thin-film with solvents commonly used in photolithography [704].

3. Advances to address these challenges

In recent years, diverse measures have been introduced to address the challenges in the fabrication and application of halide perovskite FETs. To address the issues in rapid thin-film crystallization of tin-based perovskites, tin fluoride (SnF_2) marks its place as a representative additive to produce high-quality thin-film and regulate high hole density [705]. However, the sole use of SnF_2 can cause aggregation due to low solubility of the material. Hence, alternative combinations of additives, such as SnF_2-pyrazine or SnF_2-SbF_3 have been introduced to enhance solubility and fabricate highly uniform thin-film, as shown in Fig. 42a [706,707]. In addition, dimethyl sulfoxide (DMSO) is often used to retard the thin-film crystallization by forming Lewis acid-base DMSO intermediate adducts. While effective, the Sn^{2+}-DMSO complex can accelerate Sn^{2+} oxidation in tin-based perovskite solutions [182,699]. To prevent this issue, precursor aging of perovskite precursor solution dissolved only in dimethylformamide was introduced to promote uniform distribution of perovskite colloids and enhance film crystallinity without the addition of DMSO, as shown in Fig. 42b [708].

The chemical composition of halide perovskites is another critical research field to be explored to induce favorable chemical reactions and fabricate high-quality thin-film. Liu et al. introduced the incorporation of tin-lead alloy with optimized excess cesium to increase thin-film crystallinity of $CsSnI_3$-based thin-film and achieved $\mu \sim 50$ $cm^2\ V^{-1}\ s^{-1}$ and $I_{on}/I_{off} > 10^8$ through associated FETs [709]. Moreover, Zhu et al. demonstrated the fabrication of highly ordered cascaded 2D/3D thin-film using triple A-site cation combination of Cs/FA/PEA, elevating μ up to 70 $cm^2\ V^{-1}\ s^{-1}$ and $I_{on}/I_{off} > 10^8$. The use of triple cations regulated the formation of nucleation sites to improve phase purity and thin-film crystallinity, as shown in Figs. 42c-d [606]. The combination of triple X-site halide (I/Br/Cl) also improved thin-film crystallinity by forming I-Br-Cl bridge effect to prevent the formation of halide vacancy defects [710]. In addition, pseudohalide additives can be incorporated

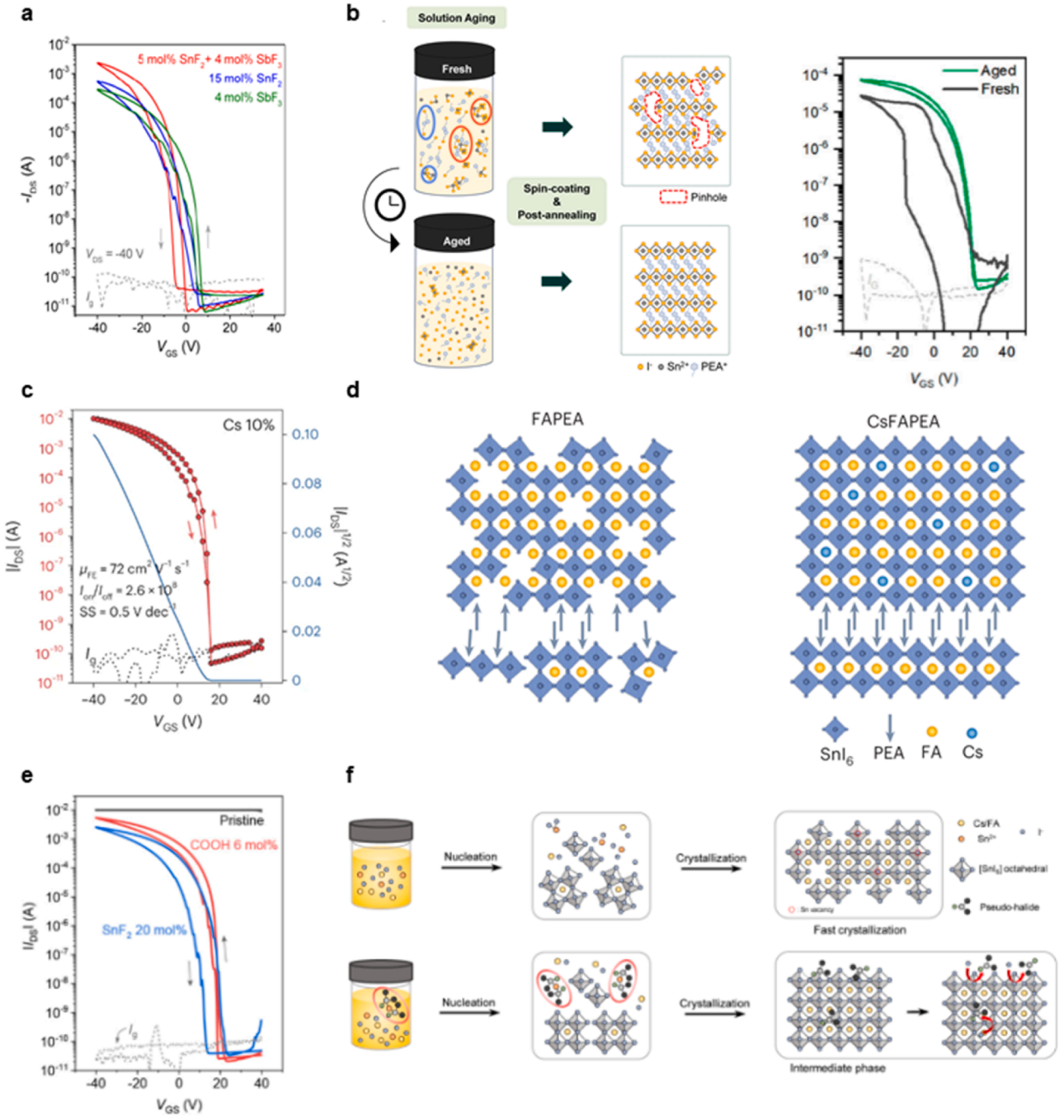

Fig. 42. **a,** Transfer curves of $CsSnI_3$-based FETs with SnF_2 and SbF_3 additives [707]. Reproduced with permission. Copyright 2023, Wiley-VCH. **b,** Precursor aging of $(PEA)_2SnI_4$ solution and associated FET transfer curves [708]. Reproduced with permission. Copyright 2023, American Chemical Society. **c,** Transfer curves of Cs/FA/PEA-based tin perovskite FETs. **d,** Effect of Cs on lattice structure of 2D/3D FAPEA-based tin perovskites [606]. Reproduced with permission. Copyright 2023, Nature Publishing Group. **e,** Transfer characteristics of Cs/FA-based tin perovskite FETs with SnF_2 and pseudohalide additives. **f,** Schematic of pseudohalide effect on tin-based perovskite thin-film crystallization [711]. Reproduced with permission. Copyright 2024, Elsevier.

to modulate rate of crystallization and adjust hole density, achieving μ~60 $cm^2\ V^{-1}\ s^{-1}$ and I_{on}/I_{off} over 10^8, as shown in Fig. 42 e-f [711]. Sufficient p-doping can be achieved by capping organic molecules [712], which also enables a dramatic improvement in PEAFASnI TFT performance, with a μ of 53 $cm^2\ V^{-1}\ s^{-1}$ and an I_{on}/I_{off} over 10^7 [713].

The research on chemical composition expands to lead-based perovskites, specifically to prevent defect formation that causes ion migration. Senanayak et al. introduced a quadruple mixed-cation structure involving Rb/Cs/MA/FA and the use of azeotropic Lewis base(acid) solvents to reduce lattice strains and defect density, increasing $\mu > 1$ $cm^2\ V^{-1}\ s^{-1}$, as shown in Fig. 43a [687]. In addition, a solvent-based cleaning and healing method was developed for surface passivation, enabling continuous mode measurements for lead-based perovskite FETs and achieving $\mu > 3$ $cm^2\ V^{-1}\ s^{-1}$, as described in Fig. 43b [714]. Fig. 43c-d illustrates one of the most recent breakthroughs in n-type lead-based perovskite FETs, where methylammonium chloride was used for perovskite lattice relaxation and tetramethylammonium fluoride was chosen for passivation of undercoordinated lead sites on interfaces by multidentate anchoring [693]. The reduced defect density recorded champion device with μ ~ 30 cm^2

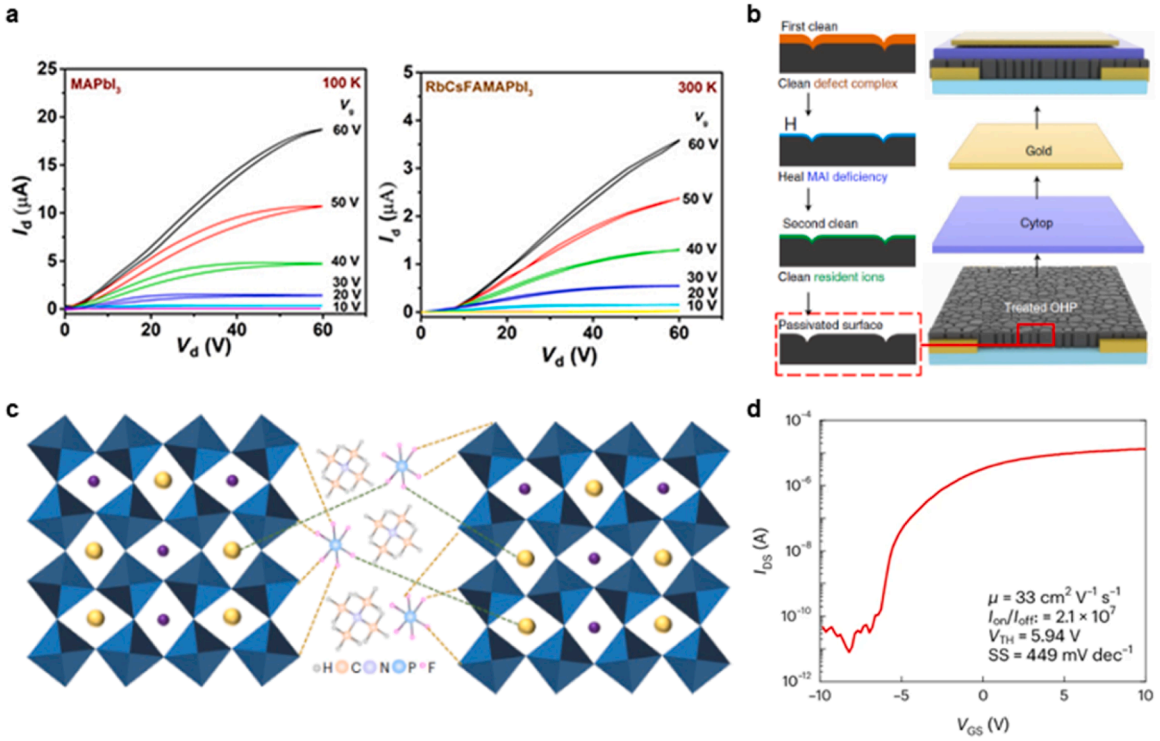

Fig. 43. a, Effect of Rb/Cs/FA/MA combination on FET hysteresis, measured by output characteristics [687]. Reproduced with permission. Copyright 2020, American Association for the Advancement of Science. **b,** Schematic of $MAPbI_3$-based FET fabrication with the solvent cleaning process [714]. Reproduced with permission. Copyright 2020, Nature Publishing Group. **c,** Schematic of strain relaxation in perovskite crystal through incorporation of MA. **d,** Corresponding transfer characteristics [693]. Reproduced with permission. Copyright 2024, Nature Publishing Group.

V^{-1} s^{-1} and I_{on}/I_{off} exceeding 10^7. Thus, the functional design of chemical composition with suitable use of additives and solvents can promote the fabrication of high-quality thin-film and high-performance halide perovskite FETs.

Furthermore, the integration of the high-performance n-type and p-type perovskite FETs for complementary circuits requires high-resolution patterning [606,699]. To avoid degradation of perovskite thin-film from photolithography solvents, another technique such as self-patterning method has been developed [710]. An alternative option is depositing perovskite thin film through an industry-compatible thermal evaporation method. Channel layers can be patterned using fine metal masks. Until now, there have been only a few reports on thermally evaporated perovskite FETs, 2D layered $K_2MnCl_2I_2$ on a KI seed layer, for example [297,715,716]. The successful commercialization of thermally evaporated photovoltaics and light emitting diodes brightens the future for thermally evaporated perovskite FETs with the ability for fine patterning and large-area fabrication.

4. Concluding remarks

The continuously growing field of halide perovskite transistors for over two decades has led their success to achieve parameters comparable to those of commercialized low-temperature polysilicon technologies. Through the combined development of tin-based perovskites as p-type FETs and lead-based perovskites as n-type FETs, halide perovskites demonstrate high compatibility in complementary electronics and logic circuits. FETs serve as an important platform for in-depth investigation of the intrinsic charge transport properties of halide perovskites. Through a step-by-step understanding of the correlation between chemical composition, thin-film deposition and crystallization, and device engineering, high-performance, highly reproducible, and stable halide perovskite FETs can be further developed for versatile electronic applications.

CRediT authorship contribution statement

Ao Liu: Conceptualization, Formal analysis, Investigation, Resources, Data curation, Supervision, Project administration, Funding acquisition, Writing – original draft, Writing – review & editing. **Jun Xi:** Formal analysis, Investigation, Resources, Data curation, Supervision, Project administration, Funding acquisition, Writing – original draft, Writing – review & editing. **Hanlin Cen:** Formal analysis, Investigation, Resources, Data curation, Writing – original draft, Writing – review & editing. **Jinfei Dai:** Formal analysis, Investigation, Resources, Data curation, Writing – original draft, Writing – review & editing. **Yi Yang:** Formal analysis, Investigation, Resources, Data curation, Writing – original draft, Writing – review & editing. **Cheng Liu:** Formal analysis, Investigation, Resources, Data curation, Supervision, Project administration, Funding acquisition, Writing – original draft, Writing – review & editing. **Shuai Guo:** Formal analysis, Investigation, Resources, Data curation, Writing – original draft, Writing – review & editing. **Xiaofang Li:** Formal analysis, Investigation, Resources, Data curation, Writing – original draft, Writing – review & editing. **Xiaotian Guo:** Formal analysis, Investigation, Resources, Data curation, Writing – original draft, Writing – review & editing. **Feng Yang:** Formal analysis, Investigation, Resources, Data curation, Supervision, Project administration, Funding acquisition, Writing – original draft, Writing – review & editing. **Meng Li:** Formal analysis, Investigation, Resources, Data curation, Supervision, Project administration, Funding acquisition, Writing – original draft, Writing – review & editing. **Haoxuan Liu:** Formal analysis, Investigation, Resources, Data curation, Writing – original draft, Writing – review & editing. **Fei Zhang:** Formal analysis, Investigation, Resources, Data curation, Supervision, Project administration, Funding acquisition, Writing – original draft, Writing – review & editing. **Huagui Lai:** Formal analysis, Investigation, Resources, Data curation, Writing – original draft, Writing – review & editing. **Fan Fu:** Formal analysis, Investigation, Resources, Data curation, Supervision, Project

administration, Funding acquisition, Writing – original draft, Writing – review & editing. **Shuaifeng Hu:** Formal analysis, Investigation, Resources, Data curation, Supervision, Project administration, Funding acquisition, Writing – original draft, Writing – review & editing. **Junke Wang:** Formal analysis, Investigation, Resources, Data curation, Writing – original draft, Writing – review & editing. **Seongrok Seo:** Formal analysis, Investigation, Resources, Data curation, Writing – original draft, Writing – review & editing. **Henry J. Snaith:** Formal analysis, Investigation, Resources, Data curation, Supervision, Project administration, Funding acquisition, Writing – original draft, Writing – review & editing. **Jinghui Li:** Formal analysis, Investigation, Resources, Data curation, Writing – original draft, Writing – review & editing. **Jiajun Luo:** Formal analysis, Investigation, Resources, Data curation, Supervision, Project administration, Funding acquisition, Writing – original draft, Writing – review & editing. **Hongjin Li:** Formal analysis, Investigation, Resources, Data curation, Writing – original draft, Writing – review & editing. **Yun Gao:** Formal analysis, Investigation, Resources, Data curation, Writing – original draft, Writing – review & editing. **Xingliang Dai:** Formal analysis, Investigation, Resources, Data curation, Supervision, Project administration, Funding acquisition, Writing – original draft, Writing – review & editing. **Jia Zhang:** Formal analysis, Investigation, Resources, Data curation, Writing – original draft, Writing – review & editing. **Feng Gao:** Formal analysis, Investigation, Resources, Data curation, Supervision, Project administration, Funding acquisition, Writing – original draft, Writing – review & editing. **Zhengxun Lai:** Formal analysis, Investigation, Resources, Data curation, Writing – original draft, Writing – review & editing. **You Meng:** Formal analysis, Investigation, Resources, Data curation, Supervision, Project administration, Funding acquisition, Writing – original draft, Writing – review & editing. **Johnny C. Ho:** Formal analysis, Investigation, Resources, Data curation, Supervision, Project administration, Funding acquisition, Writing – original draft, Writing – review & editing. **Wen Li:** Formal analysis, Investigation, Resources, Data curation, Writing – original draft, Writing – review & editing. **Yuntao Wu:** Formal analysis, Investigation, Resources, Data curation, Supervision, Project administration, Funding acquisition, Writing – original draft, Writing – review & editing. **Liping Du:** Formal analysis, Investigation, Resources, Data curation, Writing – original draft, Writing – review & editing. **Sai Bai:** Formal analysis, Investigation, Resources, Data curation, Writing – original draft, Writing – review & editing. **Huihui Zhu:** Formal analysis, Investigation, Resources, Data curation, Supervision, Project administration, Funding acquisition, Writing – original draft, Writing – review & editing. **Xianhang Lin:** Formal analysis, Investigation, Resources, Data curation, Supervision, Project administration, Funding acquisition, Writing – original draft, Writing – review & editing. **Can Deng:** Formal analysis, Investigation, Resources, Data curation, Writing – original draft, Writing – review & editing. **Liyi Yang:** Formal analysis, Investigation, Resources, Data curation, Writing – original draft, Writing – review & editing. **Liu Tang:** Formal analysis, Investigation, Resources, Data curation, Writing – original draft, Writing – review & editing. **Ahmad Imtiaz:** Formal analysis, Investigation, Resources, Data curation, Writing – original draft, Writing – review & editing. **Hanxiang Zhi:** Formal analysis, Investigation, Resources, Data curation, Writing – original draft, Writing – review & editing. **Xi Lu:** Formal analysis, Investigation, Resources, Data curation, Writing – original draft, Writing – review & editing. **Heng Li:** Formal analysis, Investigation, Resources, Data curation, Writing – original draft, Writing – review & editing. **Xiangyu Sun:** Formal analysis, Investigation, Resources, Data curation, Writing – original draft, Writing – review & editing. **Yicheng Zhao:** Formal analysis, Investigation, Resources, Data curation, Supervision, Project administration, Funding acquisition, Writing – original draft, Writing – review & editing. **Jian Xu:** Formal analysis, Investigation, Resources, Data curation, Supervision, Project administration, Funding acquisition, Writing – original draft, Writing – review & editing. **Xiaojian She:** Formal analysis, Investigation, Resources, Data curation, Supervision, Project administration, Funding acquisition, Writing – original draft, Writing – review & editing. **Jafar Iqbal Khan:** Formal analysis, Investigation, Resources, Data curation, Supervision, Project administration, Funding acquisition, Writing – original draft, Writing – review & editing. **Guanglong Ding:** Formal analysis, Investigation, Resources, Data curation, Writing – original draft, Writing – review & editing. **Su-Ting Han:** Formal analysis, Investigation, Resources, Data curation, Writing – original draft, Writing – review & editing. **Ye Zhou:** Formal analysis, Investigation, Resources, Data curation, Supervision, Project administration, Funding acquisition, Writing – original draft, Writing – review & editing. **Ruifu Zhou:** Formal analysis, Investigation, Resources, Data curation, Writing – original draft, Writing – review & editing. **Jang-Sik Lee:** Formal analysis, Investigation, Resources, Data curation, Supervision, Project administration, Funding acquisition, Writing – original draft, Writing – review & editing. **Geonwoong Park:** Formal analysis, Investigation, Resources, Data curation, Writing – original draft, Writing – review & editing. **Youjin Reo:** Formal analysis, Investigation, Resources, Data curation, Supervision, Project administration, Funding acquisition, Writing – original draft, Writing – review & editing. **Yong-Young Noh:** Formal analysis, Investigation, Resources, Data curation, Supervision, Project administration, Funding acquisition, Writing – original draft, Writing – review & editing.

Declaration of competing interest

The authors declare that they have no known competing financial interests or personal relationships that could have appeared to influence the work reported in this paper.

Supplementary materials

Supplementary material associated with this article can be found, in the online version, at doi:10.1016/j.mtelec.2025.100138.

Data availability

Data will be made available on request.

References

[1] J.Y. Kim, J.-W. Lee, H.S. Jung, H. Shin, N.-G. Park, Chem. Rev. 120 (2020) 7867–7918.
[2] L.N. Quan, B.P. Rand, R.H. Friend, S.G. Mhaisalkar, T.-W. Lee, E.H. Sargent, Chem. Rev. 119 (2019) 7444–7477.
[3] X.-K. Liu, W. Xu, S. Bai, Y. Jin, J. Wang, R.H. Friend, F. Gao, Nat. Mater. 20 (2021) 10–21.
[4] Y. He, I. Hadar, M.G. Kanatzidis, Nat. Photonics 16 (2022) 14–26.
[5] F.P.G. de Arquer, A. Armin, P. Meredith, E.H. Sargent, Nat. Rev. Mater. 2 (2017) 16100.
[6] A. Liu, H. Zhu, S. Bai, Y. Reo, M. Caironi, A. Petrozza, L. Dou, Y.-Y. Noh, Nat. Electron. 6 (2023) 559–571.
[7] W. Ahmad, C. Li, W. Yu, P. Gao, Mater. Today Electron. 9 (2024) 100106.
[8] K. Wang, D. Yang, C. Wu, M. Sanghadasa, S. Priya, Progress Mater. Sci. 106 (2019) 100580.
[9] L.M. Herz, ACS Energy Lett. 2 (2017) 1539–1548.
[10] J.S. Manser, J.A. Christians, P.V. Kamat, Chem. Rev. 116 (2016) 12956–13008.
[11] T.M. Brenner, D.A. Egger, L. Kronik, G. Hodes, D. Cahen, Nat. Rev. Mater. 1 (2016) 15007.
[12] Y. Vaynzof, Adv. Energy Mater. 10 (2020) 2003073.
[13] B. Saparov, D.B. Mitzi, Chem. Rev. 116 (2016) 4558–4596.
[14] Z. Chen, Y. Guo, E. Wertz, J. Shi, Adv. Mater. 31 (2019) 1803514.
[15] J. Duan, J. Li, G. Divitini, D. Cortecchia, F. Yuan, J. You, S. Liu, A. Petrozza, Z. Wu, J. Xi, Adv. Mater. 36 (2024) 2403455.
[16] Y. Fu, M.P. Hautzinger, Z. Luo, F. Wang, D. Pan, M.M. Aristov, I.A. Guzei, A. Pan, X. Zhu, S. Jin, ACS Central Sci. 5 (2019) 1377–1386.
[17] H. Lin, C. Zhou, Y. Tian, T. Siegrist, B. Ma, ACS Energy Lett. 3 (2018) 54–62.
[18] J. Duan, H. Cen, J. Dai, Z. Wu, J. Xi, Materials Today Electronics 8 (2024) 100097.
[19] D.B. Straus, C.R. Kagan, The Journal of Physical Chemistry Letters 9 (2018) 1434–1447.
[20] Q.A. Akkerman, G. Rainò, M.V. Kovalenko, L. Manna, Nat. Mater. 17 (2018) 394–405.
[21] J. Huang, Y. Yuan, Y. Shao, Y. Yan, Nat. Rev. Mater. 2 (2017) 17042.
[22] A.D. Wright, C. Verdi, R.L. Milot, G.E. Eperon, M.A. Pérez-Osorio, H.J. Snaith, F. Giustino, M.B. Johnston, L.M. Herz, Nat. Commun. 7 (2016) 11755.

[23] K. Miyata, T. L. Atallah and X. Y. Zhu, *Science Advances*, 3, e1701469.
[24] J.-C. Blancon, J. Even, C.C. Stoumpos, M.G. Kanatzidis, A.D. Mohite, Nature Nanotechnology 15 (2020) 969–985.
[25] S.J. Kim, S. Park, H.M. Cho, H.W. Jang, Materials Today Electronics 9 (2024) 100111.
[26] L. Mao, C.C. Stoumpos, M.G. Kanatzidis, J. Am. Chem. Soc. 141 (2019) 1171–1190.
[27] S.P. Dunfield, L. Bliss, F. Zhang, J.M. Luther, K. Zhu, M.F.A.M. van Hest, M. O. Reese, J.J. Berry, Adv. Energy Mater. 10 (2020) 1904054.
[28] M.I. Saidaminov, J. Kim, A. Jain, R. Quintero-Bermudez, H. Tan, G. Long, F. Tan, A. Johnston, Y. Zhao, O. Voznyy, E.H. Sargent, Nature Energy 3 (2018) 648–654.
[29] S. Draguta, O. Sharia, S.J. Yoon, M.C. Brennan, Y.V. Morozov, J.S. Manser, P. V. Kamat, W.F. Schneider, M. Kuno, Nat. Commun. 8 (2017) 200.
[30] Y. Zhou, I. Poli, D. Meggiolaro, F. De Angelis, A. Petrozza, Nat. Rev. Mater. 6 (2021) 986–1002.
[31] J. Sun, K. Wang, K. Ma, J.Y. Park, Z.-Y. Lin, B.M. Savoie, L. Dou, J. Am. Chem. Soc. 145 (2023) 20694–20715.
[32] J. Xi, M.A. Loi, ACS Energy Lett 6 (2021) 1803–1810.
[33] L. Duan, D. Walter, N. Chang, J. Bullock, D. Kang, S.P. Phang, K. Weber, T. White, D. Macdonald, K. Catchpole, H. Shen, Nat. Rev. Mater. 8 (2023) 261–281.
[34] E. Amerling, H. Lu, B.W. Larson, A.E. Maughan, A. Phillips, E. Lafalce, L. Whittaker-Brooks, J.J. Berry, M.C. Beard, Z.V. Vardeny, J.L. Blackburn, ACS Energy Lett 6 (2021) 1104–1123.
[35] K. Sakhatskyi, R.A. John, A. Guerrero, S. Tsarev, S. Sabisch, T. Das, G.J. Matt, S. Yakunin, I. Cherniukh, M. Kotyrba, Y. Berezovska, M.I. Bodnarchuk, S. Chakraborty, J. Bisquert, M.V. Kovalenko, ACS Energy Lett. 7 (2022) 3401–3414.
[36] J. Thiesbrummel, S. Shah, E. Gutierrez-Partida, F. Zu, F. Peña-Camargo, S. Zeiske, J. Diekmann, F. Ye, K.P. Peters, K.O. Brinkmann, P. Caprioglio, A. Dasgupta, S. Seo, F.A. Adeleye, J. Warby, Q. Jeangros, F. Lang, S. Zhang, S. Albrecht, T. Riedl, A. Armin, D. Neher, N. Koch, Y. Wu, V.M. Le Corre, H. Snaith, M. Stolterfoht, Nat. Energy 9 (2024) 664–676.
[37] L.N. Quan, M. Yuan, R. Comin, O. Voznyy, E.M. Beauregard, S. Hoogland, A. Buin, A.R. Kirmani, K. Zhao, A. Amassian, D.H. Kim, E.H. Sargent, J. Am. Chem. Soc. 138 (2016) 2649–2655.
[38] S. Teale, M. Degani, B. Chen, E.H. Sargent, G. Grancini, Nat. Energy 9 (2024) 779–792.
[39] J. Jiang, J. You, S.F. Liu, J. Xi, ACS Energy Lett. 9 (2024) 17–29.
[40] B. Murali, H.K. Kolli, J. Yin, R. Ketavath, O.M. Bakr, O.F. Mohammed, ACS Mater. Lett. 2 (2020) 184–214.
[41] K. Jeong, J. Byeon, J. Jang, N. Ahn, M. Choi, Joule 6 (2022) 1087–1102.
[42] J. Li, Z. Chen, S. Saha, J.K. Utterback, M.L. Aubrey, R. Yuan, H.L. Weaver, N. S. Ginsberg, K.W. Chapman, M.R. Filip, H.I. Karunadasa, J. Am. Chem. Soc. 144 (2022) 22403–22408.
[43] I. Mora-Seró, Joule 2 (2018) 585–587.
[44] C. Liu, Y. Yang, H. Chen, J. Xu, A. Liu, A.S.R. Bati, H. Zhu, L. Grater, S.S. Hadke, C. Huang, V.K. Sangwan, T. Cai, D. Shin, L.X. Chen, M.C. Hersam, C.A. Mirkin, B. Chen, M.G. Kanatzidis, E.H. Sargent, Science 382 (2023) 810–815.
[45] H. Chen, A. Maxwell, C. Li, S. Teale, B. Chen, T. Zhu, E. Ugur, G. Harrison, L. Grater, J. Wang, Z. Wang, L. Zeng, S.M. Park, L. Chen, P. Serles, R.A. Awni, B. Subedi, X. Zheng, C. Xiao, N.J. Podraza, T. Filleter, C. Liu, Y. Yang, J.M. Luther, S. De Wolf, M.G. Kanatzidis, Y. Yan, E.H. Sargent, Nature 613 (2023) 676–681.
[46] Z. Zhang, L. Qiao, K. Meng, R. Long, G. Chen, P. Gao, Chem. Soc. Rev. 52 (2023) 163–195.
[47] Z. Wu, E. Bi, L.K. Ono, D. Li, O.M. Bakr, Y. Yan, Y. Qi, Nano Energy 115 (2023) 108731.
[48] W.-J. Yin, T. Shi, Y. Yan, Applied Physics Letters 104 (2014) 063903.
[49] L.K. Ono, S. Liu, Y. Qi, Angew. Chem. Int. Ed. 59 (2020) 6676–6698.
[50] J.M. Ball, A. Petrozza, Nature Energy 1 (2016) 16149.
[51] L. Wang, H. Zhou, J. Hu, B. Huang, M. Sun, B. Dong, G. Zheng, Y. Huang, Y. Chen, L. Li, Z. Xu, N. Li, Z. Liu, Q. Chen, L.-D. Sun, C.-H. Yan, Science 363 (2019) 265–270.
[52] Y. Yang, C. Liu, Y. Ding, B. Ding, J. Xu, A. Liu, J. Yu, L. Grater, H. Zhu, S.S. Hadke, V.K. Sangwan, A.S.R. Bati, X. Hu, J. Li, S.M. Park, M.C. Hersam, B. Chen, M. K. Nazeeruddin, M.G. Kanatzidis, E.H. Sargent, Nature Energy 9 (2024) 316–323.
[53] Y. Miyazawa, G.M. Kim, A. Ishii, M. Ikegami, T. Miyasaka, Y. Suzuki, T. Yamamoto, T. Ohshima, S. Kanaya, H. Toyota, K. Hirose, The Journal of Physical Chemistry C 125 (2021) 13131–13137.
[54] D. Menzel, A. Al-Ashouri, A. Tejada, I. Levine, J.A. Guerra, B. Rech, S. Albrecht, L. Korte, Adv. Energy Mater. 12 (2022) 2201109.
[55] S. Hu, K. Otsuka, R. Murdey, T. Nakamura, M.A. Truong, T. Yamada, T. Handa, K. Matsuda, K. Nakano, A. Sato, K. Marumoto, K. Tajima, Y. Kanemitsu, A. Wakamiya, Energy Environ. Sci. 15 (2022) 2096–2107.
[56] H. Zhu, Y. Liu, F.T. Eickemeyer, L. Pan, D. Ren, M.A. Ruiz-Preciado, B. Carlsen, B. Yang, X. Dong, Z. Wang, H. Liu, S. Wang, S.M. Zakeeruddin, A. Hagfeldt, M. I. Dar, X. Li, M. Grätzel, Adv. Mater. 32 (2020) 1907757.
[57] T. Duan, S. You, M. Chen, W. Yu, Y. Li, P. Guo, J.J. Berry, J.M. Luther, K. Zhu, Y. Zhou, Science 384 (2024) 878–884.
[58] S. You, F.T. Eickemeyer, J. Gao, J.-H. Yum, X. Zheng, D. Ren, M. Xia, R. Guo, Y. Rong, S.M. Zakeeruddin, K. Sivula, J. Tang, Z. Shen, X. Li, M. Grätzel, Nature Energy 8 (2023) 515–525.
[59] N.K. Noel, A. Abate, S.D. Stranks, E.S. Parrott, V.M. Burlakov, A. Goriely, H. J. Snaith, ACS Nano 8 (2014) 9815–9821.
[60] S. Wang, A. Wang, X. Deng, L. Xie, A. Xiao, C. Li, Y. Xiang, T. Li, L. Ding, F. Hao, J. Mater. Chem. A 8 (2020) 12201–12225.
[61] C. Liu, X. Sun, Y. Yang, O.A. Syzgantseva, M.A. Syzgantseva, B. Ding, N. Shibayama, H. Kanda, F. Fadaei Tirani, R. Scopelliti, S. Zhang, K.G. Brooks, S. Dai, G. Cui, M.D. Irwin, Z. Shao, Y. Ding, Z. Fei, P.J. Dyson, M.K. Nazeeruddin, Science Advances 9 (2023) eadg0087.
[62] H. Zhu, B. Shao, Z. Shen, S. You, J. Yin, N. Wehbe, L. Wang, X. Song, M. Abulikemu, A. Basaheeh, A. Jamal, I. Gereige, M. Freitag, O.F. Mohammed, K. Zhu, O.M. Bakr, Nat. Photonics 19 (2024) 28–35.
[63] C. Liu, Y. Yang, K. Rakstys, A. Mahata, M. Franckevicius, E. Mosconi, R. Skackauskaite, B. Ding, K.G. Brooks, O.J. Usiobo, J.-N. Audinot, H. Kanda, S. Driukas, G. Kavaliauskaite, V. Gulbinas, M. Dessimoz, V. Getautis, F. De Angelis, Y. Ding, S. Dai, P.J. Dyson, M.K. Nazeeruddin, Nat. Commun. 12 (2021) 6394.
[64] W. Kong, C. Zhao, J. Xing, Y. Zou, T. Huang, F. Li, J. Yang, W. Yu, C. Guo, Solar RRL 4 (2020) 2000189.
[65] C.-C. Zhang, S. Yuan, Y.-H. Lou, H. Okada and Z.-K. Wang, *Small*, 2022, 18, 2107556.
[66] F. Wang, Y. Zhang, M. Yang, D. Han, L. Yang, L. Fan, Y. Sui, Y. Sun, X. Liu, X. Meng, J. Yang, Adv. Funct. Mater. 31 (2021) 2008052.
[67] Z. He, C. Zhong, X. Huang, W.-Y. Wong, H. Wu, L. Chen, S. Su, Y. Cao, Adv. Mater. 23 (2011) 4636–4643.
[68] B. Chen, P.N. Rudd, S. Yang, Y. Yuan, J. Huang, Chem. Soc. Rev. 48 (2019) 3842–3867.
[69] Q. Jiang, K. Zhu, Nat. Rev. Mater. 9 (2024) 399–419.
[70] G. Szabó, P.V. Kamat, ACS Energy Lett. 9 (2023) 193–200.
[71] M. Wang, Z. Shi, C. Fei, Z.J.D. Deng, G. Yang, S.P. Dunfield, D.P. Fenning, J. Huang, Nat. Energy 8 (2023) 1229–1239.
[72] Q. Jiang, J. Tong, Y. Xian, R.A. Kerner, S.P. Dunfield, C. Xiao, R.A. Scheidt, D. Kuciauskas, X. Wang, M.P. Hautzinger, R. Tirawat, M.C. Beard, D.P. Fenning, J.J. Berry, B.W. Larson, Y. Yan, K. Zhu, Nature 611 (2022) 278–283.
[73] W. Peng, K. Mao, F. Cai, H. Meng, Z. Zhu, T. Li, S. Yuan, Z. Xu, X. Feng, J. Xu, M. D. McGehee, J. Xu, Science 379 (2023) 683–690.
[74] K. Hossain, A. Kulkarni, U. Bothra, B. Klingebiel, T. Kirchartz, M. Saliba, D. Kabra, ACS Energy Lett. 8 (2023) 3860–3867.
[75] C. Fei, A. Kuvayskaya, X. Shi, M. Wang, Z. Shi, H. Jiao, T.J. Silverman, M. Owen-Bellini, Y. Dong, Y. Xian, R. Scheidt, X. Wang, G. Yang, H. Gu, N. Li, C.J. Dolan, Z. J.D. Deng, D.N. Cakan, D.P. Fenning, Y. Yan, M.C. Beard, L.T. Schelhas, A. Sellinger, J. Huang, Science 384 (2024) 1126–1134.
[76] T. Leijtens, G.E. Eperon, S. Pathak, A. Abate, M.M. Lee, H.J. Snaith, Nat. Commun. 4 (2013) 2885.
[77] H. Chen, C. Liu, J. Xu, A. Maxwell, W. Zhou, Y. Yang, Q. Zhou, A.S.R. Bati, H. Wan, Z. Wang, L. Zeng, J. Wang, P. Serles, Y. Liu, S. Teale, Y. Liu, M. I. Saidaminov, M. Li, N. Rolston, S. Hoogland, T. Filleter, M.G. Kanatzidis, B. Chen, Z. Ning, E.H. Sargent, Science 384 (2024) 189–193.
[78] C. Liu, Y. Yang, H. Chen, I. Spanopoulos, A.S.R. Bati, I.W. Gilley, J. Chen, A. Maxwell, B. Vishal, R.P. Reynolds, T.E. Wiggins, Z. Wang, C. Huang, J. Fletcher, Y. Liu, L.X. Chen, S. De Wolf, B. Chen, D. Zheng, T.J. Marks, A. Facchetti, E.H. Sargent, M.G. Kanatzidis, Nature 633 (2024) 359–364.
[79] S.M. Park, M. Wei, J. Xu, H.R. Atapattu, F.T. Eickemeyer, K. Darabi, L. Grater, Y. Yang, C. Liu, S. Teale, B. Chen, H. Chen, T. Wang, L. Zeng, A. Maxwell, Z. Wang, K.R. Rao, Z. Cai, S.M. Zakeeruddin, J.T. Pham, C.M. Risko, A. Amassian, M.G. Kanatzidis, K.R. Graham, M. Grätzel, E.H. Sargent, Science 381 (2023) 209–215.
[80] L. Luo, H. Zeng, Z. Wang, M. Li, S. You, B. Chen, A. Maxwell, Q. An, L. Cui, D. Luo, J. Hu, S. Li, X. Cai, W. Li, L. Li, R. Guo, R. Huang, W. Liang, Z.-H. Lu, L. Mai, Y. Rong, E.H. Sargent, X. Li, Nat. Energy 8 (2023) 294–303.
[81] Y. Yang, H. Chen, C. Liu, J. Xu, C. Huang, C.D. Malliakas, H. Wan, A.S.R. Bati, Z. Wang, R.P. Reynolds, I.W. Gilley, S. Kitade, T.E. Wiggins, S. Zeiske, S. Suragtkhuu, M. Batmunkh, L.X. Chen, B. Chen, M.G. Kanatzidis, E.H. Sargent, Science 386 (2024) 898–902.
[82] R. Azmi, D.S. Utomo, B. Vishal, S. Zhumagali, P. Dally, A.M. Risqi, A. Prasetio, E. Ugur, F. Cao, I.F. Imran, A.A. Said, A.R. Pininti, A.S. Subbiah, E. Aydin, C. Xiao, S.I. Seok, S. De Wolf, Nature 628 (2024) 93–98.
[83] A. Magomedov, A. Al-Ashouri, E. Kasparavičius, S. Strazdaite, G. Niaura, M. Jošt, T. Malinauskas, S. Albrecht, V. Getautis, Adv. Energy Mater. 8 (2018) 1801892.
[84] H. Chen, S. Teale, B. Chen, Y. Hou, L. Grater, T. Zhu, K. Bertens, S.M. Park, H. R. Atapattu, Y. Gao, M. Wei, A.K. Johnston, Q. Zhou, K. Xu, D. Yu, C. Han, T. Cui, E.H. Jung, C. Zhou, W. Zhou, A.H. Proppe, S. Hoogland, F. Laquai, T. Filleter, K. R. Graham, Z. Ning, E.H. Sargent, Nat. Photonics 16 (2022) 352–358.
[85] Y. Sun, X. Fang, Z. Ma, L. Xu, Y. Lu, Q. Yu, N. Yuan, J. Ding, J. Mater. Chem. C 5 (2017) 8682–8687.
[86] A. Kojima, K. Teshima, Y. Shirai, T. Miyasaka, J. Am. Chem. Soc. 131 (2009) 6050–6051.
[87] M.A. Green, A. Ho-Baillie, H.J. Snaith, Nat. Photonics 8 (2014) 506–514.
[88] J. Wu, R. Zhu, G. Li, Z. Zhang, J. Pascual, H. Wu, M.H. Aldamasy, L. Wang, Z. Su, S.-H. Turren-Cruz, R. Roy, F.A. Alharthi, A. Alsalme, J. Zhang, X. Gao, M. Saliba, A. Abate, M. Li, Adv. Mater. 36 (2024) 2407433.
[89] Best research-cell efficiencies, 2024.
[90] H.S. Jung, N.-G. Park, Small 11 (2015) 10–25.
[91] Y. Rong, Y. Hu, A. Mei, H. Tan, M.I. Saidaminov, S.I. Seok, M.D. McGehee, E. H. Sargent, H. Han, Science 361 (2018) 1214.
[92] R. Wang, M. Mujahid, Y. Duan, Z.-K. Wang, J. Xue, Y. Yang, Adv. Funct. Mater. 29 (2019) 1808843.
[93] Y. Yang, J. You, Nature 544 (2017) 155–156.
[94] Z. Li, X. Sun, X. Zheng, B. Li, D. Gao, S. Zhang, X. Wu, S. Li, J. Gong, J.M. Luther, Z. a. Li, Z. Zhu, Science 382 (2023) 284–289.

[95] Q. Wang, E. Mosconi, C. Wolff, J. Li, D. Neher, F. De Angelis, G.P. Suranna, R. Grisorio, A. Abate, Adv. Energy Mater. 9 (2019) 1900990.
[96] E. Yalcin, M. Can, C. Rodriguez-Seco, E. Aktas, R. Pudi, W. Cambarau, S. Demic, E. Palomares, Energy Environ. Sci. 12 (2019) 230–237.
[97] G. Qu, S. Cai, Y. Qiao, D. Wang, S. Gong, D. Khan, Y. Wang, K. Jiang, Q. Chen, L. Zhang, Y.-G. Wang, X. Chen, A.K.Y. Jen, Z.-X. Xu, Joule 8 (2024) 2123–2134.
[98] X. Yu, X. Sun, Z. Zhu, Z. Li, Angew. Chem. Int. Ed. Engl. (2024) e202419608, https://doi.org/10.1002/anie.202419608.
[99] T. Wu, X. Xu, L.K. Ono, T. Guo, S. Mariotti, C. Ding, S. Yuan, C. Zhang, J. Zhang, K. Mitrofanov, Q. Zhang, S. Raj, X. Liu, H. Segawa, P. Ji, T. Li, R. Kabe, L. Han, A. Narita, Y. Qi, Adv. Mater. 35 (2023) 2300169.
[100] T. Wu, S. Mariotti, P. Ji, L.K. Ono, T. Guo, I.-N. Rabehi, S. Yuan, J. Zhang, C. Ding, Z. Guo, Y. Qi, Adv. Funct. Mater. 34 (2024) 2316500.
[101] C. Zhang, S. Mariotti, L.K. Ono, C. Ding, K. Mitrofanov, C. Zhang, S. Yuan, P. Ji, J. Zhang, T. Wu, R. Kabe, Y. Qi, J. Mater. Chem. C 11 (2023) 2851–2862.
[102] Z. Zhang, R. Zhu, Y. Tang, Z. Su, S. Hu, X. Zhang, J. Zhang, J. Zhao, Y. Xue, X. Gao, G. Li, J. Pascual, A. Abate, M. Li, Adv. Mater. 36 (2024) 2312264.
[103] J. Zeng, L. Bi, Y. Cheng, B. Xu, A.K.Y. Jen, Nano Res. Energy 1 (2022) 9120004.
[104] S. Zhang, F. Ye, X. Wang, R. Chen, H. Zhang, L. Zhan, X. Jiang, Y. Li, X. Ji, S. Liu, M. Yu, F. Yu, Y. Zhang, R. Wu, Z. Liu, Z. Ning, D. Neher, L. Han, Y. Lin, H. Tian, W. Chen, M. Stolterfoht, L. Zhang, W.-H. Zhu, Y. Wu, Science 380 (2023) 404–409.
[105] J. Wu, P. Yan, D. Yang, H. Guan, S. Yang, X. Cao, X. Liao, P. Ding, H. Sun, Z. Ge, Adv. Mater. 36 (2024) 2401537.
[106] A. Farag, T. Feeney, I. M. Hossain, F. Schackmar, P. Fassl, K. Küster, R. Bäuerle, M. A. Ruiz-Preciado, M. Hentschel, D. B. Ritzer, A. Diercks, Y. Li, B. A. Nejand, F. Laufer, R. Singh, U. Starke and U. W. Paetzold, *Adv. Energy Mater.*, 2023, 13, 2203982.
[107] Q. Tan, Z. Li, G. Luo, X. Zhang, B. Che, G. Chen, H. Gao, D. He, G. Ma, J. Wang, J. Xiu, H. Yi, T. Chen, Z. He, Nature 620 (2023) 545–551.
[108] X. Zheng, Z. Li, Y. Zhang, M. Chen, T. Liu, C. Xiao, D. Gao, J.B. Patel, D. Kuciauskas, A. Magomedov, R.A. Scheidt, X. Wang, S.P. Harvey, Z. Dai, C. Zhang, D. Morales, H. Pruett, B.M. Wieliczka, A.R. Kirmani, N.P. Padture, K. R. Graham, Y. Yan, M.K. Nazeeruddin, M.D. McGehee, Z. Zhu, J.M. Luther, Nature Energy 8 (2023) 462–472.
[109] K. Choi, H. Choi, J. Min, T. Kim, D. Kim, S.Y. Son, G.-W. Kim, J. Choi, T. Park, Solar RRL 4 (2020) 1900251.
[110] M. Li, M. Liu, F. Qi, F.R. Lin, A.K. Jen, Chem. Rev. 124 (2024) 2138–2204.
[111] T. Bauer, T. Schmaltz, T. Lenz, M. Halik, B. Meyer, T. Clark, ACS Appl. Mater. Interfaces 5 (2013) 6073–6080.
[112] M. Sohail, A.R. Bassindale, P.G. Taylor, A.A. Korlyukov, D.E. Arkhipov, L. Male, S. J. Coles, M.B. Hursthouse, Organometallics 32 (2013) 1721–1731.
[113] S.Y. Kim, S.J. Cho, S.E. Byeon, X. He, H.J. Yoon, Adv. Energy Mater. 10 (2020) 2002606.
[114] F. Ali, C. Roldán-Carmona, M. Sohail, M.K. Nazeeruddin, Adv. Energy Mater. 10 (2020) 2002989.
[115] J. Suo, B. Yang, D. Bogachuk, G. Boschloo, A. Hagfeldt, Adv. Energy Mater. (2024), https://doi.org/10.1002/aenm.202400205.
[116] A. Ullah, K.H. Park, Y. Lee, S. Park, A.B. Faheem, H.D. Nguyen, Y. Siddique, K.-K. Lee, Y. Jo, C.-H. Han, S. Ahn, I. Jeong, S. Cho, B. Kim, Y.S. Park, S. Hong, Adv. Funct. Mater. 32 (2022) 2208793.
[117] G. Wang, J. Zheng, W. Duan, J. Yang, M.A. Mahmud, Q. Lian, S. Tang, C. Liao, J. Bing, J. Yi, T.L. Leung, X. Cui, H. Chen, F. Jiang, Y. Huang, A. Lambertz, M. Jankovec, M. Topič, S. Bremner, Y.-Z. Zhang, C. Cheng, K. Ding, A. Ho-Baillie, Joule 7 (2023) 2583–2594.
[118] Z. Yi, W. Wang, R. He, J. Zhu, W. Jiao, Y. Luo, Y. Xu, Y. Wang, Z. Zeng, K. Wei, J. Zhang, S.-W. Tsang, C. Chen, W. Tang, D. Zhao, Energy Environ. Sci. 17 (2024) 202–209.
[119] C. Li, Z. Zhang, H. Zhang, W. Yan, Y. Li, L. Liang, W. Yu, X. Yu, Y. Wang, Y. Yang, M.K. Nazeeruddin, P. Gao, Angew. Chem. Int. Ed. 63 (2024) e202315281.
[120] L.V. Torres Merino, C.E. Petoukhoff, O. Matiash, A.S. Subbiah, C.V. Franco, P. Dally, B. Vishal, S. Kosar, D. Rosas Villalva, V. Hnapovskyi, E. Ugur, S. Shah, F. Peña Camargo, O. Karalis, H. Hempel, I. Levine, R.R. Pradhan, S. Kralj, N. Kalasariya, M. Babics, B.K. Yildirim, A.A. Said, E. Aydin, H. Bristow, S. Mannar, W. Raja, A.R. Pininti, A. Prasetio, A. Razzaq, H. Al Nasser, T.G. Allen, F.H. Isikgor, D. Baran, T.D. Anthopoulos, M.M. Masis, U. Schwingenschlögl, T. Unold, M. Stolterfoht, F. Laquai, S. De Wolf, Joule 8 (2024) 2585–2606.
[121] D.A. González, C.E. Puerto Galvis, W. Li, M. Méndez, E. Aktas, M.-F. Eugenia, E. Palomares, Nanoscale Adv. 5 (2023) 6542–6547.
[122] H.-L. Yip, S.K. Hau, N.S. Baek, H. Ma, A.K.-Y. Jen, Adv. Mater. 20 (2008) 2376–2382.
[123] P. Guo, Q. Ye, X. Yang, J. Zhang, F. Xu, D. Shchukin, B. Wei, H. Wang, J. Mater. Chem. A 7 (2019) 2497–2506.
[124] A.-F. Castro-Méndez, J. Hidalgo, J.-P. Correa-Baena, Adv. Energy Mater. 9 (2019) 1901489.
[125] C. Bi, Q. Wang, Y. Shao, Y. Yuan, Z. Xiao, J. Huang, Nat. Commun. 6 (2015) 7747.
[126] J.A. Christians, S.N. Habisreutinger, J.J. Berry, J.M. Luther, ACS Energy Lett. 3 (2018) 2136–2143.
[127] I.M. Peters, J. Hauch, C. Brabec, P. Sinha, Joule 5 (2021) 3137–3153.
[128] H. Zhu, S. Teale, M.N. Lintangpradipto, S. Mahesh, B. Chen, M.D. McGehee, E. H. Sargent, O.M. Bakr, Nat. Rev. Mater. 8 (2023) 569–586.
[129] M. Li, H. Li, Q. Zhuang, D. He, B. Liu, C. Chen, B. Zhang, T. Pauporté, Z. Zang, J. Chen, Angew. Chem. Int. Ed. 61 (2022) e202206914.
[130] T. Zhou, Z. Xu, R. Wang, X. Dong, Q. Fu, Y. Liu, Adv. Mater. 34 (2022) 2200705.
[131] A. Al-Ashouri, A. Magomedov, M. Roß, M. Jošt, M. Talaikis, G. Chistiakova, T. Bertram, J.A. Márquez, E. Köhnen, E. Kasparavičius, S. Levcenco, L. Gil-Escrig, C.J. Hages, R. Schlatmann, B. Rech, T. Malinauskas, T. Unold, C.A. Kaufmann, L. Korte, G. Niaura, V. Getautis, S. Albrecht, Energy Environ. Sci. 12 (2019) 3356–3369.
[132] E. Aktas, N. Phung, H. Köbler, D.A. González, M. Méndez, I. Kafedjiska, S.-H. Turren-Cruz, R. Wenisch, I. Lauermann, A. Abate, E. Palomares, Energy Environ. Sci. 14 (2021) 3976–3985.
[133] M. Liu, M. Li, Y. Li, Y. An, Z. Yao, B. Fan, F. Qi, K. Liu, H.-L. Yip, F.R. Lin, A.K.-Y. Jen, Adv. Energy Mater. 14 (2024) 2303742.
[134] M. Liu, L. Bi, W. Jiang, Z. Zeng, S.-W. Tsang, F.R. Lin, A.K.-Y. Jen, Adv. Mater. 35 (2023) 2304415.
[135] W. Shockley, H.J. Queisser, J. Appl. Phys. 32 (1961) 510–519.
[136] A. Martí, G.L. Araújo, Sol. Energy Mater. Sol. Cells 43 (1996) 203–222.
[137] X.Y. Chin, D. Turkay, J.A. Steele, S. Tabean, S. Eswara, M. Mensi, P. Fiala, C. M. Wolff, A. Paracchino, K. Artuk, D. Jacobs, Q. Guesnay, F. Sahli, G. Andreatta, M. Boccard, Q. Jeangros, C. Ballif, Science 381 (2023) 59–63.
[138] M. Jošt, E. Köhnen, A. Al-Ashouri, T. Bertram, Š. Tomšič, A. Magomedov, E. Kasparavicius, T. Kodalle, B. Lipovšek, V. Getautis, R. Schlatmann, C. A. Kaufmann, S. Albrecht, M. Topič, ACS Energy Lett 7 (2022) 1298–1307.
[139] K. Dolia, S. Neupane, S. Fu, Y. Yin, A. Abudulimu, A. Rahimi, M. Hattarki, B. Dokken, T. Zhu, A. Adhikari, M.K. Jamarkattel, R.E. Irving, A.B. Phillips, M. J. Heben, R.J. Ellingson, Y. Yan, Z. Song, Solar RRL 8 (2024) 2400148.
[140] K.O. Brinkmann, T. Becker, F. Zimmermann, C. Kreusel, T. Gahlmann, M. Theisen, T. Haeger, S. Olthof, C. Tückmantel, M. Günster, T. Maschwitz, F. Göbelsmann, C. Koch, D. Hertel, P. Caprioglio, F. Peña-Camargo, L. Perdigón-Toro, A. Al-Ashouri, L. Merten, A. Hinderhofer, L. Gomell, S. Zhang, F. Schreiber, S. Albrecht, K. Meerholz, D. Neher, M. Stolterfoht, T. Riedl, Nature 604 (2022) 280–286.
[141] R. He, W. Wang, Z. Yi, F. Lang, C. Chen, J. Luo, J. Zhu, J. Thiesbrummel, S. Shah, K. Wei, Y. Luo, C. Wang, H. Lai, H. Huang, J. Zhou, B. Zou, X. Yin, S. Ren, X. Hao, L. Wu, J. Zhang, J. Zhang, M. Stolterfoht, F. Fu, W. Tang, D. Zhao, Nature 618 (2023) 80–86.
[142] J. Lim, N.-G. Park, S. Il Seok, M. Saliba, Energy Environ. Sci. 17 (2024) 4390–4425.
[143] M.A. Green, E.D. Dunlop, M. Yoshita, N. Kopidakis, K. Bothe, G. Siefer, D. Hinken, M. Rauer, J. Hohl-Ebinger, X. Hao, Prog. Photovolt.: Res. Appl. 32 (2024) 425–441.
[144] L. Li, Y. Wang, X. Wang, R. Lin, X. Luo, Z. Liu, K. Zhou, S. Xiong, Q. Bao, G. Chen, Y. Tian, Y. Deng, K. Xiao, J. Wu, M.I. Saidaminov, H. Lin, C.-Q. Ma, Z. Zhao, Y. Wu, L. Zhang, H. Tan, Nat. Energy 7 (2022) 708–717.
[145] H. Lai, J. Luo, Y. Zwirner, S. Olthof, A. Wieczorek, F. Ye, Q. Jeangros, X. Yin, F. Akhundova, T. Ma, R. He, R.K. Kothandaraman, X. Chin, E. Gilshtein, A. Müller, C. Wang, J. Thiesbrummel, S. Siol, J.M. Prieto, T. Unold, M. Stolterfoht, C. Chen, A.N. Tiwari, D. Zhao, F. Fu, Adv. Energy Mater. 12 (2022) 2202438.
[146] R. He, S. Ren, C. Chen, Z. Yi, Y. Luo, H. Lai, W. Wang, G. Zeng, X. Hao, Y. Wang, J. Zhang, C. Wang, L. Wu, F. Fu, D. Zhao, Energy Environ. Sci. 14 (2021) 5723–5759.
[147] H.J. Bolink, Nat. Energy 3 (2018) 1027–1028.
[148] Z. Yang, Z. Yu, H. Wei, X. Xiao, Z. Ni, B. Chen, Y. Deng, S.N. Habisreutinger, X. Chen, K. Wang, J. Zhao, P.N. Rudd, J.J. Berry, M.C. Beard, J. Huang, Nat. Commun. 10 (2019) 4498.
[149] M. Zhang, Z. Lin, Energy Environ. Sci. 15 (2022) 3152–3170.
[150] T. J. Jacobsson, A. Hultqvist, A. García-Fernández, A. Anand, A. Al-Ashouri, A. Hagfeldt, A. Crovetto, A. Abate, A. G. Ricciardulli, A. Vijayan, A. Kulkarni, A. Y. Anderson, B. P. Darwich, B. Yang, B. L. Coles, C. A. R. Perini, C. Rehermann, D. Ramirez, D. Fairen-Jimenez, D. Di Girolamo, D. Jia, E. Avila, E. J. Juarez-Perez, F. Baumann, F. Mathies, G. S. A. González, G. Boschloo, G. Nasti, G. Paramasivam, G. Martínez-Denegri, H. Näsström, H. Michaels, H. Köbler, H. Wu, I. Benesperi, M. I. Dar, I. Bayrak Pehlivan, I. E. Gould, J. N. Vagott, J. Dagar, J. Kettle, J. Yang, J. Li, J. A. Smith, J. Pascual, J. J. Jerónimo-Rendón, J. F. Montoya, J.-P. Correa-Baena, J. Qiu, J. Wang, K. Sveinbjörnsson, K. Hirselandt, K. Dey, K. Frohna, L. Mathies, L. A. Castriotta, M. H. Aldamasy, M. Vasquez-Montoya, M. A. Ruiz-Preciado, M. A. Flatken, M. V. Khenkin, M. Grischek, M. Kedia, M. Saliba, M. Anaya, M. Veldhoen, N. Arora, O. Shargaieva, O. Maus, O. S. Game, O. Yudilevich, P. Fassl, Q. Zhou, R. Betancur, R. Munir, R. Patidar, S. D. Stranks, S. Alam, S. Kar, T. Unold, T. Abzieher, T. Edvinsson, T. W. David, U. W. Paetzold, W. Zia, W. Fu, W. Zuo, V. R. F. Schröder, W. Tress, X. Zhang, Y.-H. Chiang, Z. Iqbal, Z. Xie and E. Unger, *Nat. Energy*, 2021, 7, 107-115.
[151] H. Cui, L. Huang, S. Zhou, C. Wang, X. Hu, H. Guan, S. Wang, W. Shao, D. Pu, K. Dong, J. Zhou, P. Jia, W. Wang, C. Tao, W. Ke, G. Fang, Energy Environ. Sci. 16 (2023) 5992–6002.
[152] S. Wu, Y. Yan, J. Yin, K. Jiang, F. Li, Z. Zeng, S.-W. Tsang, A.K.Y. Jen, Nat. Energy 9 (2024) 411–421.
[153] J. Zhou, T. Wen, J. Sun, Z. Shi, C. Zou, Z. Shen, Y. Li, Y. Wang, Y. Lin, S. Yang, F. Liu, Z. Yang, ACS Energy Lett 9 (2024) 1984–1992.
[154] X. Lv, W. Li, J. Zhang, Y. Yang, X. Jia, Y. Ji, Q. Lin, W. Huang, T. Bu, Z. Ren, C. Yao, F. Huang, Y.-B. Cheng, J. Tong, J. Energy Chem. 93 (2024) 64–70.
[155] Y. An, N. Zhang, Z. Zeng, Y. Cai, W. Jiang, F. Qi, L. Ke, F.R. Lin, S.W. Tsang, T. Shi, A.K.Y. Jen, H.L. Yip, Adv. Mater. 36 (2024) 2306568.
[156] Q. Jiang, J. Tong, R.A. Scheidt, X. Wang, A.E. Louks, Y. Xian, R. Tirawat, A. F. Palmstrom, M.P. Hautzinger, S.P. Harvey, S. Johnston, L.T. Schelhas, B. W. Larson, E.L. Warren, M.C. Beard, J.J. Berry, Y. Yan, K. Zhu, Science 378 (2022) 1295–1300.
[157] X. Ji, S. Zhang, F. Yu, H. Zhang, L. Zhan, Y. Hu, W.-H. Zhu, Y. Wu, Sci. China Chem. 67 (2024) 2102–2110.
[158] A. Maxwell, H. Chen, L. Grater, C. Li, S. Teale, J. Wang, L. Zeng, Z. Wang, S. M. Park, M. Vafaie, S. Sidhik, I.W. Metcalf, Y. Liu, A.D. Mohite, B. Chen, E. H. Sargent, ACS Energy Lett 9 (2024) 520–527.

[159] F. Yang, P. Tockhorn, A. Musiienko, F. Lang, D. Menzel, R. Macqueen, E. Köhnen, K. Xu, S. Mariotti, D. Mantione, L. Merten, A. Hinderhofer, B. Li, D.R. Wargulski, S.P. Harvey, J. Zhang, F. Scheler, S. Berwig, M. Roß, J. Thiesbrummel, A. Al-Ashouri, K.O. Brinkmann, T. Riedl, F. Schreiber, D. Abou-Ras, H. Snaith, D. Neher, L. Korte, M. Stolterfoht, S. Albrecht, Adv. Mater. 36 (2024) 2307743.
[160] Y. Zhao, C. Wang, T. Ma, L. Zhou, Z. Wu, H. Wang, C. Chen, Z. Yu, W. Sun, A. Wang, H. Huang, B. Zou, D. Zhao, X. Li, Energy Environ. Sci. 16 (2023) 2080–2089.
[161] H. Lai, J. Luo, Y. Zwirner, S. Olthof, A. Wieczorek, F. Ye, Q. Jeangros, X. Yin, F. Akhundova, T. Ma, R. He, R.K. Kothandaraman, X. Chin, E. Gilshtein, A. Müller, C. Wang, J. Thiesbrummel, S. Siol, J.M. Prieto, T. Unold, M. Stolterfoht, C. Chen, A.N. Tiwari, D. Zhao, F. Fu, Adv. Energy Mater. 12 (2022) 2202438.
[162] R. Lin, J. Xu, M. Wei, Y. Wang, Z. Qin, Z. Liu, J. Wu, K. Xiao, B. Chen, S.M. Park, G. Chen, H.R. Atapattu, K.R. Graham, J. Xu, J. Zhu, L. Li, C. Zhang, E.H. Sargent, H. Tan, Nature 603 (2022) 73–78.
[163] R. Lin, Y. Wang, Q. Lu, B. Tang, J. Li, H. Gao, Y. Gao, H. Li, C. Ding, J. Wen, P. Wu, C. Liu, S. Zhao, K. Xiao, Z. Liu, C. Ma, Y. Deng, L. Li, F. Fan, H. Tan, Nature 620 (2023) 994–1000.
[164] J. Wen, Y. Zhao, P. Wu, Y. Liu, X. Zheng, R. Lin, S. Wan, K. Li, H. Luo, Y. Tian, L. Li, H. Tan, Nat. Commun. 14 (2023) 7118.
[165] S. Tan, C. Li, C. Peng, W. Yan, H. Bu, H. Jiang, F. Yue, L. Zhang, H. Gao, Z. Zhou, Nat. Commun. 15 (2024) 4136.
[166] C. Liu, R. Lin, Y. Wang, H. Gao, P. Wu, H. Luo, X. Zheng, B. Tang, Z. Huang, H. Sun, S. Zhao, Y. Guo, J. Wen, F. Fan, H. Tan, Angew. Chem. Int. Ed. 135 (2023) e202313374.
[167] R. Lin, K. Xiao, Z. Qin, Q. Han, C. Zhang, M. Wei, M.I. Saidaminov, Y. Gao, J. Xu, M. Xiao, A. Li, J. Zhu, E.H. Sargent, H. Tan, Nat. Energy 4 (2019) 864–873.
[168] Z. Chen, G. Brocks, S. Tao, P.A. Bobbert, Nat. Commun. 12 (2021) 2687.
[169] F. Hao, C.C. Stoumpos, D.H. Cao, R.P.H. Chang, M.G. Kanatzidis, Nat. Photonics 8 (2014) 489–494.
[170] R. Prasanna, T. Leijtens, S.P. Dunfield, J.A. Raiford, E.J. Wolf, S.A. Swifter, J. Werner, G.E. Eperon, C. De Paula, A.F. Palmstrom, C.C. Boyd, M.F.A.M. Van Hest, S.F. Bent, G. Teeter, J.J. Berry, M.D. McGehee, Nat. Energy 4 (2019) 939–947.
[171] B. Abdollahi Nejand, D.B. Ritzer, H. Hu, F. Schackmar, S. Moghadamzadeh, T. Feeney, R. Singh, F. Laufer, R. Schmager, R. Azmi, M. Kaiser, T. Abzieher, S. Gharibzadeh, E. Ahlswede, U. Lemmer, B.S. Richards, U.W. Paetzold, Nat. Energy 7 (2022) 620–630.
[172] K. Xiao, Y.-H. Lin, M. Zhang, R.D.J. Oliver, X. Wang, Z. Liu, X. Luo, J. Li, D. Lai, H. Luo, R. Lin, J. Xu, Y. Hou, H.J. Snaith, H. Tan, Science 376 (2022) 762–767.
[173] H. Gao, K. Xiao, R. Lin, S. Zhao, W. Wang, S. Dayneko, C. Duan, C. Ji, H. Sun, A. D. Bui, C. Liu, J. Wen, W. Kong, H. Luo, X. Zheng, Z. Liu, H. Nguyen, J. Xie, L. Li, M.I. Saidaminov, H. Tan, Science 383 (2024) 855–859.
[174] H. Sun, K. Xiao, H. Gao, C. Duan, S. Zhao, J. Wen, Y. Wang, R. Lin, X. Zheng, H. Luo, C. Liu, P. Wu, W. Kong, Z. Liu, L. Li, H. Tan, Adv. Mater. 36 (2024) 2308706.
[175] Ewan Martin, M. Yoshita, N. Kopidakis, K. Bothe, G. Siefer, X. Hao, Jessica, Prog. Photovolt.: Res. Appl. 33 (2024) 3–15.
[176] S.W. Lee, S. Bae, D. Kim, H.S. Lee, Adv. Mater. 32 (2020) 2002202.
[177] F.U. Kosasih, E. Erdenebileg, N. Mathews, S.G. Mhaisalkar, A. Bruno, Joule 6 (2022) 2692–2734.
[178] S.J. Lee, S.S. Shin, Y.C. Kim, D. Kim, T.K. Ahn, J.H. Noh, J. Seo, S.I. Seok, J. Am. Chem. Soc. 138 (2016) 3974–3977.
[179] K. Xiao, R. Lin, Q. Han, Y. Hou, Z. Qin, H.T. Nguyen, J. Wen, M. Wei, V. Yeddu, M. I. Saidaminov, Y. Gao, X. Luo, Y. Wang, H. Gao, C. Zhang, J. Xu, J. Zhu, E. H. Sargent, H. Tan, Nat. Energy 5 (2020) 870–880.
[180] X. Xu, C.-C. Chueh, Z. Yang, A. Rajagopal, J. Xu, S.B. Jo, A.K.Y. Jen, Nano Energy 34 (2017) 392–398.
[181] J. Cao, H.L. Loi, Y. Xu, X. Guo, N. Wang, C.K. Liu, T. Wang, H. Cheng, Y. Zhu, M. G. Li, W.Y. Wong, F. Yan, Adv. Mater. 34 (2022) 2107729.
[182] M.I. Saidaminov, I. Spanopoulos, J. Abed, W. Ke, J. Wicks, M.G. Kanatzidis, E. H. Sargent, ACS Energy Lett 5 (2020) 1153–1155.
[183] J. Pascual, G. Nasti, M.H. Aldamasy, J.A. Smith, M. Flatken, N. Phung, D. Di Girolamo, S.-H. Turren-Cruz, M. Li, A. Dallmann, R. Avolio, A. Abate, Mater. Adv. 1 (2020) 1066–1070.
[184] J. Pascual, D. Di Girolamo, M.A. Flatken, M.H. Aldamasy, G. Li, M. Li, A. Abate, Chem. – A Eur. J. 28 (2022) e202103919.
[185] S. Tian, G. Li, R.C. Turnell-Ritson, Z. Fei, A. Bornet, M.K. Nazeeruddin, P.J. Dyson, Angew. Chem. Int. Ed. 63 (2024) e202407193.
[186] T. Ma, H. Wang, Z. Wu, Y. Zhao, C. Chen, X. Yin, L. Hu, F. Yao, Q. Lin, S. Wang, D. Zhao, X. Li, C. Wang, Adv. Mater. 36 (2024) 2308240.
[187] J. Zhu, Y. Luo, R. He, C. Chen, Y. Wang, J. Luo, Z. Yi, J. Thiesbrummel, C. Wang, F. Lang, H. Lai, Y. Xu, J. Wang, Z. Zhang, W. Liang, G. Cui, S. Ren, X. Hao, H. Huang, Y. Wang, F. Yao, Q. Lin, L. Wu, J. Zhang, M. Stolterfoht, F. Fu, D. Zhao, Nat. Energy 8 (2023) 714–724.
[188] J. Zhang, W. Li, X. Lv, Y. Ji, W. Huang, T. Bu, Z. Ren, C. Yao, F. Huang, Y. B. Cheng, J. Tong, Sol. RRL 8 (2024) 2400184.
[189] J.K. Pious, H. Lai, J. Hu, D. Luo, E. Gilshtein, S. Siegrist, R.K. Kothandaraman, Z.-H. Lu, C.M. Wolff, A.N. Tiwari, F. Fu, ACS Appl. Mater. Interfaces 16 (2024) 39399–39407.
[190] J. Zhu, Y. Xu, Y. Luo, J. Luo, R. He, C. Wang, Y. Wang, K. Wei, Z. Yi, Z. Gao, J. Wang, J. You, Z. Zhang, H. Lai, S. Ren, X. Liu, C. Xiao, C. Chen, J. Zhang, F. Fu, D. Zhao, Sci. Adv. 10 (2024) eadl2063.
[191] P. Wu, J. Wen, Y. Wang, Z. Liu, R. Lin, H. Li, H. Luo, H. Tan, Adv. Energy Mater. 12 (2022) 2202948.
[192] J. Zheng, W. Duan, Y. Guo, Z.C. Zhao, H. Yi, F.-J. Ma, L. Granados Caro, C. Yi, J. Bing, S. Tang, J. Qu, K.C. Fong, X. Cui, Y. Zhu, L. Yang, A. Lambertz, M. Arafat Mahmud, H. Chen, C. Liao, G. Wang, M. Jankovec, C. Xu, A. Uddin, J.M. Cairney, S. Bremner, S. Huang, K. Ding, D.R. McKenzie, A.W.Y. Ho-Baillie, Energy Environ. Sci. 16 (2023) 1223–1233.
[193] E. Aydin, E. Ugur, B.K. Yildirim, T.G. Allen, P. Dally, A. Razzaq, F. Cao, L. Xu, B. Vishal, A. Yazmaciyan, A.A. Said, S. Zhumagali, R. Azmi, M. Babics, A. Fell, C. Xiao, S. De Wolf, Nature 623 (2023) 732–738.
[194] B. Chen, Z. Yu, A. Onno, Z. Yu, S. Chen, J. Wang, Z.C. Holman, J. Huang, Sci. Adv. 8 (2022) eadd0377.
[195] H. Li, Y. Wang, H. Gao, M. Zhang, R. Lin, P. Wu, K. Xiao, H. Tan, eLight 2 (2022) 21.
[196] M.T. Hörantner, T. Leijtens, M.E. Ziffer, G.E. Eperon, M.G. Christoforo, M. D. McGehee, H.J. Snaith, ACS Energy Lett 2 (2017) 2506–2513.
[197] G.E. Eperon, M.T. Hörantner, H.J. Snaith, Nat. Rev. Chem. 1 (2017) 0095.
[198] D.P. McMeekin, S. Mahesh, N.K. Noel, M.T. Klug, J. Lim, J.H. Warby, J.M. Ball, L. M. Herz, M.B. Johnston, H.J. Snaith, Joule 3 (2019) 387–401.
[199] J. Wang, V. Zardetto, K. Datta, D. Zhang, M.M. Wienk, R.A.J. Janssen, Nat. Commun. 11 (2020) 5254.
[200] K. Xiao, J. Wen, Q. Han, R. Lin, Y. Gao, S. Gu, Y. Zang, Y. Nie, J. Zhu, J. Xu, H. Tan, ACS Energy Lett 5 (2020) 2819–2826.
[201] Z. Wang, L. Zeng, T. Zhu, H. Chen, B. Chen, D.J. Kubicki, A. Balvanz, C. Li, A. Maxwell, E. Ugur, R. Dos Reis, M. Cheng, G. Yang, B. Subedi, D. Luo, J. Hu, J. Wang, S. Teale, S. Mahesh, S. Wang, S. Hu, E.D. Jung, M. Wei, S.M. Park, L. Grater, E. Aydin, Z. Song, N.J. Podraza, Z.-H. Lu, J. Huang, V.P. Dravid, S. De Wolf, Y. Yan, M. Grätzel, M.G. Kanatzidis, E.H. Sargent, Nature 618 (2023) 74–79.
[202] J. Wang, L. Zeng, D. Zhang, A. Maxwell, H. Chen, K. Datta, A. Caiazzo, W.H. M. Remmerswaal, N.R.M. Schipper, Z. Chen, K. Ho, A. Dasgupta, G. Kusch, R. Ollearo, L. Bellini, S. Hu, Z. Wang, C. Li, S. Teale, L. Grater, B. Chen, M. M. Wienk, R.A. Oliver, H.J. Snaith, R.A.J. Janssen, E.H. Sargent, Nat. Energy 9 (2023) 70–80.
[203] Z. Yu, Z. Yang, Z. Ni, Y. Shao, B. Chen, Y. Lin, H. Wei, Z.J. Yu, Z. Holman, J. Huang, Nat. Energy 5 (2020) 657–665.
[204] S. Fu, N. Sun, Y. Xian, L. Chen, Y. Li, C. Li, A. Abudulimu, P.N. Kaluarachchi, Z. Huang, X. Wang, K. Dolia, D.S. Ginger, M.J. Heben, R.J. Ellingson, B. Chen, E. H. Sargent, Z. Song, Y. Yan, Joule 8 (2024) 2220–2237.
[205] T. Li, J. Xu, R. Lin, S. Teale, H. Li, Z. Liu, C. Duan, Q. Zhao, K. Xiao, P. Wu, B. Chen, S. Jiang, S. Xiong, H. Luo, S. Wan, L. Li, Q. Bao, Y. Tian, X. Gao, J. Xie, E. H. Sargent, H. Tan, Nat. Energy 8 (2023) 610–620.
[206] Y. Wang, R. Lin, X. Wang, C. Liu, Y. Ahmed, Z. Huang, Z. Zhang, H. Li, M. Zhang, Y. Gao, H. Luo, P. Wu, H. Gao, X. Zheng, M. Li, Z. Liu, W. Kong, L. Li, K. Liu, M. I. Saidaminov, L. Zhang, H. Tan, Nat. Commun. 14 (2023) 1819.
[207] E. Eperon Giles, T. Leijtens, A. Bush Kevin, R. Prasanna, T. Green, T.-W. Wang Jacob, P. McMeekin David, G. Volonakis, L. Milot Rebecca, R. May, A. Palmstrom, J. Slotcavage Daniel, A. Belisle Rebecca, B. Patel Jay, S. Parrott Elizabeth, J. Sutton Rebecca, W. Ma, F. Moghadam, B. Conings, A. Babayigit, H.-G. Boyen, S. Bent, F. Giustino, M. Herz Laura, B. Johnston Michael, D. McGehee Michael, J. Snaith Henry, Science 354 (2016) 861–865.
[208] D.P. McMeekin, S. Mahesh, N.K. Noel, M.T. Klug, J. Lim, J.H. Warby, J.M. Ball, L. M. Herz, M.B. Johnston, H.J. Snaith, Joule 3 (2019) 387–401.
[209] J. Werner, F. Sahli, F. Fu, J.J. Diaz Leon, A. Walter, B.A. Kamino, B. Niesen, S. Nicolay, Q. Jeangros, C. Ballif, ACS Energy Lett 3 (2018) 2052–2058.
[210] J.P. Mailoa, C.D. Bailie, E.C. Johlin, E.T. Hoke, A.J. Akey, W.H. Nguyen, M. D. McGehee, T. Buonassisi, Appl. Phys. Lett. 106 (2015) 121105.
[211] S. Hu, J. Thiesbrummel, J. Pascual, M. Stolterfoht, A. Wakamiya, H.J. Snaith, Chem. Rev. 124 (2024) 4079–4123.
[212] I.M. Peters, C.D.R. Gallegos, L. Lüer, J.A. Hauch, C.J. Brabec, Prog. Photovolt. 31 (2023) 1006–1015.
[213] M.T. Hörantner, T. Leijtens, M.E. Ziffer, G.E. Eperon, M.G. Christoforo, M. D. McGehee, H.J. Snaith, ACS Energy Lett 2 (2017) 2506–2513.
[214] H. Li, W. Zhang, Chem. Rev. 120 (2020) 9835–9950.
[215] R. Wang, T. Huang, J. Xue, J. Tong, K. Zhu, Y. Yang, Nat. Photonics 15 (2021) 411–425.
[216] G.E. Eperon, M.T. Hörantner, H.J. Snaith, Nat. Rev. Chem. 1 (2017) 0095.
[217] LONGi, *LONGi News*, 2024, DOI: https://www.longi.com/en/news/2024-snec-silicon-perovskite-tandem-solar-cells-new-world-efficiency/.
[218] W. Shockley, H.J. Queisser, J. Appl. Phys. 32 (1961) 510–519.
[219] LONGi, 2024, DOI: https://www.longi.com/en/news/is-m6-wafer-silicon-perovskite-tandem-cells-new-efficiency-record/.
[220] O. PV, 2024, DOI: https://www.oxfordpv.com/news/oxford-pv-debuts-residential-solar-module-record-setting-269-efficiency.
[221] H. Gao, K. Xiao, R. Lin, S. Zhao, W. Wang, S. Dayneko, C. Duan, C. Ji, H. Sun, A. D. Bui, C. Liu, J. Wen, W. Kong, H. Luo, X. Zheng, Z. Liu, H. Nguyen, J. Xie, L. Li, M.I. Saidaminov, H. Tan, Science 383 (2024) 855–859.
[222] M.A. Green, E.D. Dunlop, M. Yoshita, N. Kopidakis, K. Bothe, G. Siefer, D. Hinken, M. Rauer, J. Hohl-Ebinger, X. Hao, Prog. Photovolt.: Res. Appl. 32 (2024) 425–441.
[223] J. Wang, L. Zeng, D. Zhang, A. Maxwell, H. Chen, K. Datta, A. Caiazzo, W.H. M. Remmerswaal, N.R.M. Schipper, Z. Chen, K. Ho, A. Dasgupta, G. Kusch, R. Ollearo, L. Bellini, S. Hu, Z. Wang, C. Li, S. Teale, L. Grater, B. Chen, M. M. Wienk, R.A. Oliver, H.J. Snaith, R.A.J. Janssen, E.H. Sargent, Nat. Energy 9 (2023) 70–80.
[224] Z. Wang, L. Zeng, T. Zhu, H. Chen, B. Chen, D.J. Kubicki, A. Balvanz, C. Li, A. Maxwell, E. Ugur, R. Dos Reis, M. Cheng, G. Yang, B. Subedi, D. Luo, J. Hu, J. Wang, S. Teale, S. Mahesh, S. Wang, S. Hu, E.D. Jung, M. Wei, S.M. Park,

L. Grater, E. Aydin, Z. Song, N.J. Podraza, Z.H. Lu, J. Huang, V.P. Dravid, S. De Wolf, Y. Yan, M. Gratzel, M.G. Kanatzidis, E.H. Sargent, Nature 618 (2023) 74–79.
[225] F. Xu, E. Aydin, J. Liu, E. Ugur, G.T. Harrison, L. Xu, B. Vishal, B.K. Yildirim, M. Wang, R. Ali, A.S. Subbiah, A. Yazmaciyan, S. Zhumagali, W. Yan, Y. Gao, Z. Song, C. Li, S. Fu, B. Chen, A. ur Rehman, M. Babics, A. Razzaq, M. De Bastiani, T.G. Allen, U. Schwingenschlögl, Y. Yan, F. Laquai, E.H. Sargent, S. De Wolf, Joule 8 (2024) 224–240.
[226] S. Liu, Y. Lu, C. Yu, J. Li, R. Luo, R. Guo, H. Liang, X. Jia, X. Guo, Y.-D. Wang, Q. Zhou, X. Wang, S. Yang, M. Sui, P. Müller-Buschbaum, Y. Hou, Nature 628 (2024) 306–312.
[227] S. Hu, J. Wang, P. Zhao, A. Wakamiya, H.J. Snaith, Nature (2024), https://doi.org/10.1038/s41586-024-08546-y.
[228] S. Hu, J. Wang and H. J. Snaith, 2024, DOI: https://www.ox.ac.uk/news/2024-08-09-solar-energy-breakthrough-could-reduce-need-solar-farms.
[229] L. Duan, D. Walter, N. Chang, J. Bullock, D. Kang, S.P. Phang, K. Weber, T. White, D. Macdonald, K. Catchpole, H. Shen, Nat. Rev. Mater. 8 (2023) 261–281.
[230] E. Aydin, T. G. Allen, M. De Bastiani, A. Razzaq, L. Xu, E. Ugur, J. Liu and S. De Wolf, *Science*, 383, eadh3849.
[231] S. Mariotti, E. Köhnen, F. Scheler, K. Sveinbjörnsson, L. Zimmermann, M. Piot, F. Yang, B. Li, J. Warby, A. Musiienko, D. Menzel, F. Lang, S. Keßler, I. Levine, D. Mantione, A. Al-Ashouri, M.S. Härtel, K. Xu, A. Cruz, J. Kurpiers, P. Wagner, H. Köbler, J. Li, A. Magomedov, D. Mecerreyes, E. Unger, A. Abate, M. Stolterfoht, B. Stannowski, R. Schlatmann, L. Korte, S. Albrecht, Science 381 (2023) 63–69.
[232] R. Lin, Y. Wang, Q. Lu, B. Tang, J. Li, H. Gao, Y. Gao, H. Li, C. Ding, J. Wen, P. Wu, C. Liu, S. Zhao, K. Xiao, Z. Liu, C. Ma, Y. Deng, L. Li, F. Fan, H. Tan, Nature 620 (2023) 994–1000.
[233] M. Khenkin, H. Köbler, M. Remec, R. Roy, U. Erdil, J. Li, N. Phung, G. Adwan, G. Paramasivam, Q. Emery, E. Unger, R. Schlatmann, C. Ulbrich, A. Abate, Energy Environ. Sci. 17 (2024) 602–610.
[234] C. Fei, A. Kuvayskaya, X. Shi, M. Wang, Z. Shi, H. Jiao, T.J. Silverman, M. Owen-Bellini, Y. Dong, Y. Xian, R. Scheidt, X. Wang, G. Yang, H. Gu, N. Li, C.J. Dolan, Z. J.D. Deng, D.N. Cakan, D.P. Fenning, Y. Yan, M.C. Beard, L.T. Schelhas, A. Sellinger, J. Huang, Science 384 (2024) 1126–1134.
[235] E. Aydin, T.G. Allen, M. De Bastiani, L. Xu, J. Ávila, M. Salvador, E. Van Kerschaver, S. De Wolf, Nat. Energy 5 (2020) 851–859.
[236] M.V. Khenkin, E.A. Katz, A. Abate, G. Bardizza, J.J. Berry, C. Brabec, F. Brunetti, V. Bulović, Q. Burlingame, A. Di Carlo, R. Cheacharoen, Y.-B. Cheng, A. Colsmann, S. Cros, K. Domanski, M. Dusza, C.J. Fell, S.R. Forrest, Y. Galagan, D. Di Girolamo, M. Grätzel, A. Hagfeldt, E. von Hauff, H. Hoppe, J. Kettle, H. Köbler, M.S. Leite, S. Liu, Y.-L. Loo, J.M. Luther, C.-Q. Ma, M. Madsen, M. Manceau, M. Matheron, M. McGehee, R. Meitzner, M.K. Nazeeruddin, A. F. Nogueira, Ç. Odabaşı, A. Osherov, N.-G. Park, M.O. Reese, F. De Rossi, M. Saliba, U.S. Schubert, H.J. Snaith, S.D. Stranks, W. Tress, P.A. Troshin, V. Turkovic, S. Veenstra, I. Visoly-Fisher, A. Walsh, T. Watson, H. Xie, R. Yıldırım, S.M. Zakeeruddin, K. Zhu, M. Lira-Cantu, Nat. Energy 5 (2020) 35–49.
[237] T. Todorov, O. Gunawan, S. Guha, Mol. Syst. Design Eng. 1 (2016) 370–376.
[238] F. Xu, J. Liu, L. Xu, A. Razzaq, X. Zhang, E. Aydin, S. De Wolf, ACS Energy Lett 9 (2024) 3501–3504.
[239] T. Leijtens, K.A. Bush, R. Prasanna, M.D. McGehee, Nat. Energy 3 (2018) 828–838.
[240] L. Wagner, J. Suo, B. Yang, D. Bogachuk, E. Gervais, R. Pietzcker, A. Gassmann, J. C. Goldschmidt, Joule 8 (2024) 1142–1160.
[241] Z. Yu, M. Leilaeioun, Z. Holman, Nat. Energy 1 (2016) 16137.
[242] Y.-H. Lin, V. null, F. Yang, X.-L. Cao, A. Dasgupta, R.D.J. Oliver, A.M. Ulatowski, M.M. McCarthy, X. Shen, Q. Yuan, M.G. Christoforo, F.S.Y. Yeung, M.B. Johnston, N.K. Noel, L.M. Herz, M.S. Islam, H.J. Snaith, Science 384 (2024) 767–775.
[243] L. Gil-Escrig, S. Hu, K.P.S. Zanoni, A. Paliwal, M.A. Hernandez-Fenollosa, C. Roldan-Carmona, M. Sessolo, A. Wakamiya, H.J. Bolink, ACS Mater. Lett. 4 (2022) 2638–2644.
[244] F. Fu, T. Feurer, Thomas P. Weiss, S. Pisoni, E. Avancini, C. Andres, S. Buecheler, Ayodhya N. Tiwari, Nat. Energy 2 (2016) 16190.
[245] F. Hao, C.C. Stoumpos, R.P.H. Chang, M.G. Kanatzidis, J. Am. Chem. Soc. 136 (2014) 8094–8099.
[246] A. Goyal, S. McKechnie, D. Pashov, W. Tumas, M. van Schilfgaarde, V. Stevanovic, Chem. Mater. 30 (2018) 3920–3928.
[247] B. Chen, Z. Yu, A. Onno, Z. Yu, S. Chen, J. Wang, Z.C. Holman, J. Huang, Sci. Adv. 8 (2022) eadd0377.
[248] E.T. Hoke, D.J. Slotcavage, E.R. Dohner, A.R. Bowring, H.I. Karunadasa, M. D. McGehee, Chem. Sci. 6 (2015) 613–617.
[249] S. Hu, J.A. Smith, H.J. Snaith, A. Wakamiya, Precis. Chem. 1 (2023) 69–82.
[250] J. Zheng, G. Wang, W. Duan, M.A. Mahmud, H. Yi, C. Xu, A. Lambertz, S. Bremner, K. Ding, S. Huang, A.W.Y. Ho-Baillie, ACS Energy Lett 7 (2022) 3003–3005.
[251] Y.J. Choi, S.Y. Lim, J.H. Park, S.G. Ji, J.Y. Kim, ACS Energy Lett 8 (2023) 3141–3146.
[252] M. Heydarian, M. Heydarian, A.J. Bett, M. Bivour, F. Schindler, M. Hermle, M. C. Schubert, P.S.C. Schulze, J. Borchert, S.W. Glunz, ACS Energy Lett 8 (2023) 4186–4192.
[253] F. Li, D. Wu, L. Shang, R. Xia, H. Zhang, Z. Huang, J. Gong, L. Mao, H. Zhang, Y. Sun, T. Yang, X. Sun, Z. Feng, M. Liu, Adv. Mater. 36 (2024) 2311595.
[254] H. Hu, S.X. An, Y. Li, S. Orooji, R. Singh, F. Schackmar, F. Laufer, Q. Jin, T. Feeney, A. Diercks, F. Gota, S. Moghadamzadeh, T. Pan, M. Rienäcker, R. Peibst, B.A. Nejand, U.W. Paetzold, Energy Environ. Sci. 17 (2024) 2800–2814.
[255] J. Cao, F. Yan, Energy Environ. Sci. 14 (2021) 1286–1325.
[256] F. Hao, C.C. Stoumpos, D.H. Cao, R.P.H. Chang, M.G. Kanatzidis, Nat. Photonics 8 (2014) 489–494.
[257] D.B. Mitzi, C.A. Feild, W.T.A. Harrison, A.M. Guloy, Nature 369 (1994) 467–469.
[258] S. Rühle, Sol. Energy 130 (2016) 139–147.
[259] W. Liu, H. Raza, X. Hu, S. Liu, Z. Liu, W. Chen, Mater. Futures 2 (2023) 012103.
[260] M. Jošt, G. Matič, E. Köhnen, B. Li, B. Glažar, M. Jankovec, S. Albrecht, M. Topič, Sol. RRL 5 (2021) 2100311.
[261] A.J. Ramadan, R.D.J. Oliver, M.B. Johnston, H.J. Snaith, Nat. Rev. Mater. 8 (2023) 822–838.
[262] T.C.-J. Yang, P. Fiala, Q. Jeangros, C. Ballif, Joule 2 (2018) 1421–1436.
[263] E. Aktas, N. Rajamanickam, J. Pascual, S. Hu, M.H. Aldamasy, D. Di Girolamo, W. Li, G. Nasti, E. Martínez-Ferrero, A. Wakamiya, E. Palomares, A. Abate, Commun. Mater. 3 (2022) 104.
[264] J. Zheng, H. Wei, Z. Ying, X. Yang, J. Sheng, Z. Yang, Y. Zeng, J. Ye, Adv. Energy Mater. 13 (2023) 2203006.
[265] Research Briefing, Nat. Energy 8 (2023) 1190–1191.
[266] H. Lin, M. Yang, X. Ru, G. Wang, S. Yin, F. Peng, C. Hong, M. Qu, J. Lu, L. Fang, C. Han, P. Procel, O. Isabella, P. Gao, Z. Li, X. Xu, Nat. Energy 8 (2023) 789–799.
[267] Y. Li, X. Ru, M. Yang, Y. Zheng, S. Yin, C. Hong, F. Peng, M. Qu, C. Xue, J. Lu, L. Fang, C. Su, D. Chen, J. Xu, C. Yan, Z. Li, X. Xu, Z. Shao, Nature 626 (2024) 105–110.
[268] X. Ru, M. Yang, S. Yin, Y. Wang, C. Hong, F. Peng, Y. Yuan, C. Sun, C. Xue, M. Qu, J. Wang, J. Lu, L. Fang, H. Deng, T. Xie, S. Liu, Z. Li, X. Xu, Joule 8 (2024) 1092–1104.
[269] K. Domanski, J.-P. Correa-Baena, N. Mine, M.K. Nazeeruddin, A. Abate, M. Saliba, W. Tress, A. Hagfeldt, M. Grätzel, ACS Nano 10 (2016) 6306–6314.
[270] J.J. Yoo, G. Seo, M.R. Chua, T.G. Park, Y. Lu, F. Rotermund, Y.-K. Kim, C.S. Moon, N.J. Jeon, J.-P. Correa-Baena, V. Bulović, S.S. Shin, M.G. Bawendi, J. Seo, Nature 590 (2021) 587–593.
[271] H. Min, M. Kim, S.-U. Lee, H. Kim, G. Kim, K. Choi, J.H. Lee, S.I. Seok, Science 366 (2019) 749–753.
[272] F. Zhang, S.Y. Park, C. Yao, H. Lu, S.P. Dunfield, C. Xiao, S. Uličná, X. Zhao, L. Du Hill, X. Chen, X. Wang, L.E. Mundt, K.H. Stone, L.T. Schelhas, G. Teeter, S. Parkin, E.L. Ratcliff, Y.-L. Loo, J.J. Berry, M.C. Beard, Y. Yan, B.W. Larson, K. Zhu, Science 375 (2022) 71–76.
[273] P. Wu, S. Wang, X. Li, F. Zhang, Matter 5 (2022) 1137–1161.
[274] X.Y. Jiang, H.S. Li, Q.L. Zhou, Q. Wei, M.Y. Wei, L.Z. Jiang, Z. Wang, Z.J. Peng, F. Wang, Z.H. Zang, K.M. Xu, Y. Hou, S. Teale, W.J. Zhou, R. Si, X.Y. Gao, E. H. Sargent, Z.J. Ning, J. Am. Chem. Soc. 143 (2021) 10970–10976.
[275] T. Ye, K. Wang, Y. Hou, D. Yang, N. Smith, B. Magill, J. Yoon, R. Mudiyanselage, G. Khodaparast, K. Wang, S. Priya, J. Am. Chem. Soc. 143 (2021) 4319–4328.
[276] B. Chen, C.B. Fei, S.S. Chen, H.Y. Gu, X. Xiao, J.S. Huang, Nat. Commun. 12 (2021) 5859.
[277] M. Ren, Y.F. Miao, T.Y. Zhang, Z.X. Qin, Y.T. Chen, N. Wei, X.F. Qian, T.F. Wang, Y.X. Zhao, ACS Sustain. Chem. Eng. 9 (2021) 16519–16525.
[278] C.H. Chen, S.N. Cheng, F. Hu, Z.H. Su, K.L. Wang, L. Cheng, J. Chen, Y.R. Shi, Y. Xia, T.Y. Teng, X.Y. Gao, I. Yavuz, Y.H. Lou, Z.K. Wang, Adv Mater 36 (2024) 2403038.
[279] W. Yu, Y. Zou, H. Wang, S. Qi, C. Wu, X. Guo, Y. Liu, Z. Chen, B. Qu, L. Xiao, Chem. Soc. Rev. 53 (2024) 1769–1788.
[280] J. Zhao, Z. Zhang, G. Li, M.H. Aldamasy, M. Li, A. Abate, Adv. Energy Mater. 13 (2023) 2204233.
[281] J. Kang, S. Chen, M. Hao, J. Liu, M. Al-Mamun, P. Liu, Y. Wang, H. Yin, H. Zhao, J. Mater. Chem. A 10 (2022) 19618–19625.
[282] S. Lal, M. Righetto, B.W.J. Putland, H.C. Sansom, S.G. Motti, H. Jin, M. B. Johnston, H.J. Snaith, L.M. Herz, Adv. Funct. Mater. 34 (2024) 2315942.
[283] S. Valastro, E. Smecca, G. Mannino, C. Bongiorno, G. Fisicaro, S. Goedecker, V. Arena, C. Spampinato, I. Deretzis, S. Dattilo, A. Scamporrino, S. Carroccio, E. Fazio, F. Neri, F. Bisconti, A. Rizzo, C. Spinella, A. La Magna, A. Alberti, Nat. Sustain. 6 (2023) 974–983.
[284] S.S. Chen, Y.H. Deng, H.Y. Gu, S. Xu, S. Wang, Z.H. Yu, V. Blum, J.S. Huang, Nat Energy 5 (2020) 1003–1011.
[285] S.S. Chen, Y.H. Deng, X. Xiao, S. Xu, P.N. Rudd, J.S. Huang, Nat. Sustain. 4 (2021) 636–643.
[286] X. Li, F. Zhang, H.Y. He, J.J. Berry, K. Zhu, T. Xu, Nature 578 (2020) 555.
[287] X. Li, F. Zhang, J.X. Wang, J.H. Tong, T. Xu, K. Zhu, Nat. Sustain. 4 (2021) 1038.
[288] Z.X. Zhang, Y.T. Shi, J.J. Chen, P. Shen, H.S. Li, M.J. Yang, S.R. Wang, X.G. Li, F. Zhang, Mater. Horizons 11 (2024) 2449–2456.
[289] D. Prat, A. Wells, J. Hayler, H. Sneddon, C.R. McElroy, S. Abou-Shehada, P. J. Dunn, Green Chem 18 (2016) 288–296.
[290] S.Y. Park, J.S. Park, B.J. Kim, H. Lee, A. Walsh, K. Zhu, D.H. Kim, H.S. Jung, Nat. Sustain. 3 (2020) 1044–1051.
[291] K. Panigrahi, A. Nag, J. Phys. Chem. C 126 (2022) 8553–8564.
[292] J. Luo, X. Wang, S. Li, J. Liu, Y. Guo, G. Niu, L. Yao, Y. Fu, L. Gao, Q. Dong, C. Zhao, M. Leng, F. Ma, W. Liang, L. Wang, S. Jin, J. Han, L. Zhang, J. Etheridge, J. Wang, Y. Yan, E.H. Sargent, J. Tang, Nature 563 (2018) 541–545.
[293] H. Chen, L. Zhu, C. Xue, P. Liu, X. Du, K. Wen, H. Zhang, L. Xu, C. Xiang, C. Lin, M. Qin, J. Zhang, T. Jiang, C. Yi, L. Cheng, C. Zhang, P. Yang, M. Niu, W. Xu, J. Lai, Y. Cao, J. Chang, H. Tian, Y. Jin, X. Lu, L. Jiang, N. Wang, W. Huang, J. Wang, Nat. Commun. 12 (2021) 1421.
[294] A. Wang, Y. Guo, Z. Zhou, X. Niu, Y. Wang, F. Muhammad, H. Li, T. Zhang, J. Wang, S. Nie, Z. Deng, Chem. Sci. 10 (2019) 4573–4579.
[295] R. Wang, H. Xiang, J. Chen, Y. Li, Y. Zhou, W.C.H. Choy, Z. Fan, H. Zeng, ACS Energy Lett. 7 (2022) 2173–2188.
[296] J. Li, L. Yang, Q. Guo, P. Du, L. Wang, X. Zhao, N. Liu, X. Yang, J. Luo, J. Tang, Sci. Bull. 67 (2022) 178–185.

[297] J. Li, P. Du, Q. Guo, L. Sun, Z. Shen, J. Zhu, C. Dong, L. Wang, X. Zhang, L. Li, C. Yang, J. Pan, Z. Liu, B. Xia, Z. Xiao, J. Du, B. Song, J. Luo, J. Tang, Nat. Photon. 17 (2023) 435–441.
[298] J. Chen, J. Wang, X. Xu, J. Li, J. Song, S. Lan, S. Liu, B. Cai, B. Han, J.T. Precht, D. Ginger, H. Zeng, Nat. Photon. 15 (2021) 238–244.
[299] P. Chenna, S. Gandi, S. Pookatt, S.R. Parne, Mater. Today Electron. 5 (2023) 100057.
[300] R. Sun, D. Zhou, Y. Ding, Y. Wang, Y. Wang, X. Zhuang, S. Liu, N. Ding, T. Wang, W. Xu, H. Song, Light: Sci. Appl. 11 (2022) 340.
[301] Z. Ma, X. Ji, M. Wang, F. Zhang, Z. Liu, D. Yang, M. Jia, X. Chen, D. Wu, Y. Zhang, X. Li, Z. Shi, C. Shan, Adv. Sci. 9 (2022) 2202408.
[302] S. Jin, H. Yuan, T. Pang, M. Zhang, J. Li, Y. Zheng, T. Wu, R. Zhang, Z. Wang, D. Chen, Adv. Mater. 36 (2024) 2308487.
[303] Z. Li, S. Chu, Y. Zhang, W. Chen, J. Chen, Y. Yuan, S. Yang, H. Zhou, T. Chen, Z. Xiao, Adv. Mater. 34 (2022) 2203529.
[304] R. Wang, H. Xiang, H. Zeng, J. Inorg. Mater. 38 (2023) 1062.
[305] X.K. Liu, W.D. Xu, S. Bai, Y.Z. Jin, J.P. Wang, R.H. Friend, F. Gao, Nat. Mater. 20 (2021) 10–21.
[306] A. Fakharuddin, M.K. Gangishetty, M. Abdi-Jalebi, S.-H. Chin, A.R. bin Mohd Yusoff, D.N. Congreve, W. Tress, F. Deschler, M. Vasilopoulou, H.J. Bolink, Nat. Electron. 5 (2022) 203–216.
[307] J.S. Kim, J.-M. Heo, G.-S. Park, S.-J. Woo, C. Cho, H.J. Yun, D.-H. Kim, J. Park, S.-C. Lee, S.-H. Park, E. Yoon, N.C. Greenham, T.-W. Lee, Nature 611 (2022) 688–694.
[308] Y. Jiang, C. Sun, J. Xu, S. Li, M. Cui, X. Fu, Y. Liu, Y. Liu, H. Wan, K. Wei, T. Zhou, W. Zhang, Y. Yang, J. Yang, C. Qin, S. Gao, J. Pan, Y. Liu, S. Hoogland, E. H. Sargent, J. Chen, M. Yuan, Nature 612 (2022) 679–684.
[309] Y.-K. Wang, H. Wan, S. Teale, L. Grater, F. Zhao, Z. Zhang, H.-W. Duan, M. Imran, S.-D. Wang, S. Hoogland, L.-S. Liao, Nature 629 (2024) 586–591.
[310] J. Song, J. Li, X. Li, L. Xu, Y. Dong, H. Zeng, Adv. Mater. 27 (2015) 7162–7167.
[311] H. Li, Y. Feng, M. Zhu, Y. Gao, C. Fan, Q. Cui, Q. Cai, K. Yang, H. He, X. Dai, J. Huang, Z. Ye, Nat. Nanotechnol. 19 (2024) 638–645.
[312] Y. Gao, Q. Cai, Y. He, D. Zhang, Q. Cao, M. Zhu, Z. Ma, B. Zhao, H. He, D. Di, Z. Ye, X. Dai, Sci. Adv. 10 (2024) eado5645.
[313] G. Li, F.W.R. Rivarola, N.J.L.K. Davis, S. Bai, T.C. Jellicoe, F. de la Peña, S. Hou, C. Ducati, F. Gao, R.H. Friend, N.C. Greenham, Z.-K. Tan, Adv. Mater. 28 (2016) 3528–3534.
[314] X. Zhang, C. Sun, Y. Zhang, H. Wu, C. Ji, Y. Chuai, P. Wang, S. Wen, C. Zhang, W. W. Yu, J. Phys. Chem. Lett. 7 (2016) 4602–4610.
[315] T. Chiba, Y. Hayashi, H. Ebe, K. Hoshi, J. Sato, S. Sato, Y.-J. Pu, S. Ohisa, J. Kido, Nat. Photonics 12 (2018) 681–687.
[316] Y.-K. Wang, F. Yuan, Y. Dong, J.-Y. Li, A. Johnston, B. Chen, M.I. Saidaminov, C. Zhou, X. Zheng, Y. Hou, K. Bertens, H. Ebe, D. Ma, Z. Deng, S. Yuan, R. Chen, L. K. Sagar, J. Liu, J. Fan, P. Li, X. Li, Y. Gao, M.-K. Fung, Z.-H. Lu, O.M. Bakr, L.-S. Liao, E.H. Sargent, Angew. Chem. Int. Ed. 60 (2021) 16164–16170.
[317] Y.-K. Wang, K. Singh, J.-Y. Li, Y. Dong, X.-Q. Wang, J.M. Pina, Y.-J. Yu, R. Sabatini, Y. Liu, D. Ma, J. Liu, Z. Liu, Y. Gao, O. Voznyy, W. Ma, M.-K. Fung, L.-S. Liao, E.H. Sargent, Adv. Mater. 34 (2022) 2200854.
[318] J. Guo, M. Lu, X. Zhang, S. Sun, C. Han, Y. Zhang, X. Yang, S.V. Kershaw, W. Zheng, A.L. Rogach, ACS Nano 17 (2023) 9290–9301.
[319] H. Huang, F. Zhao, L. Liu, F. Zhang, X.G. Wu, L. Shi, B. Zou, Q. Pei, H. Zhong, ACS Appl. Mater. Interfaces 7 (2015) 28128–28133.
[320] X. Zhang, B. Xu, J. Zhang, Y. Gao, Y. Zheng, K. Wang, X.W. Sun, Adv. Funct. Mater. 26 (2016) 4595–4600.
[321] J. Li, L. Xu, T. Wang, J. Song, J. Chen, J. Xue, Y. Dong, B. Cai, Q. Shan, B. Han, H. Zeng, Adv. Mater. 29 (2017) 1603885.
[322] T. Chiba, K. Hoshi, Y.-J. Pu, Y. Takeda, Y. Hayashi, S. Ohisa, S. Kawata, J. Kido, ACS Appl. Mater. Interfaces 9 (2017) 18054–18060.
[323] J. Song, J. Li, L. Xu, J. Li, F. Zhang, B. Han, Q. Shan, H. Zeng, Adv. Mater. 30 (2018) 1800764.
[324] J. Song, T. Fang, J. Li, L. Xu, F. Zhang, B. Han, Q. Shan, H. Zeng, Adv. Mater. 30 (2018) 1805409.
[325] H. Wang, X. Gong, D. Zhao, Y.-B. Zhao, S. Wang, J. Zhang, L. Kong, B. Wei, R. Quintero-Bermudez, O. Voznyy, Y. Shang, Z. Ning, Y. Yan, E.H. Sargent, X. Yang, Joule 4 (2020) 1977–1987.
[326] Y.-H. Kim, S. Kim, A. Kakekhani, J. Park, J. Park, Y.-H. Lee, H. Xu, S. Nagane, R. B. Wexler, D.-H. Kim, S.H. Jo, L. Martínez-Sarti, P. Tan, A. Sadhanala, G.-S. Park, Y.-W. Kim, B. Hu, H.J. Bolink, S. Yoo, R.H. Friend, A.M. Rappe, T.-W. Lee, Nat. Photonics 15 (2021) 148–155.
[327] Q. Wan, W. Zheng, C. Zou, F. Carulli, C. Zhang, H. Song, M. Liu, Q. Zhang, L. Y. Lin, L. Kong, L. Li, S. Brovelli, ACS Energy Lett. 8 (2023) 927–934.
[328] W. Deng, X. Xu, X. Zhang, Y. Zhang, X. Jin, L. Wang, S.-T. Lee, J. Jie, Adv. Funct. Mater. 26 (2016) 4797–4802.
[329] P. Vashishtha, M. Ng, S.B. Shivarudraiah, J.E. Halpert, Chem. Mater. 31 (2019) 83–89.
[330] X. Zheng, S. Yuan, J. Liu, J. Yin, F. Yuan, W.-S. Shen, K. Yao, M. Wei, C. Zhou, K. Song, B.-B. Zhang, Y. Lin, M.N. Hedhili, N. Wehbe, Y. Han, H.-T. Sun, Z.-H. Lu, T.D. Anthopoulos, O.F. Mohammed, E.H. Sargent, L.-S. Liao, O.M. Bakr, ACS Energy Lett. 5 (2020) 793–798.
[331] Y. Dong, Y.-K. Wang, F. Yuan, A. Johnston, Y. Liu, D. Ma, M.-J. Choi, B. Chen, M. Chekini, S.-W. Baek, L.K. Sagar, J. Fan, Y. Hou, M. Wu, S. Lee, B. Sun, S. Hoogland, R. Quintero-Bermudez, H. Ebe, P. Todorovic, F. Dinic, P. Li, H. T. Kung, M.I. Saidaminov, E. Kumacheva, E. Spiecker, L.-S. Liao, O. Voznyy, Z.-H. Lu, E.H. Sargent, Nat. Nanotechnol. 15 (2020) 668–674.
[332] H. Zhu, G. Tong, J. Li, E. Xu, X. Tao, Y. Sheng, J. Tang, Y. Jiang, Adv. Mater. 34 (2022) 2205092.
[333] Y. Nong, J. Yao, J. Li, L. Xu, Z. Yang, C. Li, J. Song, Adv. Mater. 36 (2024) 2402325.
[334] Y. Gao, H. Li, X. Dai, X. Ying, Z. Liu, J. Qin, J. Guo, Z. Han, Y. Zhang, M. Zhu, X. Wu, Q. Cai, Y. Yang, L. Feng, X. Zhang, J. Huang, H. He, F. Gao, Z. Ye, Nat. Electron. 7 (2024) 487–496.
[335] D. Liu, K. Weng, H. Zhao, S. Wang, H. Qiu, X. Luo, S. Lu, L. Duan, S. Bai, H. Zhang, J. Li, ACS Nano 18 (2024) 6896–6907.
[336] Z. Yao, C. Bi, A. Liu, M. Zhang, J. Tian, Nano Energy 95 (2022) 106974.
[337] Y. Guo, Y. Jia, N. Li, M. Chen, S. Hu, C. Liu, N. Zhao, Adv. Funct. Mater. 30 (2020) 1910464.
[338] N. Li, Y. Jia, Y. Guo, N. Zhao, Adv. Mater. 34 (2022) 2108102.
[339] J. Ko, K. Ma, J.F. Joung, S. Park, J. Bang, Nano Lett 21 (2021) 2288–2295.
[340] M. Zhu, Y. Duan, N. Liu, H. Li, J. Li, P. Du, Z. Tan, G. Niu, L. Gao, Y. Huang, Z. Yin, J. Tang, Adv. Funct. Mater. 29 (2019) 1903294.
[341] X. Yang, S. Wang, Y. Hou, Y. Wang, T. Zhang, Y. Chen, G. Chen, C. Zhong, X. Fan, X. Kong, T. Wu, Y. Lu, Y. Lin, Z. Chen, Nano Lett 24 (2024) 3661–3669.
[342] J.I. Kwon, G. Park, G.H. Lee, J.H. Jang, N.J. Sung, S.Y. Kim, J. Yoo, K. Lee, H. Ma, M. Karl, T.J. Shin, M.H. Song, J. Yang, M.K. Choi, Sci. Adv. 8 (2022) eadd0697.
[343] K. Sun, D. Tan, X. Fang, X. Xia, D. Lin, J. Song, Y. Lin, Z. Liu, M. Gu, Y. Yue, J. Qiu, Science 375 (2022) 307–310.
[344] V. Heiskanen, M.R. Hamblin, Photochem. Photobiol. Sci. 17 (2018) 1003–1017.
[345] D. Botez, G.J. Herskowitz, Proc. IEEE 68 (1980) 689–731.
[346] J. Gruber, P. Marten, R. Petschacher, P. Russer, IEEE Trans. Commun. 26 (1978) 1088–1098.
[347] X. Deng, J.P.M.G. Linnartz, X. Long, G. Zhou, IEEE Access 7 (2019) 96787–96798.
[348] J.-Y. Oh, W. Stuerzlinger, Proc. - Graph. Interface (2002) 141–149.
[349] J. Carriere, W.-H. Yeh, C. Peng, P. Khulbe, L. Li, J. Choi, M. Mansuripur, R. Narayan, R. Anderson, in: E. Wolf (Ed.), Progress in Optics, Progress in Optics, 41, Elsevier, 2000, pp. 97–179.
[350] O.P. Kowalski, Semicond. Laser Diode Technol. Appl. (2012) 263–286.
[351] M. Erfanzadeh, P.D. Kumavor, Q. Zhu, Photoacoustics 9 (2018) 1–9.
[352] S.Z. Li, R. Chu, S. Liao, L. Zhang, IEEE Trans. Pattern Anal. Mach. Intell. 29 (2007) 627–639.
[353] K. Ohira, K. Kobayashi, N. Iizuka, H. Yoshida, M. Ezaki, H. Uemura, A. Kojima, K. Nakamura, H. Furuyama, H. Shibata, Opt. Express 18 (2010) 15440–15447.
[354] C. Basu, M. Wollweber, B. Roth, Adv. Opt. Technol. 2 (2013) 213–321.
[355] A.J.C. Kuehne, M.C. Gather, Chem. Rev. 116 (2016) 12823–12864.
[356] H. Jung, N. Ahn, V.I. Klimov, Nature Photonics 15 (2021) 643–655.
[357] J. Qin, Y. Tang, J. Zhang, T. Shen, M. Karlsson, T. Zhang, W. Cai, L. Shi, W.-X. Ni, F. Gao, Mater. Horizons 10 (2023) 1446–1453.
[358] J. Qin, X.-K. Liu, C. Yin, F. Gao, Trends Chem. 3 (2021) 34–46.
[359] H. Kim, L. Zhao, J.S. Price, A.J. Grede, K. Roh, A.N. Brigeman, M. Lopez, B. P. Rand, N.C. Giebink, Nat. Commun. 9 (2018) 4893.
[360] C. Zou, Y. Liu, D.S. Ginger, L.Y. Lin, ACS Nano 14 (2020) 6076–6086.
[361] L. Zhao, K. Roh, S. Kacmoli, K. Al Kurdi, S. Jhulki, S. Barlow, S.R. Marder, C. Gmachl, B.P. Rand, Adv. Mater. 32 (2020) 2000752.
[362] L. Zhao, K. Roh, S. Kacmoli, K. Al Kurdi, X. Liu, S. Barlow, S.R. Marder, C. Gmachl, B.P. Rand, Adv. Mater. 33 (2021) 2104867.
[363] S. Chen, C. Zhang, J. Lee, J. Han, A. Nurmikko, Adv. Mater. 29 (2017) 1604781.
[364] M. Saliba, S.M. Wood, J.B. Patel, P.K. Nayak, J. Huang, J.A. Alexander-Webber, B. Wenger, S.D. Stranks, M.T. Hörantner, J.T.-W. Wang, R.J. Nicholas, L.M. Herz, M.B. Johnston, S.M. Morris, H.J. Snaith, M.K. Riede, Adv. Mater. 28 (2016) 923–929.
[365] A. Zhizhchenko, S. Syubaev, A. Berestennikov, A.V. Yulin, A. Porfirev, A. Pushkarev, I. Shishkin, K. Golokhvast, A.A. Bogdanov, A.A. Zakhidov, A. A. Kuchmizhak, Y.S. Kivshar, S.V. Makarov, ACS Nano 13 (2019) 4140–4147.
[366] T. Kondo, T. Azuma, T. Yuasa, R. Ito, Solid State Commun. 105 (1998) 253–255.
[367] G. Xing, N. Mathews, S.S. Lim, N. Yantara, X. Liu, D. Sabba, M. Grätzel, S. Mhaisalkar, T.C. Sum, Nat. Mater. 13 (2014) 476–480.
[368] H. Dong, C. Zhang, X. Liu, J. Yao, Y.S. Zhao, Chem. Soc. Rev. 49 (2020) 951–982.
[369] C. Qin, A.S.D. Sandanayaka, C. Zhao, T. Matsushima, D. Zhang, T. Fujihara, C. Adachi, Nature 585 (2020) 53–57.
[370] J. Zhang, J. Qin, W. Cai, Y. Tang, H. Zhang, T. Wang, A. Bakulin, B. Hu, X.-K. Liu, F. Gao, Adv. Mater. 35 (2023) 2300922.
[371] W. Zou, R. Li, S. Zhang, Y. Liu, N. Wang, Y. Cao, Y. Miao, M. Xu, Q. Guo, D. Di, L. Zhang, C. Yi, F. Gao, R.H. Friend, J. Wang, W. Huang, Nat. Commun. 9 (2018) 608.
[372] A.P. Schlaus, M.S. Spencer, X.Y. Zhu, Acc. Chem. Res. 52 (2019) 2950–2959.
[373] K. Wang, S. Wang, S. Xiao, Q. Song, Adv. Opt. Mater. 6 (2018) 1800278.
[374] L. Li, S. Ye, J. Qu, F. Zhou, J. Song, G. Shen, Small 17 (2021) e2005606.
[375] C. Li, Y. Ma, Y. Xiao, L. Shen, L. Ding, InfoMat 2 (2020) 1247–1256.
[376] D. Zheng, T. Pauporté, Adv. Funct. Mater. 34 (2023) 2311205.
[377] Y. Meng, Z. Lai, F. Li, W. Wang, S. Yip, Q. Quan, X. Bu, F. Wang, Y. Bao, T. Hosomi, T. Takahashi, K. Nagashima, T. Yanagida, J. Lu, J.C. Ho, ACS Nano 14 (2020) 12749–12760.
[378] Z. Guo, J. Zhang, X. Liu, L. Wang, L. Xiong, J. Huang, Adv. Funct. Mater. 33 (2023) 2305508.
[379] X. Zhou, Z. Lu, L. Zhang, Q. Ke, Nano Energy 117 (2023) 108908.
[380] W. Yang, Y. Lei, Z. Jin, J. Mater. Chem. C 12 (2024) 7497–7512.
[381] G. Tong, H. Li, Z. Zhu, Y. Zhang, L. Yu, J. Xu, Y. Jiang, J. Phys. Chem. Lett. 9 (2018) 1592–1599.
[382] D. Li, W. Xu, D. Zhou, Y. Ji, N. Ding, X. Chen, J. Zhu, R. Sun, S. Lu, C. Ma, Z. Jia, G. Qin, X. Bai, H. Song, Adv. Opt. Mater. 9 (2021) 2100423.
[383] L. Lu, W. Weng, Y. Ma, Y. Liu, S. Han, X. Liu, H. Xu, W. Lin, Z. Sun, J. Luo, Angew. Chem. Int. Ed. 61 (2022) e202205030.
[384] C.-X. Li, S.-B. Cho, S.-H. Sohn, I.-K. Park, J. Alloys Comp. 973 (2024) 172925.

[385] J. Ma, M. Zhang, H. Jiang, X. Chen, W. Di, X. Li, Y. Zhang, C. Shan, Z. Shi, Nano Today 52 (2023) 101970.
[386] J. Ma, X. Xia, S. Yan, Y. Li, W. Liang, J. Yan, X. Chen, D. Wu, X. Li, Z. Shi, ACS Appl. Mater. Interfaces 13 (2021) 15409–15419.
[387] Y. Zhao, X. Yin, P. Li, Z. Ren, Z. Gu, Y. Zhang, Y. Song, Nano-Micro Lett. 15 (2023) 187.
[388] Z. Lai, Y. Meng, Q. Zhu, F. Wang, X. Bu, F. Li, W. Wang, C. Liu, F. Wang, J.C. Ho, Small 17 (2021) e2100442.
[389] B. Yao, Q. Wei, Y. Yang, W. Zhou, X. Jiang, H. Wang, M. Ma, D. Yu, Y. Yang, Z. Ning, Nano Lett. 23 (2023) 1938–1945.
[390] X. Feng, Y. He, W. Qu, J. Song, W. Pan, M. Tan, B. Yang, H. Wei, Nat. Commun. 13 (2022) 6106.
[391] C. Li, H. Wang, F. Wang, T. Li, M. Xu, H. Wang, Z. Wang, X. Zhan, W. Hu, L. Shen, Light Sci. Appl. 9 (2020) 31.
[392] Q. Dai, K. Xu, Y. Peng, W. Lv, Z. Zhao, L. Sun, Y. Wang, Q. Li, H. Zhu, Z. Zhou, C. Gu, Infrared Phys. Technol. 108 (2020) 103358.
[393] W. Ahmad, L. Pan, K. Khan, L. Jia, Q. Zhuang, Z. Wang, Adv. Funct. Mater. 33 (2023) 2300686.
[394] A. Elbanna, H. Jiang, Q. Fu, J.-F. Zhu, Y. Liu, M. Zhao, D. Liu, S. Lai, X.W. Chua, J. Pan, Z.X. Shen, L. Wu, Z. Liu, C.-W. Qiu, J. Teng, ACS Nano 17 (2023) 4134–4179.
[395] C. Hu, R. Chai, Z. Wei, L. Li, G. Shen, J. Semicond. 45 (2024) 052601.
[396] N. Alwadai, M.A. Haque, S. Mitra, T. Flemban, Y. Pak, T. Wu, I. Roqan, ACS Appl. Mater. Interfaces 9 (2017) 37832–37838.
[397] C. Perumal Veeramalai, S. Yang, R. Zhi, M. Sulaman, M.I. Saleem, Y. Cui, Y. Tang, Y. Jiang, L. Tang, B. Zou, Adv. Opt. Mater. 8 (2020) 2000215.
[398] D. Han, J. Wang, L. Agosta, Z. Zang, B. Zhao, L. Kong, H. Lu, I. Mosquera-Lois, V. Carnevali, J. Dong, J. Zhou, H. Ji, L. Pfeifer, S.M. Zakeeruddin, Y. Yang, B. Wu, U. Rothlisberger, X. Yang, M. Grätzel, N. Wang, Nature 622 (2023) 493–498.
[399] T. Wang, H.L. Loi, Q. Cao, G. Feng, Z. Guan, Q. Wei, C. Chen, M. Li, Y. Zhu, C. S. Lee, F. Yan, Adv. Mater. 36 (2024) 2402947.
[400] A. Ajayakumar, C. Muthu, M.G. Basavarajappa, A.V. Dev, R. Nishikubo, S. Chakraborty, A. Saeki, L. Dou, C. Vijayakumar, Adv. Funct. Mater. 34 (2023) 2304899.
[401] J. Zou, J. Liu, X. Wang, Z. Han, Y. Gu, Z. He, X. Lu, X. Xu, Y. Zou, ACS Appl. Electron. Mater. 5 (2023) 2829–2837.
[402] B.S. Qiao, S.Y. Wang, Z.H. Zhang, Z.D. Lian, Z.Y. Zheng, Z.P. Wei, L. Li, K.W. Ng, S.P. Wang, Z.B. Liu, Adv. Mater. 35 (2023) 2300632.
[403] Z. Lai, Z. Zeng, Y. Meng, Y. Zhang, Y. Shen, W. Wang, D. Li, D. Chen, D. Yin, S. W. Tsang, S. Yip, J.C. Ho, Adv. Funct. Mater. 33 (2023) 2305539.
[404] L. Wang, Y. Xue, M. Cui, Y. Huang, H. Xu, C. Qin, J. Yang, H. Dai, M. Yuan, Angew. Chem. Int. Ed. 132 (2020) 6504–6512.
[405] X. Wang, J. Li, Y. Chen, J. Ran, Y. Yuan, B. Yang, ACS Appl. Mater. Interfaces 14 (2022) 24583–24591.
[406] J. Liu, Y. Zou, B. Huang, Y. Gu, Y. Yang, Z. Han, Y. Zhang, X. Xu, H. Zeng, Nanoscale 12 (2020) 20386–20395.
[407] Q. Lin, A. Armin, P.L. Burn, P. Meredith, Laser Photon. Rev. 10 (2016) 1047–1053.
[408] Y. Zhao, C. Li, J. Jiang, B. Wang, L. Shen, Small 16 (2020) e2001534.
[409] H.L. Zhu, H. Lin, Z. Song, Z. Wang, F. Ye, H. Zhang, W.-J. Yin, Y. Yan, W.C. H. Choy, ACS Nano 13 (2019) 11800–11808.
[410] W. Wang, D. Zhao, F. Zhang, L. Li, M. Du, C. Wang, Y. Yu, Q. Huang, M. Zhang, L. Li, J. Miao, Z. Lou, G. Shen, Y. Fang, Y. Yan, Adv. Funct. Mater. 27 (2017) 1703953.
[411] W. Hu, H. Cong, W. Huang, Y. Huang, L. Chen, A. Pan, C. Xue, Light Sci. Appl. 8 (2019) 106.
[412] F. Zhao, K. Xu, X. Luo, Y. Liang, Y. Peng, F. Lu, Adv. Opt. Mater. 6 (2017) 1700509.
[413] W. Xu, Y. Guo, X. Zhang, L. Zheng, T. Zhu, D. Zhao, W. Hu, X. Gong, Adv. Funct. Mater. 28 (2017) 1705541.
[414] R.A.H. Tsai, J.-C. Blancon, C.C. Stoumpos, O. Durand, J.W. Strzalka, B. Chen, R. Verduzco, P.M. Ajayan, S. Tretiak, J. Even, M.A. Alam, M.G. Kanatzidis, W. Nie, A.D. Mohite, Science 360 (2018) 67–70.
[415] Y. Zou, J. Eichhorn, J. Zhang, F.A.C. Apfelbeck, S. Yin, L. Wolz, C.-C. Chen, I. D. Sharp, P. Müller-Buschbaum, ACS Energy Lett. 9 (2024) 388–399.
[416] X. Qiu, J. Xia, Y. Liu, P.A. Chen, L. Huang, H. Wei, J. Ding, Z. Gong, X. Zeng, C. Peng, C. Chen, X. Wang, L. Jiang, L. Liao, Y. Hu, Adv. Mater. 35 (2023) 2305648.
[417] I. López-Fernández, D. Valli, C.Y. Wang, S. Samanta, T. Okamoto, Y.T. Huang, K. Sun, Y. Liu, V.S. Chirvony, A. Patra, J. Zito, L. De Trizio, D. Gaur, H.T. Sun, Z. Xia, X. Li, H. Zeng, I. Mora-Seró, N. Pradhan, J.P. Martínez-Pastor, P. Müller-Buschbaum, V. Biju, T. Debnath, M. Saliba, E. Debroye, R.L.Z. Hoye, I. Infante, L. Manna, L. Polavarapu, Adv. Funct. Mater. 34 (2023) 2307896.
[418] M. Xiao, F. Huang, W. Huang, Y. Dkhissi, Y. Zhu, J. Etheridge, A. Gray-Weale, U. Bach, Y.B. Cheng, L. Spiccia, Angew. Chem. Int. Ed. Engl. 53 (2014) 9898–9903.
[419] Z. Xiao, Q. Dong, C. Bi, Y. Shao, Y. Yuan, J. Huang, Adv. Mater. 26 (2014) 6503–6509.
[420] Y. Zhang, G. Grancini, Y. Feng, A.M. Asiri, M.K. Nazeeruddin, ACS Energy Lett. 2 (2017) 802–806.
[421] M.I. Saidaminov, A.L. Abdelhady, B. Murali, E. Alarousu, V.M. Burlakov, W. Peng, I. Dursun, L. Wang, Y. He, G. Maculan, A. Goriely, T. Wu, O.F. Mohammed, O. M. Bakr, Nat. Commun. 6 (2015) 7586.
[422] Y.F.Q. Dong, Y. Shao, P. Mulligan, J. Qiu, L. Cao, J. Huang, Science 347 (2015) 6225.
[423] D. Pan, Y. Fu, N. Spitha, Y. Zhao, C.R. Roy, D.J. Morrow, D.D. Kohler, J.C. Wright, S. Jin, Nat. Nanotechnol. 16 (2021) 159–165.
[424] Y. Meng, C. Lan, F. Li, S. Yip, R. Wei, X. Kang, X. Bu, R. Dong, H. Zhang, J.C. Ho, ACS Nano 13 (2019) 6060–6070.
[425] X. Fu, W. Li, X. Zeng, C. Yan, X. Peng, Y. Gao, Q. Wang, J. Cao, S. Yang, W. Yang, J. Phys. Chem. Lett. 13 (2022) 2217–2225.
[426] L. He, G. Hu, J. Jiang, W. Wei, X. Xue, K. Fan, H. Huang, L. Shen, Adv. Mater. 35 (2023) 2210016.
[427] W. Zheng, X. Peng, W. Zhai, L. Huang, P. Chen, P. Shi, X. Zhou, J. Wan, Z. Yan, J. M. Liu, J. Mater. Chem. A 12 (2024) 11020–11027.
[428] Z. Lai, R. Dong, Q. Zhu, Y. Meng, F. Wang, F. Li, X. Bu, X. Kang, H. Zhang, Q. Quan, W. Wang, F. Wang, S. Yip, J.C. Ho, ACS Appl. Mater. Interfaces 12 (2020) 39567–39577.
[429] X. Sun, F. Wang, X. Guo, J. Wu, S. Li, Y. Shi, L. Pan, IEEE Electron Device Lett. 45 (2024) 621–624.
[430] Y. Zhan, Q. Cheng, Y. Song, M. Li, Adv. Funct. Mater. 32 (2022) 2200385.
[431] T. Wang, D. Zheng, K. Vegso, N. Mrkyvkova, P. Siffalovic, X. Yuan, M.G. Somekh, L. Coolen, T. Pauporte, F. Fu, Nano Energy 116 (2023) 108827.
[432] L. Huang, L. Wu, Q. Sun, C. Jin, J. Wang, S. Fu, Z. Wu, X. Liu, Z. Hu, J. Zhang, J. Sun, X. Zhu, Y. Zhu, J. Phys. Chem. Lett. 12 (2021) 12098–12106.
[433] Y. Fang, A. Armin, P. Meredith, J. Huang, Nat. Photonics 13 (2019) 1–4.
[434] F. Wang, T. Zhang, R. Xie, Z. Wang, W. Hu, Nat. Commun. 14 (2023) 2224.
[435] Y. Wu, J. Feng, Z. Yang, Y. Liu, S. Liu, Adv. Sci. 10 (2023) 2205536.
[436] Q. Zhou, W. Li, J. Xiao, A. Li, X. Han, Adv. Funct. Mater. 34 (2024) 2402902.
[437] Y. Zhou, J. Chen, O.M. Bakr, O.F. Mohammed, ACS Energy Lett. 6 (2021) 739–768.
[438] V.B. Mykhaylyk, H. Kraus, M. Saliba, Mater. Horizons 6 (2019) 1740–1747.
[439] B. Jia, D. Chu, N. Li, Y. Zhang, Z. Yang, Y. Hu, Z. Zhao, J. Feng, X. Ren, H. Zhang, G. Zhao, H. Sun, N. Yuan, J. Ding, Y. Liu, S.F. Liu, ACS Energy Lett. 8 (2023) 590–599.
[440] N. Kawano, M. Koshimizu, G. Okada, Y. Fujimoto, N. Kawaguchi, T. Yanagida, K. Asai, Sci. Rep. 7 (2017) 14754.
[441] A. Xie, C. Hettiarachchi, F. Maddalena, M.E. Witkowski, M. Makowski, W. Drozdowski, A. Arramel, A.T.S. Wee, S.V. Springham, P.Q. Vuong, H.J. Kim, C. Dujardin, P. Coquet, M.D. Birowosuto, C. Dang, Commun. Mater. 1 (2020) 37.
[442] D. Nakauchi, N. Kawano, N. Kawaguchi, T. Yanagida, Jpn. J. Appl. Phys. 59 (2020) SCCB04.
[443] M. Akatsuka, N. Kawano, T. Kato, D. Nakauchi, G. Okada, N. Kawaguchi, T. Yanagida, Nucl. Inst. Methods Phys. Res. Sec. A-Acceler. Spectrometers Detect. Assoc. Equip. 954 (2020) 161372.
[444] T. Jin, Z. Liu, J. Luo, J.-H. Yuan, H. Wang, Z. Xie, W. Pan, H. Wu, K.-H. Xue, L. Liu, Z. Hu, Z. Zheng, J. Tang, G. Niu, Nat. Commun. 14 (2023) 2808.
[445] M. Xia, Z. Xie, H. Wang, T. Jin, L. Liu, J. Kang, Z. Sang, X. Yan, B. Wu, H. Hu, J. Tang, G. Niu, Adv. Mater. 35 (2023) 2211769.
[446] Z. Bao, Y.-J. Tseng, W. You, W. Zheng, X. Chen, S. Mahlik, A. Lazarowska, T. Lesniewski, M. Grinberg, C. Ma, W. Sun, W. Zhou, R.-S. Liu, J.P. Attfield, J. Phys. Chem. Lett. 11 (2020) 7637–7642.
[447] Z. Qin, S. Dai, V.G. Hadjiev, C. Wang, L. Xie, Y. Ni, C. Wu, G. Yang, S. Chen, L. Deng, Q. Yu, G. Feng, Z.M. Wang, J. Bao, Chem. Mater. 31 (2019) 9098–9104.
[448] Y. Li, W. Shao, L. Chen, J. Wang, J. Nie, H. Zhang, S. Zhang, R. Gao, X. Ouyang, X. Ouyang, Q. Xu, NPG Asia Mater. 13 (2021) 40.
[449] F. Cao, D. Yu, W. Ma, X. Xu, B. Cai, Y.M. Yang, S. Liu, L. He, Y. Ke, S. Lan, K.-L. Choy, H. Zeng, ACS Nano 14 (2020) 5183–5193.
[450] S. Cheng, A. Beitlerova, R. Kucerkova, M. Nikl, G. Ren, Y. Wu, physica status solidi (RRL) – Rapid Res. Lett. 14 (2020) 2000374.
[451] S. Cheng, M. Nikl, A. Beitlerova, R. Kucerkova, X. Du, G. Niu, Y. Jia, J. Tang, G. Ren, Y. Wu, Adv. Opt. Mater. 9 (2021) 2100460.
[452] Q. Wang, Q. Zhou, M. Nikl, J. Xiao, R. Kucerkova, A. Beitlerova, V. Babin, P. Prusa, V. Linhart, J. Wang, X. Wen, G. Niu, J. Tang, G. Ren, Y. Wu, Adv. Opt. Mater. 10 (2022) 2200304.
[453] Q. Yao, J. Li, X. Li, Y. Ma, H. Song, Z. Li, Z. Wang, X. Tao, Adv. Mater. 35 (2023) 2304938.
[454] H. Wu, Q. Wang, A. Zhang, G. Niu, M. Nikl, C. Ming, J. Zhu, Z. Zhou, Y.-Y. Sun, G. Nan, G. Ren, Y. Wu, J. Tang, Sci. Adv. 9 (2023) eadh1789.
[455] S. Cao, J. a. Lai, Y. Wang, K. An, T. Jiang, M. Wu, P. Feng, P. He, X. Tang, Laser Photon. Rev. 18 (2024) 2400799.
[456] H.-J. Yang, W. Xiang, X. Zhang, J.-Y. Wang, L.-J. Xu, Z.-N. Chen, J. Mater. Chem. C 12 (2024) 438–442.
[457] L.-J. Xu, X. Lin, Q. He, M. Worku, B. Ma, Nat. Commun. 11 (2020) 4329.
[458] Z.-L. He, J.-H. Wei, J.-B. Luo, Z.-Z. Zhang, J.-H. Chen, X.-X. Guo, D.-B. Kuang, Laser Photon. Rev. 18 (2024) 2301249.
[459] B. Li, J. Jin, M. Yin, K. Han, Y. Zhang, X. Zhang, A. Zhang, Z. Xia, Y. Xu, Chem. Sci. 14 (2023) 12238–12245.
[460] Y. Wu, D. Han, B.C. Chakoumakos, H. Shi, S. Chen, M.-H. Du, I. Greeley, M. Loyd, D.J. Rutstrom, L. Stand, M. Koschan, C.L. Melcher, J. Mater. Chem. C 6 (2018) 6647–6655.
[461] D. Rutstrom, L. Stand, C. Delzer, M. Kapusta, J. Glodo, E. van Loef, K. Shah, M. Koschan, C.L. Melcher, M. Zhuravleva, Opt. Mater. 133 (2022) 112912.
[462] Q. He, C. Zhou, L. Xu, S. Lee, X. Lin, J. Neu, M. Worku, M. Chaaban, B. Ma, ACS Mater. Lett. 2 (2020) 633–638.
[463] M. Zhang, X. Wang, B. Yang, J. Zhu, G. Niu, H. Wu, L. Yin, X. Du, M. Niu, Y. Ge, Q. Xie, Y. Yan, J. Tang, Adv. Funct. Mater. 31 (2021) 2007921.
[464] H. Sun, X. Yang, P. Li, Y. Bai, Q. Meng, H. Zhao, Q. Wang, Z. Wen, L. Huang, D. Huang, W.W. Yu, H. Chen, F. Liu, Nano Letters 24 (2024) 10355–10361.
[465] A. Burger, E. Rowe, M. Groza, K. Morales Figueroa, N.J. Cherepy, P.R. Beck, S. Hunter, S.A. Payne, Appl. Phys. Lett. 107 (2015) 143505.

[466] V. Morad, Y. Shynkarenko, S. Yakunin, A. Brumberg, R.D. Schaller, M. V. Kovalenko, J. Am. Chem. Soc. 141 (2019) 9764–9768.
[467] S.-B. Xiao, X. Zhang, X. Mao, H.-J. Yang, Z.-N. Chen, L.-J. Xu, Adv. Funct. Mater. 34 (2024) 2404003.
[468] X. Xu, Y.-M. Xie, H. Shi, Y. Wang, X. Zhu, B.-X. Li, S. Liu, B. Chen, Q. Zhao, Adv. Mater. 36 (2024) 2303738.
[469] M. H. Miah, M. U. Khandaker, M. Aminul Islam, E. A. M. Nur, H. Osman and M. H. Ullah, *RSC Adv.*, 2024, 14, 6656-6698.
[470] S. Cheng, A. Beitlerova, R. Kucerkova, E. Mihokova, M. Nikl, Z. Zhou, G. Ren, Y. Wu, ACS Appl. Mater. Interfaces 13 (2021) 12198–12202.
[471] D. Yu, P. Wang, F. Cao, Y. Gu, J. Liu, Z. Han, B. Huang, Y. Zou, X. Xu, H. Zeng, Nat. Commun. 11 (2020) 3395.
[472] X. Li, J. Chen, D. Yang, X. Chen, D. Geng, L. Jiang, Y. Wu, C. Meng, H. Zeng, Nat. Commun. 12 (2021) 3879.
[473] Q. Wang, C. Wang, H. Shi, J. Chen, J. Yang, A. Beitlerova, R. Kucerkova, Z. Zhou, Y. Li, M. Nikl, X. Sun, X. OuYang, Y. Wu, Light: Sci. Appl. 13 (2024) 190.
[474] D. Han, H. Shi, W. Ming, C. Zhou, B. Ma, B. Saparov, Y.-Z. Ma, S. Chen, M.-H. Du, J. Mater. Chem. C 6 (2018) 6398–6405.
[475] M. Zhou, H. Jiang, T. Hou, S. Hou, J. Li, X. Chen, C. Di, J. Xiao, H. Li, D. Ju, Chem. Eng. J. 490 (2024) 151823.
[476] Z.-Z. Zhang, J.-H. Wei, J.-B. Luo, X.-D. Wang, Z.-L. He, D.-B. Kuang, ACS Appl. Mater. Interfaces 14 (2022) 47913–47921.
[477] X. Song, L. Liu, P. Wan, X. Ouyang, T. Bai, Q. Wang, R. Gao, R. Jia, Q. Gao, Y. Wu, W. Zheng, X. Ouyang, ACS Appl. Electron. Mater. 5 (2023) 6805–6812.
[478] R. Zheng, L. Wang, Y. Liu, J. Chen, P. Xiao, Q. Xie, J. Cryst. Growth 627 (2024) 127512.
[479] M. Zhang, J. Zhu, B. Yang, G. Niu, H. Wu, X. Zhao, L. Yin, T. Jin, X. Liang, J. Tang, Nano Lett. 21 (2021) 1392–1399.
[480] W. Shao, T. He, L. Wang, J.-X. Wang, Y. Zhou, B. Shao, E. Ugur, W. Wu, Z. Zhang, H. Liang, S. De Wolf, O.M. Bakr, O.F. Mohammed, Adv. Mater. 36 (2024) 2312053.
[481] K. Han, K. Sakhatskyi, J. Jin, Q. Zhang, M.V. Kovalenko, Z. Xia, Adv. Mater. 34 (2022) 2110420.
[482] W. Li, Z.J. Coppens, L.V. Besteiro, W. Wang, A.O. Govorov, J. Valentine, Nat. Commun. 6 (2015) 8379.
[483] S.D. Namgung, R.M. Kim, Y.-C. Lim, J.W. Lee, N.H. Cho, H. Kim, J.-S. Huh, H. Rhee, S. Nah, M.-K. Song, J.-Y. Kwon, K.T. Nam, Nat. Commun. 13 (2022) 5081.
[484] H. Han, Y.J. Lee, J. Kyhm, J.S. Jeong, J.-H. Han, M.K. Yang, K.M. Lee, Y. Choi, T.-H. Yoon, H. Ju, S.-k. Ahn, J.A. Lim, Adv. Funct. Mater. 30 (2020) 2006236.
[485] A.V. Kimel, A. Kirilyuk, P.A. Usachev, R.V. Pisarev, A.M. Balbashov, T. Rasing, Nature 435 (2005) 655–657.
[486] H.C. Aspinall, Chem. Rev. 102 (2002) 1807–1850.
[487] Y. Yang, R.C. da Costa, M.J. Fuchter, A.J. Campbell, Nat. Photonics 7 (2013) 634–638.
[488] Z.G. Yu, Sci. Rep. 6 (2016) 28576.
[489] H. Lu, Z.V. Vardeny, M.C. Beard, Nat. Rev. Chem. 6 (2022) 470–485.
[490] Y. Zheng, X. Han, P. Cheng, X. Jia, J. Xu, X.-H. Bu, J. Am. Chem. Soc. 144 (2022) 16471–16479.
[491] D.G. Billing, A. Lemmerer, Acta Crystallograph. Sec. E 59 (2003) m381–m383.
[492] D.G. Billing, A. Lemmerer, CrystEngComm 8 (2006) 686–695.
[493] J. Ahn, E. Lee, J. Tan, W. Yang, B. Kim, J. Moon, Mater. Horizons 4 (2017) 851–856.
[494] J. Ma, C. Fang, C. Chen, L. Jin, J. Wang, S. Wang, J. Tang, D. Li, ACS Nano 13 (2019) 3659–3665.
[495] C. Chen, L. Gao, W. Gao, C. Ge, X. Du, Z. Li, Y. Yang, G. Niu, J. Tang, Nat. Commun. 10 (2019) 1927.
[496] J. Wang, C. Fang, J. Ma, S. Wang, L. Jin, W. Li, D. Li, ACS Nano 13 (2019) 9473–9481.
[497] L. Wang, Y. Xue, M. Cui, Y. Huang, H. Xu, C. Qin, J. Yang, H. Dai, M. Yuan, Angew. Chem. Int. Ed. 59 (2020) 6442–6450.
[498] A. Ishii, T. Miyasaka, Sci. Adv. 6 (2020) eabd3274.
[499] D. Li, X. Liu, W. Wu, Y. Peng, S. Zhao, L. Li, M. Hong, J. Luo, Angew. Chem. 133 (2021) 8496–8499.
[500] J. Hao, H. Lu, L. Mao, X. Chen, M.C. Beard, J.L. Blackburn, ACS Nano 15 (2021) 7608–7617.
[501] Y. Peng, X. Liu, L. Li, Y. Yao, H. Ye, X. Shang, X. Chen, J. Luo, J. Am. Chem. Soc. 143 (2021) 14077–14082.
[502] J. Wu, X. Zhang, S. You, Z.-K. Zhu, T. Zhu, Z. Wang, R. Li, Q. Guan, L. Liang, X. Niu, J. Luo, Small 19 (2023) 2302443.
[503] G. Long, C. Jiang, R. Sabatini, Z. Yang, M. Wei, L.N. Quan, Q. Liang, A. Rasmita, M. Askerka, G. Walters, X. Gong, J. Xing, X. Wen, R. Quintero-Bermudez, H. Yuan, G. Xing, X.R. Wang, D. Song, O. Voznyy, M. Zhang, S. Hoogland, W. Gao, Q. Xiong, E.H. Sargent, Nat. Photonics 12 (2018) 528–533.
[504] H. Dong, C. Ran, W. Gao, N. Sun, X. Liu, Y. Xia, Y. Chen, W. Huang, Adv. Energy Mater. 12 (2022) 2102213.
[505] T. Imran, S. Rauf, H. Raza, L. Aziz, R. Chen, S. Liu, J. Wang, M.A. Ahmad, S. Zhang, Y. Zhang, Z. Liu, W. Chen, Adv. Energy Mater. 12 (2022) 2200305.
[506] B. Li, B. Chang, L. Pan, Z. Li, L. Fu, Z. He, L. Yin, ACS Energy Lett. 5 (2020) 3752–3772.
[507] J. Wang, Z. Gao, J. Yang, M. Lv, H. Chen, D.-J. Xue, X. Meng, S. Yang, Adv. Energy Mater. 11 (2021) 2102131.
[508] D.G. Billing, A. Lemmerer, Acta Crystallograp. Sec. E 59 (2003) m381–m383.
[509] H.-Y. Ye, Y.-Y. Tang, P.-F. Li, W.-Q. Liao, J.-X. Gao, X.-N. Hua, H. Cai, P.-P. Shi, Y.-M. You, R.-G. Xiong, Science 361 (2018) 151–155.
[510] J.R. Brandt, F. Salerno, M.J. Fuchter, Nat. Rev. Chem. 1 (2017) 0045.
[511] J.L. Greenfield, J. Wade, J.R. Brandt, X. Shi, T.J. Penfold, M.J. Fuchter, Chem. Sci. 12 (2021) 8589–8602.
[512] B. Ni, H. Cölfen, SmartMat 2 (2021) 17–32.
[513] B. Gholipour, G. Adamo, D. Cortecchia, H.N.S. Krishnamoorthy, M.D. Birowosuto, N.I. Zheludev, C. Soci, Adv. Mater. 29 (2017) 1604268.
[514] S.V. Makarov, V. Milichko, E.V. Ushakova, M. Omelyanovich, A. Cerdan Pasaran, R. Haroldson, B. Balachandran, H. Wang, W. Hu, Y.S. Kivshar, A.A. Zakhidov, ACS Photonics 4 (2017) 728–735.
[515] Z. Wang, Y. Wang, G. Adamo, J. Teng, H. Sun, Laser Photon. Rev. 13 (2019) 1800276.
[516] C. Zhang, S. Xiao, Y. Wang, Y. Gao, Y. Fan, C. Huang, N. Zhang, W. Yang, Q. Song, Laser Photon. Rev. 13 (2019) 1900079.
[517] P. Schulz, D. Cahen, A. Kahn, Chem. Rev. 119 (2019) 3349–3417.
[518] M. Xiao, F. Huang, W. Huang, Y. Dkhissi, Y. Zhu, J. Etheridge, A. Gray-Weale, U. Bach, Y.-B. Cheng, L. Spiccia, Angew. Chem. Int. Ed. 53 (2014) 9898–9903.
[519] K.O. Brinkmann, J. He, F. Schubert, J. Malerczyk, C. Kreusel, F. van gen Hassend, S. Weber, J. Song, J. Qu, T. Riedl, ACS Appl. Mater. Interfaces 11 (2019) 40172–40179.
[520] L. Fu, H. Li, L. Wang, R. Yin, B. Li, L. Yin, Energy Environ. Sci. 13 (2020) 4017–4056.
[521] B.-w. Park, N. Kedem, M. Kulbak, D.Y. Lee, W.S. Yang, N.J. Jeon, J. Seo, G. Kim, K.J. Kim, T.J. Shin, G. Hodes, D. Cahen, S.I. Seok, Nat. Commun. 9 (2018) 3301.
[522] F. Wang, S. Bai, W. Tress, A. Hagfeldt, F. Gao, NPJ Flexible Electron. 2 (2018) 22.
[523] G. Long, Y. Zhou, M. Zhang, R. Sabatini, A. Rasmita, L. Huang, G. Lakhwani, W. Gao, Adv. Mater. 31 (2019) 1807628.
[524] G. Chen, X. Liu, J. An, S. Wang, X. Zhao, Z. Gu, C. Yuan, X. Xu, J. Bao, H.S. Hu, J. Li, X. Wang, Nat. Chem. 15 (2023) 1581–1590.
[525] T. Sanders, Y. Liu, V. Buchner, P.B. Tchounwou, Rev. Environ. Health 24 (2009) 15–46.
[526] H. Lu, C. Xiao, R. Song, T. Li, A.E. Maughan, A. Levin, R. Brunecky, J.J. Berry, D. B. Mitzi, V. Blum, M.C. Beard, J. Am. Chem. Soc. 142 (2020) 13030–13040.
[527] F.P.G. de Arquer, A. Armin, P. Meredith, E.H. Sargent, Nat. Rev. Mater. 2 (2017) 16100.
[528] J.W. Park, B.H. Kang, H.J. Kim, Adv. Funct. Mater. 30 (2020) 1904632.
[529] C. Chen, J. Gao, S.-P. Feng, Int. Mater. Rev. 68 (2023) 301–322.
[530] Z. Saki, M.M. Byranvand, N. Taghavinia, M. Kedia, M. Saliba, Energy Environ. Sci. 14 (2021) 5690–5722.
[531] M. Saliba, Adv. Energy Mater. 9 (2019) 1803754.
[532] M. Anaya, G. Lozano, M.E. Calvo, H. Miguez, Joule 1 (2017) 769–793.
[533] X. Rodriguez-Martinez, E. Pascual-San-Jose, M. Campoy-Quiles, Energy Environ. Sci. 14 (2021) 3301–3322.
[534] W.Y. Wang, J. Li, W. Liu, Z.-K. Liu, Computat. Mater. Sci. 158 (2019) 42–48.
[535] S. Hong, C.H. Liow, J.M. Yuk, H.R. Byon, Y. Yang, E. Cho, J. Yeom, G. Park, H. Kang, S. Kim, Y. Shim, M. Na, C. Jeong, G. Hwang, H. Kim, H. Kim, S. Eom, S. Cho, H. Jun, Y. Lee, A. Baucour, K. Bang, M. Kim, S. Yun, J. Ryu, Y. Han, A. Jetybayeva, P.-P. Choi, J.C. Agar, S.V. Kalinin, P.W. Voorhees, P. Littlewood, H.M. Lee, ACS Nano 15 (2021) 3971–3995.
[536] M. Ahmadi, M. Ziatdinov, Y. Zhou, E.A. Lass, S.V. Kalinin, Joule 5 (2021) 2797–2822.
[537] X. Q. Wang, P. Chen, C. L. Chow and D. Lau, *Matter*, 2023, 6, 1831-1859.
[538] X. Zheng, X. Zhang, T.-T. Chen, I. Watanabe, Adv. Mater. 35 (2023) 2302530.
[539] L. Luer, I.M. Peters, V.M. Le Corre, K. Forberich, D.M. Guldi, C.J. Brabec, Adv. Mater. 36 (2024) 2308578.
[540] M. Ziatdinov, Y. Liu, K. Kelley, R. Vasudevan, S.V. Kalinin, Acs Nano 16 (2022) 13492–13512.
[541] B. Burger, P.M. Maffettone, V.V. Gusev, C.M. Aitchison, Y. Bai, X. Wang, X. Li, B. M. Alston, B. Li, R. Clowes, N. Rankin, B. Harris, R.S. Sprick, A.I. Cooper, Nature 583 (2020) 237–241.
[542] C.W. Coley, D.A. Thomas, J.A.M. Lummiss, J.N. Jaworski, C.P. Breen, V. Schultz, T. Hart, J.S. Fishman, L. Rogers, H. Gao, R.W. Hicklin, P.P. Plehiers, J. Byington, J.S. Piotti, W.H. Green, A.J. Hart, T.F. Jamison, K.F. Jensen, Science 365 (2019) eaax1566.
[543] H. Zhao, W. Chen, H. Huang, Z. Sun, Z. Chen, L. Wu, B. Zhang, F. Lai, Z. Wang, M. L. Adam, C.H. Pang, P.K. Chu, Y. Lu, T. Wu, J. Jiang, Z. Yin, X.-F. Yu, Nat. Synth. 2 (2023) 505–514.
[544] S. Langner, F. Häse, J.D. Perea, T. Stubhan, J. Hauch, L.M. Roch, T. Heumueller, A. Aspuru-Guzik, C.J. Brabec, Adv. Mater. 32 (2020) 1907801.
[545] X. Zhang, Z. Wang, A. M. Lawan, J. Wang, C. Y. Hsieh, C. Duan, C. H. Pang, P. K. Chu, X. F. Yu and H. Zhao, *InfoMat*, 2023, 5, e12406.
[546] B.P. MacLeod, F.G.L. Parlane, C.C. Rupnow, K.E. Dettelbach, M.S. Elliott, T. D. Morrissey, T.H. Haley, O. Proskurin, M.B. Rooney, N. Taherimakhsousi, D. J. Dvorak, H.N. Chiu, C.E.B. Waizenegger, K. Ocean, M. Mokhtari, C. P. Berlinguette, Nat. Commun. 13 (2022) 995.
[547] S. Sun, A. Tiihonen, F. Oviedo, Z. Liu, J. Thapa, Y. Zhao, N. T. P. Hartono, A. Goyal, T. Heumueller, C. Batali, A. Encinas, J. J. Yoo, R. Li, Z. Ren, I. M. Peters, C. J. Brabec, M. G. Bawendi, V. Stevanovic, J. Fisher, III and T. Buonassisi, *Matter*, 2021, 4, 1305-1322.
[548] B. Yilmaz, R. Yildirim, Nano Energy 80 (2021) 105546.
[549] M.A. Surmiak, T. Zhang, J. Lu, K.J. Rietwyk, S.R. Raga, D.P. McMeekin, U. Bach, Solar RRL 4 (2020) 2000097.
[550] B.P. MacLeod, F.G.L. Parlane, T.D. Morrissey, F. Häse, L.M. Roch, K.E. Dettelbach, R. Moreira, L.P.E. Yunker, M.B. Rooney, J.R. Deeth, V. Lai, G.J. Ng, H. Situ, R. H. Zhang, M.S. Elliott, T.H. Haley, D.J. Dvorak, A. Aspuru-Guzik, J.E. Hein, C. P. Berlinguette, Sci. Adv. 6 (2020) eaaz8867.
[551] J. Zhang, J.A. Hauch, C.J. Brabec, Acc. Chem. Res. 57 (2024) 1434–1445.

[552] Y. Zhao, J. Zhang, Z. Xu, S. Sun, S. Langner, N.T.P. Hartono, T. Heumueller, Y. Hou, J. Elia, N. Li, G.J. Matt, X. Du, W. Meng, A. Osvet, K. Zhang, T. Stubhan, Y. Feng, J. Hauch, E.H. Sargent, T. Buonassisi, C.J. Brabec, Nat. Commun. 12 (2021) 2191.
[553] X. Du, Y. Wang, Y. Cui, G. Rao, J. Huang, X. Chen, T. Zhou, C. Wu, Z. Yang, H. Cui, Y. Zhao, J. Xiong, Nat. Electron. 7 (2024) 984–990.
[554] Y. Li, S. Guo, B. Wang, J. Sun, L. Zhao, T. Wang, X. Yan, F. Liu, P. Sun, J. Wang, InfoMat 6 (2024) e12544.
[555] Y. Li, L. Yang, S. Deng, H. Huang, Y. Wang, Z. Xiong, S. Feng, S. Wang, T. Li, T. Zhang, InfoMat 5 (2023) e12463.
[556] H. Sun, X. Gao, L.Y. Guo, L.Q. Tao, Z.H. Guo, Y. Shao, T. Cui, Y. Yang, X. Pu, T. L. Ren, InfoMat 5 (2023) e12385.
[557] M. Xu, M. Xu, X. Miao, InfoMat 4 (2022) e12315.
[558] Z. Liu, J. Zhang, G. Rao, Z. Peng, Y. Huang, S. Arnold, B. Liu, C. Deng, C. Li, H. Li, H. Zhi, Z. Zhang, W. Zhou, J. Hauch, C. Yan, C.J. Brabec, Y. Zhao, ACS Energy Lett. 9 (2024) 662–670.
[559] Z. Qu, Y. Zhao, F. Ma, L. Mei, X.-K. Chen, H. Zhou, X. Chu, Y. Yang, Q. Jiang, X. Zhang, J. You, Nat. Commun. 15 (2024) 8620.
[560] H.L. Wei, T. Mukherjee, W. Zhang, J.S. Zuback, G.L. Knapp, A. De, T. DebRoy, Progr. Mater. Sci. 116 (2021) 100703.
[561] Z. Wang, A. Chen, K. Tao, Y. Han, J. Li, Adv. Mater. 36 (2024) 2306733.
[562] D. Meggiolaro, S.G. Motti, E. Mosconi, A.J. Barker, J. Ball, C. Andrea Riccardo Perini, F. Deschler, A. Petrozza, F. De Angelis, Energy Environ. Sci. 11 (2018) 702–713.
[563] M.H. Du, J. Phys. Chem. Lett. 6 (2015) 1461–1466.
[564] X. Zhang, M.E. Turiansky, J.-X. Shen, C.G. Van de Walle, Phys. Rev. B 101 (2020), 140101(R).
[565] J. Xu, A. Maxwell, M. Wei, Z. Wang, B. Chen, T. Zhu, E.H. Sargent, ACS Energy Lett 6 (2021) 4220–4227.
[566] X. Zhang, J. Kang, S.H. Wei, Nat. Comput. Sci. 3 (2023) 210–220.
[567] R. Grau-Crespo, S. Hamad, C.R.A. Catlow, N.H. de Leeuw, J. Phys.: Condensed Matter 19 (2007) 256201.
[568] M. Huang, Z. Zheng, Z. Dai, X. Guo, S. Wang, L. Jiang, J. Wei, S. Chen, J. Semicond. 43 (2022) 042101.
[569] I. Mosquera-Lois, S.R. Kavanagh, A. Walsh, D.O. Scanlon, J. Open Source Softw. 7 (2022) 4817.
[570] J.S. Park, S. Kim, Z. Xie, A. Walsh, Nat. Rev. Mat. 3 (2018) 194–210.
[571] K. Park, J.-H. Lee, J.-W. Lee, ACS Energy Lett 7 (2022) 1230–1239.
[572] A. Walsh, NPJ Comput. Mater. 7 (2021) 72.
[573] D. Wang, D. Han, X.-B. Li, S.-Y. Xie, N.-K. Chen, W.Q. Tian, D. West, H.-B. Sun, S. B. Zhang, Phys. Rev. Lett. 114 (2015) 196801.
[574] J. Xiao, K. Yang, D. Guo, T. Shen, H.-X. Deng, S.-S. Li, J.-W. Luo, S.-H. Wei, Phys. Rev. B 101 (2020) 165306.
[575] M. Chagas da Silva, M. Lorke, B. Aradi, M. Farzalipour Tabriz, T. Frauenheim, A. Rubio, D. Rocca, P. Deak, Phys. Rev. Lett. 126 (2021) 076401.
[576] J. Xu, A. Maxwell, Z. Song, A.S.R. Bati, H. Chen, C. Li, S.M. Park, Y. Yan, B. Chen, E.H. Sargent, Nat. Commun. 15 (2024) 2035.
[577] H. Wang, L. Zhang, J. Han, W. E, Comput. Phys. Commun. 228 (2018) 178–184.
[578] Z. Fan, Y. Wang, P. Ying, K. Song, J. Wang, Y. Wang, Z. Zeng, K. Xu, E. Lindgren, J.M. Rahm, A.J. Gabourie, J. Liu, H. Dong, J. Wu, Y. Chen, Z. Zhong, J. Sun, P. Erhart, Y. Su, T. Ala-Nissila, J. Chem. Phys. 157 (2022) 114801.
[579] J.S. Smith, B. Nebgen, N. Lubbers, O. Isayev, A.E. Roitberg, J. Chem. Phys. 148 (2018) 241733.
[580] S. Liu, J. Li, W. Xiao, R. Chen, Z. Sun, Y. Zhang, X. Lei, S. Hu, M. Kober-Czerny, J. Wang, F. Ren, Q. Zhou, H. Raza, Y. Gao, Y. Ji, S. Li, H. Li, L. Qiu, W. Huang, Y. Zhao, B. Xu, Z. Liu, H.J. Snaith, N.-G. Park, W. Chen, Nature 632 (2024) 536–542.
[581] R.L. Milot, G.E. Eperon, H.J. Snaith, M.B. Johnston, L.M. Herz, Adv. Funct. Mater. 25 (2015) 6218–6227.
[582] D.H. Kim, J. Park, Z. Li, M. Yang, J.S. Park, I.J. Park, J.Y. Kim, J.J. Berry, G. Rumbles, K. Zhu, Adv. Mater. 29 (2017) 1606831.
[583] Z. Guo, J.S. Manser, Y. Wan, P.V. Kamat, L. Huang, Nat. Commun. 6 (2015) 7471.
[584] Q. Dong, Y. Fang, Y. Shao, P. Mulligan, J. Qiu, L. Cao, J. Huang, Science 347 (2015) 967–970.
[585] S. Jana, E. Carlos, S. Panigrahi, R. Martins, E. Fortunato, ACS Nano 14 (2020) 14790–14797.
[586] D. Shi, V. Adinolfi, R. Comin, M. Yuan, E. Alarousu, A. Buin, Y. Chen, S. Hoogland, A. Rothenberger, K. Katsiev, Y. Losovyj, X. Zhang, P.A. Dowben, O. F. Mohammed, E.H. Sargent, O.M. Bakr, Science 347 (2015) 519–522.
[587] C. Wehrenfennig, M. Liu, H.J. Snaith, M.B. Johnston, L.M. Herz, Energy Environ. Sci. 7 (2014) 2269–2275.
[588] E.M. Hutter, G.E. Eperon, S.D. Stranks, T.J. Savenije, J. Phys. Chem. Lett. 6 (2015) 3082–3090.
[589] S.D. Stranks, G.E. Eperon, G. Grancini, C. Menelaou, M.J. Alcocer, T. Leijtens, L. M. Herz, A. Petrozza, H.J. Snaith, Science 342 (2013) 341–344.
[590] W. Rehman, R.L. Milot, G.E. Eperon, C. Wehrenfennig, J.L. Boland, H.J. Snaith, M.B. Johnston, L.M. Herz, Adv. Mater. 27 (2015) 7938–7944.
[591] G.E. Eperon, S.D. Stranks, C. Menelaou, M.B. Johnston, L.M. Herz, H.J. Snaith, Energy Environ. Sci. 7 (2014) 982–988.
[592] A.A. Zhumekenov, M.I. Saidaminov, M.A. Haque, E. Alarousu, S.P. Sarmah, B. Murali, I. Dursun, X.-H. Miao, A.L. Abdelhady, T. Wu, O.F. Mohammed, O. M. Bakr, ACS Energy Lett. 1 (2016) 32–37.
[593] V. Nketia-Yawson, B. Nketia-Yawson, J. Woong Jo, Appl. Surf. Sci. 623 (2023) 156984.
[594] W. Rehman, D.P. McMeekin, J.B. Patel, R.L. Milot, M.B. Johnston, H.J. Snaith, L. M. Herz, Energy Environ. Sci. 10 (2017) 361–369.
[595] R. Sheng, A. Ho-Baillie, S. Huang, S. Chen, X. Wen, X. Hao, M.A. Green, J. Phys. Chem. C 119 (2015) 3545–3549.
[596] J. Xing, Y. Zou, C. Zhao, Z. Yu, Y. Shan, W. Kong, X. Zheng, X. Li, W. Yu, C. Guo, Mater. Today Phys. 14 (2020) 100240.
[597] G. Maculan, A.D. Sheikh, A.L. Abdelhady, M.I. Saidaminov, M.A. Haque, B. Murali, E. Alarousu, O.F. Mohammed, T. Wu, O.M. Bakr, J. Phys. Chem. Lett. 6 (2015) 3781–3786.
[598] R. Ferreira, M. Shaikh, S.K. Jakka, J. Deuermeier, P. Barquinha, S. Ghosh, E. Fortunato, R. Martins, S. Jana, Nano Lett 22 (2022) 9020–9026.
[599] N.K. Noel, S.D. Stranks, A. Abate, C. Wehrenfennig, S. Guarnera, A.-A. Haghighirad, A. Sadhanala, G.E. Eperon, S.K. Pathak, M.B. Johnston, A. Petrozza, L.M. Herz, H.J. Snaith, Energy Environ. Sci. 7 (2014) 3061–3068.
[600] Y. Takahashi, H. Hasegawa, Y. Takahashi, T. Inabe, J. Solid State Chem. 205 (2013) 39–43.
[601] T. Matsushima, S. Hwang, A.S. Sandanayaka, C. Qin, S. Terakawa, T. Fujihara, M. Yahiro, C. Adachi, Adv. Mater. 28 (2016) 10275–10281.
[602] P. Sebastia-Luna, U. Pokharel, B.A.H. Huisman, L.J.A. Koster, F. Palazon, H. J. Bolink, ACS Appl. Energy Mater. 5 (2022) 10216–10223.
[603] H. Zhu, A. Liu, K.I. Shim, H. Jung, T. Zou, Y. Reo, H. Kim, J.W. Han, Y. Chen, H. Y. Chu, J.H. Lim, H.J. Kim, S. Bai, Y.Y. Noh, Nat. Commun. 13 (2022) 1741.
[604] J.Y. Go, H. Zhu, Y. Reo, H. Kim, A. Liu, Y.Y. Noh, ACS Appl. Mater. Interfaces 14 (2022) 9363–9367.
[605] A. Liu, H. Zhu, S. Kim, Y. Reo, Y.S. Kim, S. Bai, Y.Y. Noh, InfoMat 5 (2022) e12386.
[606] H. Zhu, W. Yang, Y. Reo, G. Zheng, S. Bai, A. Liu, Y.-Y. Noh, Nat. Electron. 6 (2023) 650–657.
[607] X. Yang, Y. Liu, S. Yang, Y. Wu, Y. Lei, Y. Yang, A. Liu, J. Chu, W. Li, Adv. Funct. Mater. 34 (2024) 2403917.
[608] W. Yang, G. Park, A. Liu, H.B. Lee, J.W. Kang, H. Zhu, Y.Y. Noh, Adv. Funct. Mater. 33 (2023) 2303309.
[609] A. Liu, H. Zhu, Y. Reo, M.-G. Kim, H.Y. Chu, J.H. Lim, H.-J. Kim, W. Ning, S. Bai, Y.-Y. Noh, Cell Rep. Phys. Sci. 3 (2022) 100812.
[610] H. Oga, A. Saeki, Y. Ogomi, S. Hayase, S. Seki, J. Am. Chem. Soc. 136 (2014) 13818–13825.
[611] T.J. Savenije, C.S. Ponseca Jr., L. Kunneman, M. Abdellah, K. Zheng, Y. Tian, Q. Zhu, S.E. Canton, I.G. Scheblykin, T. Pullerits, A. Yartsev, V. Sundstrom, J. Phys. Chem. Lett. 5 (2014) 2189–2194.
[612] M. Karakus, S.A. Jensen, F. D'Angelo, D. Turchinovich, M. Bonn, E. Canovas, J. Phys. Chem. Lett. 6 (2015) 4991–4996.
[613] Y.H. Chang, C.H. Park, J. Korean Phys. Soc. 44 (2004) 889–893.
[614] E. Menéndez-Proupin, P. Palacios, P. Wahnón, J.C. Conesa, Phys. Rev. B 90 (2014) 045207.
[615] G. Giorgi, J. Fujisawa, H. Segawa, K. Yamashita, J. Phys. Chem. Lett. 4 (2013) 4213–4216.
[616] P. Umari, E. Mosconi, F. De Angelis, Sci. Rep. 4 (2014) 4467.
[617] F. Brivio, K.T. Butler, A. Walsh, M. van Schilfgaarde, Phys. Rev. B 89 (2014) 155204.
[618] M. Hirasawa, T. Ishihara, T. Goto, K. Uchida, N. Miura, Physica B 201 (1994) 427–430.
[619] A. Miyata, A. Mitioglu, P. Plochocka, O. Portugall, J.T.-W. Wang, S.D. Stranks, H. J. Snaith, R.J. Nicholas, Nat. Phys. 11 (2015) 582–587.
[620] K. Galkowski, A. Mitioglu, A. Miyata, P. Plochocka, O. Portugall, G.E. Eperon, J. T.-W. Wang, T. Stergiopoulos, S.D. Stranks, H.J. Snaith, R.J. Nicholas, Energy Environ. Sci. 9 (2016) 962–970.
[621] Y. Peter, M. Cardona, Fundamentals of semiconductors: physics and materials properties, Springer Science & Business Media, 2010.
[622] F. Seitz, Phys. Rev. 73 (1948) 549.
[623] J. Bardeen, W. Shockley, Phys. Rev. 80 (1950) 72.
[624] Y. He, G. Galli, Chem. Mater. 26 (2014) 5394–5400.
[625] Y. Wang, Y. Zhang, P. Zhang, W. Zhang, Phys. Chem. Chem. Phys. 17 (2015) 11516–11520.
[626] Z.-G. Yu, J. Phys. Chem. Lett. 7 (2016) 3078–3083.
[627] A. Filippetti, A. Mattoni, C. Caddeo, M. Saba, P. Delugas, Phys. Chem. Chem. Phys. 18 (2016) 15352–15362.
[628] Y. Chen, H. Yi, X. Wu, R. Haroldson, Y. Gartstein, Y. Rodionov, K. Tikhonov, A. Zakhidov, X.-Y. Zhu, V. Podzorov, Nat. Commun. 7 (2016) 12253.
[629] S.A. Bretschneider, I. Ivanov, H.I. Wang, K. Miyata, X. Zhu, M. Bonn, Adv. Mater. 30 (2018) 1707312.
[630] K. Miyata, D. Meggiolaro, M.T. Trinh, P.P. Joshi, E. Mosconi, S.C. Jones, F. De Angelis, X.-Y. Zhu, Sci. Adv. 3 (2017) e1701217.
[631] S. Liu, R. Guo, F. Xie, Mater. Design 221 (2022) 110951.
[632] C. Motta, F. El-Mellouhi, S. Kais, N. Tabet, F. Alharbi, S. Sanvito, Nat. Commun. 6 (2015) 7026.
[633] K. Bhowmik, A. Dutta, M.K. Vyas, J. Ota, S.K. Hait, V. Kagdiyal, D. Saxena, S.S. V. Ramakumar, Electrochem. Sci. Adv. 2 (2021) e2100064.
[634] M.C. Gélvez-Rueda, D.H. Cao, S. Patwardhan, N. Renaud, C.C. Stoumpos, G. C. Schatz, J.T. Hupp, O.K. Farha, T.J. Savenije, M.G. Kanatzidis, F.C. Grozema, J. Phys. Chem. C 120 (2016) 16577–16585.
[635] T. Kirchartz, J.A. Márquez, M. Stolterfoht, T. Unold, Adv. Energy Mater. 10 (2020) 1904134.
[636] L. Krückemeier, Z. Liu, T. Kirchartz, U. Rau, Adv. Mater. 35 (2023) 2300872.
[637] L. Krückemeier, B. Krogmeier, Z. Liu, U. Rau, T. Kirchartz, Adv. Energy Mater. 11 (2021) 2003489.
[638] M.B. Johnston, L.M. Herz, Acc. Chem. Res. 49 (2016) 146–154.

[639] J.I. Khan, Y. Yang, J.R. Palmer, S.B. Tyndall, S. Chaudhuri, C. Liu, L. Grater, J. D. North, B. Chen, R.M. Young, G.C. Schatz, M.R. Wasielewski, M.G. Kanatzidis, D.F. Swearer, E.H. Sargent, Matter 7 (2024) 2536–2550.
[640] J.I. Khan, F.H. Isikgor, E. Ugur, W. Raja, G.T. Harrison, E. Yengel, T. D. Anthopoulos, S. De Wolf, F. Laquai, ACS Energy Lett. 6 (2021) 4155–4164.
[641] X. Chen, P.V. Kamat, C. Janáky, G.F. Samu, ACS Energy Lett. 9 (2024) 3187–3203.
[642] E. Ugur, J.I. Khan, E. Aydin, M. Wang, M. Kirkus, M. Neophytou, I. McCulloch, S. De Wolf, F. Laquai, J. Phys. Chem. Lett. 10 (2019) 6921–6928.
[643] L.M. Herz, Annu. Rev. Phys. Chem. 67 (2016) 65–89.
[644] J.S. Manser, P.V. Kamat, Nat. Photonics 8 (2014) 737–743.
[645] J. Shi, Y. Li, Y. Li, D. Li, Y. Luo, H. Wu, Q. Meng, Joule 2 (2018) 879–901.
[646] S.D. Stranks, V.M. Burlakov, T. Leijtens, J.M. Ball, A. Goriely, H.J. Snaith, Phys. Rev. Appl. 2 (2014) 034007.
[647] Y. Yuan, G. Yan, C. Dreessen, T. Rudolph, M. Hülsbeck, B. Klingebiel, J. Ye, U. Rau, T. Kirchartz, Nat. Materials 23 (2024) 391–397.
[648] Y. Yang, D.P. Ostrowski, R.M. France, K. Zhu, J. van de Lagemaat, J.M. Luther, M. C. Beard, Nat. Photonics 10 (2016) 53–59.
[649] C.M. Wolff, P. Caprioglio, M. Stolterfoht, D. Neher, Adv. Mater. 31 (2019) 1902762.
[650] M. Stolterfoht, P. Caprioglio, C.M. Wolff, J.A. Márquez, J. Nordmann, S. Zhang, D. Rothhardt, U. Hörmann, Y. Amir, A. Redinger, L. Kegelmann, F. Zu, S. Albrecht, N. Koch, T. Kirchartz, M. Saliba, T. Unold, D. Neher, Energy Environ. Sci. 12 (2019) 2778–2788.
[651] P. Caprioglio, J.A. Smith, R.D.J. Oliver, A. Dasgupta, S. Choudhary, M.D. Farrar, A.J. Ramadan, Y.-H. Lin, M.G. Christoforo, J.M. Ball, J. Diekmann, J. Thiesbrummel, K.-A. Zaininger, X. Shen, M.B. Johnston, D. Neher, M. Stolterfoht, H.J. Snaith, Nat. Commun. 14 (2023) 932.
[652] M. Stolterfoht, C.M. Wolff, J.A. Márquez, S. Zhang, C.J. Hages, D. Rothhardt, S. Albrecht, P.L. Burn, P. Meredith, T. Unold, D. Neher, Nat. Energy 3 (2018) 847–854.
[653] Y. Yamada, T. Nakamura, M. Endo, A. Wakamiya, Y. Kanemitsu, J. Am. Chem. Soc. 136 (2014) 11610–11613.
[654] M. Taddei, S. Jariwala, R.J.E. Westbrook, S. Gallagher, A.C. Weaver, J. Pothoof, M.E. Ziffer, H.J. Snaith, D.S. Ginger, ACS Energy Lett. 9 (2024) 2508–2516.
[655] V. D'Innocenzo, G. Grancini, M.J.P. Alcocer, A.R.S. Kandada, S.D. Stranks, M. M. Lee, G. Lanzani, H.J. Snaith, A. Petrozza, Nat. Commun. 5 (2014) 3586.
[656] Y. Gao, J. Liu, F.H. Isikgor, M. Wang, J.I. Khan, S. De Wolf, F. Laquai, ACS Appl. Mater. Interfaces 14 (2022) 34281–34290.
[657] W. Rehman, R.L. Milot, G.E. Eperon, C. Wehrenfennig, J.L. Boland, H.J. Snaith, M.B. Johnston, L.M. Herz, Adv. Mater. 27 (2015) 7938–7944.
[658] S.G. Motti, J.B. Patel, R.D.J. Oliver, H.J. Snaith, M.B. Johnston, L.M. Herz, Nat. Commun. 12 (2021) 6955.
[659] Q. Liu, Y. Yuan, J. Liu, W. Wang, J. Chen, W. Xu, Mater. Today Electron. 8 (2024) 100099.
[660] F. Du, X. Liu, J. Liao, D. Yu, N. Zhang, Y. Chen, C. Liang, S. Yang, G. Fang, Adv. Funct. Mater. 34 (2024) 2312175.
[661] B. Li, S. Li, J. Gong, X. Wu, Z. Li, D. Gao, D. Zhao, C. Zhang, Y. Wang, Z. Zhu, Chem 10 (2024) 35–47.
[662] N. Phung, A. Abate, Small 14 (2018) 1802573.
[663] W.B. Han, G.-J. Ko, K.-G. Lee, D. Kim, J.H. Lee, S.M. Yang, D.-J. Kim, J.-W. Shin, T.-M. Jang, S. Han, H. Zhou, H. Kang, J.H. Lim, K. Rajaram, H. Cheng, Y.-D. Park, S.H. Kim, S.-W. Hwang, Nat. Commun. 14 (2023) 2263.
[664] W. Hui, L. Chao, H. Lu, F. Xia, Q. Wei, Z. Su, T. Niu, L. Tao, B. Du, D. Li, Y. Wang, H. Dong, S. Zuo, B. Li, W. Shi, X. Ran, P. Li, H. Zhang, Z. Wu, C. Ran, L. Song, G. Xing, X. Gao, J. Zhang, Y. Xia, Y. Chen, W. Huang, Science 371 (2021) 1359–1364.
[665] L.-W. Chen, W.-C. Wang, S.-H. Ko, C.-Y. Chen, C.-T. Hsu, F.-C. Chiao, T.-W. Chen, K.-C. Wu, H.-W. Lin, Adv. Intell. Syst. 3 (2021) 2000196.
[666] Z. Xu, S.-H. Chin, B.-I. Park, Y. Meng, S. Kim, S. Han, Y. Li, D.-H. Kim, B.-S. Kim, J.-W. Lee, S.-H. Bae, Next Mater 3 (2024) 100103.
[667] G. Wang, D. Li, H.-C. Cheng, Y. Li, C.-Y. Chen, A. Yin, Z. Zhao, Z. Lin, H. Wu, Q. He, M. Ding, Y. Liu, Y. Huang, X. Duan, Sci. Adv. 1 (2015) e1500613.
[668] S. Poddar, Y. Zhang, L. Gu, D. Zhang, Q. Zhang, S. Yan, M. Kam, S. Zhang, Z. Song, W. Hu, L. Liao, Z. Fan, Nano Lett 21 (2021) 5036–5044.
[669] Y. Zhang, S. Poddar, H. Huang, L. Gu, Q. Zhang, Y. Zhou, S. Yan, S. Zhang, Z. Song, B. Huang, G. Shen, Z. Fan, Sci. Adv. 7 (2021) eabg3788.
[670] Y. Zhang, Z. Ma, Z. Chen, S. Poddar, Y. Zhu, B. Han, C.L.J. Chan, Y. Ding, X. Kong, Z. Fan, Adv. Intell. Syst. 6 (2024) 2300586.
[671] Z. Long, X. Qiu, C.L.J. Chan, Z. Sun, Z. Yuan, S. Poddar, Y. Zhang, Y. Ding, L. Gu, Y. Zhou, W. Tang, A.K. Srivastava, C. Yu, X. Zou, G. Shen, Z. Fan, Nat. Commun. 14 (2023) 1972.
[672] T.-K. Su, W.-K. Cheng, C.-Y. Chen, W.-C. Wang, Y.-T. Chuang, G.-H. Tan, H.-C. Lin, C.-H. Hou, C.-M. Liu, Y.-C. Chang, J.-J. Shyue, K.-C. Wu, H.-W. Lin, ACS Nano 16 (2022) 12979–12990.
[673] S. Liu, Z. Cheng, M.-Y. Li, S. Liu, H. Lu, X. Wen, C. Wang, X. Ding and L. Wang, *Matter*, 2024, 7, 2810-2825.
[674] C.C. Li, T.Yu Huang, Y.H. Lai, Y.C. Huang, C.S. Tan, Mater. Today Electron. 8 (2024) 100095.
[675] Y. Park, L.-S. Lee, J. Phys. Chem. Lett. 13 (2022) 5638–5647.
[676] S. Lee, J. Son, B. Jeong, Mater. Today Electron. 9 (2024) 100114.
[677] W. Hu, W. Huang, S. Yang, X. Wang, Z. Jiang, X. Zhu, H. Zhou, H. Liu, Q. Zhang, X. Zhuang, J. Yang, D.H. Kim, A. Pan, Adv. Mater. 29 (2017) 1703256.
[678] B. Li, F. Xia, B. Du, S. Zhang, L. Xu, Q. Su, D. Zhang, J. Yang, Adv. Sci. 11 (2024) 2310263.
[679] E.J. Yoo, M. Lyu, J.-H. Yun, C.J. Kang, Y.J. Choi, L. Wang, Adv. Mater. 27 (2015) 6170–6175.
[680] X. Guan, Z. Lei, X. Yu, C.H. Lin, J.K. Huang, C.Y. Huang, L. Hu, F. Li, A. Vinu, J. Yi, T. Wu, Small 18 (2022) 2203311.
[681] B.W. Zhang, C.H. Lin, S. Nirantar, E. Han, Y. Zhang, Z. Wang, M. Lyu, L. Wang, Small Struct. (2024) 2300524.
[682] J.-Y. Seo, J. Choi, H.-S. Kim, J. Kim, J.-M. Yang, C. Cuhadar, J.S. Han, S.-J. Kim, D. Lee, H. Jang, N.-G. Park, Nanoscale 9 (2017) 15278–15285.
[683] Y. Park, J.-S. Lee, ACS Appl. Mater. Interfaces 14 (2022) 4371–4377.
[684] S. Lee, H. Kim, D.H. Kim, W.B. Kim, J.M. Lee, J. Choi, H. Shin, G.S. Han, H. W. Jang, H.S. Jung, ACS Appl. Mater. Interfaces 12 (2020) 17039–17045.
[685] S.I. Kim, Y. Lee, M.H. Park, G.T. Go, Y.H. Kim, W. Xu, H.D. Lee, H. Kim, D.G. Seo, W. Lee, T.-W. Lee, Adv. Electron. Mater. 5 (2019) 1900008.
[686] B. Li, W. Hui, X. Ran, Y. Xia, F. Xia, L. Chao, Y. Chen, W. Huang, J. Mater. Chem. C 7 (2019) 7476–7493.
[687] S.P. Senanayak, K. Dey, R. Shivanna, W. Li, D. Ghosh, Y. Zhang, B. Roose, S. J. Zelewski, Z. Andaji-Garmaroudi, W. Wood, N. Tiwale, J.L. MacManus-Driscoll, R.H. Friend, S.D. Stranks, H. Sirringhaus, Nat. Mater. 22 (2023) 216–224.
[688] J.Y.W. Seto, J. Appl. Phys. 46 (1975) 5247–5254.
[689] K. Myny, Nat. Electron. 1 (2018) 30.
[690] Y.-H. Lin, Nat. Electron. 7 (2024) 430–431.
[691] D. Meggiolaro, D. Ricciarelli, A.A. Alasmari, F.A.S. Alasmary, F. De Angelis, J. Phys. Chem. Lett. 11 (2020) 3546–3556.
[692] S.G. Motti, D. Meggiolaro, S. Martani, R. Sorrentino, A.J. Barker, F. De Angelis, A. Petrozza, Adv. Mater. 31 (2019) 1901183.
[693] R.N. Bukke, O.A. Syzgantseva, M.A. Syzgantseva, K. Aidinis, A. Soultati, A. Verykios, M. Tountas, V. Psycharis, T. Alshahrani, H. Ullah, L.P. Zorba, G. C. Vougioukalakis, J. Wang, X. Bao, J. Jang, M.K. Nazeeruddin, M. Vasilopoulou, A.R. b. Mohd Yusoff, Nat. Electron. 7 (2024) 444–453.
[694] A. Liu, H. Zhu, Y. Reo, M.-G. Kim, H.Y. Chu, J.H. Lim, H.-J. Kim, W. Ning, S. Bai, Y.-Y. Noh, Cell. Rep. Phys. Sci. 3 (2022) 100812.
[695] J.-J. Cao, Y.-H. Lou, K.-L. Wang, Z.-K. Wang, J. Mater. Chem. C 10 (2022) 7423–7436.
[696] S. Shao, W. Talsma, M. Pitaro, J. Dong, S. Kahmann, A.J. Rommens, G. Portale, M. A. Loi, Adv. Funct. Mater. 31 (2021) 2008478.
[697] C.R. Kagan, D.B. Mitzi, C.D. Dimitrakopoulos, Science 286 (1999) 945–947.
[698] T. Matsushima, S. Hwang, A.S.D. Sandanayaka, C. Qin, S. Terakawa, T. Fujihara, M. Yahiro, C. Adachi, Adv. Mater. 28 (2016) 10275–10281.
[699] H. Zhu, A. Liu, K.I. Shim, J. Hong, J.W. Han, Y.-Y. Noh, Adv. Mater. 32 (2020) 2002717.
[700] T. Nakamura, S. Yakumaru, M.A. Truong, K. Kim, J. Liu, S. Hu, K. Otsuka, R. Hashimoto, R. Murdey, T. Sasamori, H.D. Kim, H. Ohkita, T. Handa, Y. Kanemitsu, A. Wakamiya, Nat. Commun. 11 (2020) 3008.
[701] J.G. Labram, D.H. Fabini, E.E. Perry, A.J. Lehner, H. Wang, A.M. Glaudell, G. Wu, H. Evans, D. Buck, R. Cotta, L. Echegoyen, F. Wudl, R. Seshadri, M.L. Chabinyc, J. Phys. Chem. Lett. 6 (2015) 3565–3571.
[702] A.R. Pininti, J.M. Ball, M.D. Albaqami, A. Petrozza, M. Caironi, ACS Appl. Energy Mater. 4 (2021) 10603–10609.
[703] W. Yang, G. Park, A. Liu, H.B. Lee, J.-W. Kang, H. Zhu, Y.-Y. Noh, Adv. Funct. Mater. 33 (2023) 2303309.
[704] B. Jeong, H. Han, C. Park, Adv. Mater. 32 (2020) 2000597.
[705] I. Chung, B. Lee, J. He, R.P.H. Chang, M.G. Kanatzidis, Nature 485 (2012) 486–489.
[706] S.J. Lee, S.S. Shin, Y.C. Kim, D. Kim, T.K. Ahn, J.H. Noh, J. Seo, S.I. Seok, J. Am. Chem. Soc. 138 (2016) 3974–3977.
[707] A. Liu, H. Zhu, S. Kim, Y. Reo, Y.-S. Kim, S. Bai, Y.-Y. Noh, InfoMat 5 (2023) e12386.
[708] Y. Reo, T. Choi, J.-Y. Go, S. Jeon, B. Lim, H. Zhu, A. Liu, Y.-Y. Noh, ACS Energy Lett 8 (2023) 3088–3094.
[709] A. Liu, H. Zhu, S. Bai, Y. Reo, T. Zou, M.-G. Kim, Y.-Y. Noh, Nat. Electron. 5 (2022) 78–83.
[710] H. Zhu, A. Liu, K.I. Shim, H. Jung, T. Zou, Y. Reo, H. Kim, J.W. Han, Y. Chen, H. Y. Chu, in: J.H. Lim, H.-J. Kim, S. Bai, Y.-Y. Noh (Eds.), Nat. Commun. 13 (2022) 1741.
[711] G. Park, W. Yang, A. Liu, H. Zhu, F. De Angelis, Y.-Y. Noh, Mater. Sci. Eng.: R: Rep. 159 (2024) 100806.
[712] Y. Reo, H. Zhu, A. Liu, Y.-Y. Noh, Adv. Funct. Mater. 32 (2022) 2204870.
[713] J.-H. Kim, C.-M. Oh, I.-W. Hwang, K. Park, K. Lee, Adv. Funct. Mater. 35 (2024) 2411836.
[714] X.-J. She, C. Chen, G. Divitini, B. Zhao, Y. Li, J. Wang, J.F. Orri, L. Cui, W. Xu, J. Peng, S. Wang, A. Sadhanala, H. Sirringhaus, Nat. Electron. 3 (2020) 694–703.
[715] T. Matsushima, K. Fujita, T. Tsutsui, Japanese J. Appl. Phys. 43 (2004) L1199.
[716] T. Soto-Montero, S. Kralj, W. Soltanpoor, J.S. Solomon, J.S. Gómez, K.P.S. Zanoni, A. Paliwal, H.J. Bolink, C. Baeumer, A.P.M. Kentgens, M. Morales-Masis, Adv. Funct. Mater. 34 (2023) 2300588.